Defense Threat Reduction Agency
8725 John J. Kingman Road, MS 6201
Fort Belvoir, VA 22060-6201

TECHNICAL REPORT

Analysis of Russian Hydroacoustic Data

Approved for public release; distribution is unlimited.

November 2004

DISTRIBUTION LIST UPDATE

This mailer is provided to enable DTRA to maintain current distribution lists for reports. (We would appreciate you providing the requested information.)

☐ Add the individual listed to your distribution list.

☐ Delete the cited organization/individual.

☐ Change of address.

Note:
Please return the mailing label from the document so that any additions, changes, corrections or deletions can be made easily. For distribution cancellation or more information call DTRA/BDMI (703) 767-4724.

NAME: _____

ORGANIZATION: _____

OLD ADDRESS	NEW ADDRESS
_____	_____
_____	_____
_____	_____

TELEPHONE NUMBER: ( ) _____

DTRA PUBLICATION NUMBER/TITLE	CHANGES/DELETIONS/ADDITONS, etc. *(Attach Sheet if more Space is Required)*
_____	_____
_____	_____
_____	_____

DTRA or other GOVERNMENT CONTRACT NUMBER: _____

CERTIFICATION of NEED-TO-KNOW BY GOVERNMENT SPONSOR (if other than DTRA):

SPONSORING ORGANIZATION: _____

CONTRACTING OFFICER or REPRESENTATIVE: _____

SIGNATURE: _____

DEFENSE THREAT REDUCTION AGENCY
ATTN: BDMI
8725 John J. Kingman Road, MS-6201
Ft Belvoir, VA 22060-6201

REPORT DOCUMENTATION PAGE

Form Approved
OMB No. 0704-0188

1. AGENCY USE ONLY (Leave Blank)	2. REPORT DATE 041100	3. REPORT TYPE AND DATES COVERED Technical 970926 – 001231

4. TITLE AND SUBTITLE

Analysis of Russian Hydroacoustic Data

5. FUNDING NUMBERS

DSWA 01-97-C-0166
PE-RDT&E
PR-CD
TA-CD
WU-DH65161

6. AUTHORS

Mariana Eneva
Jeffry L. Stevens
John Murphy

7. PERFORMING ORGANIZATION NAME(S) AND ADDRESS(ES)

Science Applications International Corporation
10260 Campus Point Drive
San Diego, CA 92121-1578

8. PERFORMING ORGANIZATION REPORT NUMBER

MTSD-DTR-00-16641

9. SPONSORING / MONITORING AGENCY NAME(S) AND ADDRESS(ES)

Defense Threat Reduction Agency
8725 John J. Kingman Road, MS 6201
Fort Belvoir, VA 22060-6201

10. SPONSORING / MONITORING AGENCY REPORT NUMBER

DTRA-TR-01-19

11. SUPPLEMENTARY NOTES

12a. DISTRIBUTION / AVAILABILITY STATEMENT

Approved for public release; distribution is unlimited.

12b. DISTRIBUTION CODE

13. ABSTRACT (Maximum 200 words)

The objective of this project is to better understand the coupling of energy from explosions near the water surface. The Institute of Dynamics of the Geospheres (IDG) has provided unique historical hydroacoustic data from Russian archives, featuring various combinations of depths of explosion, and distances and depths of recording. We analyze and model peak-pressure measurements and hydrophone records from two underwater and one above-water nuclear explosions in Novaya Zemlya, as well as digitized data set from 100-kg TNT explosions in a reservoir. Observations are compared with theoretical estimates of pressure coupling coefficients (EM-1 manual), REFMS software predictions of shock waves from underwater explosions, and LLNL modeling results. The observed pressure coupling coefficient of ~4% for the above-water nuclear explosion is in the range of 30% to 60%, depending on distance; this is in agreement with the REFMS predictions, but different from the EM-1 estimates, which are independent of distance. All results suggest that a shallow 1-kt explosion should be detectable by the IMS hydroacoustic network. We provide an edited version of the IDG report, along with the original report and data.

14. SUBJECT TERMS

Hydroacoustics
Novaya Zemlya
Underwater explosions
Historic Russian Data

15. NUMBER OF PAGES 193

16. PRICE CODE

17. SECURITY CLASSIFICATION OF REPORT UNCLASSIFIED	18. SECURITY CLASSIFICATION OF THIS PAGE UNCLASSIFIED	19. SECURITY CLASSIFICATION OF ABSTRACT UNCLASSIFIED	20. LIMITATION OF ABSTRACT SAR

NSN 7540-01-280-5500

Standard Form 298 (Rev. 2-89)
Prescribed by ANSI Std. Z39-1
298-102

i

CLASSIFIED BY:

N/A, UNCLASSIFIED

DECLASSIFY ON:

N/A, UNCLASSIFIED

6. AUTHOR(S) (Continued)

Boris Khristoforov
Vitaly Adushkin

7. PERORMING ORGANIZATION NAME(S) AND ADDRESS(ES) (Continued)

Institute of Dynamics of Geospheres
Leninsky Prosp. 38 Kor. 2
117334 Moscow
Russia

SUMMARY

The objective of this project is to better understand the coupling of energy from explosions near the water surface. This is important to CTBT (Comprehensive Nuclear-Test-Ban Treaty) monitoring, because the hydroacoustic energy from such blasts is greatly diminished by comparison with deeply immersed charges. Consequently, explosions in the ocean may be more difficult to identify if they are on or near the ocean surface. In a collaborative effort with researchers from the Institute for Dynamics of the Geosphere (IDG) at the Russian Academy of Sciences, we examine, analyze and model unique historic hydroacoustic data from the Russian archives. We received diverse data sets from IDG, but for the purposes of this project we concentrate on records featuring various combinations of depths of explosion, and distances and depths of recording. We analyze two types of data: (1) peak pressure measurements and hydrophone records from nuclear explosions, and (2) a comprehensive digitized data set from 100-kg TNT explosions in a reservoir. We model the Russian observations using the REFMS code for modeling of shock-wave reflection and refraction in multi-layered ocean and ocean bottoms. We also study Russian publications reporting on the HE experiments and make comparisons with existing relationships depicting the dependence of the coupling coefficient on charge depth/height.

A number of near-surface nuclear blasts were carried out in or above the shallow waters (≤ 60 m) of the Bay of Chernaya (Novaya Zemlya) in the late 50's and early 60's. Data is available from three of these explosions. The first underwater nuclear blast (October 10, 1957) was reported as yield 10 kt and charge depth 30 m. Seven peak-pressure measurements are available from this explosion, which average about 300 kg/cm^2 at a 235-m distance and sensor depths 10 to 50 m. Hydrophone records from the two other nuclear blasts (October 23 and 27, 1961) are available at much larger distances, 35 km to 160 km, at sensor depths of 1 m above the bottom. These records show levels of sound pressure measured in three different bands from low to high frequencies. The records from the first of these nuclear explosions, of yield 4.8 kt and charge depth 20 m, indicate peak levels of sound pressure between 103 dB and 125 dB. The records from the second 1961 nuclear explosion, of 16-kt yield and height above water 1.1 m, show levels between 90 dB and 130 dB, with the pressure of the direct shock wave being diminished to ~4% of the pressure that would have been observed in unbounded water. Distinct arrivals are seen for both 1961 blasts, including direct shock waves in water, refractions in the crust and the bottom layers, and signals corresponding to the sound speed of shock waves in air.

Data sets have also become available from explosions of 100-kg TNT cast spherical charges in a shallow reservoir (87 m length, 25 m to 55 m width, and 3 m depth) with a low-velocity air-saturated layer of sand on the bottom. 29 tests were conducted with varying water level and charge depths from 0 to 2.75 m. Measurements of pressures and impulse were taken at varying depths and horizontal distances in the water. Of these, we analyzed and modeled with the REFMS code twelve explosions carried out in a full pool (3-m water level). The modeling results match the peak-pressure observations rather well, especially in mid-pool, where the measurements suggest free-water-like environment. The estimated pressure coupling coefficients for the shallowest charges, in the range of 30% to 60%, are compared with existing relationships. We find that while these relationships predict coupling to be independent of distance to sensor,

our estimates based on the Russian HE data decrease with distance. This suggests that the coupling is more complex than in theory and may have to be adjusted for more accurate modeling of the effect of charge depth.

We also used REFMS to simulate peak-pressure measurements and pressure-time histories at 10 km distance from hypothetical 1-kt and 10-kt nuclear explosions conducted at various depths in the ocean. The ocean water in this simulation is characterized by a realistic sound velocity profile featuring a velocity minimum at 700 m depth. Modeled measurements at that same depth predict at least a tenfold increase in peak pressures from explosions in the SOFAR channel as compared with very shallow explosions (e.g., ~ 3 m depth).

The observations and the modeling results were also compared with predictions calculated at the Lawrence Livermore National Laboratory using a different modeling approach. All results suggest that although the coupling is reduced for very shallow explosions, a shallow 1-kt explosion should be detectable by the IMS hydroacoustic network.

IDG provided data in addition to those directly used in this project, along with extensive text material including numerous figures and descriptions of all data. Based on ongoing communication with our Russian collaborators, we clarified and edited the IDG text. This edited version is made available as part of the final products of this project, along with electronic files containing the original IDG report and data.

PREFACE

Conversion Table

Conversion factors for U.S. Customary to metric (SI) units of measurement

MULTIPLY → TO GET ←	BY → BY ←	TO GET DIVIDE
angstrom	1.000 000 X E -10	meters (m)
atmosphere (normal)	1.013 25 X E +2	kilo pascal (kPa)
bar	1.000 000 X E +2	kilo pascal (kPa)
barn	1.000 000 X E -28	meter^2 (m^2)
British thermal unit (thermochemical)	1.054 350 X E +3	joule (J)
calorie (thermochemical)	4.184 000	joule (J)
cal (thermochemical)/cm^2	4.184 000 X E -2	mega joule/m^2 (MJ/m^2)
curie	3.700 000 C E +1	* giga becquerel (GBq)
degree (angle)	1.745 329 X E -2	radian (rad)
degree Fahrenheit	$t_k = (t°f + 459.67)/1.8$	degree kelvin (K)
electron volt	1.602 19 X E -19	joule (J)
erg	1.000 000 X E -7	joule (J)
erg/second	1.000 000 X E -7	watt (W)
foot	3.048 000 X E -1	meter (m)
foot-pound-force	1.355 818	joule (J)
gallon (U.S. liquid)	3.785 412 X E -3	meter^3 (m^3)
inch	2.540 000 X E -2	meter (m)
jerk	1.000 000 X E +9	joule (J)
joule/kilogram (J/kg) (radiation dose absorbed)	1.000 000	Gray (Gy)
kilotons	4.183	terajoules
kip (1000 lbf)	4.448 222 X E +3	newton (N)
kip/inch^2 (ksi)	6.894 757 X E +3	kilo pascal (kPa)
ktap	1.000 000 X E +2	newton-second/m^2 (N-s/m^2)
micron	1.000 000 X E -6	meter (m)
mil	2.540 000 X E -5	meter (m)
mile(international)	1.609 344 X E +3	meter (m)
ounce	2.834 952 X E -2	kilogram (kg)
pound-force (lbs avoirdupois)	4.448 222	newton (N)
pound-force inch	1.129 848 X E -1	newton-meter (N•m)
pound-force/inch	1.751 268 X E +2	newton/meter (N/m)
pound-force/foot^2	4.788 026 X E -2	kilo pascal (kPa)
pound-force/inch^2 (psi)	6.894 757	kilo pascal (kPa)
pound-mass (lbm avoirdupois)	4.535 924 X E -1	kilogram (kg)
pound-force/foot^2 (moment of inertia)	4.214 011 X E -2	kilogram-meter^2 (kg•m^2)
pound-mass/foot^3	1.601 846 X E +1	kilogram-meter^3 (kg•m^3)
rad (radiation dose absorbed)	1.000 000 X E -2	** Gray (Gy)
roentgen	2.579 760 X E -4	coulomb/kilogram (C/kg)
shake	1.000 000 X E -8	second (s)
slug	1.459 390 X E +1	kilogram (kg)
torr (mm HG, 0°C)	1.333 22 X E -1	kilo pascal (kPa)

* The becquerel (Bq) is the SI unit of radioactivity; 1Bq = 1 event/s.

** The Gray (GY) is the SI unit of absorbed radiation.

A more complete listing of conversions may be found in "Metric Practice Guide E 380-74,"
American Society for Testing and Materials.

TABLE OF CONTENTS

FIGURES

FIGURES (CONTINUED)

SECTION 1
INTRODUCTION

As part of a collaborative research program for the purpose of monitoring the Comprehensive Nuclear-Test-Ban Treaty (CTBT), we examine and analyze hydroacoustic data from underwater explosions conducted in the former Soviet Union. The CTBT hydroacoustic network consists of 11 stations that monitor the oceans for underwater explosions, as well as for atmospheric explosions conducted close to the ocean surface. The reason such a small network can monitor the whole world is that hydroacoustic waves propagate very efficiently in the acoustic waveguide known as the world sound channel, or the SOFAR channel (e.g. Walker et al., 1992). Since a significant portion of the energy from underwater explosions couples to this channel as acoustic waves, even kilogram-sized explosions at depth generate signals easily observable at large distances. For example, Stevens et al. (1999) discuss hydroacoustic signals from four-pound charges detonated off the coast of San Francisco that were recorded as far away as Wake Island, a distance of about 7,000 km.

The coupled energy is the energy transferred from the source to the water, manifested as a point-source explosion generating an initially spherically divergent underwater shock wave. The amount of energy coupled to the water depends strongly on the explosion depth. Of interest to the CTBT are shallow and surface sources, as the explosion energy from such tests would be significantly decoupled from the ocean and could be much more difficult to detect. Thus while small deep explosions generate signals easily observable at great distances in the SOFAR channel, shallow and surface explosions produce signals of significantly diminished energy. Understanding the difference in coupling from deep underwater explosions versus shallow and near surface explosions is therefore very important.

In light of this, finding, analyzing and modeling hydroacoustic data featuring various combinations of explosion depths and distances to sensors, can be very useful in evaluating and modeling the difference in the effects of fully-immersed and shallow charges. Unique historic Russian hydroacoustic data have become available recently, consisting of a number of such measurements. We are using these data as constraints on modeling the hydroacoustic source as a function of depth below the water surface. The focus in this work is on analyzing and modeling data from Russian nuclear explosions near the water surface, as well as data from smaller-scale HE explosions (100-kg TNT) in a shallow reservoir. Scaling rules can be applied to relate smaller explosions to the nuclear explosions of interest to the CTBT. Most of the results described in this report are discussed by Eneva et al. (1999, 2000, 2001).

The nuclear explosions analyzed in this project include two underwater and one above-water nuclear blasts in the shallow Bay of Chernaya, Novaya Zemlya, detonated in 1957 and 1961 (*USSR Nuclear Weapons Tests and Peaceful Nuclear Explosions 1949 through 1990*, 1996). The available data from these explosions are copies of hydrophone records at several distances. Although limited, these data do make it possible to identify some arrivals in the records and speculate on the effect of charge depth/height on the energy coupling.

The small-scale HE explosions analyzed and modeled in the project were carried out in a reservoir with air-saturated sand on the bottom (Kozachenko and Khristoforov, 1970; Korobeinikov and Khristoforov, 1976). The available data include a complete digitized data set of pressure- and impulse-time histories and shock-wave parameters (peak pressures, specific impulse, pulse duration, and energy estimates) from twenty-nine 100-kg TNT experiments. The digitized time histories of pressure and impulse consist of 222 hydroacoustic records each, 36 records in air, and 50 in ground. Here we analyze and model the hydroacoustic data from twelve experiments performed in a full reservoir (3-m water level). These are more relevant analogues for our purpose, as we seek to evaluate the effect of shallow explosions in relatively deep water, from which signals are likely to propagate to large distances in the SOFAR channel. In contrast, signals from explosions in shallow water are greatly diminished and are unlikely to reach the sound channel above-noise level. The remaining seventeen 100-kg TNT tests, carried out in very shallow water (1-m and 0.5-m water level), are not considered at this time. Also, although we did examine the records in air and ground from all explosions, their analysis is left for future work.

Understanding the effects of underwater explosions is largely based on measurements and modeling of the related shock waves and bubble pulsations (e.g. NRC, 1997). During the early stages of an underwater explosion, the materials of the device attain high temperatures and pressures. Energy acquired by these materials heats and compresses the surrounding water. This mechanism forms a hydrodynamic compression wave that moves outward at a faster rate than the material it engulfs. An almost instantaneous increase in pressure occurs at the shock front, while the pressure decreases more gradually behind it. This is the primary shock wave. As the shock front moves away from the source region, energy dissipated as heat raises the temperature of the ambient water, with the largest temperature increase occurring near the center of the explosion. This causes both vaporization and dissociation of water in the explosion center, while at greater distances the water is vaporized into steam, forming an expanding steam bubble. If the explosion is deep enough, several cycles of bubble expansions and contractions may occur, resulting in progressively weaker pulses. Both the small-scale Russian experiments and the underwater nuclear explosions were conducted in shallow water, so that the hydroacoustic data analyzed here do not include bubble pulses.

As part of this project, the shock-wave data were modeled using a numerical code for modeling of surface reflections, and bottom reflections and refractions due to sound-velocity gradients, known as REFMS (e.g., Britt, 1986). This code is also discussed at some length in *Handbook of Nuclear Weapon Effects* (1996) – further referred to as *EM-1* (1996). REFMS uses spherical wavefronts and finite-element calculations taking into account deviations from acoustic properties, i.e., nonlinear effects. Although shallow-water and near-surface blasts are known to be particularly difficult to model accurately, many of the measurements in the Russian explosions are predicted very well using this modeling. REFMS is also used here to simulate pressure-time histories and maximum peak pressures from 1-kt and 10-kt nuclear sources detonated in the ocean, in the presence of a realistic sound-velocity profile.

Furthermore, the observations and the REFMS modeling results are compared with a different type of modeling performed by a group at the Lawrence Livermore National Laboratory (LLNL), linking two different computational codes for strong- and weak-shock calculations (Clarke et al., 1995). We find that rates of change in peak pressures as charge depth increases in the Russian

data are very similar to that predicted by REFMS, and somewhat similar to the LLNL predictions. However, the LLNL calculations for nuclear explosions appear to be much more similar to the high-explosive (HE) predictions of REFMS than to the nuclear REFMS calculations. The latter reach full coupling for much shallower explosion depths than in the hydrodynamic modeling. In any case, these different approaches to modeling are not directly comparable and the relevance of small-scale HE tests to the study of the effect of charge depth of nuclear underwater explosions is not well understood.

We note that IDG provided data additional to the ones directly used in this project, along with extensive text and figures describing all data. These include materials on explosions of 136-kg bombs in the Sea of Okhotsk, a detonation of a 500-kg cord in the Black Sea, and underground nuclear explosions. Based on ongoing communication with our Russian collaborators, we clarified and edited the IDG text, in an effort to facilitate its potential readers. This edited version is included in Appendix A to our report. The original text and data submitted by IDG is made available in electronic form. These files are described in Appendix B.

The final products of this project are as follows:

(1) Our analysis of IDG data
(2) Edited version of Russian (IDG) report
(3) Unedited version of IDG report
(4) IDG digitized data

SECTION 2
CLASSIC RELATIONSHIPS FOR UNDERWATER EXPLOSIONS

Impulse, pulse duration, and energy in boundless (free) water have been discussed in the classic work of Cole (1948). The pressure of the shock wave P (overpressure above the hydrostatic pressure), as a function of time t after arrival of the shock wave, is given by $P(t) = P_{max}e^{-t/\theta}$, where P_{max} is the initial peak pressure, and θ is so-called time constant, i.e., the time over which the pressure-time history can be approximated with an exponential decay. For many purposes, the effect of a shock wave depends on the time-integral of pressure, or impulse, more significantly than on the detailed form of pressure change with time. The specific impulse of unit area of the shock wavefront, up to a time τ after its arrival, is given by $I(\tau) = \int_0^\tau P(t)\,dt$. Another significant measure of the shock wave is energy flux density, E_f, representing the energy flux across unit area of a fixed surface normal to the direction of propagation (often referred to as energy flux, or simply energy); $E_f(\tau) \sim \int_0^\tau P^2(t)\,dt$. All these parameters can be represented by power laws $\sim 1/R^\alpha$, where R is distance from source and α is a constant. The empirical relationships given by Cole (1948) for HE charges of TNT, after modification of the units to accommodate the small-scale experiments of 100-kg TNT, are as follows:

$$P_{max} = 533(W^{1/3}/R)^{1.13} \qquad I = 588\,W^{1/3}(W^{1/3}/R)^{0.89} \qquad E_f = 8300\,W^{1/3}$$

$$(W^{1/3}/R)^{2.05}, \tag{2.1}$$

where W is yield in kg, and the impulse and energy flux are estimated in time $\tau = 6.6\theta$. The units in eq. (1) are m for distance, kg/cm^2 for pressure, $kg*s/m^2$ for impulse, and $kg*m/m^2$ for energy flux. These relationships show that the peak pressure decreases with distance faster than an inversely proportional relationship (i.e., than acoustic approximation would imply), while the energy decreases faster than inversely proportional to the square root of the distance.

Existing relationships for coupling coefficients.

In an attempt to put the observations in perspective, we searched for relevant literature discussing coupling for shallow and above-water explosions. The *EM-1* (1996) manual lists relationships between pressure coupling coefficients and depth/height of blast, derived from theory of radiation hydrodynamics for low-yield non-radiative (<1 kt), high-yield radiative (>20 kt), and intermediate-yield (1 to 20 kt) nuclear explosions. The coupling coefficient, ε, is given as a function of charge depth/height x, and is used to estimate the direct shock-wave peak pressure:

$$P_{max} = A\varepsilon/R^n$$

$$A = 10^4(217.6)^n$$

$$n = 1.4e^{-D/35.4} + 1.13 \ \ \text{for } 2.5 \le D \le 100$$

$$\varepsilon_L = 0.2 \exp\{1.268[\exp(0.76x) - 1] + 0.128x\}; \qquad \text{for } -10 \le x \le 0$$
$$= 0.2 \exp\{1.109[1 - \exp(-0.36x - 0.011x^2)] + 0.0334x\}; \qquad \text{for } 0 \le x \le 15$$

$$\varepsilon_H = 0.00357 \exp\{3.05[1 - \exp(F)] - 0.000486(0.333 - x)^3\}; \qquad \text{for } -10 \le x \le 0$$
$$= 0.018 \exp(2.967x); \qquad \text{for } 0 \le x \le 0.82$$
$$= 0.205 \exp\{1.109[1 - \exp(G)] + 0.0336(x - 0.82)\}; \qquad \text{for } 0.82 \le x \le 15$$

$$\varepsilon_I = \varepsilon_H - (W - 20)(\varepsilon_L - \varepsilon_H)/19$$

$$\varepsilon_{HE} = 0.47 \exp[0.125(x + 11.67)^{2/3}]$$

In the above equations, scaled distance (R) is in $ft/kt^{1/3}$; pressure P_{max} is in psi; the coefficient A is in $psi\text{-}(ft/kt^{1/3})^n$; D is scaled sensor depth in $fr/kt^{1/3}$; x is scaled depth of explosion in $ft/kt^{1/3}$ (negative values are height above water surface); the subscripts L, H, and I indicate low-yield, high-yield and intermediate-yield nuclear sources; the subscript HE denotes high-explosive sources; W is yield in kt; and F and G are cubic and quadratic functions of x (see *EM-1* (1996) for details). In this formulation, n approaches 1.13 for deep sensors (i.e., in unbounded water), but is much larger for shallow sensors, in order to account for faster decrease of peak pressure with distance. The *EM-1* (1996) manual also includes formulae for the upper and lower bounds of these relationships, spanning rather wide bands of values (not shown here).

According to these relationships, the coupling phenomena for the two types of nuclear sources differ greatly. As an example, for the very-near-surface region, $-0.5 \le x \le 1.5$ $ft/kt^{1/3}$, ε_L increases from 0.06 to 0.33 (a factor of $\gtrsim 5$), while ε_H increases much more dramatically, from 0.018 to 0.3 (a factor of $\gtrsim 15$). The uncertainty in this region is also much larger for the high-yield sources than for the low-yield nuclear blasts. According to these equations, full coupling, i.e. $\varepsilon = 1$, is reached at depth 15 $ft/kt^{1/3}$.

The relationship for the HE explosions indicates that the expected effect of charge depth/height is much smaller than the one for nuclear blasts, and changes are much smoother around the interface. The HE estimate above approaches 1.5 for full coupling at depth, rather than 1, to account for the expected relationship between HE and nuclear sources (Cole, 1948). The *EM-1* relationships are illustrated further in the report (Section 3.2, Figure 3-3), with the scaled depth/height shown in $m/kt^{1/3}$.

We note that while the coupling coefficient is estimated as the ratio between the pressure from a given charge depth to the pressure from a deep charge (for which the coupling is full), i.e. $\varepsilon = P/P_{max}$, we can also refer to the reduction in pressure as $(P_{max} - P)/P = 1 - \varepsilon$. Both measures are used further in the report.

SECTION 3
MODELING

The modeling of the shock waves was first performed using one of the codes, Underwater_Shock, included in the DNA (former Defense Nuclear Agency) Computational Aids (e.g., Stephens and Kelly, 1995, 1996). It represents a modified and simplified Windows version of a ray-tracing code, originally known as REFM (Reflection and Refraction in Multi-Layered Ocean/Ocean Bottoms), and later as REFMS (*EM-1, 1996;* Britt et al., 1991; Britt, 1985). The code is based on the Cagniard solution for expanding spherical waves in a layered medium (Cagniard et al., 1962), with the characterization of boundary interactions improved by finite difference modeling. REFMS has been evolving for more than twenty years now and still continues to undergo various improvements. Last year, its latest, 1999 version, was also made available to us (R. Britt and R. Thrun, personal communication) and we used it to continue our earlier modeling work.

REFMS has been extensively used for predicting shock-wave parameters from underwater explosions. It includes all major aspects of near-source wave propagation from underwater explosions, such as in-water refraction and bottom and surface reflection. We used the code to calculate peak pressures and impulse, as well as pressure-time histories. The term "pressure" in this context refers to overpressure as compared to the hydrostatic pressure at the points of observation. Among the reflected waves handled by REFMS, the surface-reflected and the bottom-reflected waves are particularly important, with an effect comparable to and sometimes greater than that of the direct wave. The surface-reflected wave represents a rarefaction or tension wave, and tends to have a cutoff effect on the direct shock wave, thus with the potential to greatly reduce it. Depending on the two path lengths, the pulse decay rate, and the gauge depth, the cutoff may be partial, complete, or cavitation-limited. The bottom reflections can have both positive and negative components depending on the properties of the bottom layers. Surface-bottom and surface-bottom-surface-reflected waves are also calculated in the code. Higher-order multiple-reflection paths are relatively insignificant because of their greater attenuation and longer path lengths. If gradients are present in the water sound velocity, the code also handles refraction, using the similarity between refracted shock waves and refracted sound waves. Refraction is calculated through the consideration of up to 300 discrete layers in the water and the bottom, each having a constant sound velocity and density. Regions of substantial focusing (caustics) or shadowing of pressure are predicted with significant accuracy, featuring up to tenfold changes in peak pressure for HE (high-explosive) yields, and up to fivefold changes for nuclear yields, as compared with unbounded homogeneous water.

Two of the features of REFMS are particularly relevant for the work in this project: (1) use of spherical wavefronts and (2) finite-element calculations taking into account deviations from acoustic propagation. The former is based on the acoustic spherical wave reflection theory formulated by Cagniard et al. (1962) and assures more realistic predictions of the pressure histories than if only plane waves are used. The second feature is needed because finite-amplitude effects, not considered in the regular acoustic approximation, become more important with increasing incident pressures and incidence angles (e.g., greater than 170 bars and 85^0, respectively). In an acoustic approximation, it is assumed that both the direct and surface-

reflected shock waves propagate at the speed of sound waves with infinitesimal amplitudes in undisturbed ambient water, and that the water particle velocity is negligibly small relative to the propagation velocity. While this approximation is valid at relatively short times after the underwater explosion (hence, small horizontal ranges), the reflected wave travels faster than the direct wave in the region close to the interface (water-air in this case), and both waves travel faster than the sound speed in water. Further from the explosion this discrepancy becomes quite apparent. Thus the reflected wave front tends to close in on the direct wave front, eventually catching up to and merging with it. The region of merged wavefronts extends from the surface down to a depth that increases as the waves propagate further. It is known as the region of nonregular reflection, in which neither the peak pressures, nor the pressure-time histories, are predictable by the acoustic approximation method, but only by finite-amplitude computations. The peak pressures in the region of nonregular reflection are lower than that of a direct shock wave in unbounded water and presumably decrease to zero at the surface just above this region. For gauge locations below this region, the peak pressures may be predictable by the acoustic approximation method, but finite-amplitude computations are still needed to predict the entire pressure-time history.

The finite-amplitude surface reflection calculations in REFMS have been extensively validated with a series of HE experiments. Predictions were generally very good, with the exception of some discrepancies at the shallowest gauges. In terms of refraction, the code is in good agreement with data from underwater nuclear explosion tests (Wigwam, Wahoo, Umbrella, and Swordfish), as well as from HE experimental series performed on a laboratory scale, in flooded quarries, and in the ocean (e.g., Britt e al., 1991; Brockhurst et al., 1961). REFMS has been found in many cases to predict the underwater shock-wave environment with accuracy better than or comparable with hydrodynamic computations. This is significant, because the latter require much greater computer and labor resources. Still, REFMS is valid in relatively weakly nonlinear regimes and cannot replace hydrocodes in highly nonlinear environments.

Some of the Russian observations and our modeling results are further compared with results obtained by a different type of modeling performed at Lawrence Livermore National Laboratory (LLNL) by Clarke et al. (1995). These authors combined two codes; the first one, CALE, is a LLNL hydrodynamic code used for the strong-shock calculations (up to 300-m distance from a 1-kt explosion), and the second code, NPE, is a Naval Research Laboratory (NRL) code used to model weak-shock propagation. The coupling factor was estimated by calculating the energy of the shock waves at a 10-km range from a 1-kt nuclear source for explosion depths from 0 to 1000 m below the ocean surface and heights up to 1000 m above it. A 5000-m deep ocean was assumed in these computations, along with a mid-latitude sound-velocity profile without incorporating bottom interactions.

Later in the report we attempt to bring together observations and simulations and compare the results in order to get insights in the effect of explosion depth on the hydroacoustic signals from nuclear explosions. REFMS simulations are performed extensively to match the following: observations from the 100-kg TNT small-scale Russian explosions; a 1957 Russian underwater nuclear explosion, from which peak-pressure measurements are available in the near-source field; and 1-kt and 10-kt nuclear explosions with varying charge depths. The latter are used to compare with the LLNL simulation results and to predict the variations in the hydroacoustic

signals that are likely to be observed at the IMS stations. The example of 10-kt simulations is given in more detail below, while the results from the other simulations appear later in the text along with the observations to be matched.

3.1   REFMS SIMULATED 10-KT UNDERWATER NUCLEAR EXPLOSIONS.

Since detailed observations from real underwater nuclear explosions, especially in deep ocean, are lacking, modeling results are obtained here for the realistic case of a 10-kt yield detonated in an ocean with a velocity profile modeled with 29 different layers, as shown in Figure 3-1. This profile (Stevens et al, 1999) is based on measurements in the Pacific Ocean between Hawaii and the California coast and represents a typical sound velocity profile. It features a minimum velocity at a depth of 700 m, consistent with the SOFAR channel in the ocean. An additional layer was used to model the bottom, with sound velocity 6100 m/s, density 2750 kg/m^3, and thickness 10,000 m.
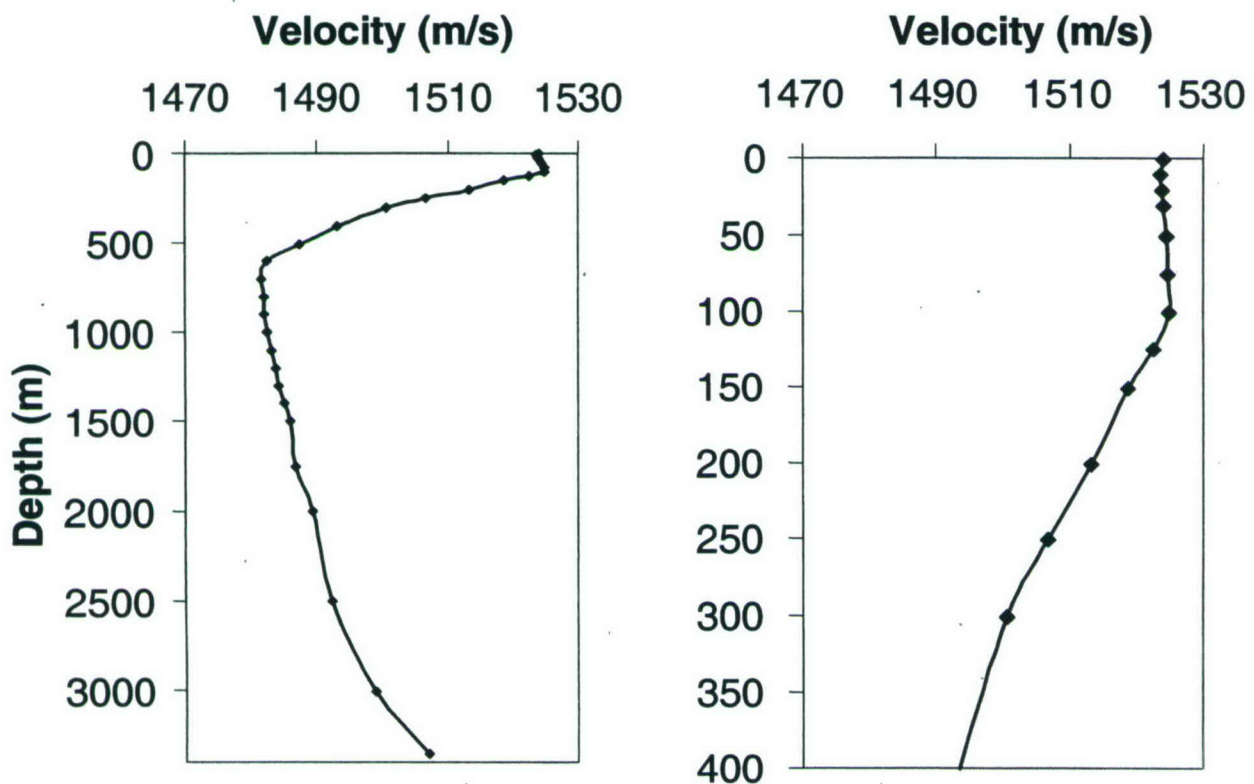
Figure 3-1. Sound velocity profile used in the REFMS simulation of pressure-time histories from 10-kt nuclear explosions.

The pressure-time histories were calculated at a hypothetical depth of 700 m (i.e., in the SOFAR channel) and a 10-km distance from the explosion. This distance is outside the nonlinear region and is expected to be a reasonable approximation to the signal that would propagate further with low attenuation to the IMS stations. Figure 3-2 shows examples of pressure-time histories versus depth of the simulated 10-kt nuclear explosions. The peak pressures decrease by more than an

order of a magnitude for explosion depths shallower than 3 m. It is uncertain how realistic this large drop for surface explosions is. At least part of the predicted strong effect is due to the modeled source being nuclear rather than a HE source. In the depth range 3 m to 800 m, peak pressures increase more than tenfold, after which they decrease at a slower rate. Thus the predicted features are consistent with channeling expected in the SOFAR channel.
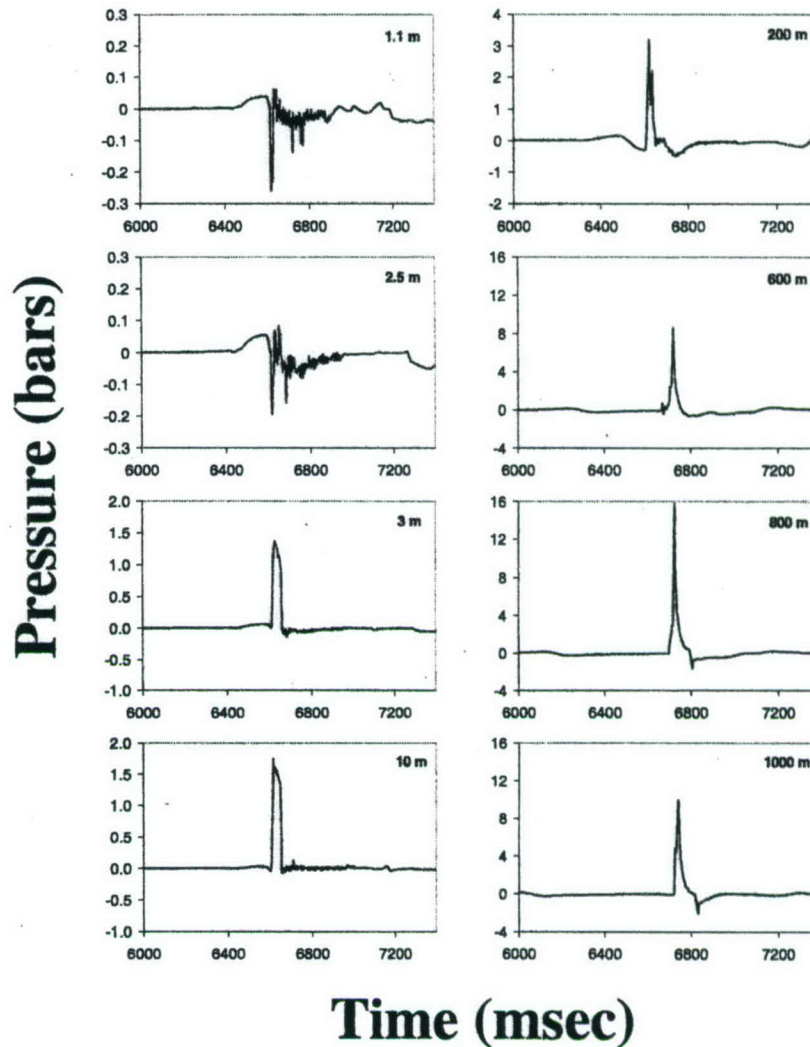
Figure 3-2. Simulated pressure-time histories recorded at 10-km distance and 700 m depth (i.e., in the SOFAR channel) from 10-kt TNT explosions conducted at various depths as indicated in the top right corners of the plots. The sound-velocity profile from Figure 3-1 is used in the simulation.

3.2 REFMS, LLNL, AND EM-1 ESTIMATES FOR THE PRESSURE COUPLING COEFFICIENT ε.

In an attempt to put in perspective the observations described further, we summarize estimates calculated from the relationships given in the *EM-1* (1996) manual between pressure coupling coefficients and depth/height of blast (see Section 2), Clarke et al. (1995)'s simulations of shock waves from 1-kt nuclear explosions at 10 km (Section 3), and REFMS simulations extensively used throughout this report (Figure 3-3). Negative charge depth refers to height above water surface.
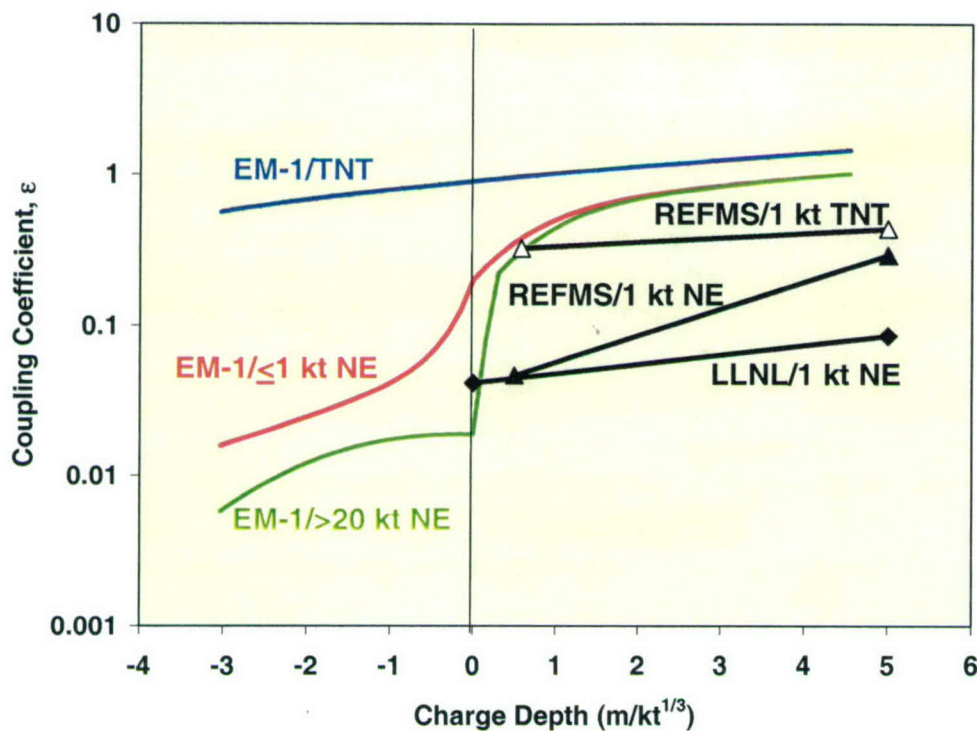
Figure 3-3. Peak-pressure coupling coefficient ε versus charge depth for nuclear (NE) and TNT explosions. Colored curves - derived from theory of radiation hydrodynamics (*EM-1*, 1996); black curves - LLNL and REFMS simulations.

To match Clarke et al. (1995)'s modeling, we performed a REFMS modeling of a 1-kt explosion using the sound-velocity profile shown in Figure 3-1. Since the REFMS code allows for different explosion sources to be modeled, both a 1-kt nuclear and a 1-kt TNT sources were modeled. This was done to address the possible difference in the way coupling of energy to water changes with depth for HE and nuclear explosions. This change is expected to be smaller for the HE explosions than for the nuclear underwater sources. The REFMS predictions in both cases (HE and nuclear) were calculated for explosions with varying charge depth, at 10 km distance and 700 m depth. The explosion depths in these REFMS simulations matched those used by Clarke et al. (1995). Thus both the LLNL and REFMS estimates for 1-kt explosions are for a fixed distance of 10 km/kt$^{1/3}$.

Note that the *EM-1* NE curves in Figure 3-3 are different for low-yield ($\leq$ 1 kt) and high-yield (> 20 kt) explosions. For intermediate-yield NE explosions, $\varepsilon_I = \varepsilon_H - [(\text{yield} - 20)/19](\varepsilon_L - \varepsilon_H)$. The plot shows that the *EM-1* estimates of ε do not depend on distance. Because of the very different set-up of the problem in these approaches, comparisons with the *EM-1* relationships, in particular, are rather difficult to make. One important difference is that in the LLNL calculations, full coupling is reached at a very large depth, 1000 m/kt$^{1/3}$, while in the *EM-1* relationships the coupling coefficients were set to 1 (i.e., to full coupling) at a very small charge depth, 4.5 m/kt$^{1/3}$. One might assume that these estimates (seemingly at two opposite extremes) should be comparable at least for 0-m/kt$^{1/3}$ charge depth (i.e., half-immersed charges). For such explosions, we calculate from the *EM-1* relationships ε = 0.2, 0.162, 0.11, and 0.057 for 1 kt, 5kt, 10 kt, and 16 kt, respectively. From the Clarke et al.'s pressure estimates, we calculated ε = 0.041, which is close only to the 16-kt *EM-1* estimate, but is very different from the *EM-1* estimate for 1 kt (i.e., 0.2). This illustrates the difficulty when attempting to bring together even results from two different modeling approaches, let alone observations and predictions.

Figure 3-3 illustrates that unlike the *EM-1* relationship, the REFMS based estimates do not reach full coupling at such small depths ($\lesssim$ 5 m/kt$^{1/3}$), neither are they as low as the LLNL estimates at this same depth. The LLNL and REFMS estimates only merge for very shallow nuclear blasts (< 1 m/kt$^{1/3}$), but diverge fast for deeper explosions. (The two estimates also merge at 1000 m/kt$^{1/3}$, but this is only seen in Figure 6-1 further in the report). Similar to the *EM-1* estimates, the REFMS coefficients are lower and change much faster with depth for nuclear explosions than for HE blasts. The rate of change with depth indicated by the LLNL simulations, however, is much more similar to that of the REFMS estimates for TNT explosions than for nuclear blasts.

In light of the above, we treat the REFMS predictions as the most reliable ones. REFMS, however, can be only used for modeling of shock waves from underwater blasts. For explosions above the water surface we can only refer to the *EM-1* and LLNL estimates.

Further in the report, it will become clear that there are additional differences between REFMS and the other approaches. In particular, the *EM-1* relationships do not include dependence of the coupling coefficient on distance, but the REFMS estimates do, and this is supported by the observations.

SECTION 4
NUCLEAR EXPLOSIONS IN THE BAY OF CHERNAYA, NOVAYA ZEMLYA

Several underwater and above-water nuclear explosions of torpedoes were carried out in the Bay of Chernaya during the period September 1955 - August 1962. These explosions were conducted in shallow water, as the bottom in the Bay of Chernaya is 60 m to 100 m deep. The purpose was to test torpedo launches with various nuclear charges and to study their effects on military equipment, such as ships, submarines, and buildings on the coast. The site of these explosions is characterized by low water exchange between the Bay of Chernaya and the Barents Sea as they are connected only by a narrow strait. Thus there was relatively low radioactive contamination of the Arctic Ocean and the continental shore from these explosions.

Data are currently available for two of the underwater and one of the above-water explosions. Their location is shown on the map of the Bay of Chernaya in Figure 4-1.
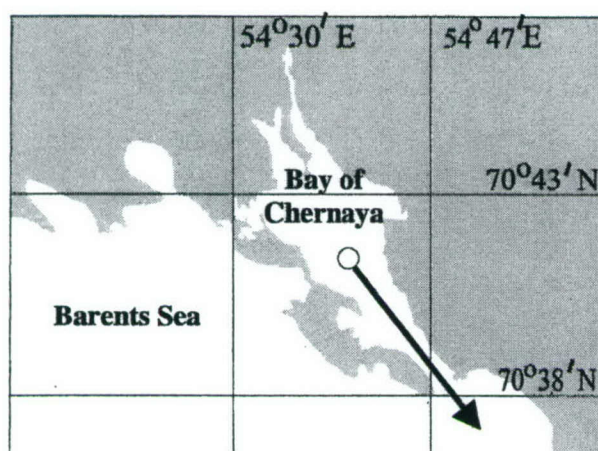
Figure 4-1. Map of the Bay of Chernaya (Novaya Zemlya). Circle shows location of two underwater and one above-water explosions (1957-1961). Arrow indicates direction to sensor locations, where long-range measurements were made from the two 1961 nuclear explosions.

The torpedoes were launched from submarines in the vicinity of the strait connecting the bay with Barents Sea. In all three cases the geographic co-ordinates noted in the archival materials were the same - 70.70^0N and 54.67^0E. However, their locations must have not been exactly identical, as the reported depths of the bottom under the blasts differ. More details about these nuclear blasts are shown in Table 4-1 (*USSR Nuclear Weapons Tests and Peaceful Nuclear Explosions 1949 through 1990*, 1996). Yield values in parentheses represent different estimates in the literature.

The measurements from the 1957 explosion were in the near field, while the hydroacoustic signals from the 1961 blasts were recorded at much larger distances. The exact geographic co-ordinates of the sensor locations are not available, but it is known for the 1961 explosions that measurements were taken along a line originating at the blast location and passing through the narrow strait connecting the bay with the Barents Sea. The hydrophones were suspended at 1 m above the

bottom in the case of the 1961 blasts and at various depths in the case of the 1957 explosion. The Russian archives cite sound velocity of 1430 m/s, characteristic for low-salinity water.

Table 4-1. Archival data from three nuclear explosions in 1957 and 1961.

Date & Moscow time	Yield [kt]	Depth/ Height Expl. [m]	Depth Bottom Under Expl. [m]	Distance to Sensors [km]	Depth Bottom Under Sensors [m]	Depth Sensors [m]	Available Data/ Type of Sensor
10/10/57 09:54:32	10	30 under	≤ 60	0.235	≤ 60	10-50	peak-pressure measurements/MID-3
10/23/61 13:30:47	4.8 (4)	20 under	47	34.84	50	49	sound, infra/ hydrophones
				104.9	60	59	sound/hydrophones
10/27/61 11:30:26.6	16 (17.5)	1.1 above	59	34.84	50	49	sound, infra, ultra/ hydrophones
				160.5	45	44	infra/hydrophone

The closest U.S. analogues of the 1957 and 1961 underwater explosions have been conducted in the West Pacific - Baker (1946, yield 23 kt, explosion depth 27 m, bottom depth 54 m) and Umbrella (1958, yield 8 kt, explosion on the bottom, bottom depth 45 m). All other U.S. underwater nuclear explosions have taken place in open-water, deep basins.

4.1   1957 UNDERWATER EXPLOSION.

The hydroacoustic data available from the 1957 explosion consist of several peak-pressure measurements (Figure 4-2) at a distance of 235 m. The reported yield and depth of explosion were 10 kt and 30 m, respectively (*USSR Nuclear Weapons Tests and Peaceful Nuclear Explosions 1949 through 1990*, 1996). For this test, a torpedo was launched from a submarine at periscope depth. Its target was an old ship at a distance of 10 km. Shock wave parameters were measured using mechanical and tourmaline piezoelectric gauges and piston impulsemeters hung from boats at various distances and depths. In order to assure more precise measurements, four to six sensors were used at any given location. A measurement accuracy of about 15% is mentioned in the archival materials. The decrease in peak-pressure seen at sensor depth of 40 m is slightly larger than this error estimate, and if real, may be due to some shadowing effect. No information is available for the sound-velocity profile of water and bottom, and it is thus difficult to distinguish between a real effect and a measurement error.

An attempt was made to use REFMS to model the seven peak-pressure measurements depicted in Figure 4-2. Using bottom depth of 60 m and a constant sound velocity in water (the profile is unknown), various reasonable bottom velocities and densities were tried, as well as and variable yields and explosion depths. Peak pressures were matched quite well, except for the drop at sensor depth of 40 m. Despite all uncertainties, this limited modeling revealed that the yield was quite likely smaller than the reported 10 kt, and probably didn't exceed 5 kt. Unlike the yield estimate, the explosion depth predicted by the REFMS modeling (between 30 m and 40 m) is in good agreement with the reported depth.
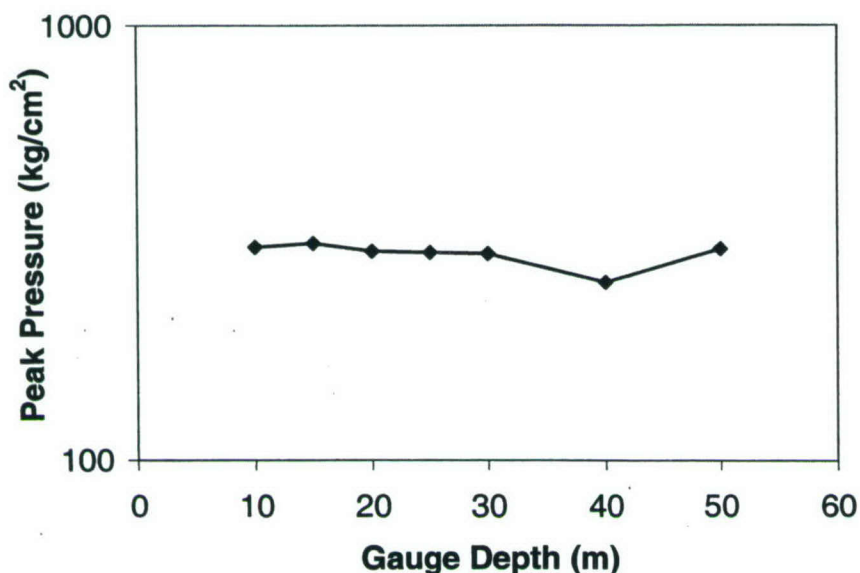
Figure 4-2. Peak-pressure measurements at 235 m from the 1957 underwater explosion. Average peak pressure is ~300 kg/cm². Compared with results from REFMS modeling and scaled measurements from 100-kg TNT explosions, this pressure indicates a likely yield of ~5 kt, i.e., about half of the reported 10 kt.

The lower yield estimate is further confirmed by the similarity between the peak-pressure measurements at 235 m from this nuclear explosion and the 100-kg TNT explosion at a distance of 7.5 m (around 300 kg/cm² in both cases). Section 6 and Figure 6-2 later in the report show this comparison. Thus a scaling factor (Cole, 1948) of about 235/7.5 = 31.33 may be applicable, which leads to 100 kg X 31.33^3 = 3.08 kt TNT-equivalent. Accounting for the difference between HE and nuclear sources, the yield estimate for the 1957 nuclear explosion becomes 3.08/0.667 = 4.62 kt. The factor of 0.667 has been determined using a similitude equation for the peak pressure from an underwater TNT shock wave (Cole, 1948); it simply means that a 1-kt nuclear yield is equivalent to 0.667 kt of TNT, with respect to the underwater shock wave.

4.2   1961 EXPLOSIONS.

The available hydroacoustic signals from the 1961 explosions were recorded with hydrophones suspended from ships at different distances (see Table 1), much further than the sensors used for the 1957 underwater explosion. Three channels with different filters were used, referred to as "sound", "infrasound", and "ultrasound" in the Russian archives. These correspond to frequency bands 60-10,000 Hz, 5-100 Hz, and 8-100 kHz, respectively. The records in Figures 4-3 to 4-6 below are of somewhat compromised quality, as they were scanned from the archival materials. The level of sound pressure in these figures is shown in dB (decibels), better suited to represent small pressures.

As a reminder, the pressure level p in the units of dB is given by 20 x $\log_{10}(p/p_0)$, where $p_0 = 2$ x 10^{-4} dyn/cm² = 2 x 10^{-5} Pa = 2 x 10^{-10} kg/cm² = 0 dB, is the threshold of audibility. Thus, 1 μbar = 1 dyn/cm² = 0.1 Pa = 74 dB, 1 mbar = 134 dB, and 100 mbar = 174 dB (e.g., a normal conversation is about 60 dB). An equivalent illustration of the dB-unit is in terms of intensity

14

level (or energy), $10 \times \log_{10}(E/E_0)$, where the hearing threshold is $E_0 = 10^{-12}$ watts/m^2. It is believed that the reference pressure used by the Russian scientists at the time was the standard p_0 = 2×10^{-4} dyn/cm^2, but this is not known with certainty at present (B. Khristoforov, personal communication).

Figures 4-3 and 4-4 show records from the underwater 1961 explosion at two distances and in different frequency bands. In Figure 4-3a (35-km distance), the time of explosion is at 0 s. The pre-signal noise levels are ~60 dB in the sound band of frequencies and ~70-80 dB in the infrasound band. The maximum signal levels in both cases reach 102-103 dB. As might be expected, attenuation is much less in the lower frequencies (Figure 4-3b). Three distinct arrivals are observed in the sound band (Figure 4-3a) – at ~12 s, ~21 s, and ~92 s. The corresponding effective sound velocities are ~2900 m/s, ~1660 m/s, and ~380 m/s, respectively. Thus the first arrival likely represents a wave reflected from the top of the crust and passing through the layer of deposits on the bottom. The low-velocity third arrival may indicate propagation of shock wave in air, which can travel at larger velocities than that of regular acoustic waves. For such an arrival to be observed, the shock wave in air from the explosion plume must have propagated through an air sound channel and then refracted towards the water. The second arrival is a few seconds earlier than a direct shock hydroacoustic wave at 1430 m/s would arrive (i.e., at ~24.4 s). While such a phase is not seen in the higher-frequency band (Figure 4-3a), the lower-frequency record (Figure 4-3b) indicates substantial energy around 24.4 s, in a pack with earlier and later arrivals. Compared with the higher-frequency record (Figure 4-3a), the onset of the first arrival is earlier in the low-frequency band (~10 s, or a velocity of ~3500 m/s), while the third arrival is later (~93-94s, or velocity of ~370-375 m/s).
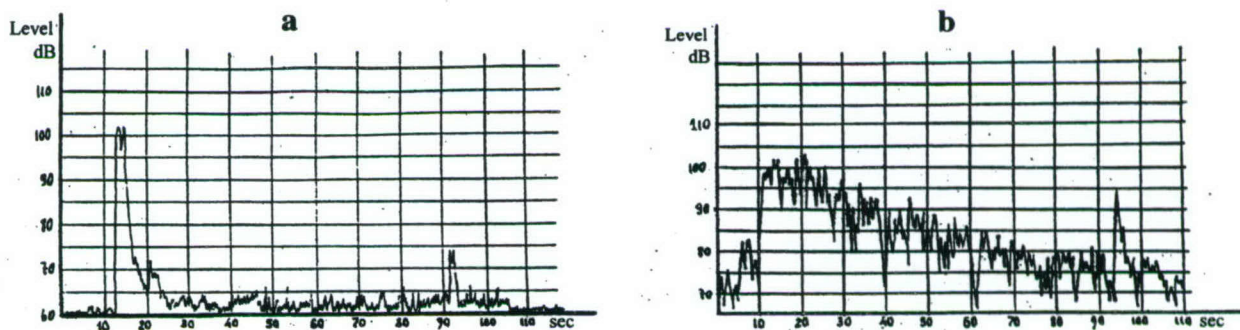
Figure 4-3. Hydrophone records at ~35 km from the 10/23/61 underwater nuclear explosion: (a) sound band of frequencies; (b) infrasound band.

Figure 4-4 shows the available short portion (~25 s) of the record made in the sound band of frequencies, at a distance of ~105 km from the underwater 1961 explosion. The noise level is at ~75 dB, while the signal level reaches ~125 dB. The horizontal axis has its 0 at 13:36:18 Moscow time; i.e., 331 s after the time of explosion. Thus the earliest arrival observed on this record may have propagated mostly in air with a velocity of ~317 m/s. More energy is observed later, arriving at velocities ~310 m/s.
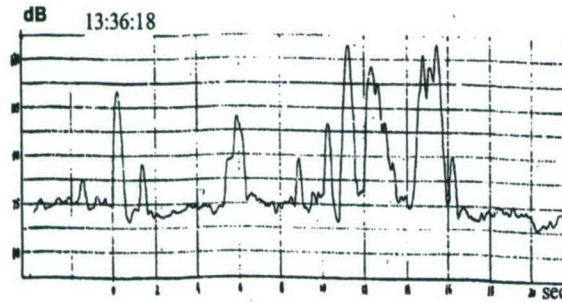
Figure 4-4. Hydropone record in the sound frequency band at ~105 km from the 10/23/61 underwater explosion.

Figures 4-5 and 4-6 show records from the above-water 1961 nuclear explosion of 16-kt yield at two distances. The records in Figure 4-5 have been made in the same location as the records from the underwater explosion, at a distance of ~35 km. The pre-signal noise levels were higher than four days earlier prior to the underwater explosion - ~90 dB, ~110 dB, and ~73 dB in the sound, infrasound, and ultrasound bands, respectively. Maximum signal levels in the three bands were ~130 dB, ~120 dB, and ~90 dB. The sound and the infrasound records have their 0's on the time axes at 11:30:51 Moscow time, which is 24.4 s after the time of explosion (see Table 4-1). The direct shock wave is clearly seen, with corresponding significantly stronger attenuation for the higher frequencies (Figure 4-5a). A smaller arrival ~12 s earlier in the sound record, is likely to be of the same type as the first arrival in the records from the underwater explosion, i.e., reflected in the crust and passing through the sediments on the bottom. It is not seen, however, in the infrasound record (Figure 4-5b). The sound record also reveals a distinct slow phase at ~162 s (+24.4 s), i.e. ~ 3 min after the explosion. The available portion of the infrasound record is too short to see a corresponding signal. The ultrasound record shown in Figure 4-5c is the longest (~ 4 min). The distinct phases in the ultrasound band around 40 s (+24.4 s), i.e. ~ 1 min after the explosion, may correspond to the lower-frequency arrivals around the same time in Figure 4-5a and 4-5b. As high frequencies attenuate much faster than the lower frequencies, the arrivals in Figure 4-5c appear more emergent than in Figure 4-5a-b.

Figure 4-6 shows the available short portion of an infrasound record from the above-water 1961 nuclear explosion made at ~160-km distance. The pre-signal noise level is ~83 dB, while the signal level reaches ~115 dB. The 0 of the time axis is at 11:30:52 Moscow time, which is 25.4 s after explosion. The arrival seen at this time has traveled with an effective speed of ~6320 m/s, indicating likely reflection from the crust-mantle transition zone.

16
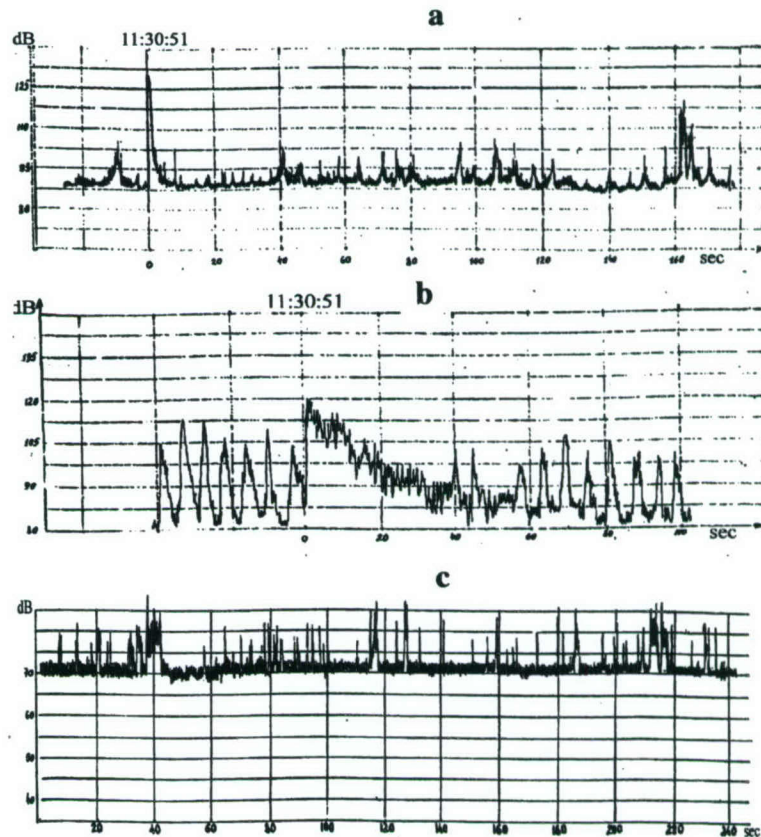
Figure 4-5. Hydrophone records at ~35 km from the 10/27/61 above-water explosion: (a) sound frequency band; (b) infrasound; (c) ultrasound.
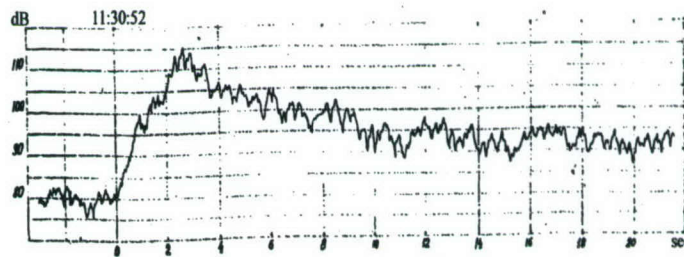
Figure 4-6. Hydrophone record in the infrasound frequency band at ~160 km from the 10/27/61 above-water nuclear explosion.

REFMS cannot be used to estimate hydroacoustic pressures from above-water explosions, neither can it be used at such large distances from underwater explosions. Thus we resort to calculations based on *EM-1* (1996) and Clarke et al. (1995). For a 1.1-m charge height above water of the 16-kt 1961 explosion (0.44-m/kt$^{1/3}$ scaled height), we calculate $\varepsilon = 0.0412$ from the *EM-1* relationships (see Sections 2.1, Section 3.2 and Figure 3-3). Compared with 0.057 for a half-immersed charge, the difference is not large for this yield. Incidentally, the LLNL (Clarke et al., 1995) estimate, 0.041, is the same as the *EM-1* value, only it is for a 1-kt yield. Thus the peak pressure of the direct shock wave from this explosion might be expected to be ~4 % of the

17

pressure that would be measured from a deep charge. Using further the *EM-1* relationships, and converting the pressure estimates in dB, we calculate that the free-water pressure levels from a 16-kt nuclear explosion are 158 dB at 35 km and 143 dB at 160 km. 4 % of these values yield 130 dB and 115 dB, respectively. The former is in excellent agreement with the level observed at 35 km in Figure 4-5a, while the latter cannot be verified, as the direct wave at 160 km arrives much later than the time window shown in Figure 4-6.

The 4.8-kt 1961 underwater explosion at 20-m depth (~12-m/kt$^{1/3}$ scaled depth) cannot be viewed in light of the *EM-1* coupling coefficients, because full coupling is assumed for such depths. REFMS cannot be used to model the observations either, because the distances are too large. Using the LLNL pressure estimates, we calculate that ε might be ~10%, interpolating between 0.041 for 0 m/kt$^{1/3}$ and 0.176 for 20 m/kt$^{1/3}$ (no pressure estimates available in between). This is a very crude estimate, especially because the LLNL calculations are only for 1 kt at 10 km. The free-water direct shock-wave pressures for this explosion are 154 dB at 35 km and 143 dB at 105 km. Thus the free-water estimate at 105 km for a 4.8-kt explosion is the same as the estimate for a 16-kt explosion at 160 km (see previous paragraph), which might have influenced the particular choices of yields and distances in the Russian tests. A ~10% coupling coefficient would reduce the pressure levels to 134 dB and 123 dB at the two distances. There is no observation in this time window at 105 km, but the observed level for the direct shock wave at 35 km is only ~100 dB in the infrasound record around ~24.4 s (Figure 4-5b); this translates into an observed coupling coefficient of only 0.2%. Even lower level, < 70dB, is seen in the sound record at this time (Figure 4-5a). As to the pressure level of ~103 dB observed for the arrivals reflected from the crust (~10-12 s at 35 km), it is the same as for the other 1961 explosion, given the difference in yields (4.8 kt vs. 16 kt) and positions in respect to the water surface (under and above); compare Figure 4-3a (~12 s on the time axis) and 8a (~ −10 s on the time axis).

In addition to the arrivals of clearer origin discussed above, Figures 4-3 to 4-6 show phases likely due to multiple hydroacoustic reflections from the bottom, water surface and surrounding margins, known also as reverberations (*EM-1*, 1996). Due to much more efficient attenuation at higher frequencies, reverberations are relatively short-lived for frequencies exceeding 300 Hz. Shot Swordfish is cited in *EM-1* (1996) as the only nuclear explosion from which reverberation measurements were made at long ranges, but numerous such measurements exist from HE explosions. Once in the water however, it does not matter in terms of reverberations if the energy originates from nuclear or HE sources.

18

SECTION 5
100-KG TNT EXPLOSIONS IN A RESERVOIR

In 1956 twenty-nine explosion experiments were conducted in a shallow reservoir in the former Soviet Union (Kozachenko and Khristoforov, 1970; Korobeinikov and Khristoforov, 1976). In many respects, these explosions were similar to recent small-scale explosions carried out in the U.S. (e.g., Voss and Schmidt, 1995). Figure 5-1 schematically represents the experimental setup of the Russian explosions.
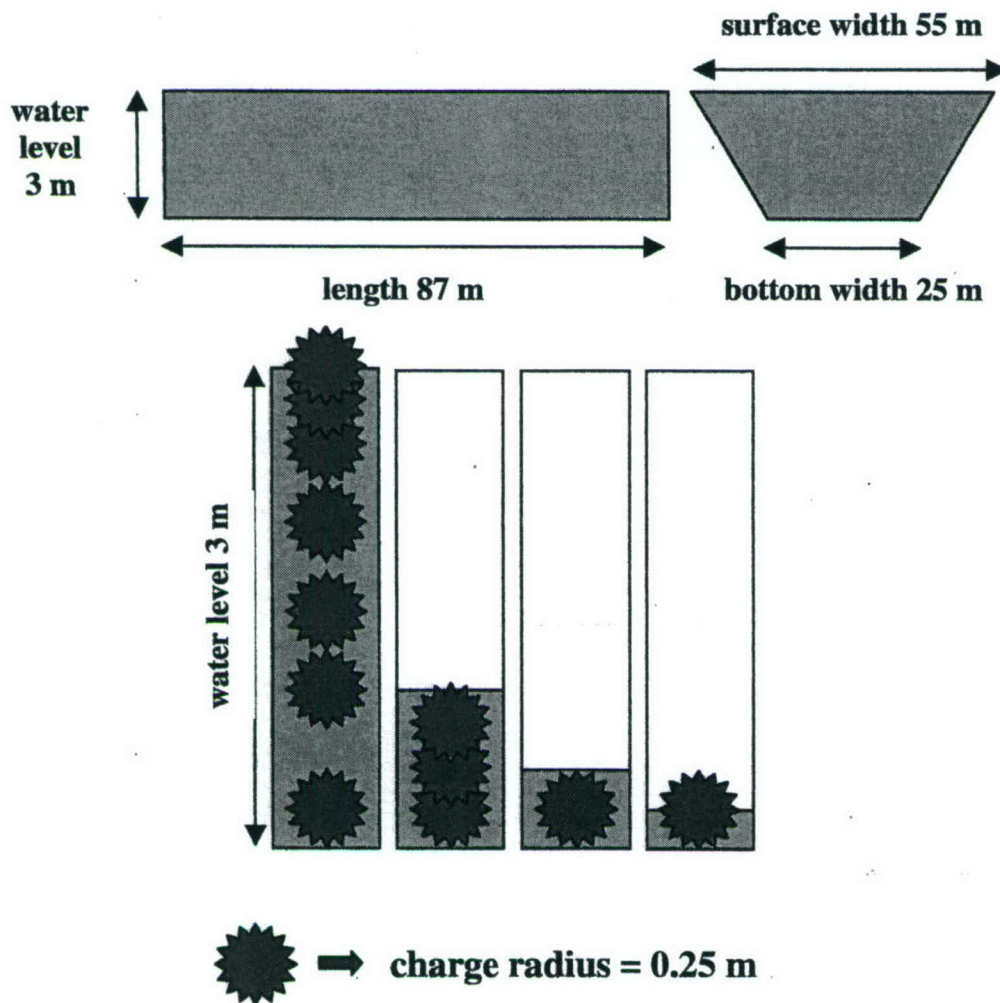
Figure 5-1. Schematic representation of the reservoir and the experiments with underwater explosions. Top – cross-sections of the reservoir (dimensions not to scale). Bottom – 29 explosions were carried out featuring various combinations of water levels (0.25 m to 3 m) and charge depths (0 m to 2.75 m).

The radius of the 100-kg TNT cast spherical charges was about 0.25 m. The dimensions of the reservoir were as follows: 87 m length, 3 m depth, and 55 m to 25 m width from top to bottom. Comprehensive measurements of shock wave time-histories and parameters (peak pressures,

specific impulse and pulse duration) were made with piezoelectric gauges at four distances in water. Most of the experiment configurations were applied twice, taking measurements at 7.5 m and 22.5 m from one of the explosions, and at 15 m and 30 m from the other. Sensor depths were varied from 0.25 m to 2.75 m, charge depths from 0 m (half-immersed) to 2.75 m, and water level from 3 m to 0.5 m. The bottom consisted of a 1-m thick layer of air-saturated sand, with a very low sound velocity (270 m/s), which for all practical purposes had an effect similar to the air above the water surface. The low-velocity bottom must have contributed to assuring that the reservoir was not destroyed by the repeated tests. Water was pumped out after each explosion, the crater was leveled out and water was pumped in again for the next explosion. The experiment configurations led to the observation of both regular and irregular reflections from the water surface and the bottom, depending on the locations of explosions and sensors.

We have a total of 222 digitized pressure-time histories and as many impulse-time histories in water. 36 records in air and 50 records in ground have been also digitized for each of the pressure- and impulse-time histories, but are not used in this report. Of the hydroacoustic observations, we utilize measurements from 12 explosions performed in a full reservoir (water level of 3 m) and do not consider at this time data from the remaining 17 explosions in shallower water (water levels 1 m and 0.5 m). The reason is that only the explosions in full reservoir are relevant to our interest in near-surface blasts in relatively deep water, and not in shallow water.

Figure 5-2 below shows a summary of the shock wave parameters measured from the twelve explosions in full reservoir. Shown are peak-pressure and specific-impulse measurements from the twelve experiments, versus charge depth. The impulse is estimated over the duration τ_+ of the positive phase of the shock wave. The dependence of positive pulse duration, τ_+, on explosion depth is similar to that of the impulse and is not shown. The semi-symmetric appearance of the overall dependence of peak pressure on charge depth is due to the similar sound velocities of air and the sand on the bottom. Thus in the following we will mostly refer to results down to mid-pool depth (1.5 m). Figure 5-2 shows a number of features of peak pressures: increase with charge depth, reaching maximum values around mid-pool; decrease with distance; mostly increase with sensor depth for any given shallow charge depth, but nearly constant values for mid-pool charge depths (especially closer to the explosions, at 7.5-m distance). The impulse also shows general increase with charge depth and decrease with distance. However, for any given explosion depth, the dependence on sensor depth is nearly symmetrical, with maximum reached around 1.5-m depth (mid-pool). This effect is due to reflections from the water surface and the bottom, which reduce the positive pulse duration, and therefore the impulse, when measurements are taken near the two boundaries. Kozachenko and Khristoforov (1970) have suggested semi-empirical formulae to fit the observations shown in Figure 5-2, representing the shock-wave parameters through the free-water estimates in eq. (1) above, after application of certain correction factors. These correction factors are rather complicated functions of distance, sensor depth, and charge depths, and are not shown here.

Furthermore, Figures 5-3 and 5-4 show examples of pressure-time histories from fully- and half-immersed charges, respectively, along with modeling results to be discussed further. Comparing the peak pressures measured at depth of 1.5 m from half-immersed and fully-immersed explosions shows that close to a 60% reduction (i.e., $\varepsilon = 0.4$) is observed at a distance of 15 m and 70% ($\varepsilon = 0.3$) at 30 m (measurements at distances 7.5 m and 22.5 m are not available for the

half-immersed charges). These percentages were calculated from the relative peak-pressure differences at the two distances, (147.5–60.5)/147.5 and (66–19.3)/66, respectively. The sensor depth of 1.5 m (mid-pool) is chosen in this comparison because measurements at this depth are least affected by surface and bottom reflections and because the largest peak pressures were usually observed at these intermediate sensor depths.
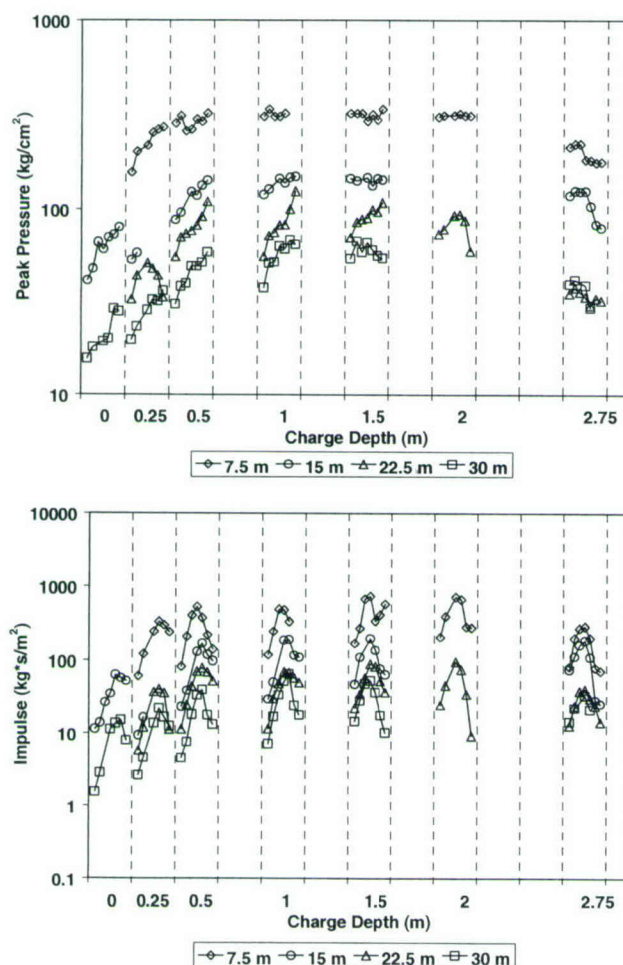
Figure 5-2. Peak pressure (left) and impulse (right) measurements from the 100-kg TNT experiments in a reservoir with water level of 3 m. Vertical dashed lines delimit bands containing measurements for the same charge depth, with data points from left to right showing measurements at increasing sensor depths (0.25 m to 2.75 m). The charge depths, for which data are available, are marked with bold numbers along the horizontal axes (0 m to 2.75 m). Different symbols indicate four different distances at which measurements were taken, as shown in legend.
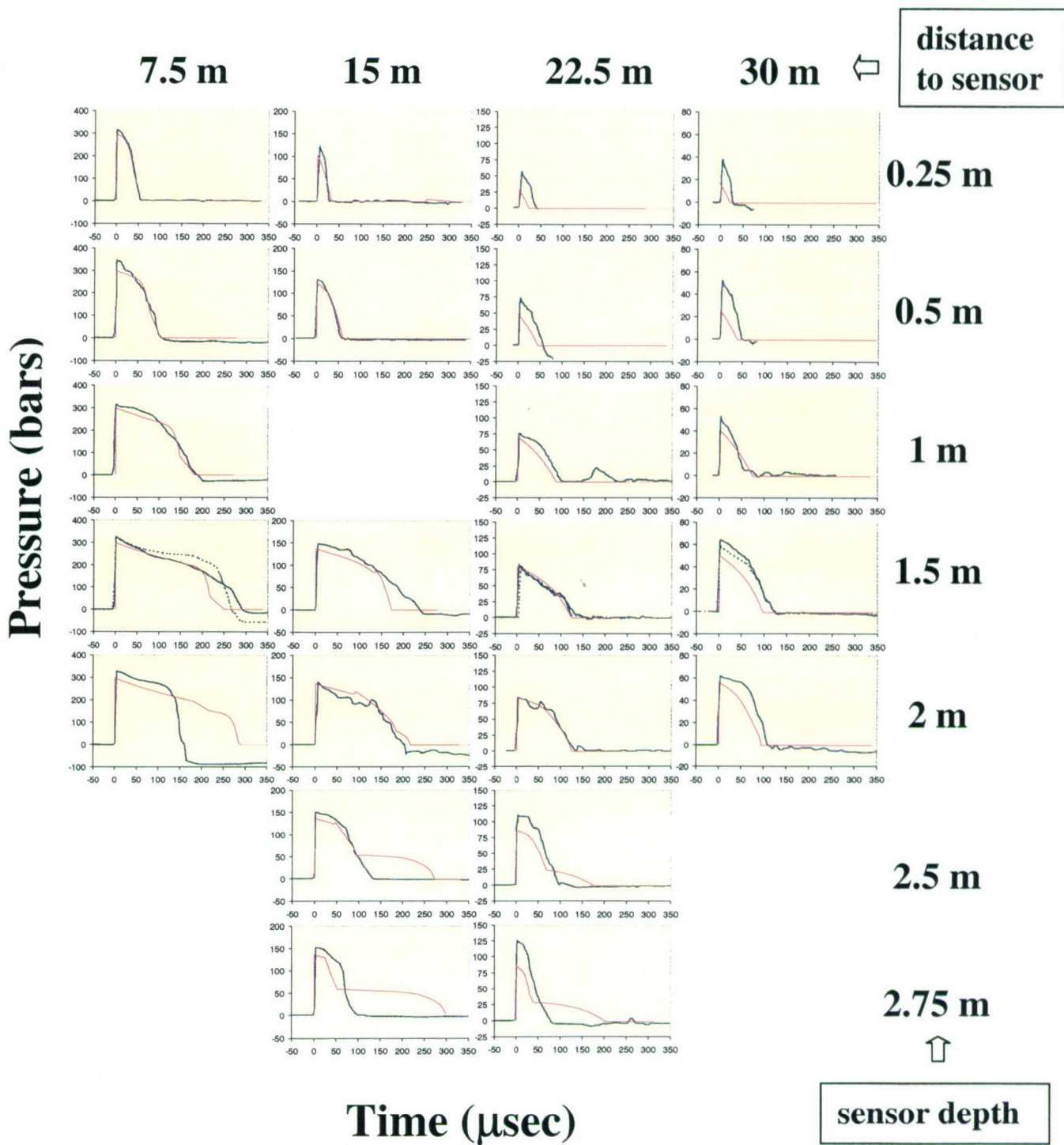
Figure 5-3. Observed and modeled pressure-time histories for fully-immersed charges (charge depth 1 m, water level 3 m). Modeled – red solid lines; observed – blue solid lines, with dashed lines indicating additional measurements at sensor depth 1.5 m.
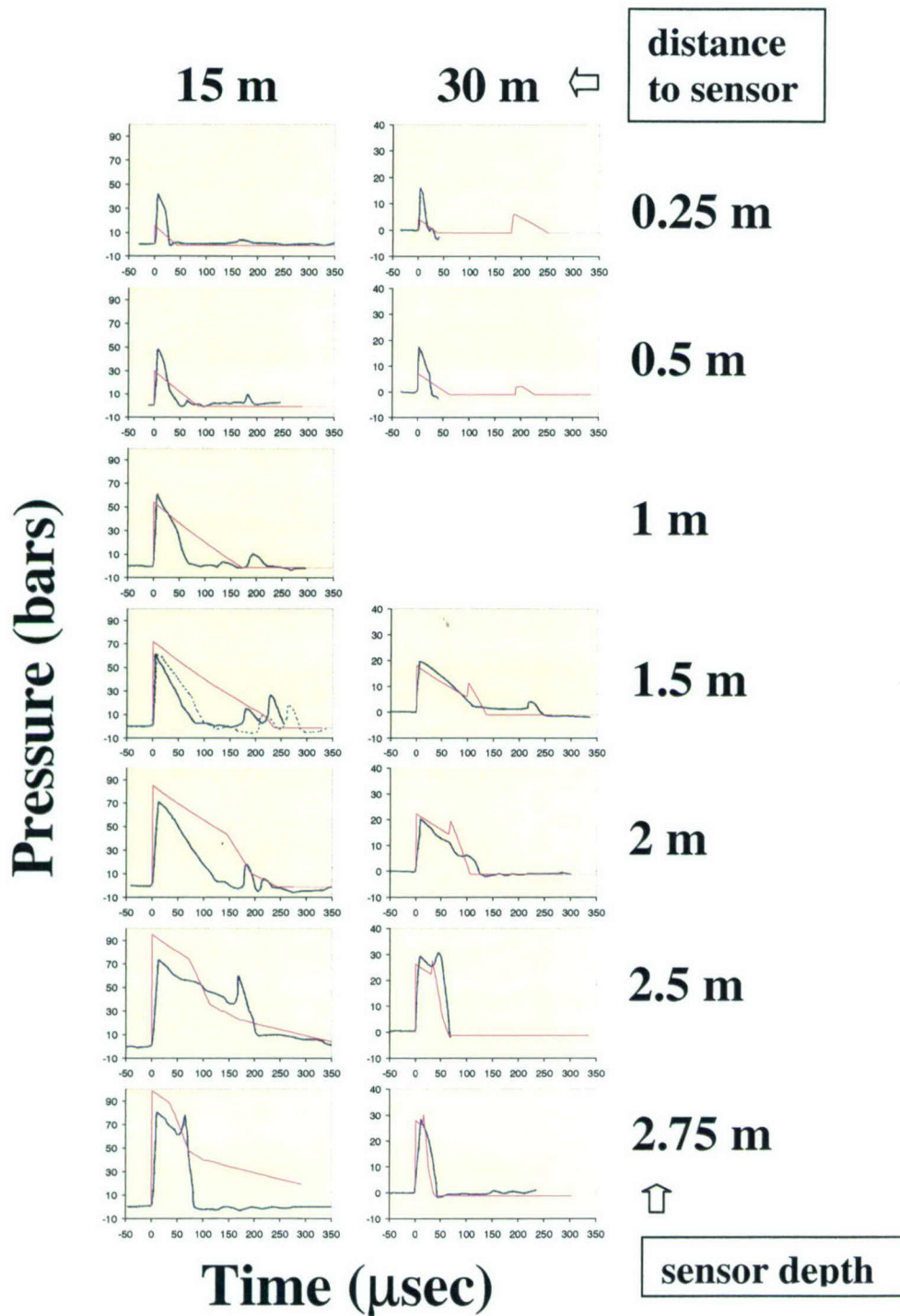
Figure 5-4. Observed and modeled pressure-time histories for a half-immersed charge (charge depth 0 m, water level 3 m). Modeled – red solid lines; observed – blue solid lines, with dashed lines indicating additional measurements at sensor depth 1.5 m.

5.1   MEASUREMENT ERRORS.

There is almost no specific information about the errors involved in these measurements. Errors of 8%, 10%, and 18% were cited in the archives for the measurements of peak pressure, specific impulse, and energy, respectively, in one case only (B. Khristoforov, personal communication). This lack of error estimates is in contrast to the error control apparently intended in the test design. It is known that several gauges were suspended in water at identical distances and depths to take measurements from identical explosions. In addition, many of the explosion configurations were repeated in several tests. The former would provide information on measurement errors *per se*, while the latter would add differences due to difficulties in repeating the explosion configurations exactly (e.g., discrepancies in measurements of distances and depths in field conditions, changes from test to test in sound speed of the bottom, etc.). Differences in measurements from different explosions are therefore expected to be larger on average than the differences between measurements from the same experiments.

We attempted to make some representative estimates of the differences among peak-pressure measurements for the same experiment configurations, whenever these are available (Figure 5-5). Water level, explosion depth, sensor depth, and distance, are marked in meters next to the plotted values; for example, "1-0.5-0.25-15" means an experiment with water level 1 m and charge depth 0.5 m, for which peak overpressure has been measured at depth 0.25 m and distance 15 m. The designation "st" means "same test", for which two different measurements are available at the same depth and distance. Absence of "st" means that measurements are taken from different explosions, but with the same configurations. Early estimates based on one case involving fully-immersed charges (explosion depth 1 m) in a full pool (water level 3 m), depicted in Figure 5-3, led to the reassuring observation that none of the relative differences among two different measurements for each of three combinations of sensor distance and depth (7.5 m - 1.5 m, 7.5 m – 0.25 m, and 15 m – 0.25 m) exceeded 1.3%. Differences in pulse duration turned out to be rather large by comparison, from 6% to 28%. This one case is apparently representative for the remaining explosions in a full pool (water level of 3 m). Thirteen of the measurements at sensor depth 1.5 m have been taken by two different sensors for a given explosion and distance. The discrepancies between these are the smallest for the peak pressures (3.3% on average), larger for the pulse duration (9% on average), and the largest for the impulse (14% on average). Each of these repeated measurements was made for the same test. No observations are available at identical sensor distances and depths from different fully immersed explosions, but it is reasonable to expect larger discrepancies among measurements in this case.

We also estimated discrepancies among measurements of peak pressure and pulse duration from 9 configurations, all with water levels of 1 m and 0.25 m; i.e., charges were detonated in very shallow water. These explosions are not analyzed in this report, but it is still instructive to note that peak-pressure measurements from identical explosions differed at most by 10%, while differences among some tests exceeded 20%. Thus compared to the detonation of charges in full reservoir, larger discrepancies were observed among measurements from shallow-water explosions (water level ≤ 1 m). This is likely due to more prominent nonlinear effects, and therefore, stronger sensitivity to differences among measurement and explosion conditions in very shallow water.
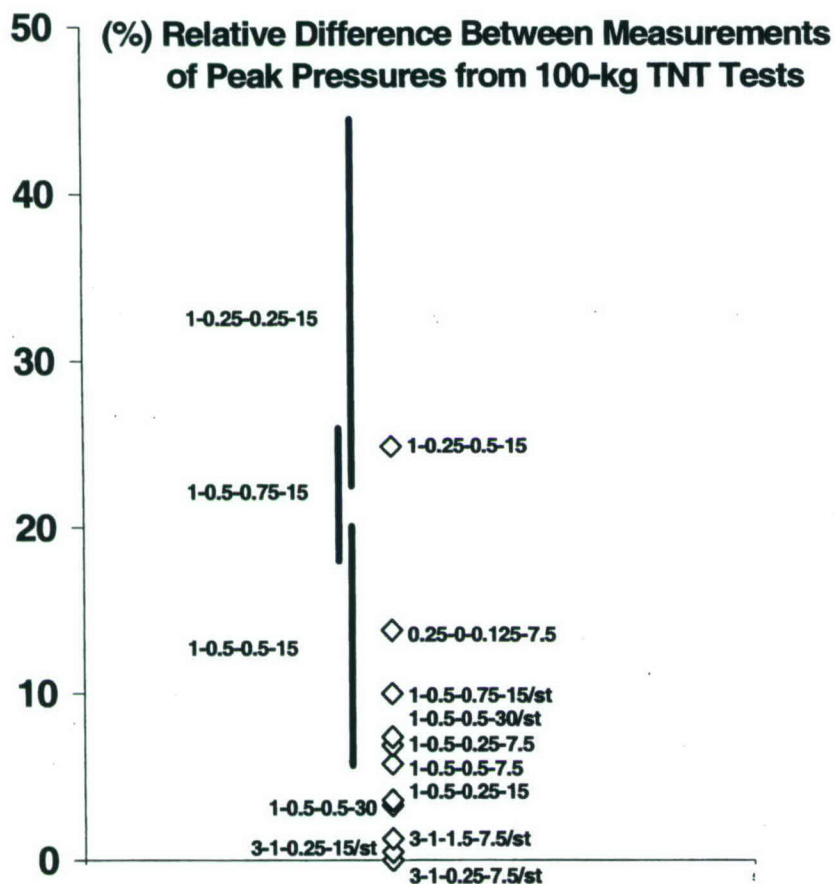
Figure 5-5. Differences among measurements of peak overpressures from the same configuration of water level, explosion depth, sensor depth, and distance, all marked in meters next to the plotted values. The designation "st" means "same test." Diamonds mark differences in per cent between two measurements for a given configuration. Bars mark ranges of differences, as indicated by more than two measurements for a given configuration.

5.2   MODELING OF 100-KG TNT EXPLOSIONS IN SHALLOW WATER.

The observed pressure-time histories from the explosions of fully immersed charges in Figure 5-3 are shown together with the predicted signals using the REFMS modeling. The modeling was done assuming a constant sound velocity in water of 1500 m/s (i.e., no velocity gradients and hence, no in-water refraction). All other parameters in the modeling matched the configuration of the explosions (depth 1 m, water level 3 m) and the sensors (depth 0.25 m to 2.75 m, horizontal distance from explosion 7.5 m to 30 m). The large discrepancies seen at smaller sensor depths (0.25 m and 0.5 m) at larger distances (22.5 m and 30 m), may be due to an "overinterpretation" of the nonregular surface reflection, with the observations not supporting the predicted spatial extent of such a region in this case. Uncontrollable experiment variations (e.g., water surface waves, refraction due to thermal gradients in the upper layers of water, etc.) may also cause such discrepancies. Predictions at larger distances are generally worse than the ones at smaller distances. Large-distance predictions show the smallest differences at intermediate sensor depths

(1 m and 1.5 m), likely because the effects of the surface and the bottom are least significant at these depths. The predicted signals for the remaining combinations of distances and sensor depths in Figure 5-3 match the observed ones very well, even in what can be considered as essentially the source region of the explosions (small distances of 7.5 m and sensor depths smaller than 2 m).

Figure 5-4 shows observed and predicted pressure-time histories from a half-immersed explosion. Due to the larger role of nonlinear effects, and in particular, the not-fully-understood change in coupling with charge depth, such explosions are much more difficult to model and larger discrepancies are to be expected. Model parameters followed the test configuration in the same manner as for the fully immersed explosions above.

Since measurements at 1.5-m depth are least affected by the boundaries, Figure 5-6 shows peak pressure and impulse measured at this depth, as a function of charge depth. Curves through predicted values in the figure are only shown for easier comparison with observed values. Compared with peak-pressures from the REFMS modeling, the observed pressures indicate very good agreement in the near field (7.5 m and 15 m) and poorer fit further from the source. However, the fit is very good for charge depths around mid-pool at all distances. The impulse measurements agree with the REFMS predictions at mid-distances (15 m and 22.5 m), but appear rather overestimated closer to the source (7.5-m distance) and somewhat underestimated further from the source (30-m distance), except for small charge depths. These discrepancies may be related to additional reflections from the walls of the reservoir, not modeled at present. Figure 5-6 also shows estimates in unbounded water calculated from eq. (1). While observed and REFMS-predicted peak pressures fit these calculations very well for mid-reservoir charge depths, the
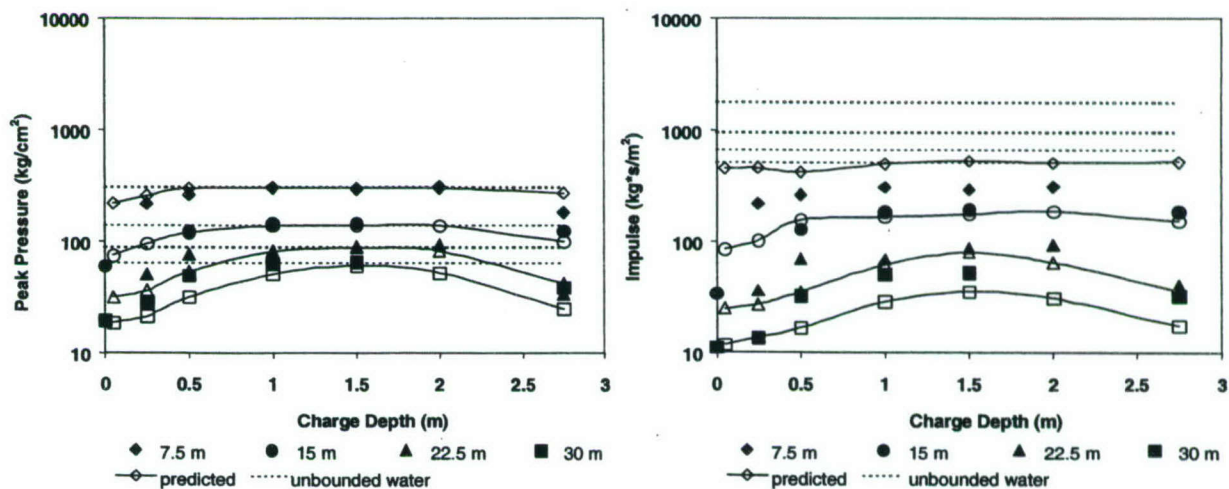
Figure 5-6. Dependence of peak pressure and impulse on charge depth for the 100-kg TNT explosions in a reservoir with water level of 3 m. Measurements (bold symbols) are taken in mid-pool, at sensor depth 1.5 m. Empty symbols mark REFMS predictions. Symbol shape changes with distance, as shown in legends. Dashed lines denote calculations for unbounded water, with larger values at smaller distances.

impulse measurements are much lower. The reason for this is that pulse duration is affected by reflections from the boundaries, significantly reducing the impulse as compared with unbounded water. As an example, note that the REFMS-predicted values at 7.5-m, already higher than the

observations, are comparable with the free-water calculations at four times larger distances (30 m). These results show that in terms of peak pressures (but not impulse), explosions and measurements at depth of ~1.5-m approximate very well an unbounded water environment.
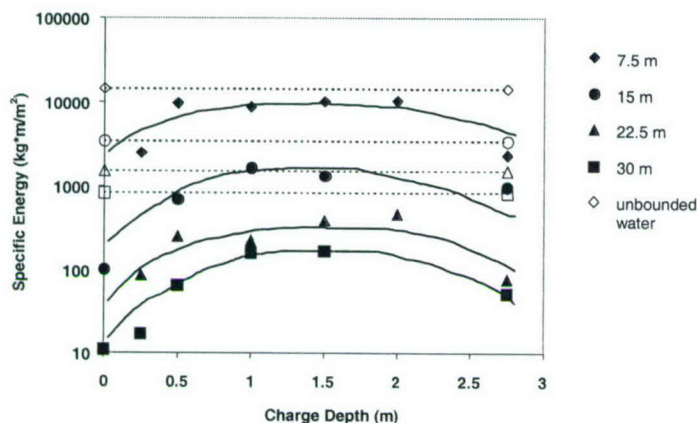
Figure 5-7. Specific energy measured in mid-pool from the 100-kg TNT explosions. Filled symbols denote distances as in legend. Dashed lines with empty symbols show unbounded-water calculations for four distances. Curves are only shown for clarity.

Similarly, the specific energy of positive pulse, E_+, measured at 1.5-m depth, is shown in Figure 5-7. These estimates are compared with calculations of the energy density flux in eq. (1), showing increasing departure for larger distances. Furthermore, Figure 5-8 shows the dependence of shock-wave energy, as a portion of total energy of explosion (418×10^5 kg∗m = 418 MJ for 100-kg TNT), on distance to sensor. The shock-wave energy in this case is calculated as $2\pi R \int_0^H E_+(h)\, dh$, where h is sensor depth, $E_+(0) = 0$ and H is the maximum sensor depth (2.75 m in these experiments). At 23-24%, the unbounded-water estimates in Figure 5-8 are much higher than the
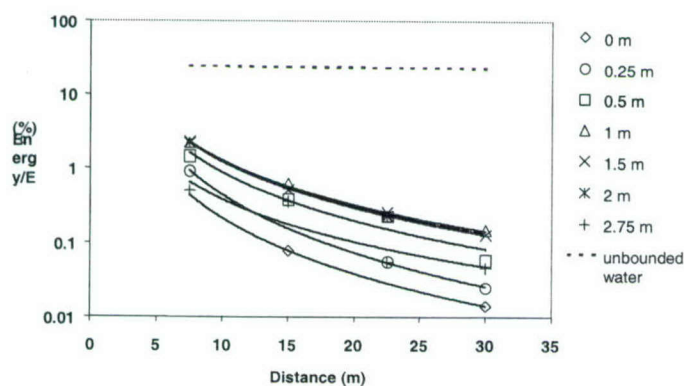
Figure 5-8. Dependence of shock-wave energy (given in per cent of energy of explosion) on distance to sensor. Symbols denote seven charge depths as in legend. Curves are calculated using power-law approximations. Dashed line shows calculations for unbounded water.

observed values, which exceed 1 to 2% only in the near field, and are measured at hundredths of a percent further from the source. A distinct dependence on charge depth is indicated; for any

given distance, these estimates are generally lowest for half-immersed charges (0-m depth), higher for 0.25-m and 2.75-m depths closer to the boundaries, still higher for 0.5-m depth, and the highest for mid-pool charge depths (1 m, 1.5 m, and 2 m).

Finally, Figure 5-9 shows a coupling coefficient in terms of pressure, versus charge depth. This coefficient is estimated by dividing the peak pressures from various charge depths by the pressure from a mid-pool explosion, best approximating an unbounded-water environment. All measurements are taken at mid-pool, i.e., at 1.5-m depth. As the charge approaches the surface, the rate of decrease is faster for larger distances. Observed and REFMS-predicted changes with depth are similar, but the observations are somewhat overestimated by the predictions in the near field (7.5 m and 15 m), possibly because in the real reservoir more energy is lost to reflections in the reservoir walls. Conversely, the observations are underestimated further from the source (22.5 m and 30 m), i.e., peak pressures tend to decrease with charge depth more slowly than predicted, except perhaps on the surface (half-immersed charges).
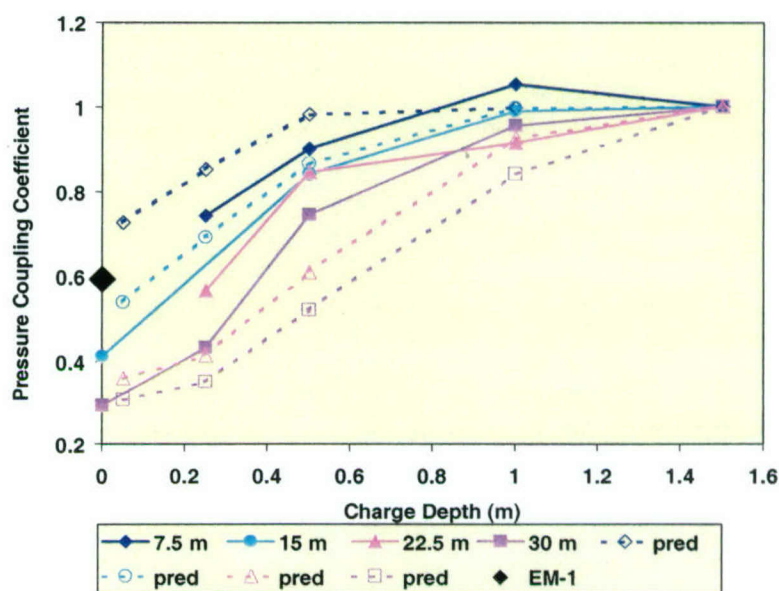
Figure 5-9. Coupling coefficient in terms of pressure versus charge depth. Filled symbols and bold lines indicate measurements, empty symbols and dashed lines denote REFMS predictions. Large diamond symbol shows the EM-1 estimate for a half-immersed charge (0-m depth). Distances to sensor as in legend. All measurements are taken in mid-pool (1.5-m depth).

Both the observations and the REFMS-predictions suggest dependence on distance that is absent in the *EM-1* relationships (see Section 2.1). The *EM-1* HE estimates of the pressure coupling coefficient are much higher and change much more slowly with charge depth, than those for nuclear blasts (see Figure 3-3). The small charge depth of 4.5 $m/kt^{1/3}$, for which full coupling is assumed in the *EM-1* manual, translates into less than 0.25 m in the 100-kg TNT case, using a scaling factor of $0.046416 = (0.0001 \text{ kt})^{1/3}$. Thus, only the observations from a half-immersed charge (0-m depth), can be compared with the analogous *EM-1* HE estimate of $\varepsilon = 0.89/1.5 = 0.59$ at 0 $m/kt^{1/3}$ (division by 1.5 is required because of transferring HE results to nuclear conditions). Two observations exist, $\varepsilon = 0.41$ at 15 m and $\varepsilon = 0.29$ at 30 m. Observations, and hence estimates of ε are not available at 7.5 m and 22.5 m from the half-immersed explosions.

However, extrapolating in Figure 5-9 the observed curve at 7.5-m distance to $\varepsilon \sim 0.6$ would match closely the *EM-1* value, and so would the REFMS predicted coefficient at a 15-m distance. Although the *EM-1* coupling coefficient is thus in general agreement with some of the observed and REFMS predicted values for ε, it is obvious that the lack of dependence on distance in the *EM-1* relationships is not realistic.

Although we do not analyze here the available observations in air and ground, it is informative to see how the energy from these small-scale explosions is partitioned between water, air and ground. Measurements of shock-wave peak pressures were performed in air at ranges of 26 m to 36 m from the shallowest explosions (charge depth 0 m and 0.25 m) in the full pool (water level 3 m). At these distances, the portion of the energy released as shock wave in water is two to three orders smaller than the shock-wave energy released in air. This proportion should grow with charge depth, but no measurements in air were made from deeper explosions to support this expectation. More pressure measurements in air and the only measurements in ground were made from the explosions in very shallow water ($\leq$ 1 m), not studied here. For these explosions, the energy released in air is by one to six orders larger than the energy in ground and water, depending on charge depth, water level, and distance. The energy in the ground is similar to the hydroacoustic energy for water level of 1 m, but is increasingly larger as the water level decreases further (to 0.5 m and 0.25 m).

SECTION 6
RELEVANCE OF SMALL-SCALE HE EXPLOSIONS TO NUCLEAR EXPLOSIONS

The relevance of the small-scale Russian experiments to larger explosions can be determined on the basis of commonly used scaling relationships, relating distances and times with the cube root of the yield (Cole, 1948). That is, the peak-pressure measurements at a distance of 30 m from a 100-kg TNT charge detonated at 1 m depth in a 3 m deep reservoir should be comparable, for example, with measurements (1) at a distance of 646 m from a 1-kt TNT explosion at 22 m depth above a 65 m deep bottom, (2) at a distance of 1400 m from a 10-kt TNT explosion at 46 m depth above a 140 m deep bottom, or (3) at a distance of 30 km from a 100-kt TNT explosion at 1000 m depth above a 3000 m deep bottom. Factors of $21.5 = (1 \text{ kt}/100 \text{ kg})^{1/3}$, $46.4 = (10 \text{ kt}/100 \text{ kg})^{1/3}$, and $1000 = (100 \text{ kt}/100 \text{ kg})^{1/3}$ respectively, are used in this comparison. The scaling in (3) above is the only one somewhat approximating the ocean environment; however, the sound velocity in water was constant in the reservoir, unlike the real sound-velocity profiles in the ocean featuring velocity gradients.

We would like to further compare the Russian observations, the REFMS modeling results obtained here, and the LLNL modeling results reported by Clarke et al. (1995). Direct comparison is not possible, because the Russian measurements were taken at much smaller scaled distances ($160 \text{ m/kt}^{1/3}$ to $646 \text{ m/kt}^{1/3}$) than the distance in the LLNL modeling (10,000 $\text{m/kt}^{1/3}$). This was dictated by the limited dimensions of the reservoir. The difference between homogeneous and refractive water is another complication. However, some general conclusions can be still drawn.

Figure 6-1 shows the peak-pressure predictions from the LLNL (Clarke et al., 1995) and REFMS modeling of 1-kt explosions, together with the previously performed modeling of 10 kt (see Section 3.1) and the most representative Russian observations in this context. The LLNL simulation of a 1-kt nuclear source is at scaled distance 10,000 $\text{m/kt}^{1/3}$, using a mid-latitude sound-velocity profile. The REFMS simulations are for the same scaled distance, using the sound-velocity profile shown in Figure 3-1. The scaled distance for the nuclear source is 4,640 $\text{m/kt}^{1/3}$, again using the sound-velocity profile from Figure 3-1. Figure 6-1 shows the largest observed peak pressures (at sensor depth of 1.5 m) from the Russian experiments, measured at explosion depths $\leq 32 \text{ m/kt}^{1/3}$ (1.5 m) and at four distances: $646 \text{m/kt}^{1/3}$ (30 m); $485 \text{ m/kt}^{1/3}$ (22.5 m); $323 \text{ m/kt}^{1/3}$ (15 m); and (7.5 m). The Russian data appear in a separate cluster in the figure, becasue they represent measurements much closer to the source. The REFMS predictions for a 1-kt nuclear source match the LLNL modeling for surface (0 m) and deep explosions (1000 m) quite well; about 95% decrease with depth is found in both cases. However, the REFMS change is much steeper for subsurface explosion depths. That is, in the REFMS modeling of the nuclear source, full coupling is approached much faster than in the LLNL modeling. Otherwise, the 1-kt TNT REFMS predictions remain above the predictions for the nuclear source by a factor of 0.667 (Cole, 1948) as expected; for explosion depth of 1000 m, the HE peak pressure is 2.77 bars and the NE pressure is 1.85 bars. The latter is rather close to the LLNL's 2 bars at the same depth.

The REFMS predicted change in peak pressure is much smaller for the HE source (67.5%) than for the nuclear source (95%), when explosion depths of 0 m and 1000 m are compared. In

addition, the change in the HE case is more gradual. In fact, the rate of change in coupling for shallow explosion depths suggested by the LLNL modeling is closer to the REFMS curve for the 1-kt TNT than to the REFMS curve for the nuclear source. Although our sound-velocity profile may be somewhat different from the profile used by Clarke et al. (1995), the discrepancies are likely due much more to differences in the modeling than to differences in the water profiles.
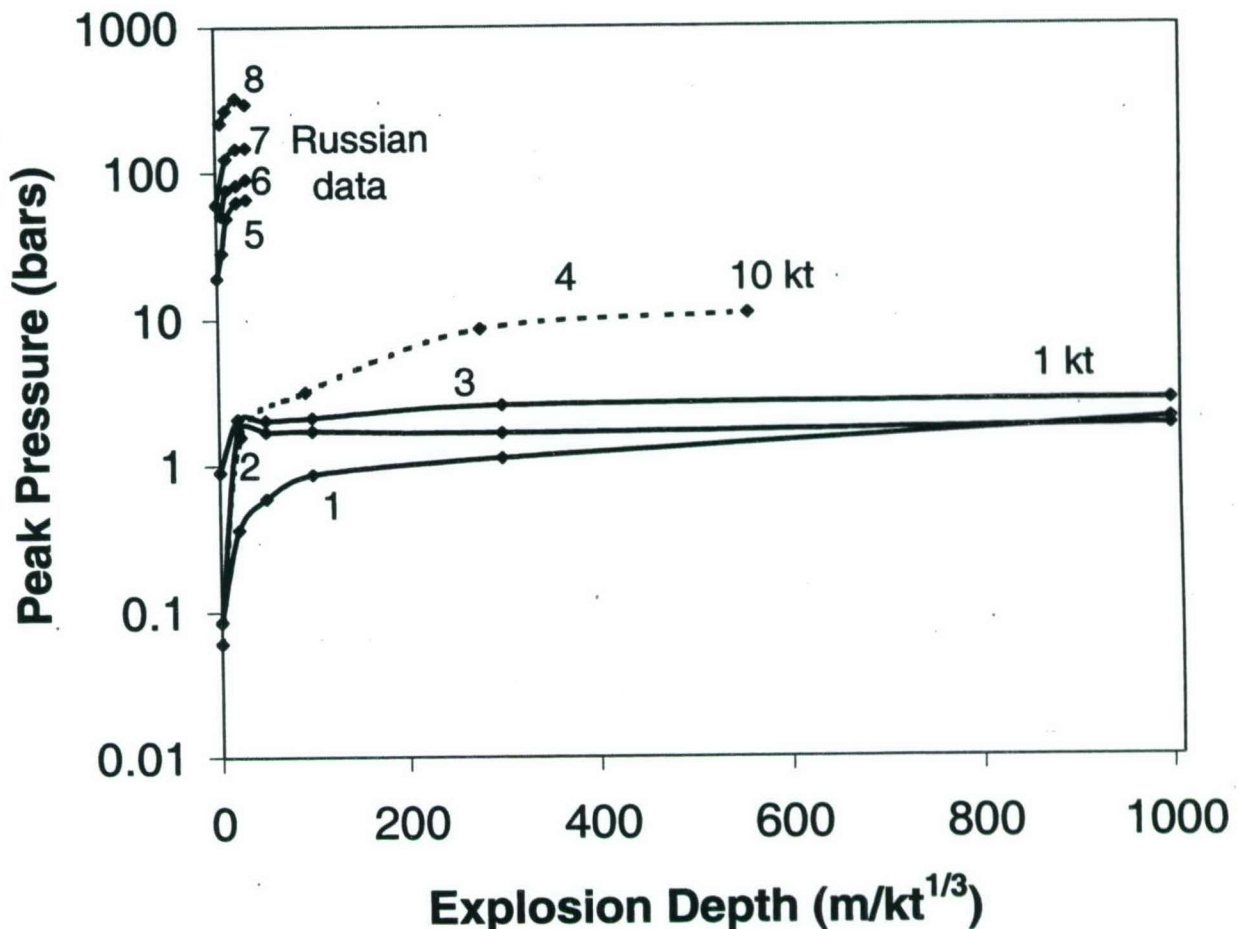
Figure 6-1. Summary of observed and simulated peak pressures. 1 – LLNL simulation of a 1-kt NE; 2 and 3 – REFMS simulations of 1-kt NE and TNT, respectively; 4 – 10-kt NE; 5 to 8 – maximum peak pressures measured from the Russian experiments at distances 30 m, 22.5 m, 15 m, and 7.5 m, respectively.

Figure 6-2 is similar to Figure 6-1, but focuses on the shallow explosion depths. It shows together the 1-kt predictions, the Russian observations in the shallow reservoir at a sensor depth of 1.5 m, and averaged data from the 1957 underwater nuclear explosion in Novaya Zemlya. The scaled distance for the latter is between 160 and 130 $m/kt^{1/3}$, if a yield between 3 kt and 6 kt is assumed, respectively. This fits well the scaled range of 162 $m/kt^{1/3}$ (real distance 7.5 m) for curve 8 of the small-scale observations, on which the circle marking the 1957 explosion falls. The rates of change in the small-scale observations agree well with the rates in the REFMS predictions of the HE source and some of the estimates in the LLNL modeling. As an example, there is a decrease of ~60% ($\varepsilon = 0.4$) at 15-m distance to ~70% ($\varepsilon = 0.3$) at 30 m in observed peak pressures when explosions on the surface are compared with explosions at mid-pool depths

(e.g., 1.5 m), for which the largest peak pressures were measured in the Russian experiments. This matches well the 67.5% decrease predicted by REFMS for the 1-kt TNT explosion when an explosion on the surface is compared with an explosion at 1000 m depth, and is predictably smaller than the 95% decrease for the nuclear sources in both the REFMS and the LLNL modeling. The decrease in peak pressure is the largest for the half-immersed charges in the Russian data and becomes smaller as explosions are detonated at larger depths. For explosion depths 0.25 m, this decrease is from ~30% ($\varepsilon = 0.7$) to ~60% ($\varepsilon = 0.4$) as distance increases, while for explosions at depths 0.5 m, the observed decrease in the peak pressures is from 15% ($\varepsilon = 0.85$) to 25 % ($\varepsilon = 0.75$) with increasing range. These data also show that for any fixed shallow explosion depth, a larger decrease is observed in peak pressures measured at increasing distances from the source, but the details of this relationship are not known at present.
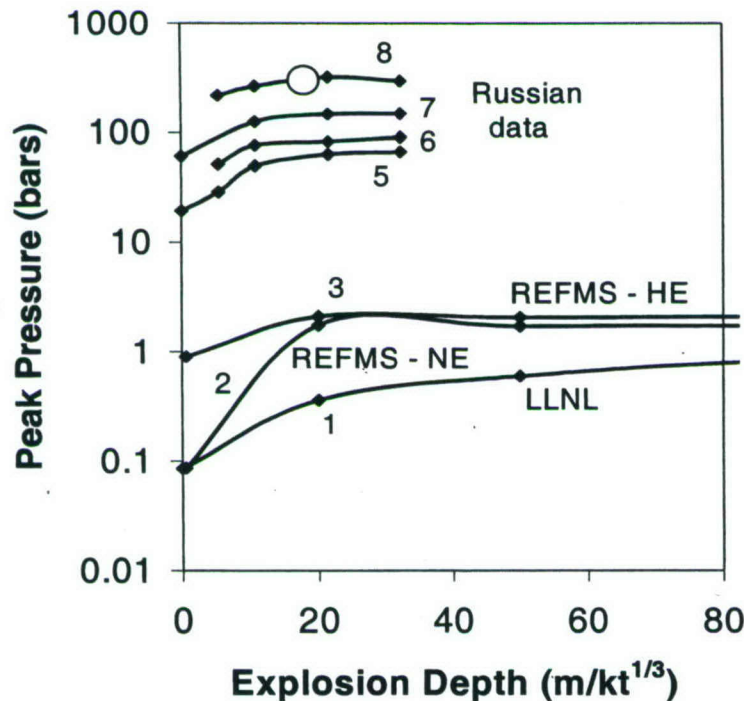
Figure 6-2. Russian observations and 1-kt simulations for small explosion depths. Numbers are same as in Figure 6-1. Circle shows average peak pressure (300 bars) measured at 235 m from the 1957 underwater nuclear explosion.

The REFMS modeling performed in this work made it possible to make detailed predictions directly relevant to the experimental setup of the Russian tests. The agreement between predictions and measurements provides a further validation of the REFMS code. Given that the modeling of these small-scale hydroacoustic data was satisfactory, especially for mid-reservoir depths of explosions and sensors, it is possible to attempt to calculate the peak pressures that would have been observed at larger distances, given that the reservoir would have also been deeper. The necessary scaled distance here is 465 m (scaled down from 10 km by a factor of 21.5). For that distance and a sensor depth of 1.5 m in a hypothetical reservoir 100 m deep, with everything else the same as in the original Russian experiments, the simulated peak pressures from 100-kg TNT explosions with depths varying from 2.5 m to the surface change from about 2.8 bars to 0.94 bars, i.e. the decrease is about 67%, same as the observed one. Peak pressures calculated for sensor

depths of 50 m (mid-depth of the hypothetical reservoir) stay at about 2.8 bars for explosion depths between 5 m and 50 m. This estimate is rather close to the peak pressure of 2 bars for the reference 1-kt explosion at 1000 m depth obtained by Clarke et al. (1995).

Good agreement is also achieved if we take the peak pressures measured in the Russian experiments and attempt to extrapolate them to the hypothetical distance of 465 m, assuming the simplest decay with distance, that is ~ $1/R^{1.13}$ (Cole, 1948) where R is the horizontal distance from the explosion (see Section 2). The measurements in the middle of the reservoir (i.e., least affected by the boundary conditions), such as for explosion and sensor depths 1.5 m, vary roughly between 300 and 60 bars for ranges 7.5 m to 30 m (see Figures 5-2 and 5-6). The decay of these peak-pressure measurements with distance can indeed be described as approximately proportional to $1/R^{1.13}$, translating into a peak pressure of around 2.8 bars at 465 m distance; i.e., the same estimate as above. This is reassuring, as the $1/R^{1.13}$-proportionality is known to be valid only for unbounded homogeneous water, and our case, although homogeneous, is anything but unbounded.

Clarke et al. (1995) estimated the total acoustic energy at 10-km range from a fully coupled reference explosion with depth 1000 m to be 31.3 metric tons (t). It gradually decreases with explosion depth, so that for explosions at depths 20 m and 0 m (on the surface), the total wave energy is 2.1 t and 0.174 t, respectively. Using these estimates, we can deduce that the energy coupling ratios are about 1:14 for a 20-m explosion depth and 1:180 for a surface explosion. The ratios in terms of peak pressures for the same explosion depths are 1:6 and 1:24, respectively. That is, 13 times change in the coupling energy ratio translates into 4 times change in peak-pressure ratio. On the basis of the energy coupling ratios (Clarke et al., 1995), we estimated that the total wave energy from the 1-kt shallow explosions at 20 m and 0 m depths is equivalent to that of about 71.4 t and 5.6 t HE, respectively, detonated at 1000 m depth. In view of this, since even kilogram-size HE explosions can be detected under favorable conditions, the IMS hydroacoustic network should not miss 1-kt explosions detonated at any depth in the ocean, including on the surface.

Given the inherent limitations of comparing near-field measurements with far-field simulations, and the additional shortcomings of comparing homogeneous, but severely bounded water, with sound-velocity profiles characteristic for the real ocean, we can assume on the basis of the above discussion that a reasonable agreement exists between the Russian observations and the REFMS predictions, as well as with some aspects of the LLNL predictions. Thus the reservoir experiments and the REFMS modeling performed here can be considered as a further confirmation that a 1-kt TNT explosion detonated at any depth in the ocean will be detected by the existing IMS network.

SECTION 7
CONCLUSIONS

Unique historic Russian data sets from three nuclear explosions in the shallow waters of the Bay of Chernaya (Novaya Zemlya) and 100-kg TNT reservoir explosions have been examined and analyzed for the purpose of characterizing the effect of charge depth on the hydroacoustic signals. This is of interest to CTBT monitoring because of the diminished signal levels from shallow explosions as compared to fully immersed charges. We made various estimates to compare with existing relationships describing the coupling of hydroacoustic energy. We have also modeled the small-scale HE explosions, using the REFMS code for modeling of shock waves in water.

In the 50's and 60's, the nuclear explosions in the Bay of Chernaya demonstrated the potential for evasion in shallow basins and reservoirs. Radioactive contamination stayed mostly in the bay and was not detected in the open sea. The acoustic waves from such explosions cannot reach the world sound channel at above-noise level and do not produce gas bubble phases as deep-water explosions do. The hydroacoustic energy is rather small by comparison with the energy transmitted in the air and the ground. Such explosions are thus not easily detectable with hydroacoustic means and could have posed a significant detection problem at that time. Today such nuclear blasts would be easily detected with the seismic network for CTBT monitoring.

The following is a summary of the findings from the analysis of the Russian nuclear explosions:

- *1957 underwater explosion* - Based on REFMS modeling and comparison with the HE small-scale observations, this explosion appears of lower yield (~5 kt) than the reported 10 kt.

- *1961 above-water explosion* - We calculate a pressure coupling coefficient $\varepsilon = 0.0412$ based on the relationships given in *EM-1* (1996). The estimate of the free-water peak pressure from a 16-kt nuclear explosion at 35 km is 158 dB. 4% of this estimate yields 130 dB, in excellent agreement with the pressure level of the observed direct shock-wave phase. In this case, the effect of shallow basin does not appear different from that of deep water.

- *1961 underwater explosion* - The estimated free-water peak pressure at 35 km is 154 dB, and the observed pressure is ~ 100 dB. Thus the observed $\varepsilon \sim 0.2\%$, while *EM-1* (1996) assumes full coupling ($\varepsilon = 100\%$) for such charge depth. This large discrepancy may be due to strong effect of the shallow bottom, measurement errors, and/or unrealistic *EM-1* predictions.

- *Closest U.S. analogues* - 1946 Baker and 1958 Umbrella.

The results from the analysis of the small-scale 100-kg TNT hydroacoustic data are summarized as follows:

- *REFMS modeling* - The REFMS predictions and the Russian measurements of shock-wave parameters and pressure time-histories agree very well. This agreement is especially good for peak pressures at mid-pool depth (~1.5 m), where the conditions can be readily approximated with free-water regime.

- *Coupling* – 40% to 70% ($\varepsilon \sim 0.6$ to 0.3) reduction of peak pressures is observed for the half-immersed charges as compared with the fully immersed charges. Unlike the *EM-1* relationships, both the observations and the REFMS prediction show marked decrease in coupling with distance.

The observations and results in this report suggest that the effect of charge depth on the hydroacoustic shock-wave energy is more complicated than currently accounted for by existing relationships. Thus these relationships may have to be adjusted, while the relevance of the effect of charge depth in small-scale HE shallow experiments to the effect of depth of nuclear explosions needs further investigation. In particular, it is desirable to examine more data from nuclear blasts, rather than making inferences from small-scale HE explosions. Although valuable in many respects, such inferences are limited by the current lack of knowledge and data. The IDG archives reportedly contain additional information on the nuclear explosions in the Bay of Chernaya, which will be made available to us for further analysis.

SECTION 8
REFERENCES

Britt, J.R., Application of Cagniard theory to reflection and refraction of explosion shock waves in soil and water, in *Proceedings II 9-th Int. Symposium on Military Applications of Blast Simulations, Oxford, England, 23-27 September 1985*, 1985. (UNCLASSIFIED)

Britt, J.R., *Shock Wave Reflection and Refraction in Multi-Layered Ocean/Ocean Bottom – A User's Manual for the REFM Code*, SAIC, DNA TR-86-49, January 1986. (UNCLASSIFIED)

Britt, J.R., R.J. Eubanks, and M.G. Lumsden, *Underwater Shock Wave Reflection and Refraction in Deep and Shallow Water. Volume I – A User's Manual for the REFMS Code (Version 4.0)*, SAIC (Science Application International Corporation), DNA-TR-91-15-VI, June 1991. (UNCLASSIFIED)

Brockhurst, R.R., J. Bruce, and A.B. Arons, Refraction of underwater explosion shock waves by a strong velocity gradient, *J. Acoust. Soc. Am.* **33**, 452-456, 1961. (UNCLASSIFIED)

Cagniard, L., E.A. Flinn, and C.H. Dix, *Reflection and Refraction of Progressive Seismic Waves*, McGraw-Hill, New York, 1962. (UNCLASSIFIED)

Clarke, D.B., J.W. White, and D.B. Harris, *Hydroacoustic Coupling Calculations for Underwater and Near-Surface Explosions*, Lawrence Livermore National Laboratory, UCRL-ID-122098, 1995. (UNCLASSIFIED)

Cole, R.H., *Underwater Explosions*, Princeton University Press, Princeton, New Jersey, 1948. (UNCLASSIFIED)

Eneva, M., J. L. Stevens, J. R. Murphy, and B. D. Khristoforov, Effect of charge depth in Russian hydroacoustic data from nuclear and HE explosions, in *Proc. 22nd Annual DOD/DOE Seismic Research Symposium, 12-15 September, 2000*, 2000. (UNCLASSIFIED)

Eneva, M., J. L. Stevens, B. D. Khristoforov, J. R. Murphy, and V. V. Adushkin, "Analysis of Russian Hydroacoustic Data for CTBT Verification", *Pure Appl. Geophys.*, 2001 (in press). (UNCLASSIFIED)

Eneva, M., J.L. Stevens, J. Murphy, B.D. Khristoforov, and V.V. Adushkin, Analysis of Russian hydroacoustic data for CTBT verification, in *Proc. 21st Annual DOD/DOE Seismic Research Symposium., 21-24 Sep., 1999*, Dept. Defense LA-UR-99-4700, 25-35, 1999. (UNCLASSIFIED)

Handbook of Nuclear Weapon Effects: Calculational Tools Abstracted from DSWA's Effects Manual One (EM-1), ed. J. Northrop, DSWA, pp. 736, 1996. (UNCLASSIFIED)

Korobeinikov, V.P. and B.D. Khristoforov, Underwater explosions, *Hydromechanics* **9**, 54-119, 1976 [in Russian]. (UNCLASSIFIED)

Kozachenko, L.S. and B.D. Khristoforov, Shock waves in a shallow-water reservoir, *J. Appl. Mech. Tech. Phys.* **4**, 166-171, 1970 [in Russian]. (UNCLASSIFIED)

Research Required to Support Comprehensive Nuclear Test Ban Treaty Monitoring, National Resource Council (NRC), National Academy Press, 1997. (UNCLASSIFIED)

Stephens, T. and C.S. Kelly, DNA updates Computational Aids, *Science & Technology Digest*, 29-30, 1995. (UNCLASSIFIED)

Stephens, T. and C.S. Kelly, Computational Aids Update, *Science & Technology Digest*, August, 42-43, 1996. (UNCLASSIFIED)

Stevens, J.L., G.E. Baker, R.W. Cook, G. D'Spain, L.P. Berger, and S.M. Day, Empirical and numerical modeling of T-phase propagation from ocean to land, *Pure Appl. Geophys.*, 2001 (in press) . (UNCLASSIFIED)

USSR Nuclear Weapons Tests and Peaceful Nuclear Explosions 1949 through 1990, Ministry of the Russian Federation for Atomic Energy, ISBN 5-85165-062-1, pp. 63, 1996. (UNCLASSIFIED)

Walker, D.A., C.S. McCreery, and Y. Hiyoshi, T-phase spectra, seismic moments and tsunamigenesis, *Bull. Seism. Soc. Am.* **82**, 1275-1305, 1992. (UNCLASSIFIED)

Voss, M.E. and R.M. Schmidt, *Explosive Shock Wave propagation in Shallow Water – Small-Scale Experiments with Rock and Layered Bottom Geologies*. Volume 1 - Text and Appendix A. Volume 2 – Appendix B, Technical Report to DNA, No. 001-89-C-0185, 1995. (UNCLASSIFIED)

APPENDIX A
EDITED RUSSIAN TEXT

The text included in this appendix is the edited version of the Russian report we received from IDG. Our version is the result of editorial efforts in terms of style and English, and extensive communication (including in Russian) with Dr. Boris Khristoforov aimed at clarifying some points. Despite our attempt to be comprehensive, some of the text may be biased due to our interpretation. If in doubt, the readers are referred to the original Russian report, which along with the IDG data, is made available in electronic form.

The titles of the chapters included in the IDG report are listed below: Of these, we extensively used data and text described in Chapters 1.1, 1.4, and 1.8. In respect to the material included in the remaining chapters, we either did not find it relevant at this time, or it came too late to be analyzed within the limits of this project.

Chapter 1.1   Measurements from nuclear explosions in the Bay of Chernaya, Novaya Zemlya

Chapter 1.2   Measurements of hydroacoustic signals in the Black Sea

Chapter 1.3   Hydroacoustic studies of deep-water bomb blasts in the Sea of Okhotsk

Chapter 1.4   Underwater explosions of cast spherical charges of 100 kg TNT in a shallow reservoir and parameters of underwater shock waves

Chapter 1.5   Parameters of shock waves in air from 100-kg TNT underwater explosions in a shallow reservoir and PETN laboratory experiments

Chapter 1.6   Parameters of shock waves in the reservoir bottom from 100-kg TNT underwater explosions

Chapter 1.7   Measurements from HE explosions above water and ground

Chapter 1.8   Influence of 100-kg TNT charge depth on the parameters of shock waves in water, air, and ground

Chapter 2.1   Characteristics of underground nuclear explosions

Chapter 2.2   Measurements of peak pressures from underground nuclear explosions 1966-1974

Chapter 2.3   Measurements at large distances from an underground nuclear explosion (November 2, 1974)

1.1. Results of Measurements from Explosions in the Bay Chernaya.

We perform research and analysis of Soviet data aiming at characterizing the processes involved in underwater, surface and coastal nuclear and chemical explosions. This work can be useful for increasing the efficiency of the hydroacoustic methods developed in the international system of monitoring (IMS) [1]. We are currently developing the database of such explosions. Results of measurements from nuclear explosions in the Bay of Chernaya are given below.

Underwater nuclear explosions of torpedoes, accompanied by tests of military equipment (?), were carried out in the fall of 1955, 1957 and 1961, in the Bay of Chernaya (Novaya Zemlya). In the water there were ships, submarines, hydroplanes, and floating stands, all with measuring equipment on. On the coast, there were several points with high-speed photographic and other equipment. In 1955, the torpedo was suspended from a ship at depth of 12 m; the ship was destroyed by the explosion. In 1957 and 1961, the torpedoes with nuclear charges were shot from submarines located near the strait connecting the bay with the sea. The depth of the bay where the explosions took place, did not exceed 60 m.

In 1957 there was also a coastal explosion; the charge was placed on a special support located on the northern coast of the bay. Surface explosions of torpedoes were also carried out in 1961 and 1962. The map of the Bay of Chernaya is shown in Figure 1. The basic characteristics of the nuclear explosions, for which there are archival data available, are listed in Table 1 [4-6].

Table 1.

№	Date, time Moscow	Energy, кT	Depth (Height), m	Coordinates
Underwater explosions				
1	21.09.55, 08:00:54	3.5	12	70.70N, 54.67E
2	10.10.57, 09:54:32.0	10	30	70.70N, 54.67E
3	23.10.61, 13:30:47	4.8 (4)	(20)	70.70N, 54.67E
Surface explosions				
4	27.10.61, 11:30:26.6	16 (17.5)	(1.1)	70.70N, 54.67E
5	22.08.62, 12:00:00	6		71.00N, 53.50E
Ground coastal explosion				
6	07.09.57, 11:00:01	32	On a tower	70.69N, 54.80 E

The purpose during the initial stages of testing was to define the basic physical characteristics and destructive potential of underwater nuclear explosions in shallow basins, to test military equipment, and to evaluate the performance of specially designed measuring devices.

The scientific research program included measurements of shock-wave (SW) parameters in water and air, seismic vibrations in the ground, plume evolution, gravitational waves and other surface phenomena, radioactive emission, radioactive conditions in water, and the environmental impact of the explosions. These data were used to evaluate the basic characteristics of the explosions and their TNT-equivalent, as well as to test existing theoretical models of underwater explosions and destructive potential on various objects.

The equipment and techniques for dynamic measurements of the explosions and their parameters was developed during the preparation stage of the tests. In order to improve the equipment and the recording of data, preliminary modeling research of explosions of TNT charges in various reservoirs was carried out.

The nuclear explosions were photographically registered from two perpendicular directions, using cameras AFA-33, AKC-1, AKC-2, etc. The use of high-speed cameras CK-2, AKC and AFABAF, was intended for registration of the fireball and its brightness temperature, as well as to take pictures of the explosions from an airplane.

The SW parameters in water were measured with mechanical gauges of pressure (MID-3), piston impulse meters (IM-1, IM-2, and IM-3), and piezoelectric gauges. Hundreds of such devices were hung from ships and floating stands at various depths, in a wide range of distances from the assumed epicenters of the explosions. To measure the surface waves, resistive sensors with signal registration on tenso-stations [?], were used. The SW parameters in air were measured with pressure recorders (SD-25).

The total γ-radiation doses were measured by photographic indicators, using automatic γ-meters, over a period of 30-40 hours, at various points of the experimental field. Various types of devices were developed for dynamic measurements of the radiation levels. The range of dose rates was from 0.001 to 100 R/sec. All X-meters were automatically triggered by outside signals [?].

The intensity of radiation that occurred with the approach of the gas bubble to the surface, gradually increased and reached a maximum as the products of explosion entered the atmosphere. It subsequently decreased to small values after the rise of the cloud. The plume from the first explosion did not shield the products of nuclear division, while the products from the second explosion did not brake through the plume and the intensity of radiation from the water column was low. [The main wave in both experiments carried about 10% of the total products of division.]

The concentration of the products of division was determined on the basis of the γ- and β-activity in samples extracted from the main wave, from the falling radioactive deposits, and also from water at various depths and distances from the explosion. Especially high levels of radioactive pollution were caused by the coastal explosion.

Table 2 shows measurements from the explosion on October 10, 1957. Peak pressure of the shock wave, P_m, were measured using mechanical gauges MID-3 at a distance R = 235 m and varying sensor depth h.

Table 2.

h, m	10	15	20	25	30	40	50
P_m, kg/cm^2	310	316	303	301	299	257	306

In each sensor location, 4 to 6 gauges were suspended. The average peak pressure from all measurements is $P_{m\ middl} = 299 \pm 12$ kg/cm^2. The equivalent charge radius based on these measurements is $R_0 = 7.5 \pm 0.8$ m, while the TNT- equivalent calculated from the shock wave is $q_{sw} = 2.83 \pm 0.9$ Kat. No gradients of the sound speed in water were taken into account in these estimates [2,3].

$$R_0, m = 5.33\ q_{sw}^{1/3}, \text{ where } q_{sw} \text{ is in kt.}$$
$$P_m, kg/cm^2 = 14700\ /\ (R/R_0)^{1.13}.$$

The total TNT-equivalent is determined by the ratio

$$q_{sum} = (q_{sw}/0.65) = 4.35 \pm 1.38 \text{ kt.}$$

The TNT-equivalent estimated on the basis of the numbers of divided uranium and plutonium (^{235}U and ^{239}Pt) nuclei, using two different methods, is $q_{sum} = 3.6 \pm 0.5$ kt. [(The first method is based on selection of samples of products of division and the second method is a bench-mark method of estimating the number of division, using a 25-kg molybdenum foil embedded in the sample)???].

Figure 2 shows (a) an infrasound signal recorded by a microbarograph at a distance of 4430 km from the coastal explosion on September 7, 1957, and (b) a seismogram recorded at a distance of 120 km, in the town of Belushya, from the underwater explosion on October 23, 1961.

Figure 3a-c show hydroacoustic signals recorded from the underwater nuclear explosion on October 23, 1961. The explosion depth was 20 m and the bottom depth under the explosion was 47 m. These records were made on two ships at distances 18.8 and 56.6 miles, along a line from the explosions through the strait connecting the bay with the sea. [Notes from M. Eneva based on e-mail communication with B.D. Khristoforov: (1) distances are in nautical miles, 1 n. mile = 1.853 km; (2) geographic co-ordinates of sensor locations are not known at time of writing]. The hydrophones were placed at 1 m from the bottom and were supplied with filters. [Note from M. Eneva based on e-mail communication with B.D. Khristoforov: three filters were used, "infrasound" (5-100 Hz), "sound" (60-10,000 Hz, and "ultrasound" (8-100 kHz).].

At distance R = 18.8 miles, the bottom depth is 50 m, and the ground consists of granite with a small layer of silt. The noise level is 94 dB and 81 dB for the sound and infrasound filters, respectively [Note by M. Eneva - After a check with B.D. Khristoforov: for some reason, not all noise levels cited in the archival materials are those seen on the records]. The times of first arrival are t=12 s and 10 s for the records in the two frequency bands, with corresponds effective speeds (R/t), 2.9 and 3.48 km/s. These arrivals probably corresponds to waves reflected from the crust and passing the layer of deposit on the bottom. The arrival time of a T-phase, with a characteristic speed of 1.43 km /sec, should be observed around 24.4 s on records. There are

indeed appreciable signals around this time. The water temperature first increased with depth, from 1.5^0 to 7.7^0 C at depth 30 m, and then decreased to 5.8^0 C at depth of 50 m.

At a distance of 56.6 miles, the noise level was 66 dB in the sound range of frequencies. The depth of bottom was 60 m. The first arrival was at time 13:36:18. Given the time of explosion, 13:30:47, the difference of 331 s corresponds to an effective speed of 0.27 km/s, which is close to the speed of sound in air. This signal may be caused by the piston action of the rising plume and then refracted in the air sound channel.

Figure 4a-d, shows hydrophone records from the above-water nuclear explosion on October 27, 1961. It was detonated at 1.1 m above the water surface. The bottom depth under the explosion was 59 m. The records at distances 18.8 and 87.6 miles by the same ships, as from the first explosion. Again, the hydrophones were placed 1 m above the bottom, along a line from the explosion through the mouth of the bay.

At the 87.6-miles distance, the noise level was 86 dB in the infrasound range of frequencies at The depth of the sandy bottom was 45 m. At time 11:30:52, as marked on the record, i.e. 25.4 s after the explosion, an arrival is seen with effective speed of 6.32 km/s. This wave is reflected from the boundary between the crust and the top of the mantle. The time of registration after this arrival is only ~22 seconds (or 47.4 s from the beginning of explosion), which is too short for a T-phase to be observed, which should come to the hydrophone within 112.2 sec at a sound speed of 1.43 km/s.

At a distance of 18.8 miles, the registration was carried out on three channels, supplied with different filters. As in the first explosion, the bottom depth was 50 m at this location. The noise levels were 96 dB, 94 dB and 76 dB for channels (b), (c), and (d), respectively. At time 11:30:51, marked on the records of channels (b) and (c), a T-phase with average speed $C = R/t$ $=18.8*1.853/24.4 = 1.43$ km/s. The arrival time of 24.4 sec follows from the difference between the time of explosion, 11:30:26.6, and the arrival time of the wave to the hydrophone, 11:30:51. On channel (d), it is also possible to discern a signal around time 24.4 sec, appropriate for a T-phase. The temperature distribution measured around the hydrophone location, at depths from 0 to 50 m, has indicated a temperature of $3.5-4.0^0$ C, in agreement with sound speed of 1.43 km/s for weakly salinated water.

These data characterize the effect of nuclear explosions in a shallow, enclosed reservoir, such as the Bay of Chernaya (Novaya Zemlya). Such reservoirs can be used for cove-up of underwater nuclear explosions, since the radioactive pollution of the water remains within the limits of the reservoir, while the acoustic waves can not reach the world sound channel, and phases due to repeated pulsation of deep-water gas bubbles are absent (the gas bubble breaks in the atmosphere). The hydroacoustic energy in such basins is substantially diminished, while the energy transmitted by the explosion to the air and the ground is increased. The nearest U.S. analogues of the underwater explosions in the Bay of Chernaya, are Shot Baker (July 24, 1946) at depth of 30 in a lagoon with bottom depth 60 m, with announced TNT-equivalent of 20 kt, and Shot Umbrella (June 8, 1958). Other underwater explosions were carried out in open, deep basins.

References

1. Stevens, J.L., G.E Baker, J.R. Murphy, R.W. Cook, G.L. D' Spain, L.P. Berger, B.D. Khristoforov, T-phase Excitation and Transfer Function Research, *20th Annual Seismic Research Symposium on Monitoring a Comprehensive Test Ban Treaty*, Santa Fe, New Mexico, September 21-23,1998.

2. Cole R., *Underwater explosions*, 1948.

3. Yakovlev, Yu.S., *Explosion Hydrodynamics*, Sudpromgiz. Publ., 1961, pp. 314 [in Russian]. (Ю.С. Яковлев. Гидродинамика взрыва. Судпромгиз. 1961, с. 314.)

4. *The Effects of Nuclear Weapons*, Washington. 1957.

5. Cochran T.B., W.M. Arkin, R.S. Norris, J.I. Sands. *Soviet Nuclear Weapons*, M.1992.

6. *Nuclear Tests of USSR*, Moscow, Izdat Publ., v.1 - 1997, v.2 – 1999. (Ядерные испытания СССР. Москва. ИЗДАТ. т.1. 1997, т.2. 1999).
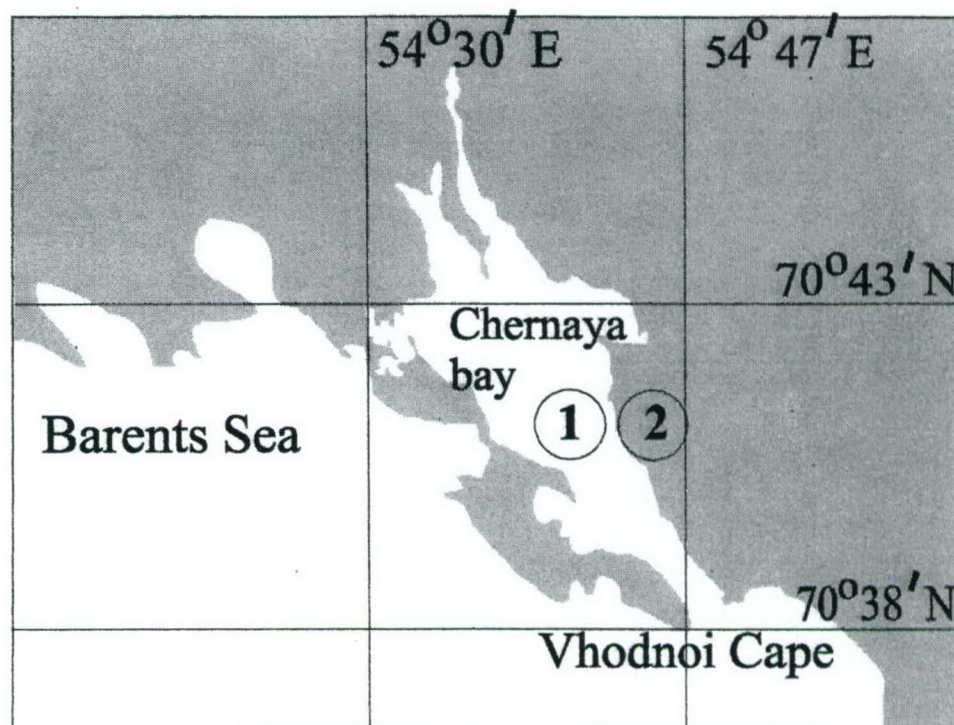
Figure 1. Map of the Bay of Chernaya. 1 - location of three underwater and one above-water explosion. 2 - location of the coastal explosion.
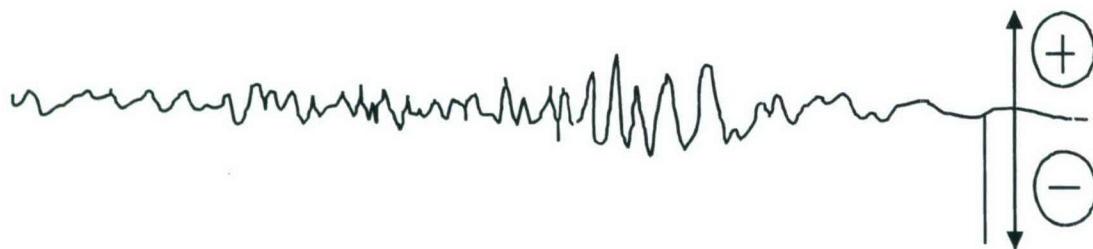
Figure 2a. Infrasound record at 4430 km from the coastal explosion near the Bay of Chernaya, September 7, 1957.
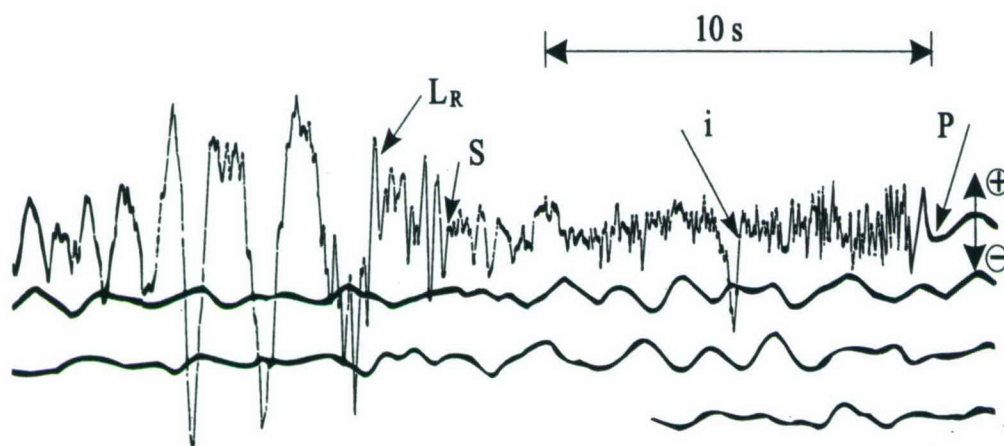
Figure2b. Seismogram from the 1961 underwater explosion recorded at 120 km (Belushya).
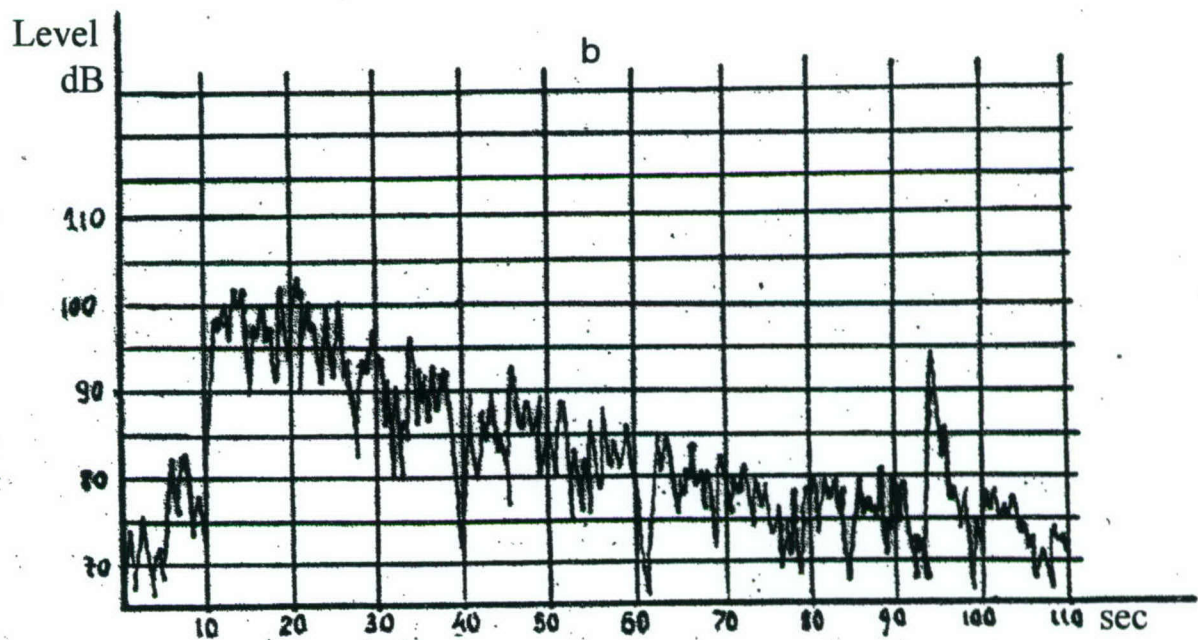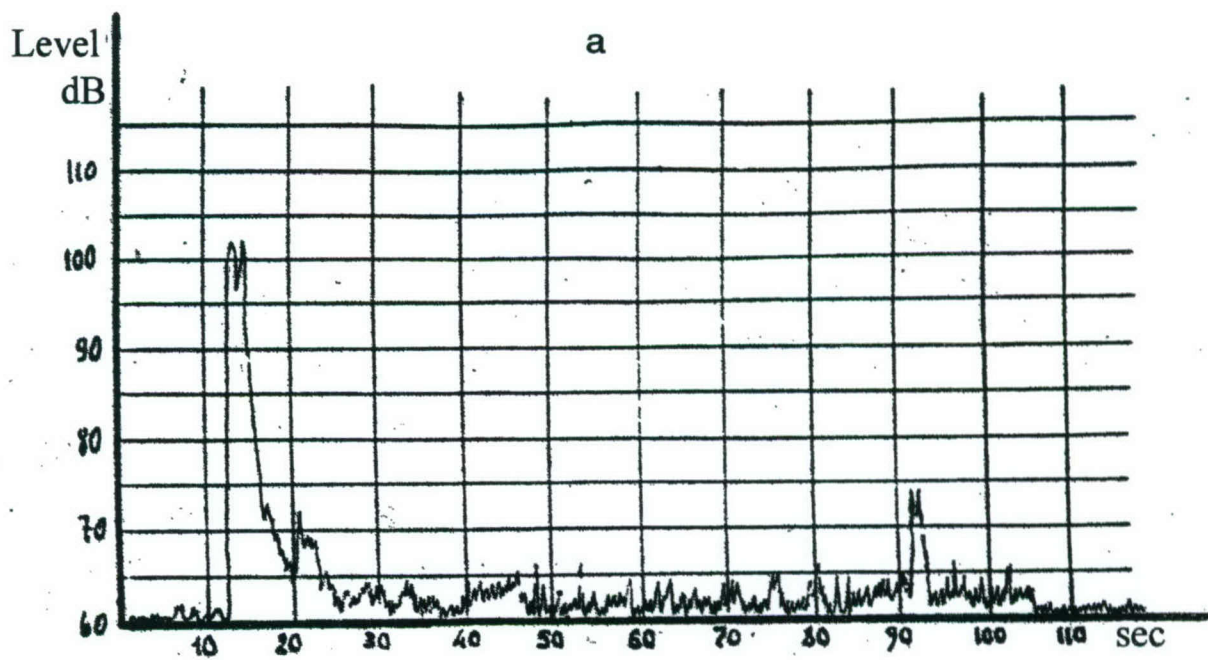
Figure 3a-b. Hydrophone records in the (a) sound and (b) infrasound band of frequencies, at a distance of 18.8 miles from the underwater nuclear explosion on October 23, 1961.
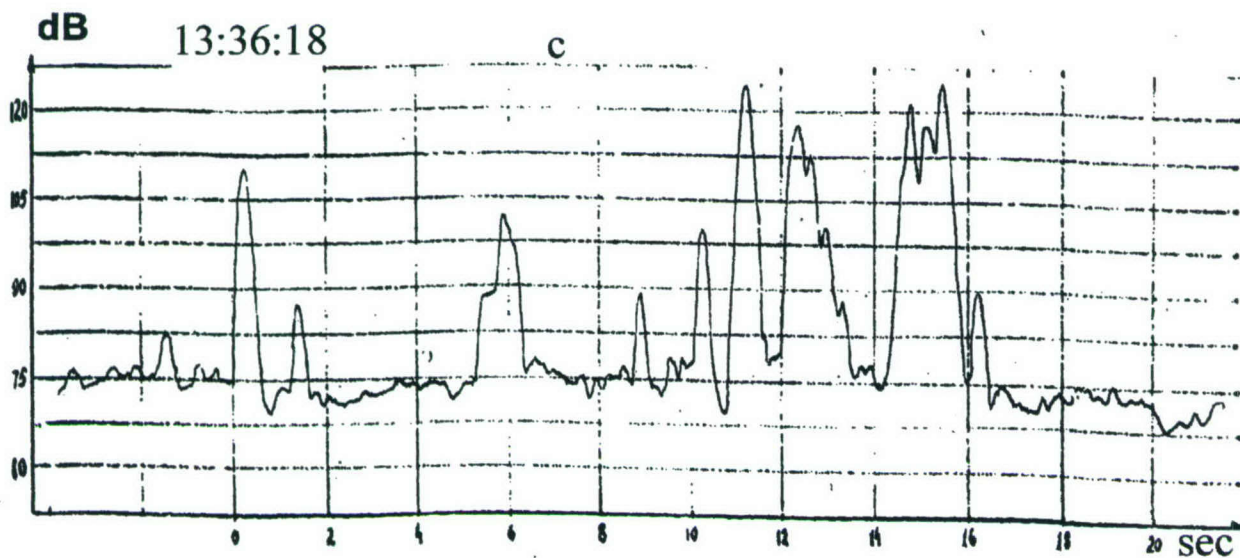
Figure 3c. Hydrophone record in the sound band of frequencies, at distance of 56.6 miles, from the underwater nuclear explosion on October 23,1961.
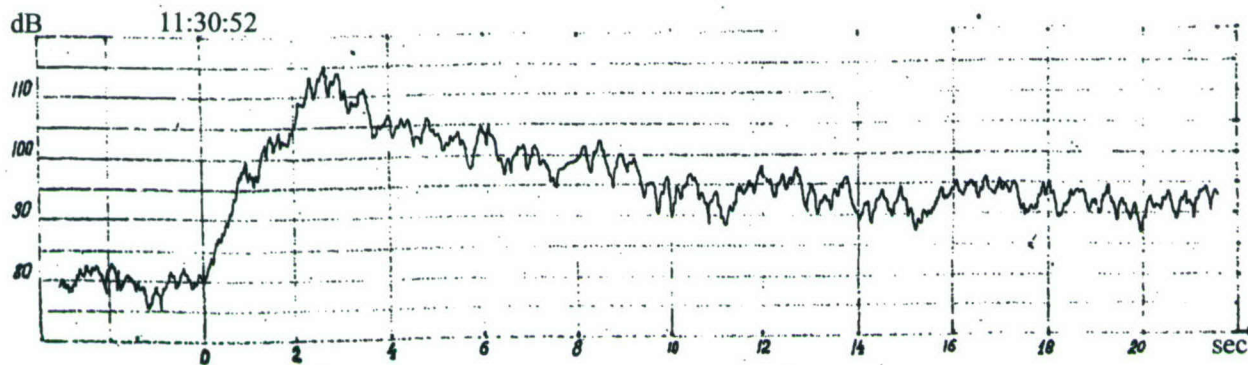
Figure 4a. Hydrophone record in the infrasound band of frequencies, at a distance of 86.6 miles and depth of 44 m, from the above-water nuclear explosion on October 27, 1961.
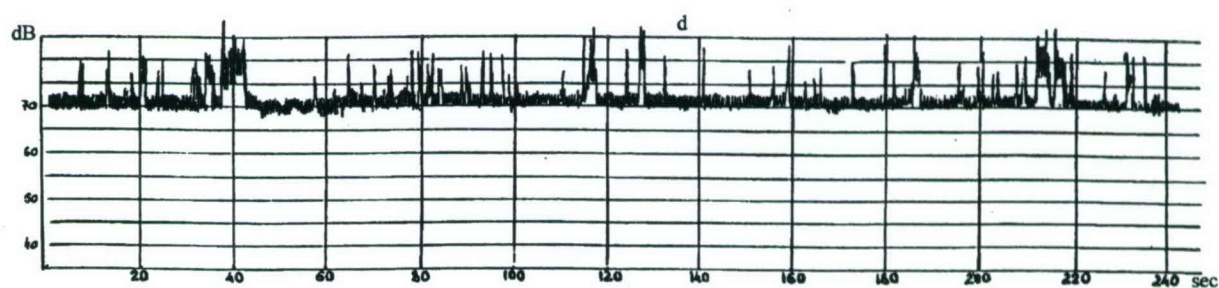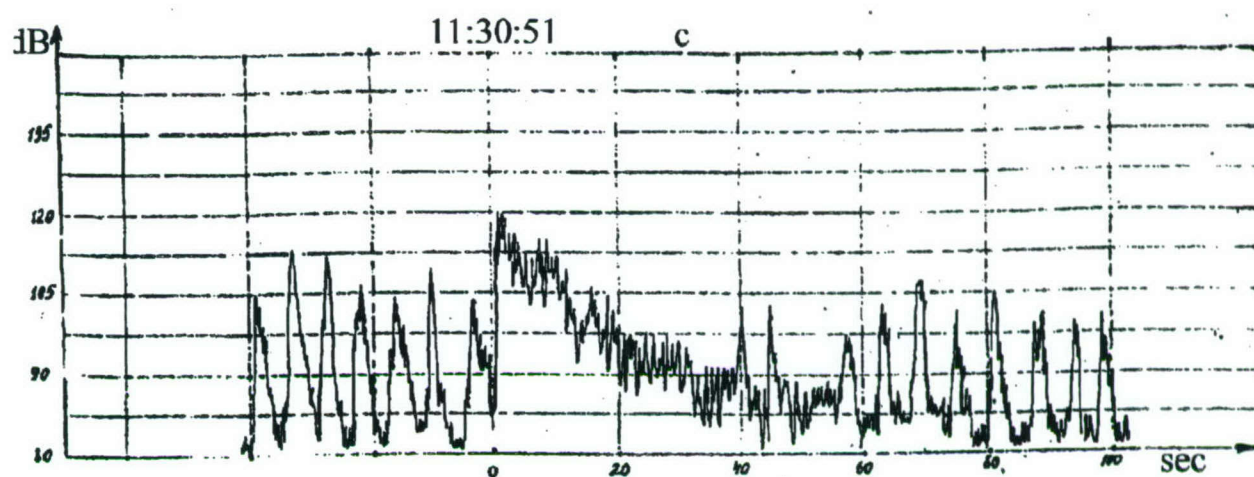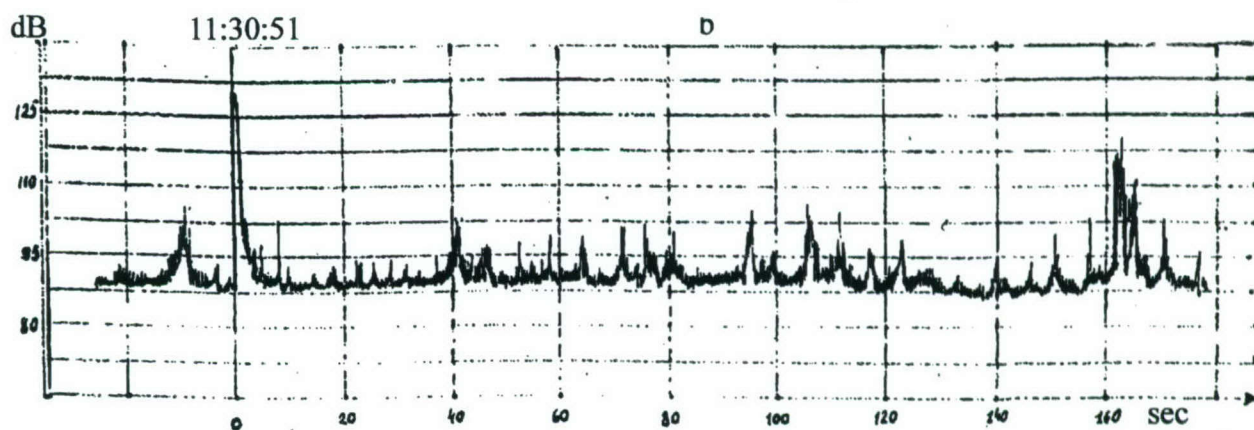
Figure 4 b-d. Hydrophone records in the (b) sound, (c) infrasound, and (d) ultrasound frequency bands, at a distance of 18.8 miles and at depth of 49 m, from the above-water nuclear explosion on October 27,1961.

1.2. Measurements of hydroacoustic signals in the Black Sea

1.2.1. Measurements with mechanical gauges MID-3 from an explosion of a detonation cord in the Black Sea. Weight 3250 kg, radius of the cord $R_0 = 3.65$ cm, length $l = 500$ m, explosion depth $H = 1$m.

In February 1957 an explosion of a 3250-kg detonation cord was conducted at a depth of 1 m in the Black Sea, near the city of Sevastopol. The radius of the cord was 3.65 cm (R_0) and its length 500 m. The explosion was recorded by a high-speed camera. Shock-wave parameters were measured at distances R = 25, 50, 100 and 200 m from the charge centre, at depths h = 1 to 10 m. The records were made with mechanic pressure gauges (MID-3) and impulse recorders (IM) - same as the ones used to record the signals from the nuclear explosions.

Table 1.2.1 lists the observed mean peak overpressures P_{ml}. Due to the free-surface effect, these values decrease as depth increases. At a distance of 200 m, a sharp increase in overpressure and impulse is observed near the free surface. This effect may be explained with certain features of sound propagation in inhomogeneous liquid with a waveguide. Peak overpressure of the shock wave for an explosion in infinite liquid space can be represented as the following function of distance normal to the charge:

$$P_{ml} = 17200/(R/R_0)^{0.74} \quad \text{for distances up to } R/R_0 = 5840, \tag{1.2.1a}$$

where P_{ml} is measured in kg/cm^2. When deriving this relationship, along with the experimental data corrected for the free-surface effect, if necessary, an initial overpressure $P_{ml} = 252.6$ kg/cm^2 at the maximum distance $R/R_0 = 300$ was used, as suggested by Reach and Ginell [1]. The asymptotic formula for the peak overpressure at a large distance from an explosion of a cylindrical charge, in an infinite liquid space, is as follows [2]:

$$P_{ml} = 18360/(R/R_0)^{0.75} \tag{1.2.1b}$$

Table 1.2.1 [Note by M. Eneva: P_c denotes the calculated values, P_m the observed values]

R, m											
25			50			100			200		
h, m	P_c, kg/cm^2	P_m, kg/cm^2	h, m	P_c, kg/cm^2	P_m, kg/cm^2	h, m	P_c, kg/cm^2	P_m, kg/cm^2	h, m	P_c, kg/cm^2	P_m, kg/cm^2
3	137	130	1.5	40.4	42	1	18	20	1.5	10	34
4	137	136	2.5	50.3	50	2	21.2	22	2.5	11.2	23
6	137	140	4.5	73.2	74	4	28.4	30	4.5	13.8	15
8	137	143	6.5	82	83	8.6	49.1	51	6.5	16.6	17
10	137	140	8.5	82	80				8.5	19.7	19

The following empirical formula was derived from laboratory experiments [3], valid for distances up to $R/R_0 = 221$:

$$P_{ml} = 15482/(R/R_0)^{0.71} \tag{1.2.1c}$$

The P_{m1} values calculated using all equations (1.2.1) are shown in Table 1.2.2. Formula (1.2.1b), with experimentally derived coefficients, is consistent with the experimental formula (1.2.1a). The difference in the values predicted by (1.2.1a) and (1.2.1c) increases with increasing range, since the latter formula is only valid to distance $R/R_0 = 221$ [Note by M. Eneva: this is ~ 80 m in this case].

The characteristics of weak shock wave propagation near the free surface have been discussed in [4, 5]. These formulas can be applied for estimates at large distances from a cylindrical charge, where the shock-wave front can be approximated with a plane (Figure 1.2.1). Incident angle of the shock wave decreases with distance as $\alpha \sim H/R$. Assuming that $P_{m1} = 17200/(R/R_0)^{0.74}$ for an explosion in infinite liquid space, a critical incident angle can be estimated as:

$$\alpha^* = [(n+1)P_{m1}/2Bn]^{1/2} = 1.8/(R/R_0)^{0.37}$$

Since $\alpha^* = H^*/R = 1.8/(R/R_0)^{0.37}$, then $H^*/R_0 = 1.8(R/R_0)^{0.63}$ and $H^* = 0.0657(R/R_0)^{0.63}$ m, while $P^1 = P_{m1}(1 + (\alpha/\alpha^*))^2/4$, where $Bn = 21800$ kg/cm^2 [1, 4, 5].

Table 1.2.2

R, m	25	50	100	200
R/R_0	685	1370	2740	5480
P_{m1}, kg/cm^2 (a)	137	82	49.1	29.4
P_{m1}, kg/cm^2 (b)	137.1	81.5	48.4	28.8
P_{m1}, kg/cm^2 (c)	150	91.8	56.1	34.3
H^*/R_0	110.1	170.4	264	408
H^*, m	4.02	6.22	9.62	14.9
α^*	0.16	0.124	0.0962	0.0745
α	0.04	0.02	0.01	0.005
h_b, m	3	5.2	8.62	13.9
P^1 kg/cm^2	53.4	27.7	15	8.37

When $H > H^*$, reflection from the free surface is regular and the overpressure at the wavefront is the same as in infinite liquid space. When $H < H^*$, the reflection is non-regular and the overpressure decreases as depth of explosion H decreases. Table 1.2.2 shows the predicted values for H^*/R_0, H^*, h_b, α^*, α, and P^1, which determine the character of interaction of the shock wave with the free surface.

Table 1.2.1 shows the predicted peak overpressure values in shock waves, P_c, corrected for the free surface effect, along with the mean observed values P_m. The predicted and the measured values are consistent at all distances, except R = 200 m, where the predicted overpressure at small depths is a factor of 2 to 3 smaller than the average from five sensors measurements, while the predicted impulse is a factor of 1.7 lower. This discrepancy may be associated with sound wave propagation in an inhomogeneous liquid, with a layer having a sound speed gradient. The characteristic winter distributions with depth of the salt concentration, temperature t, and sound speed C are presented in Table 1.2.3, where:

$$C = 1410 + 4.21t - 0.037 \, t^2 + 1.14 \, S + 0.018 \, h.$$

Figure 2.1.2 shows sound propagation in a waveguide with characteristics listed in Table 1.2.3. The sound speed distribution with depth is given by the relationship [6]:

$$C = C_0[1+ h \, d(C/C_0)/dh] = C_0((1+k(h-11)),$$

where $k = d(C/C_0)/dh = 0$ for $h < 11$ m; $k = 41 \times 10^{-4}$ m^{-1} for $h > 11$ m.
Let an explosion occur at point O, in a layer with a constant sound speed (where $k = 0$), at a height Z_0 above the interface (1) with the region with the speed gradient. In the geometric acoustic approximation, valid for short-length waves from explosions near the free surface, it is assumed that the explosion generates signals that propagating to point B at height Z above the interface (1) along various paths, as shown in Figure 1.2.2. In the top water layer, where $k = 0$, the sound rays are straight and incident angles on the interface from both sides are equal. In the lower water layer, where $k > 0$, the rays are curved towards the interface (1), as predicted by the Snellius law:

$$\cos \alpha /\cos \alpha_0 = C(h) / C_0; \quad n\cos \alpha = \cos \alpha_0; \quad n = C_0/C$$

The analysis conducted in [6] shows that the rays leaving the source at an angle $\alpha_0 < \alpha_k = \arccos[1/(1+kh_0)]$, return back to the horizontal plane, where the explosion is conducted, and are focused at a distance $R = 2(\tan\alpha_0+p/\tan\alpha_0)/k$, the focusing factor being equal to $f_1 = (\cos^2\alpha_0)(\tan^2\alpha_0 + p) / (\tan^2\alpha_0 - p)$, where $p = k(Z + Z_0) / 2 = 0.041$, and h_0 is the thickness of the layer with the velocity gradient. If h_0 is large enough, when $\alpha_k = 90°$, all incident rays return back to the upper layer at various ranges R.

Table 1.2.3

h, m	S, %₀	t, °C	C, m/s	h, m	S, %₀	t °C	C, m/s
1	8	0	1419	14	18	1.5	1437
2	8	0	1419	16	24	2.5	1448
10	8	0	1419	18	30	3.5	1460
11	8	0	1419	20			1471
12	12	0.5	1426	22			1483

In table 1.2.3, $h_0 = 11$m, $k = 41 \times 10^{-4}$ m^{-1}, $\alpha_k = 16.9°$, that is, only the rays with radiation angles $\alpha_k < 16.9°$ can return through the interface (1). When $\alpha_0 = \arctan(p)^{1/2} = 11.5°$, f_1 is infinite. For such angles the rays are concentrated near a caustic surface, where the geometric approximation is not valid and potentials should be used [6].

Table 1.2.4.

$\alpha_0°$	12	13	14	15	16	17
$\tan\alpha_0$	0.2126	0.231	0.249	0.268	0.286	0.306
R, m	198	199	201.8	205.4	204.5	214.5
f_1	19.6	7.27	4.58	3.42	2.76	2.34

Table 1.2.4 presents estimates calculated using the above formulas. These parameters indicate focusing conditions for $Z = Z_0 = 10$ m, $p = 41 \times 10^{-3}$, $k = 41 \cdot 10^{-4}$ m^{-1} in the permissible range of

angles $11.5° < \alpha_0 < 16.9°$. Mean values for R ~ 200 m, f_1 ~ 4 are consistent with the experimental data from Table 1.2.1.

The intersection of the caustic surface with a horizontal plane, where the intensity drops 3 to 5 times, represents a circle with a radius R_k, focusing factor f_2 and width of the zone Δr. Using the potential technique, the following formulas are obtained[6]:

$$R_k = 4(p)^{1/2}/k = 198 \text{ m}; \quad f_2 = 1.257(k_0 rp)^{1/3} = 8; \quad \Delta r = 0.287(\lambda^2 r)^{1/3}/p^{2/3} = 4 \text{ m}.$$

In the caustic zone, the wave amplitude is maximum, dropping rapidly outside this zone. The analysis performed and the observations demonstrate the potential for a considerable increase in sound impulse, in the presence of a water layer of a size comparable with the charge length, characterized by a positive sound speed gradient. There are also shadow zones, where sound intensity is many times lower than that in homogeneous water. Optimal conditions for hydroacoustic propagation at large distances can be created in underwater waveguides with a minimum sound speed along the waveguide. Attenuation in the waveguide is large only at frequencies above 1 kHz [6]. Inside the global sound channel (SOFAR), which is at a depth of about 1 km in the southern and central parts of the world ocean, the attenuation of the frequencies generated by standard explosions (below 100 Hz) is negligible. Thus, detection of underwater explosions by hydroacoustic methods is possible up to distances of 10,000 km.

References

1. Cole, P., *Underwater explosions*, IIL. 1950. [Russian translation].

2. Khristianovitch, S.A., Shock waves at long ranges from explosions, *JAMM*, v. 20, No. 5, 1956 [in Russian].

3. Khristoforov B.D., and E.A. Shirokova, Parameters of shock waves in water from an explosion of a detonation cord, *PMTF*, No. 4, 95-99, 1963.

4. Korobeinikov, V.P., and B.D. Khristoforov, Underwater explosions: Summary of science and technology, *Hydromechanics*, Moscow, v. 9, 54-119, 1976 [in Russian].

5. Grib, A.A., A.G. Ryabinin, and S.A. Khristianovitch, Reflection of a plane shock wave from the free surface, *JAMM*, No. 4, 532-544, 1956 [in Russian].

6. Brehovskikh, Waves in layered media, v. 20, N0. 4, 532-544, 1968 [in Russian].
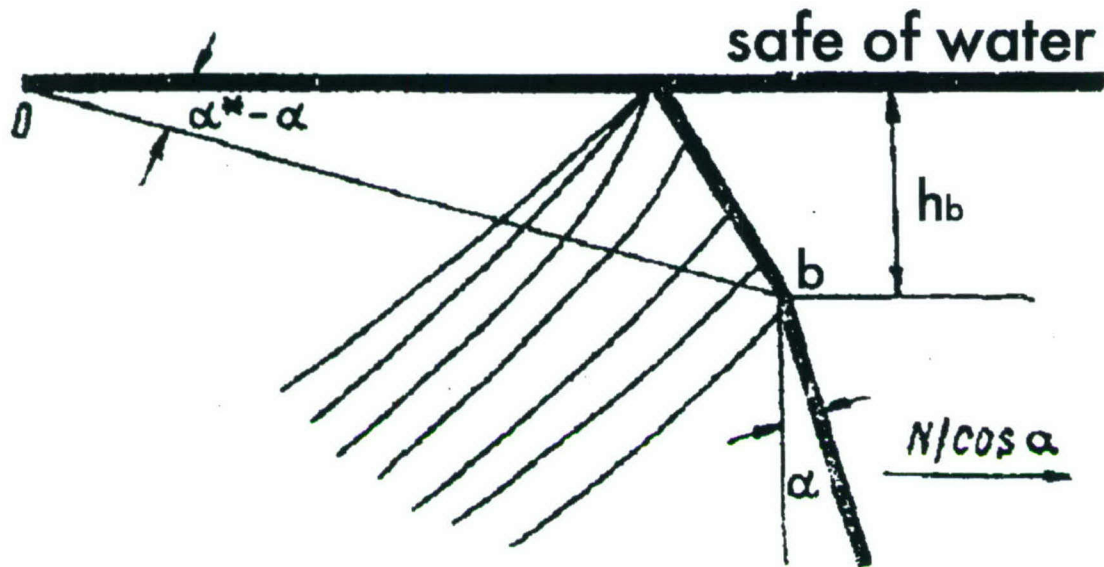
Figure 1.2.1. Reflection of a plane shock wave from the free surface.
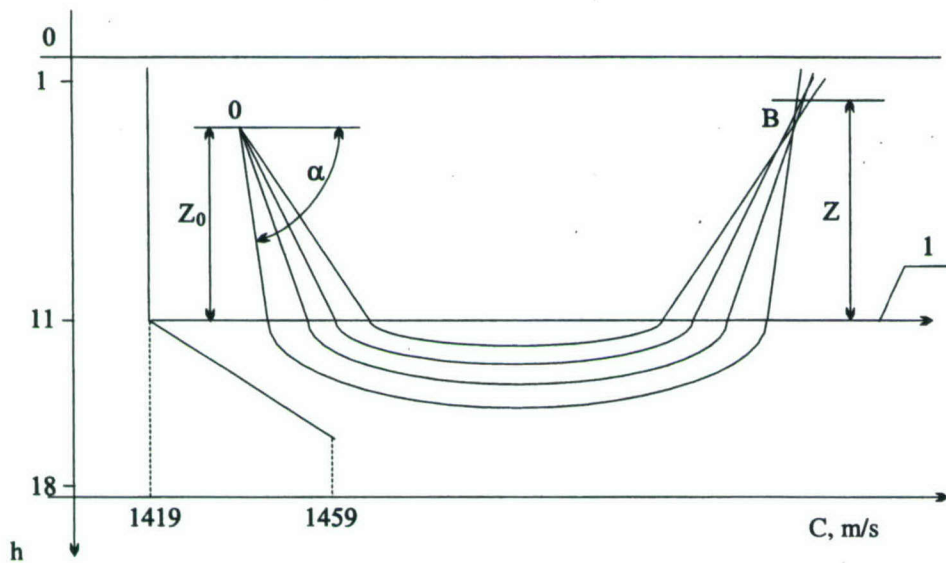
Figure 1.2.2. Sound propagation in a waveguide from an explosion at point O. Z_0 and Z are the heights from the interface to the explosion and the sensor, respectively. Interface (1) at depth $h_0 = 11$ m separates a layer with a constant sound speed from a layer with sound speed gradient. α is the emergence angle of the rays from the explosion, incidence angle upon the interface and emergence angle from the interface.

1.3. Measurements of acoustic signals from deep-water bomb blasts in the Sea of Okhotsk near the coats of Kamchatka and Sakhalin.

Hydroacoustic and seismic studies were carried out of deep-water bomb blasts of 136 kg. The experiments were aimed at seismic sounding of seismically active regions in the Sea of Okhotsk and near the Kamchatka and Sakhalin coasts. [Note by M. Eneva – maximum depth of sea bottom in this area is 2.5 km]. Signals from explosions conducted at depths from 10 to 300 m were measured on ships, submarines and seismic coastal stations at distances up to 300 km. Hydrophones of various types with pass-band filters from 1 to 1000 Hz were used. Amplitude ratio of shock wave and the following gas-bubble pulsations, their periods, noise level, and propagation characteristics at large distances were determined.

Hydrophones of three types were used for the measurements on submarines: industrial hydrophones GICh with sensitivity of 60 μV/bar and pass band up to 5 Hz; standard ship hydrophones with sensitivity from 200 to 500 μV/bar and pass band more than 1 Hz; and piezoelectric hydrophones in artificial glass cases designed at the Institute for Physics of the Earth, USSR Academy of Sciences. The latter sensors were specially designed for measuring weak deep waves of low-frequency, in the range beyond 2 to 3 Hz, comparable at large distances with sea noise, as well as for precise measurements of more intensive waves with frequencies of 10 to 300 Hz, at distances from 10 to 250 km. Sensors were placed outside on the front, middle and back of the submarines. Cables were passed through the submarine walls.

The lowest noise level was observed near the middle of the submarines, where most of the measurements were made. The noise was considerably larger than the internal sea noise at large depth (0.2 bar). To suppress the noise during storms of 5 to 6 balls, the submarines were moved to depths of at least 50 to 80 m. The optimal depth for reliable measurements at a given frequency f was determined from a well-known relationship $H = \lambda/4 = C/4f$. For $C = 1500$ m/sec and $f = 3$ and 10 Hz, the optimal depths are $H = 125$ m and 37.5 m, respectively.

On the ships (i.e., above water), the noise was investigated in the frequency bands 1.5 - 7 Hz, 2 - 12 Hz, and 4 - 12 Hz. Amplitudes and visible periods were measured. The noise level was much larger than that measured on the submarines in similar frequency band. The ship-measured noise was concentrated in the frequency band 1.5 to 17 Hz and amplitude range 0.5 to 50 bars, with noise larger than 10 bars being very rarely observed. Noise peaks were observed near 1.5 to 3 Hz and around 10 Hz. The noise level decreased as frequency increased, but was unfavourable for recording weak deep waves at large distances, even in quiet weather conditions. Thus, it was decided to record the signals primarily on submarines and deep stationary stations.
Figure 1.3.1a shows the scheme of profiles used for deep seismic sounding (DSS) in the transitional zone from the Asian continent to the Pacific Ocean.

Figure 1.3.1 and 1.3.2 show characteristic hydroacoustic records from a deep-water bomb blast at distances of 51 and 60 km as observed on a submarine located near the bottom. These signals were produced by seismic waves refracted into water. Characteristic travel times of these signals are of 10.4 and 14.5 s, with apparent velocities of ~ 4 to 5 km/s, corresponding to longitudinal (P-) wave velocity in hard rocks. [Note by M. Eneva (personal communication with B.D. Khristoforov) - The different traces in Figure 1.3.1 and 1.3.2 were recorded with different types

A-16

of hydrophones using simultaneous registration on several channels. The characteristics of the hydrophones used are described in IDG archive materials, but are not currently available to us. Several of these records are being digitized at IDG. However, in general, only the characteristic pressures, averaged from many explosions, are known at different distances. The IDG team continues to analyze archive materials and expects to uncover more precise descriptions of some of the records].

Low-frequency components of the signals from explosions and gas-bubble pulsations were recorded at depths 1200 to 2500 m from a moving ship in the sea [Not by M. Eneva – bottom depth was 1.2 to 2.5 km]. The first pulsation period T_1 and the ratio of shock wave and the first pulsation amplitudes $K_1 = a_0/a_1$ were determined. Figure 1.3.3 displays recordings from explosions at depths 70 to 180 m, while Figure 1.3.4 shows some of the estimates for K and T_1 from Figure 1.3.3, as well as additional ones. [Note by M. Eneva (personal communication with B.D. Khristoforov) - the distances to the ship and the amplitude units in Figure 1.3.3. were not found in the IDG archived reports].

For a 100-m deep explosion, the sound wave intensity at a range of 500 m and frequency 10 Hz is 50 kbar (0.05 atm), i.e. about 2 orders of magnitude lower than a shock wave amplitude calculated for TNT in homogeneous liquid. [Note by M. Eneva – it is not quite clear if this text describes Figure 1.3.4a directly or is based on calculations only. The observed ratio K in Figure 1.3.4.a is indeed ~2 at distances ~500 m].

As the explosion depth increases from 60 to 120 m, the period of the first gas-bubble pulsation T_1 decreases from 0.34 to 0.19 s. This is consistent with the predicted values. [Note by M. Eneva – the relationship that might have been used in this case, as taken from a 1996 IDG Report on Project SPC-95-4049, is $T_1 = 2.11M^{1/3}/(H+10.3)^{5/6}$, where M is the bomb mass of in kg, H is the explosion depth in m, and T_1 is in s].

Figure 1.3.5 shows records from explosions with a typical charge depth of 90 m, as recorded at coastal seismic stations at distances 60 to 220 km. [Note by M. Eneva - The characteristic period of the signal is consistent with the one calculated from the relationship for T_1, that is 0.237 s for explosion depth of 90 m for a 136-kg bomb. The times of first arrivals of are known for some of these records (personal communication with B.D. Khristoforov), such as 13.3 s at a distance of 62.3 km and 22.5 s at a distance of 124 km (Figure 1.3.5a). However, the amplitude units are unknown at present, although the IDG team hopes to identify them during the continuing archive search].

This study showed that the largest portion of the energy from deep underwater explosions is emitted into the shock wave, the first and the second bubble pulsations. Non-linear absorption effects in the shock wave from 136-kg explosions are observed at distances up to 10 km. The ratio of the peak overpressure in the shock wave to that in the first pulsation decreases with distance and reaches 1.7 to 2 beyond the non-linear zone. [Note by M. Eneva – the text of the latest version of Chapter 1.3 ends here].

[Note by M. Eneva – the following text is modified from an earlier version of this chapter and based on personal communication with B.D. Khristoforov. Figure 1.3.6 shows pressure

measurements versus distance from 136-kg explosions. Hydroacoustic measurements were made of the maximum amplitudes of the group of first arrivals from numerous explosions. Each explosion was typically initiated from a moving ship and was recorded on several hydrophones at various distances. The two following figures, Figure 1.3.7 and 1.3.8, show measurements from 90-kg bombs detonated at a depth of 100 m. The average sensor depth was 2000 m, in the SOFAR channel. The vertical axes in Figure 1.3.7 show in a logarithmic scale the square of the sound pressure. The units are in dB, but the maximum and minimum values along the vertical axes are not known at present. Each oscillogram in this figure has its own start time of digitization and its own time scale, which makes it difficult to evaluate how the signal changes with distance. The maximum pressure in Figure 1.3.8 was measured as the arithmetic average from two adjacent local maxima (one of which was the largest) and two minima around these maxima. The pressure decay with distance is compared with curves calculated for sound in homogeneous liquid, using cylindrical and spherical symmetry. Text explaining the remaining figures in this chapter, Figure 1.3.9 to 1.3.16 and 1.3.19, has not been supplied at present].
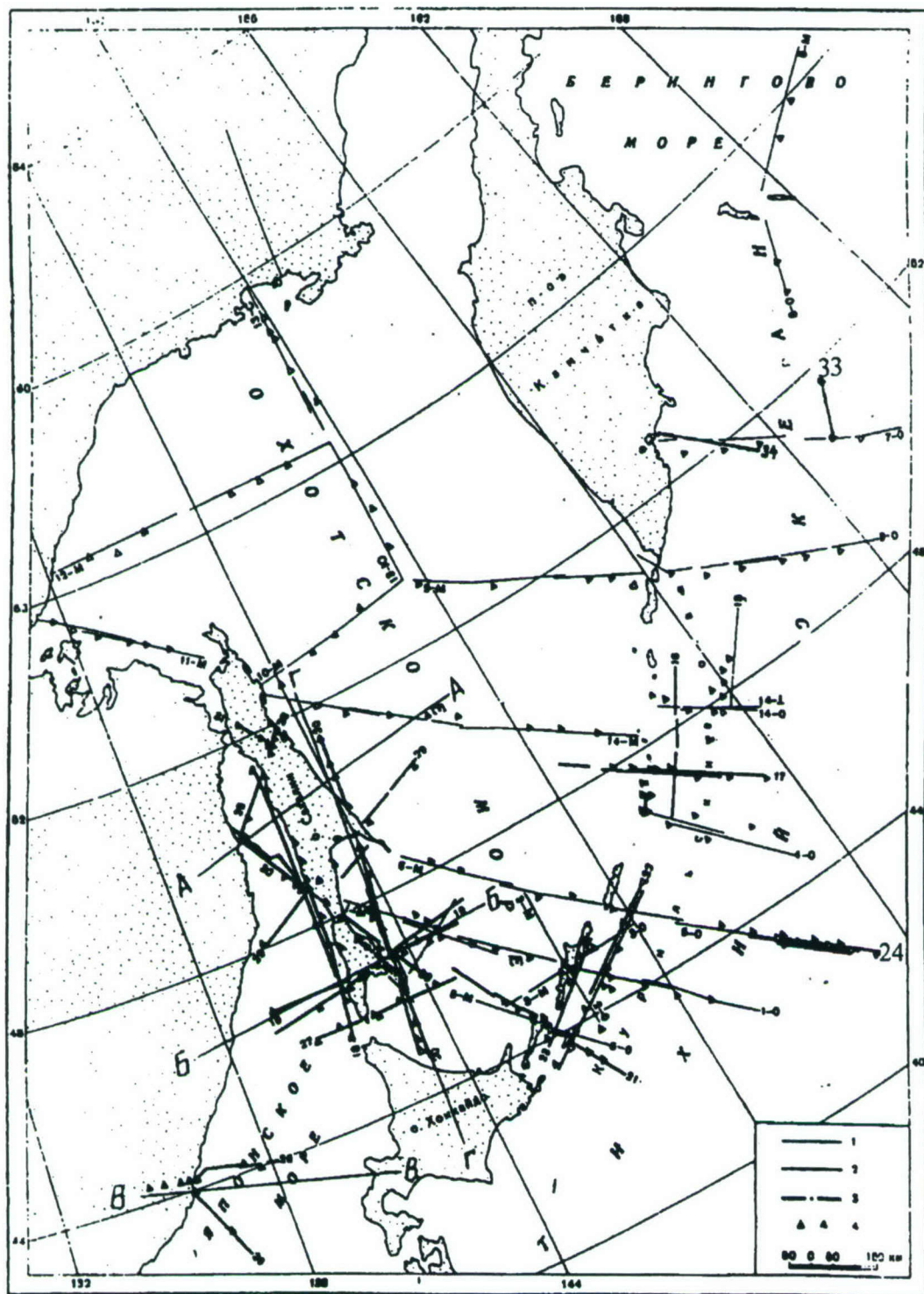
Figure 1.3.1a. Profiles of the deep seismic sounding (DSS) in the transitional zone between Asia and the Pacific Ocean (Sea of Okhotsk, Sea of Japan, Sakhalin, Kamchatka). 1 – profiles from the period 1956-1958; 2 – profiles from 1963 and 1964; 3 – ground (?) profiles on Sakhalin; and 4 – marine and ground recording stations.
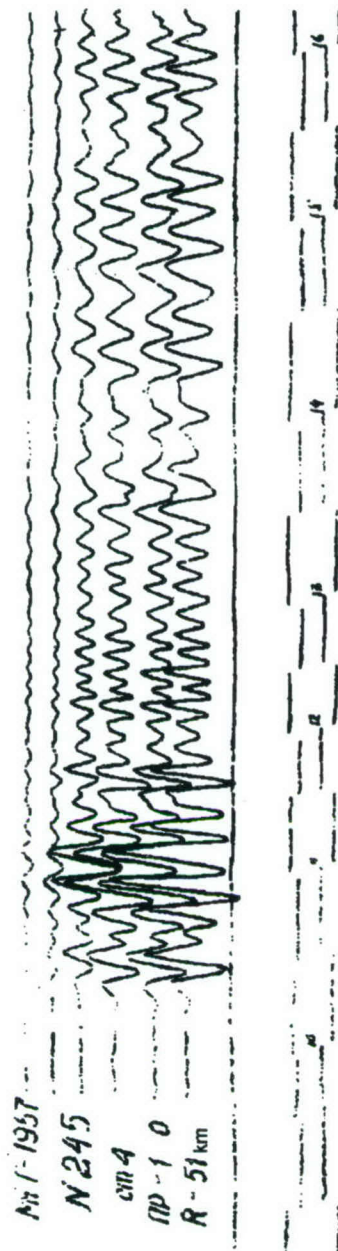
Figure 1.3.1

Figure 1.3.2

Figure 1.3.1.   Typical hydroacoustic signals from deep-water bomb blasts of weight 130 kg [Note by M. Eneva – this may be 136 kg]. Measurements were made from a submarine at a distance of 51 km.

Figure 1.3.2. Same as Figure 1.3.1 but measured at a distance of 60 km.
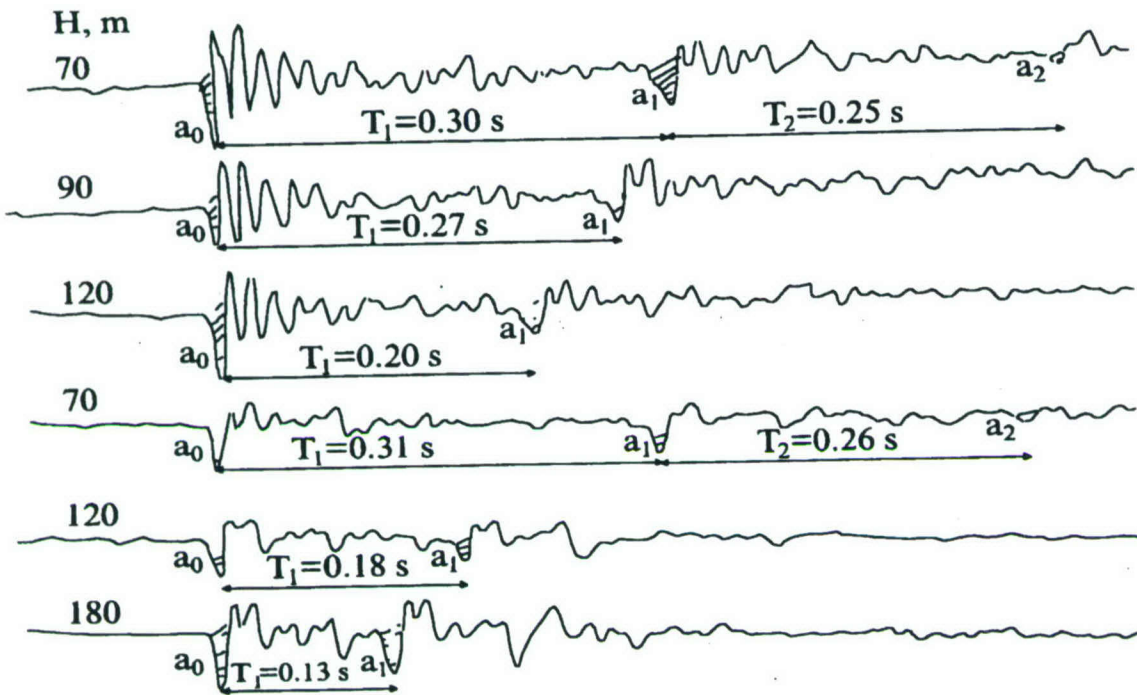
Figure 1.3.3. Hydroacoustic signals recorded on a ship from 136-kg bomb explosions conducted at various depths. T_1 and T_2 denote periods of first and second pulsations, respectively. The amplitudes of the shock wave and the first gas bubble pulsation are marked with a_0 and a_1, respectively.
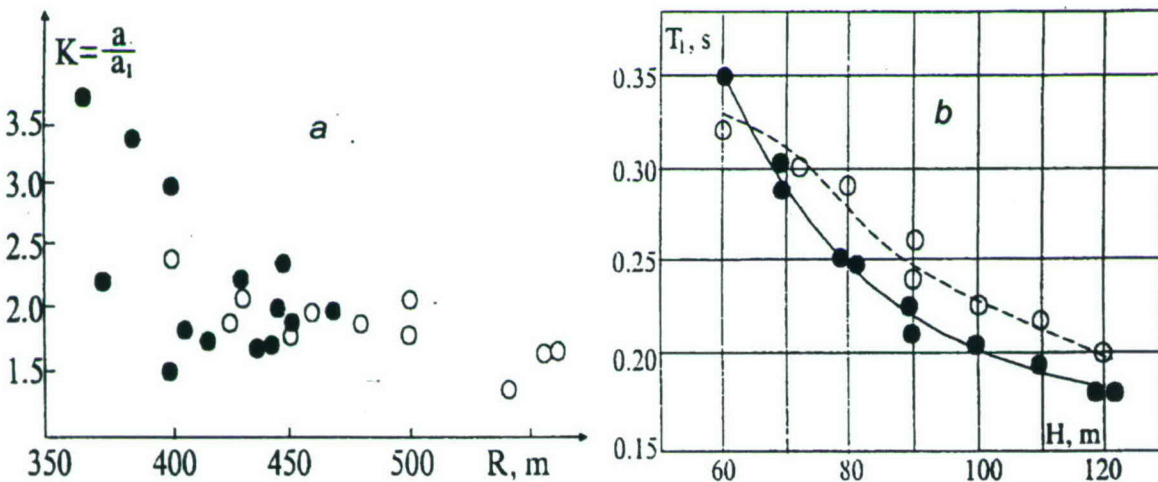
Figure 1.3.4. (a) Ratio of amplitude of shock wave to amplitude of first gas bubble pulsation versus distance. (b) Period of first gas bubble pulsation versus depth of explosion. [Note by M. Eneva - open and filled circles denote measurements from different series of experiments].
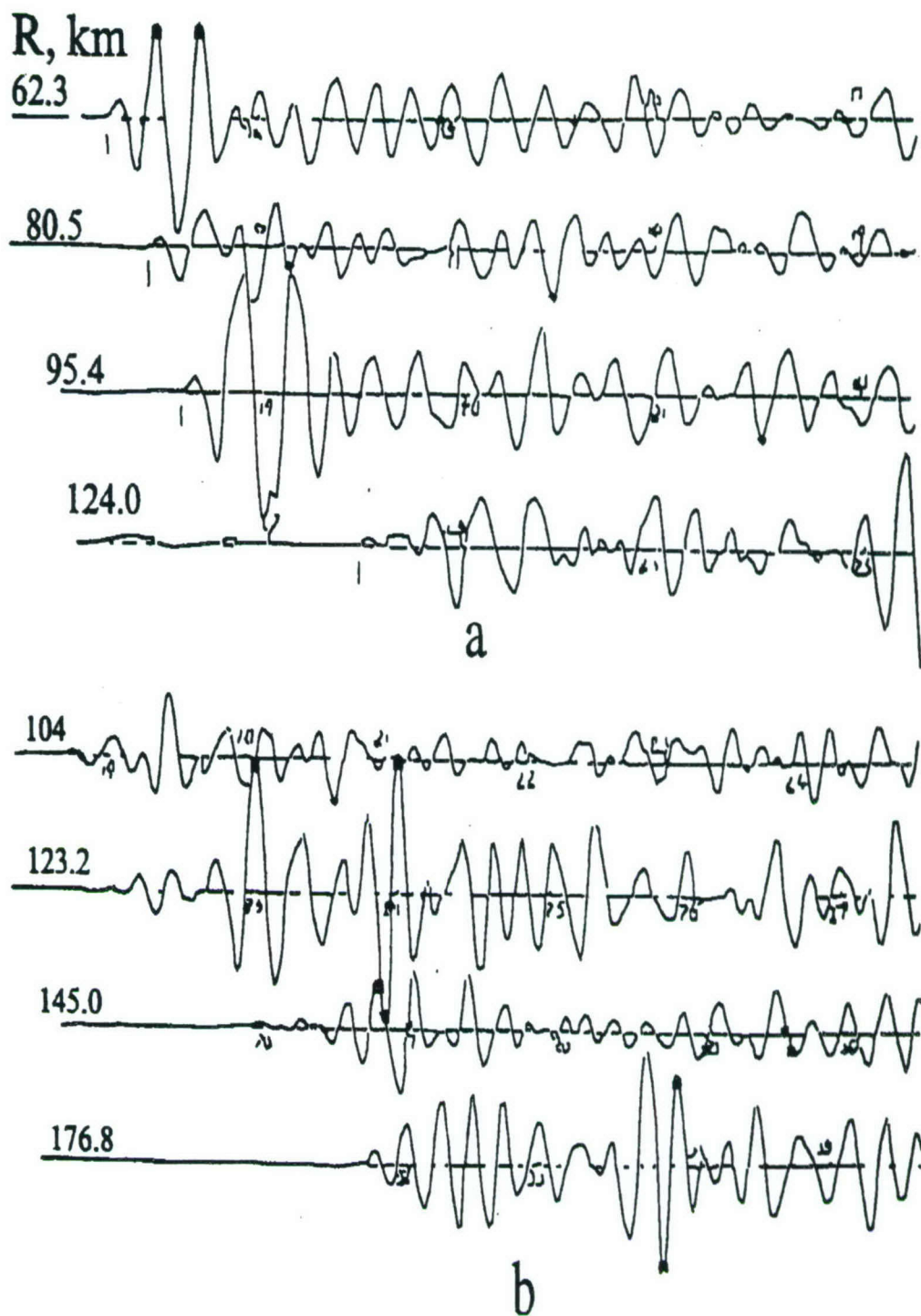
Figure 1.3.5.   (a) Typical seismograms recorded at a station located on a cape in open ocean, at various distances R from the deep-water bomb blasts. (b) Same for a station on the coast of a bay.
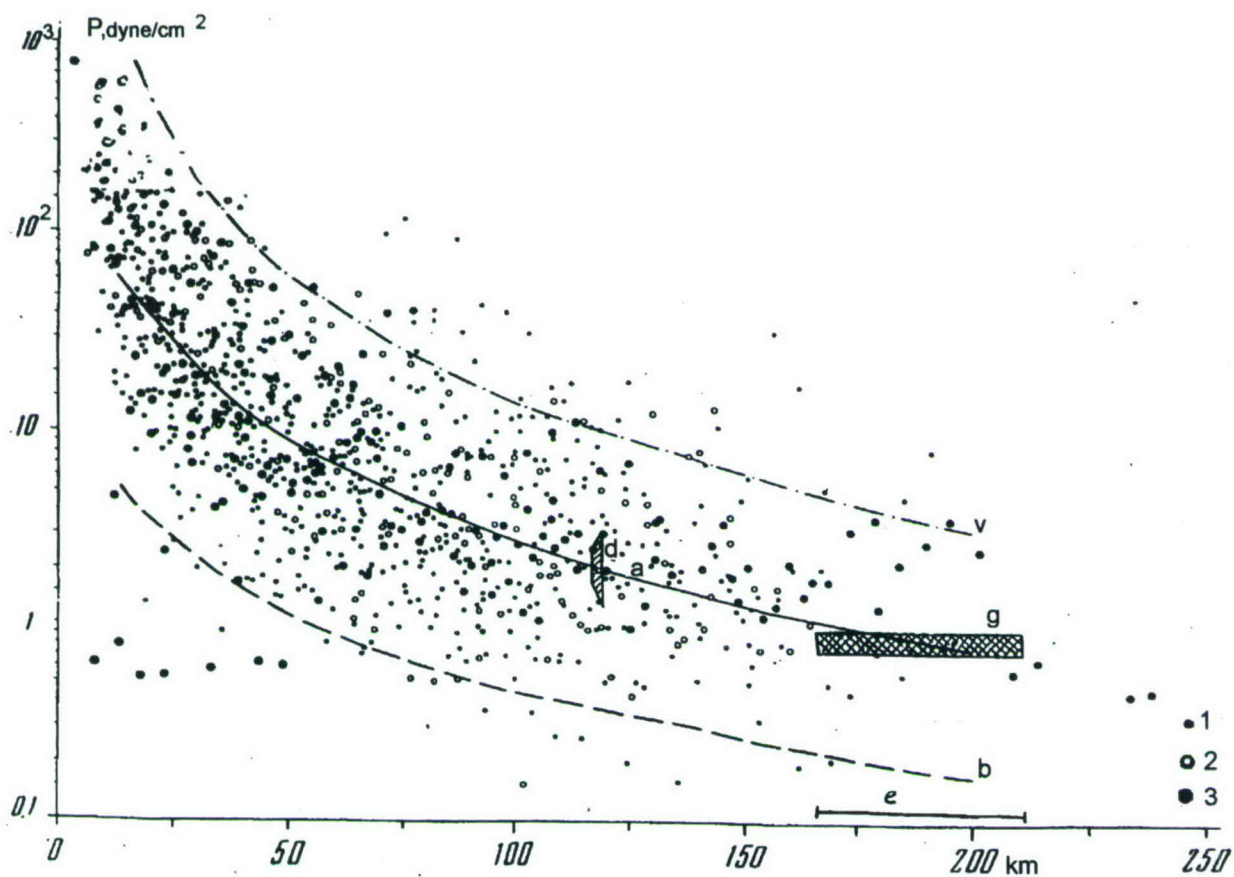
Figure 1.3.6.   Measurements of 1500 peak overpressure values from the first wave arrivals for a transition zone between the Asian continent and the Pacific Ocean. Explosion charge 136 kg, frequency band of registration 2-12 Hz. 1, 2, and 3 denote different frequency bands in the interval 2-12 Hz. [Note by M. Eneva - (a) average calibration curve; (b) and (v) minimum and maximum envelopes covering 90% of the data; (g) average microseism level; (d) error in magnitude measurements; and (e) average upper bound of distance of registration].

a

b
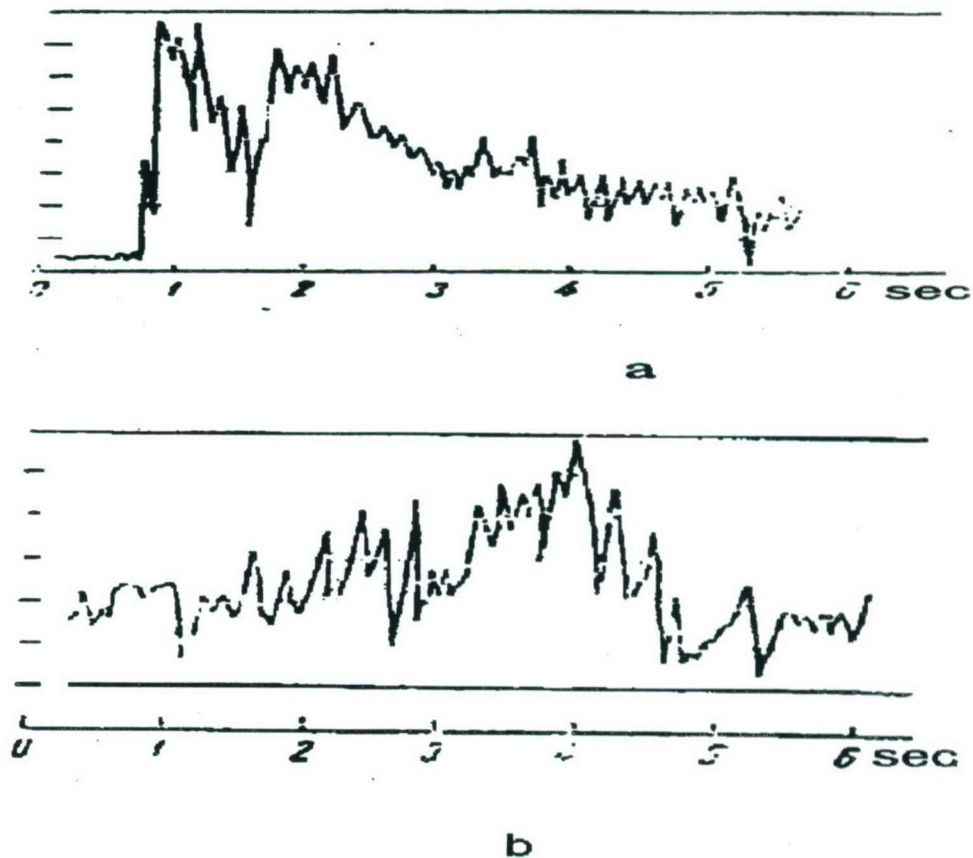
Figure 1.3.7. Hydrophone records in the underwater sound channel (2000 m depth) from a 90-kg bomb at a distance of: (a) 19 km and (b) 560 km. Explosion depth was 100 m. Tick marks on vertical scale denote increments of 5dB each. [Note by M. Eneva – differences from original IDG text are due to clarification based on communication with B.D. Khristoforov].
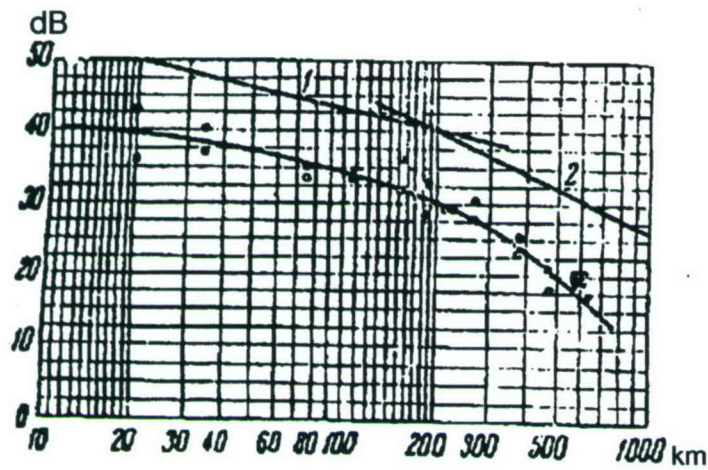
Figure 1.3.8. Peak sound pressure in the underwater sound channel (2000 m) versus distance from 90-kg explosions at depth 100 m. 1, 2 - cylindrical and spherical laws of sound-level decay with distance. [Note by M. Eneva – differences from original IDG text are due to clarification based on communication with B.D. Khristoforov].
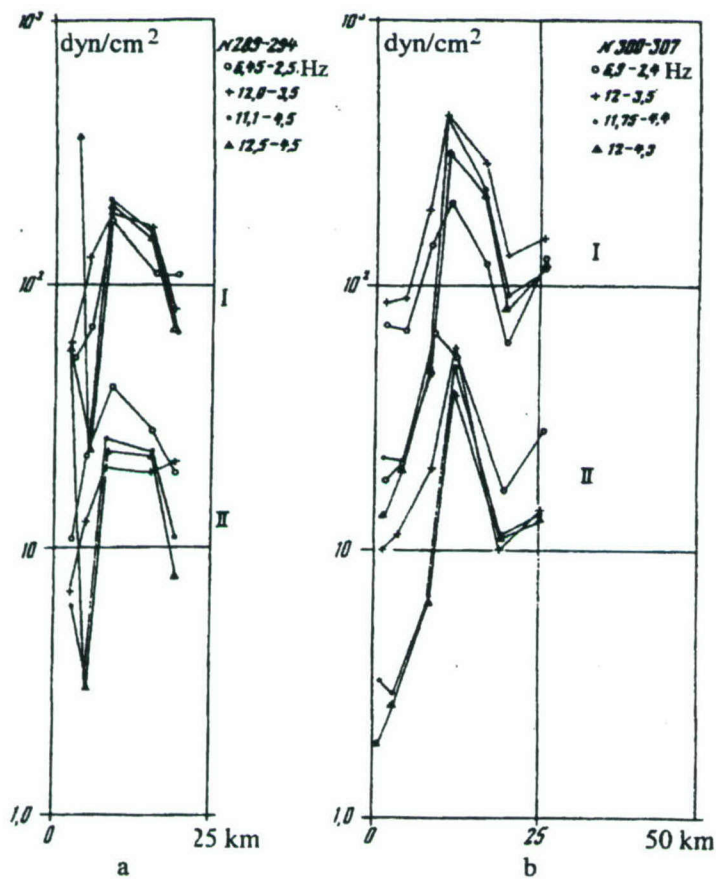
Figure 1.3.9. I – peak-pressure curves, II – pressure spectral density calculated from I in various frequency bands, as marked in legend. Profile 24, waves P^k.
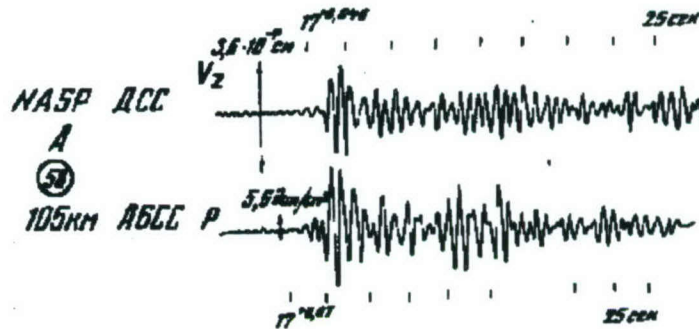
Figure 1.3.10.   Signals recorded by a vertical seismogrpah and a hydrophone at the bottom (400-m depth). Region: Iceland-Foroes [?] transition zone. Data from IFZ (Institute of Physics of the Earth), 1972.
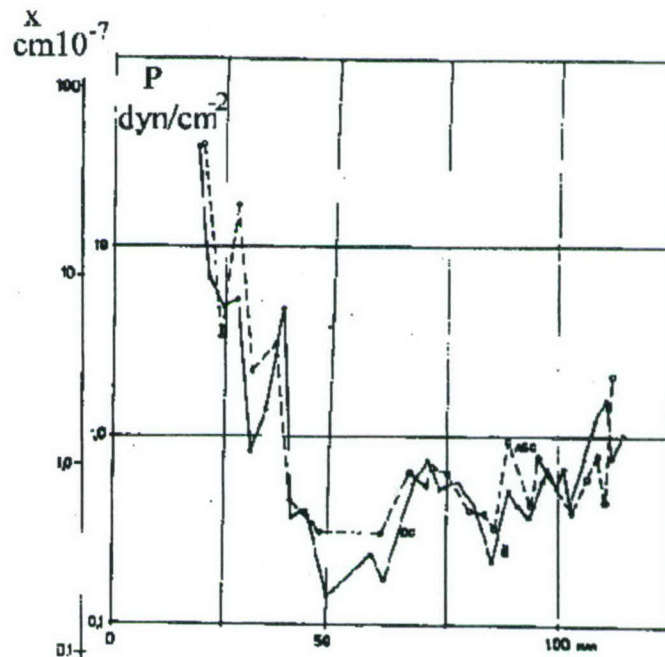
Figure 1.3.11.   Peak-pressure curves based on signals recorded with a vertical seismograph ADSS and hydropophon ABSS. Region: Iceland-Foroes [?] transition zone. Data from IFZ (Institute of Physics of the Earth), 1972. Displacement and pressure scales are calibrated [?] using the formula $P = 10^6 f x$, where the pressure P is in dyn/cm^2 and the displacement $x = 10^{-6} P/f$ is in centimeters.
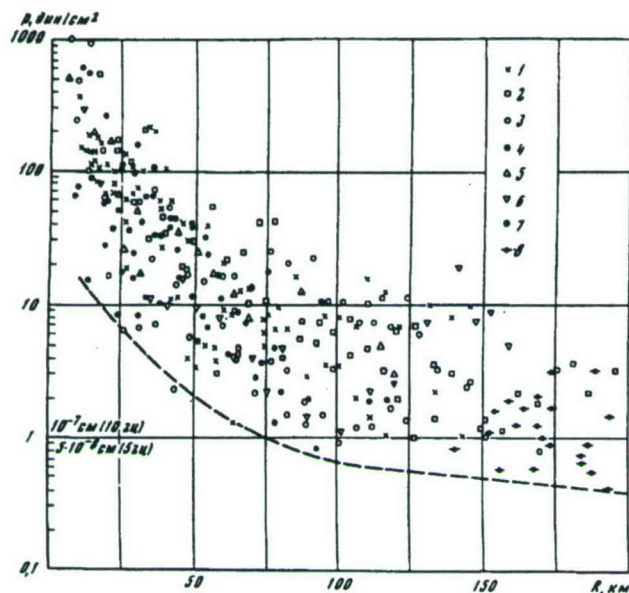
Figure 1.3.12.   Peak-pressure measurements of deep seismic waves in the Far East transitional zone. 1 - Pacific Ocean; 2 - Kuriles Islands; 3 – Laperus strait; 4 – Sea of Okhotsk east from Sakhalin; 5 and 6 – Sea of Japan, profiles 25 (5) and 26 (6); 7 - Tatar strait, 8 – Sea of Japan west of Sakhalin.
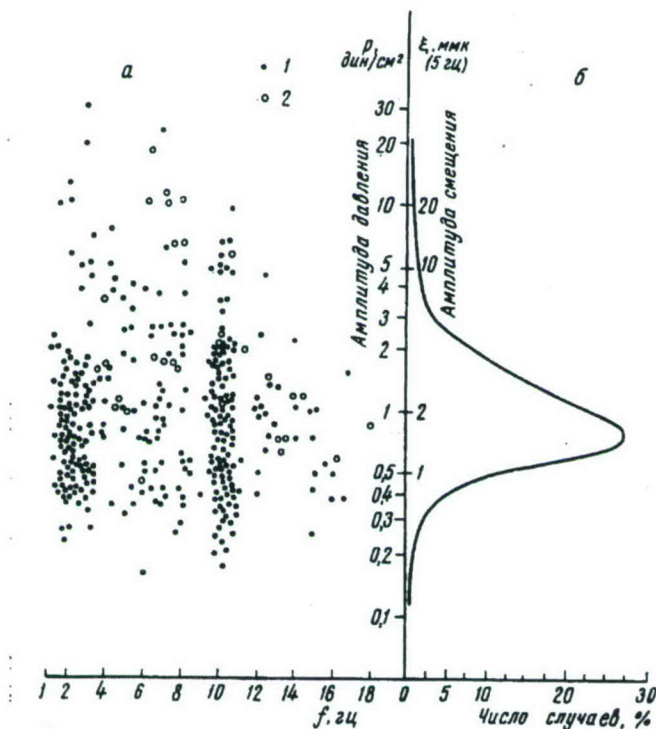
Figure 1.3.13.   Microseism (noise) frequency distribution; data from Pacific Expedition GSZ. (a) Experimental data: 1 – hydrophone on the bottom near the coast; 2 – hydrophone in water far from the coast. (b) Distribution of number of cases versus amplitude. [Note by M. Eneva. Translation of axis titles from Russian: vertical left – pressure amplitudes in dyn/cm^2; vertical right - displacement amplitude at 5 Hz in microns (?); horizontal left – frequency in Hz; and horizontal right – number of cases in %.

Prof. *24*

CT. *2*   *21.7.64 г.*

N EXP R, km   *2 – 5* Hz
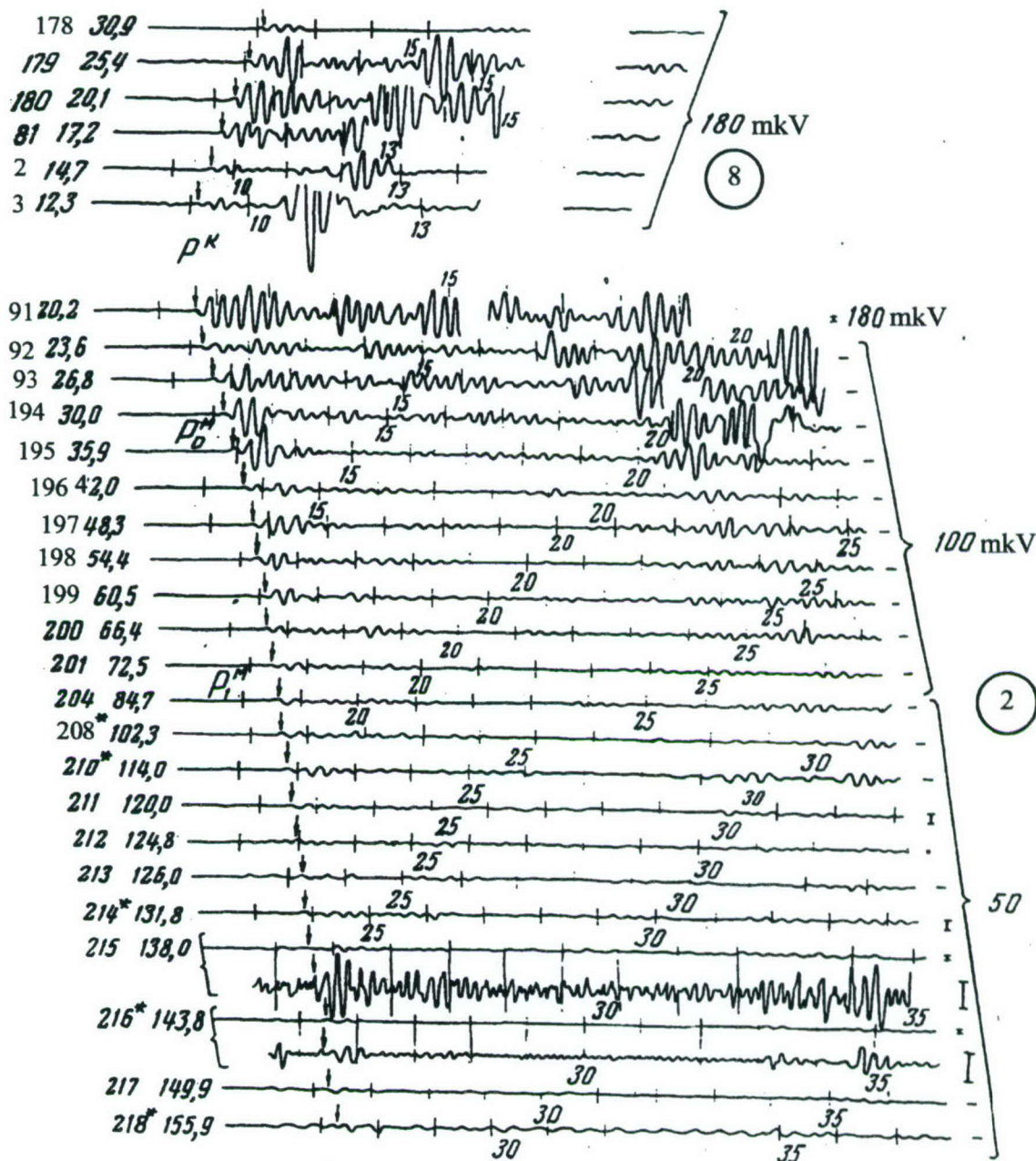
Figure 1.3.14.   Seismograms at distances R from explosions as marked. Profile 24. Travel-time curves [?] 2
and 8.
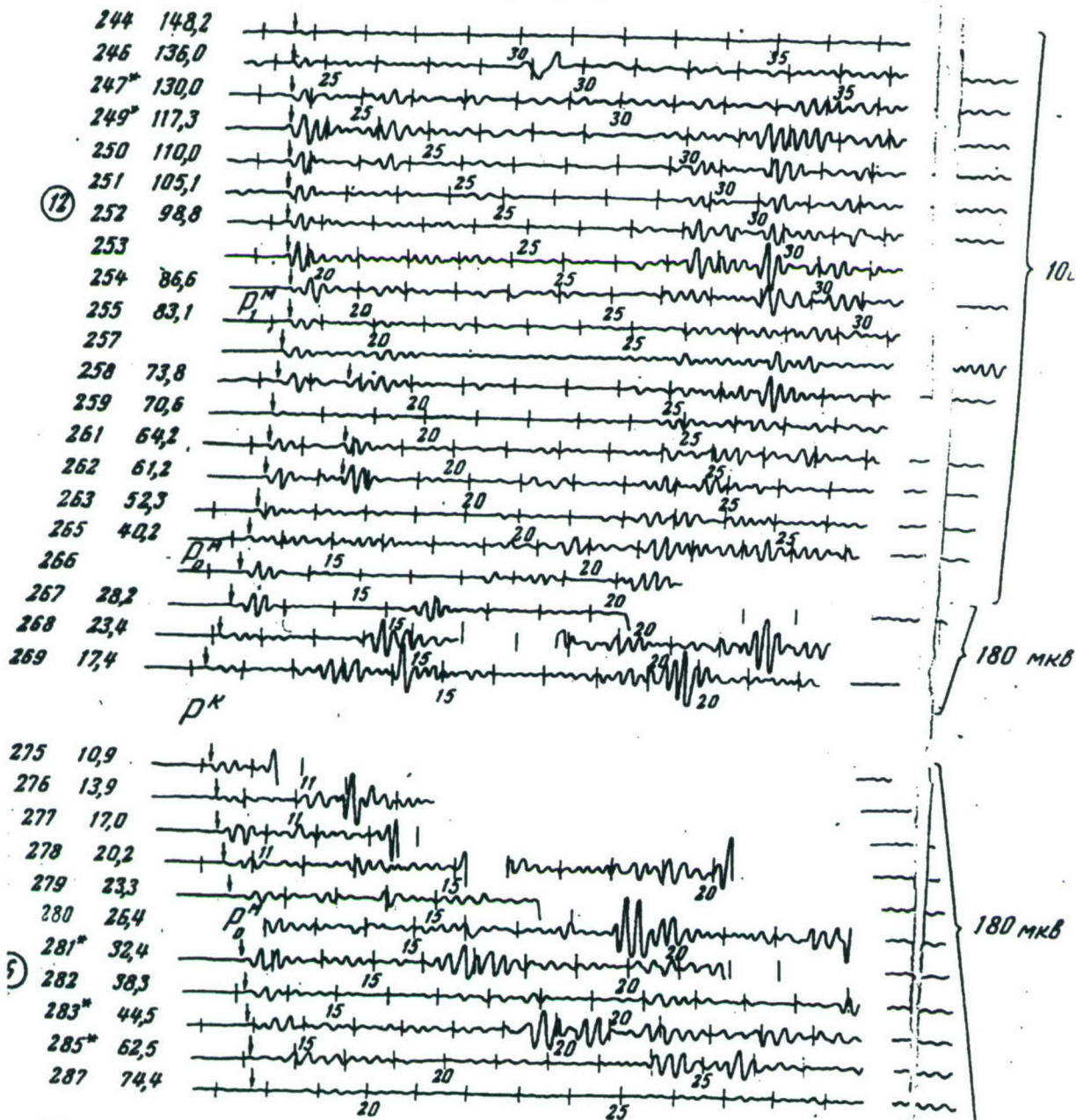
Figure 1.3.15. Seismograms at distances R from explosions as marked. Profile 24. Travel-time curves [?] 6 and 12.

Prof.24   CT. 1 22.7.64

2-6 Hz

N EXP R. km
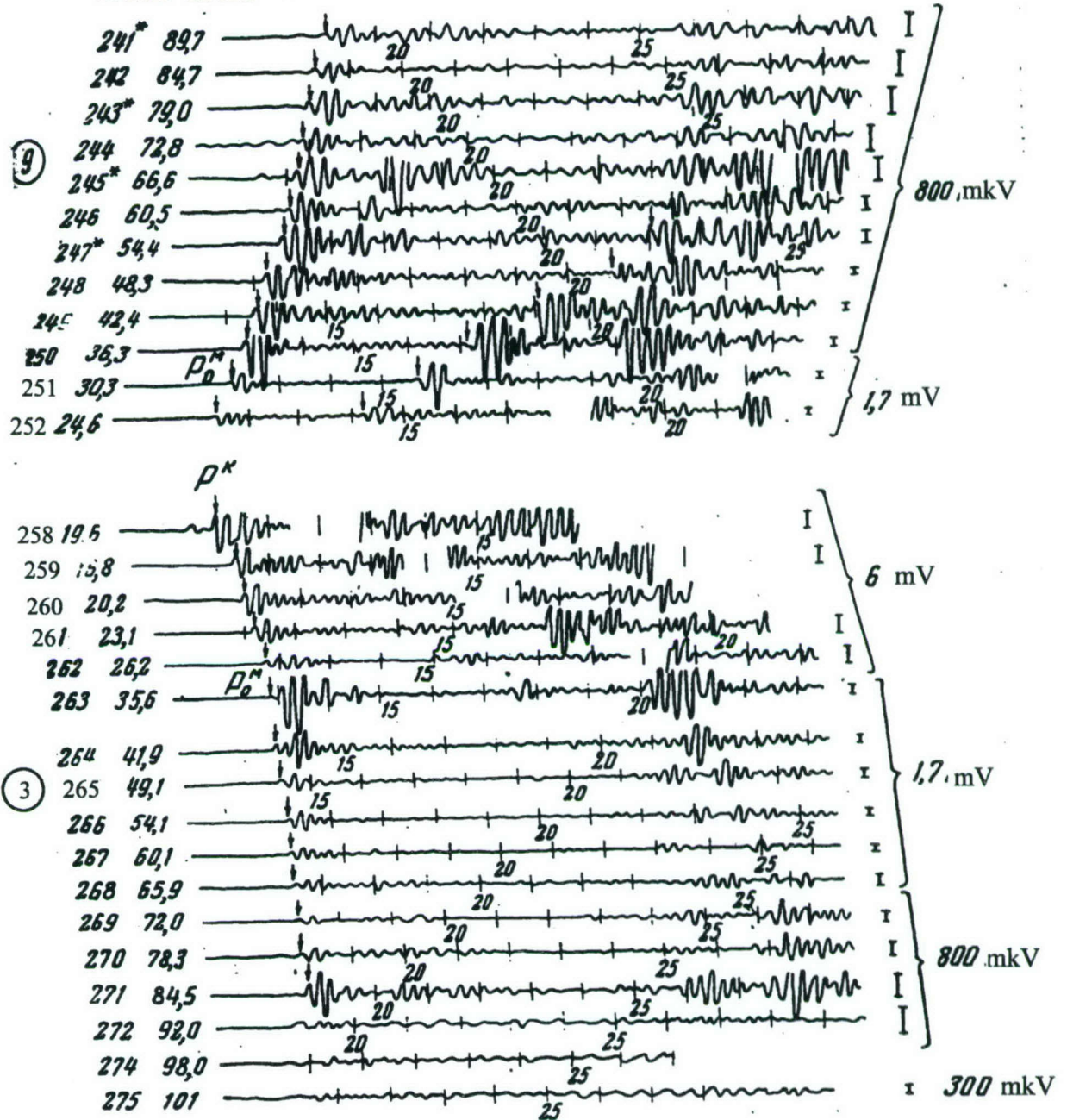
Figure 1.3.16. Seismograms at distances R from explosions as marked. Profile 24. Travel-time curves [?] 3 and 9.

пр 33
4-АБСС · 28.10.67г
4 - 8 гц
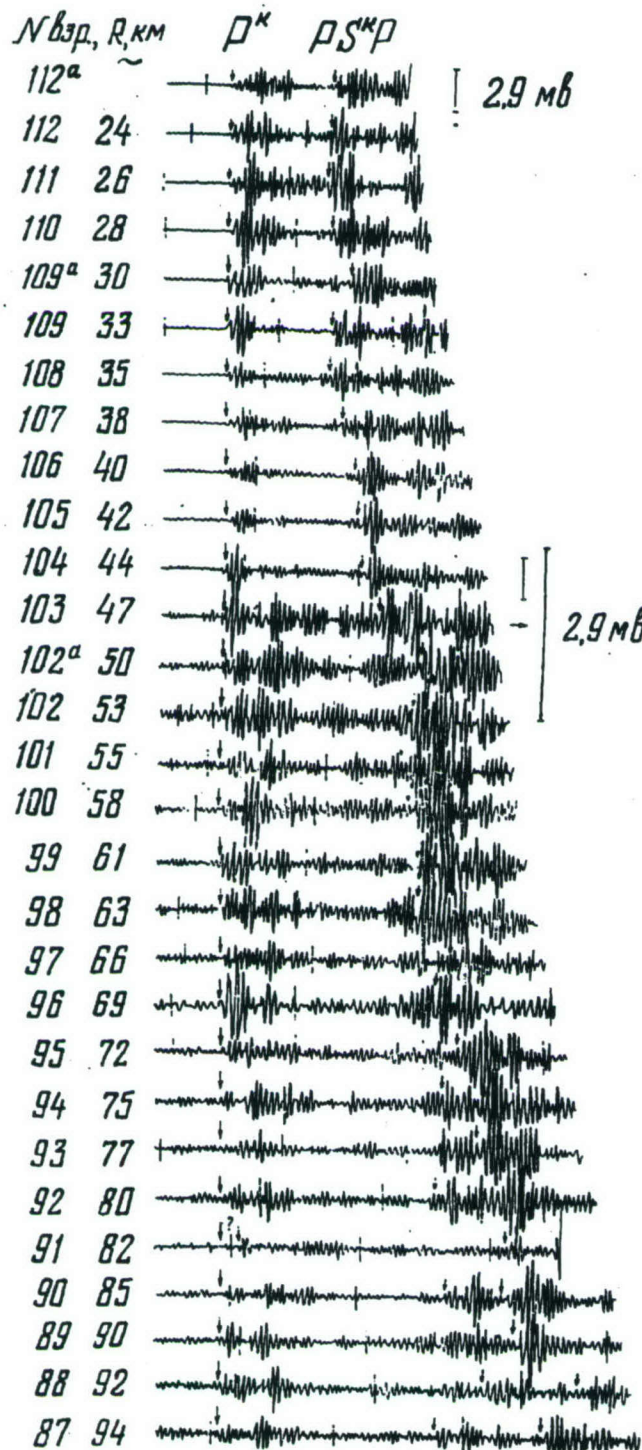
Figure 1.3.19. Seismograms at distances R from explosions as marked. Profile 33. Station ABSS.

1.4. Measurements in water from underwater explosions of cast spherical charges of 100 kg TNT in shallow reservoirs.

These experiments were carried out in an artificial reservoir of length 87 m, width 25 m [Note by M. Eneva: this is the bottom width; the width on the top was 55 m, not mentioned here], and depth $H_b = 3$ m. The bottom was covered with a layer of air-saturated sand. $R_0 \approx 0.25$ m was the radius of the charge. The level of water was varied from 0.25 m to 3 m (i.e., $H_b/R_0 = 1, 2, 4, 12$). Density, sound speed and volumetric concentration of air in the ground were 1.95 g/cm^3, $C_0 = 270$ m/s, and ~ 0.001, respectively. The measurements were made with piezoelectric gauges. 29 explosions of cast spherical charges of weight 100 kg TNT were carried out. Shock waves were measured at relative ranges $R/R_0 = 30, 60, 90, 120$ and 180 from the explosions, at various depths h. The explosion depths H, were also varied.

Table 1.4.1 shows the configurations of the 29 100-kg TNT underwater blasts.
For comparison, Table 1.4.2 shows estimates in boundless water from R. H. Cole [1], at the same distances as in the 100-kg TNT experiments. These estimates are for peak overpressure ΔP_m, kg/cm^2, specific impulse I, kg-s/m^2, and flow of energy E_f, kg-m/m^2, at time 6.6θ [Note by M. Eneva – θ is time constant, that is the time over which the pulse in boundless water can be described with exponential decay], $E_{Cole} = E_f 4\pi R^2$ and E_{Cole} / E_0. The calculations are for explosion of 100-kg spherical charge TNT with density 1.52 g/cm^3. The following formulas were used:

$$\Delta P_m = 533(M^{1/3}/R)^{1.13}$$
$$I = 588M^{1/3}(M^{1/3}/R)^{0.89} \quad\quad (1)$$
$$E_f = 8300 \ M^{1/3} \ (M^{1/3}/R)^{2.05} \ ,$$

were M is the HE mass in kg, R is the distance from the blast in m, and $E_0 = 418$ MJ $= 418 \ 10^5$ kg-m is the energy of a 100-kg TNT explosion.

Tables 1.4.2a-h show the parameters of shock waves in water from the archival materials. These were measured with devices PID-9. R and h are distance from explosion and gauge depth, respectively. ΔP_m, τ, and I are peak overpressure, pulse duration, and specific impulse of the positive phase of the shock wave.

The results from the digitization of oscillograms from the tests are given in about 270 MS-Excel files. (The notations in the filenames are as in the following examples: Ch14_153_4_3_3 - chapter 1.4, test 15, device 3, basin depth 4R_0, charge depth 3R_0, gauge depth 3R_0; Ch14_204_120_4_2 - chapter 1.4, test 20, device 4, distance 120R_0, charge depth 4R_0, gauge depth 2R_0).

Table 1.4.3 shows observed parameters of shock waves from the digitized oscillograms for all 29. E_+ denotes the specific energy of the positive phase of the shock wave, E_{+mid}, kgm/m^2 is the averaged specific energy from the values measured at different depths, at a given distance R:

$$E_{1mid}, \ kg\text{-}m = 2\pi R H_b \ E_{+mid}$$

E_{mid}, kg-m = 6.28R$\int_0^b E_+$ dh , where it is assumed that E_+ (h=0) = 0 and E_+ (h=H$_b$) = E_+ (h=h$_m$), where h$_m$ is the maximum gauge depth in the experiments. Also, E_{1mid} /E$_0$ % is calculated.

Table 1.4.4 shows shock-wave energy from tests 1-3, 14, and 15, at depth H = 0.75 m, with water level in the reservoir H_b = 1 m.

Tables 1.4.5 and 1.4.6 show shock-wave energy from tests 4-8, 12, 13, and 16-17, with H_b = 1 m, and explosion depths H = 0.5 and 0.25 m.

Tables 1.4.7 to 1.4.13 show various energy estimates (E_{+mid}, E_f, kg-m/m^2, E_{1mid} and E_{mid}, kg-m, and E_{mid} /E_0 %) for tests 18-29, H_b = 3 m, explosion depths H = 0, 0.25, 0.5, 1.0, 1.5, 2, 2.75 m. Figure 1.4.1 shows photographs of the piezoelectric gauges used and some records.

Figure 1.4.2a shows shock-wave peak overpressure P_m, duration τ, and specific impulse I, as functions of gauge depth h for various distance R, explosion depths H and water level H_b = 4R_0. Figure 1.4.2b shows peak overpressure as a function of range for explosions in the middle of the reservoir, when water levels are H_b = 2R_0, 4R_0, and 12R_0. In the same figure a similar relationship is shown for a nuclear explosion of 1-kt TNT in the center of a reservoir 20-m deep (i.e., 10-m explosion depth).

Figure 1.4.3 shows shock-wave records made by devices PID-9 from an explosion in a full reservoir, i.e., with water level 12R_0.

Figure 1.4.4 shows the specific shock-wave energy E_{+mid}, kg-m/m^2 (squares) averaged over depth, as a function of distance R, from blasts at depth 0.75 m in basin of depth H_b = 1 m. The energy density flux (E_f) is also shown for comparison. It is calculated using Cole's formula for a 100- kg TNT explosion in boundless water (triangles). It is observed that E_{+mid} << E_f . As distance R increases from 7.5 up to 44.5 m, $E_{+ mid}$ / E_f decreases from 0.04 to 0.00024.

Figure 1.4.5 compares the dependence on distance R of the ratios shock-wave energy to explosion energy in boundless liquid and in a reservoir with water level H_b = 1 m, explosion depth H = 0.75 m. In the range of distances 7.5 to 45 m , the ratio E_{Cole} / E_0 in boundless water decreases from 24.3 up to 22.3 %, while the ratio E_{mid}/E_0 for the explosions in shallow reservoirs decreases from 0.062 to 0.00004 %. That is, practically all the energy of such explosions is transferred to the air and the ground.

Figure 1.4.6 shows the averaged specific shock-wave energy $E_{+ mid}$ as a function of distance R, for blasts at depths 0.25, 0.5, and 0.75 m in a basin with water level H_b = 1 m. Variations in explosion depth practically do not affect the shock-wave energy in water.

Figure 1.4.7 presents the averaged specific shock-wave energy, $E_{+ mid}$, as a function of distance R, for explosion depths H = 0, 0.25, 0.5, 1, 1.5, 2, and 2.75 m, in a basin with water level H_b = 3 m. In this case, variations in the depth of explosion do affect the shock- wave energy in water. $E_{+ mid}$ reaches a maximum value for explosions in the middle of the reservoir, i.e. H = 1.5 m. The energy is minimum for half-immersed explosions, H = 0. The energy from explosions at depths H = 0.25 m and 2.75 m is practically the same.

Figure 1.4.8 compares the dependence on distance R of the ratio E_{Cole} / E_0 in boundless water and E_{mid}/E_0 from explosions in a reservoir with water level H_b = 3 m, with charge depths H = 0, 0.25,

0.5, 1, 1.5, 2, and 2.75 m. In the distance range 7.5 to 30 m, the ratio E_{Cole} / E_0 in boundless water decreases from 24.3 to 22.3 % (that is, it is almost a constant), while for the explosions, E_{mid}/E_0 decreases very quickly from 2.24 to 0.128 % when H = 1.5m; from 0.96 to 0.025% when H = 0.25 m, and from 0.5 to 0.045% at H = 2.75 m. For any given distance R, E_{mid}/E_0 has a maximum when the explosion depth is H = 1 or 1.5 m. Practically, all the energy of explosions in shallow basins is transferred to the air and the ground.

When the water level in the reservoir was $12R_0$, both regular and nonregular reflections from the free surface and the bottom were observed, depending on the relative positions of the charges and the sensors. For water level $4R_0$ and lower, only nonregular reflection was observed from both surfaces in the studied distance range. In such conditions shock wave parameters reach maxima in the reservoir center, independently of explosion depth, since rarefaction waves are reflected from the free surface and the bottom.

At large distances from the explosions, a critical regime is established, due to multiple reflections. In such a regime, overpressure depends only little on the charge and gauge positions and is determined by effects due to the reservoir surfaces. Asymptotic values are $P_m \sim A(H_b/R)^2$, $t \sim 1/R$. Similar relationships have been obtained theoretically for spherical and cylindrical explosions at the rigid bottom of a shallow reservoir [2]. Since the air-saturated bottom in the cases studied here has an effect similar to the free surface, an explosion in the middle of the reservoir is equivalent to a half-yield explosion at the rigid bottom of a reservoir with a half water level. The hydroacoustic wave energy decreases with decreasing water levels, due to a sharp increase of the energy radiated into the air and the ground.

References

1. Cole R., *Underwater explosions*, Princeton, New Jersey, 1948.

2. Korobeinikov V.P. and B.D. Khristoforov, Underwater explosions: Summary of science and technology, *Hydromechanics*, Moscow, v. 9, 54-119, 1976 [in Russian].

Table 1.4.1. Configurations of underwater explosions of cast spherical charges of 100-kg TNT in shallow basins with sandy bottom.

Test No.	Water Level, m	Charge Depth, m	Test No.	Water Level, m	Charge Depth, m	Test No.	Water Level, m	Charge Depth, m
1	1.0	0.75	11	0.25	0.0	21	3.0	1.50
2	1.0	0.75	12	1.0	0.50	22	3.0	2.75
3	1.0	0.75	13	1.0	0.50	23	3.0	0.0
4	1.0	0.50	14	1.0	0.75	24	3.0	2.0
5	1.0	0.50	15	1.0	0.75	25	3.0	0.25
6	1.0	0.50	16	1.0	0.25	26	3.0	0.50
7	0.95	0.25	17	1.0	0.25	27	3.0	1.0
8	0.95	0.25	18	3.0	0.25	28	3.0	1.50
9	0.50	0.25	19	3.0	0.50	29	3.0	2.75
11	0.25	0.0	20	3.0	1.0		.	

Table 1.4.2. Predicted values of shock wave parameters in water from explosions of 100-kg TNT in a boundless liquid (from [1]).

R, m	ΔP_m, kg/cm^2	I, kg-s/m^2	E_f, kg-m/m^2	E_{Cole}, kg-m	E_{Cole}, MJ	E_{Cole}/E_0
7.5	309.9	1780.6	14405.78	10177662	101.78	0.243
7.6	141.6	960.85	14019.9	10170923	101.71	0.243
15	89.55	669.78	3478.76	9830973	98.31	0.235
30	64.70	518.48	840.06	9496094	94.96	0.227
45.5	40.41	357.88	357.67	9300376	93.00	0.223

Table 1.4.2a. Shock-wave parameters from underwater explosions of cast spherical charges of 100-kg TNT in a shallow basin with sandy bottom. Devices PID-9.

Test No.	Water Level, m	Depth Charge, m	Device No.	Ray No.	Distance, m	Depth Sensor, m	ΔP_m, kg/cm^2	τ, μsec	I, kg-s/m^2
1	1.0	0.75	4	1	15	0.5	30	48	5.3
1	1.0	0.75	4	2	15	0.5	24	43	6.3
2	1.0	0.75	5	1	7.6	0.5	142	62	45
2	1.0	0.75	5	2	7.6	0.5	159	62	47
2	1.0	0.75	2	1	45.5	0.5	6.26	13.7	0.41
2	1.0	0.75	2	2	45.5	0.5	6.16	15.5	0.42
3	1.0	0.75	4	1	15	0.75	41.1	25	6.6
3	1.0	0.75	4	2	15	0.75	46.5	29	6.8
3	1.0	0.75	2	1	45.5	0.75	4.2	15.6	0.36
3	1.0	0.75	2	2	45.6	0.75	4.1	21.2	0.38
4	1.0	0.50	5	1	7.5	0.5	173	56	-
4	1.0	0.50	5	2	7.5	0.75	155	49	-
4	1.0	0.50	4	1	15	0.75	36.6	21	-
4	1.0	0.50	4	2	15	0.75	40.5	28	-
4	1.0	0.50	3	1	30	0.50	12.1	21	-
4	1.0	0.50	3	2	30	0.50	11.2	27	-
5	1.0	0.50	5	1	7.5	0.5	163	68	55.2
5	1.0.	0.50	5	2	7.5	0.25	188	57	53.4
5	1.0	0.50	4	1	15	0.50	46	34	7.9
5	1.0	0.50	4	2	15	0.50	46	37	8.9
5	1.0	0.50	3	1	30	0.75	10.0	17.3	0.87
5	1.0	0.50	3	2	30	0.75	7.8	16.6	0.65
5	1.0	0.50	2	1	45	0.50	4.6	-	-
5	1.0	0.50	2	2	45	0.50	3.9	-	-
6	1.0	0.50	5	1	15	0.75	49.4	29	7.14
6	1.0	0.50	5	2	15	0.5	48.8	36	8.75
6	1.0	0.50	4	1	15	0.125	33.4	14.5	2.42
6	1.0	0:50	4	2	15	0.25	41.8	25	5.24
6	1.0	0.50	3	1	30	0.75	12.3	19	1.16
6	1.0	0.50	3	2	30	0.50	11.7	17.9	1.05
7	0.95	0.25	5	1	15	0.75	44.3	29.9	6.7
7	0.95	0.25	5	2	15	0.50	41.7	33.1	6.9
7	0.95	0.25	4	1	15	0.125	21.0	10.0	1.05
7	0.95	0.25	4	2	15	0.25	26.4	25.4	3.36

Table 1.4.2b. Shock-wave parameters from underwater explosions of cast spherical charges of 100-kg TNT in a shallow basin with sandy bottom. Devices PID-9.

Test No.	Water Level, m	Depth Charge, m	Device No.	Ray No.	Distance, m	Depth Sensor, m	ΔP_m, kg/cm^2	τ, μsec	I, kg-s/m^2
8	0.95	0.25	5	1	15	0.75	44.0	23.2	5.1
8	0.95	0.25	5	2	15	0.50	49.4	29.0	7.0
8	0.95	0.25	4	1	15	0.125	38.5	13.6	2.57
8	0.95	0.25	4	2	15	0.25	37.0	21.9	4.05
8	0.95	0.25	3	1	30	0.75	10.4	12.3	0.64
8	0.95	0.25	3	2	30	0.5	12.0	18.7	1.12
8	0.95	0.25	2	1	30	0.25	9.6	11.9	0.52
8	0.95	0.25	2	2	30	0.125	6.9	8.3	0.28
9	0.5	0.25	5	1	7.5	0.25	61.0	18.6	5.67
9	0.5	0.25	5	2	7.5	0.25	56.8	20.6	5.68
9	0.5	0.25	4	1	7.5	0.125	57.1	10.1	2.86
9	0.5	0.25	4	2	7.5	0.375	53.1	15.7	4.17
9	0.5	0.25	3	1	15	0.25	11.7	10.4	0.607
9	0.5	0.25	3	2	15	0.25	13.5	11.6	0.78
10,11	0.25	0.0	5	1	7.5	0.125	14.4	6.4	0.66
12	1.0	0.5	9	1	15	0.5	39	35	6.7
12	1.0	0.5	5	1	15	0.75	42.6	20.3	4.4
12	1.0	0.5	4	1	15	0.125	39	15	2.92
12	1.0	0.5	4	2	15	0.125	41.2	14.1	2.88
12	1.0	0.5	6	2	22.5	0.25	26.3	14.9	1.96
12	1.0	0.5	3	2	22.5	0.75	17.8	16.1	1.46
13	1.0	0.5	9	1	7.5	0.5	190	65	61.5
13	1.0	0.5	8	1	7.5	0.25	176	79.5	70.0
13	1.0	0.5	8	2	7.5	0.25	188	83	78.0
13	1.0	0.5	5	1	7.5	0.75	146	33.6	25.0
13	1.0	0.5	4	1	7.5	0.125	142.5	28.2	20.8
13	1.0	0.5	4	2	7.5	0.125	170	26.3	22.4
13	1.0	0.5	7	1	15	0.5	39.6	34	6.7
13	1.0	0.5	6	2	15	0.25	40.5	24.8	5.0
13	1.0	0.5	3	2	15	0.75	50.5	38.4	9.7
14	1.0	0.75	3	2	15	0.75	61.2	23.4	7.3
14	1.0	0.75	6	2	15	0.25	69	27	7.8
14	1.0	0.75	4	1	22.5	0.125	23.4	10	1.17
14	1.0	0.75	4	2	22.5	0.125	22.4	8.7	0.97
14	1.0	0.75	5	1	22.5	0.75	23.2	16.2	1.82
14	1.0	0.75	9	1	22.5	0.50	24.8	26.6	3.3
14	1.0	0.75	9	2	22.5	0.875	22.5	13.2	1.42

Table 1.4.2c. Shock-wave parameters from underwater explosions of cast spherical charges of 100-kg TNT in a shallow basin with sandy bottom. Devices PID-9.

Test No.	Water Level, m	Depth Charge, m	Device No.	Ray No.	Distance R, m	Depth Sensor, m	ΔP_m, kg/cm^2	τ, μsec	I, kg-s/m^2
15	1.0	0.75	3	2	7.5	0.75	210	40	42
15	1.0	0.75	6	1	7.5	0.25	184	45	43.3
15	1.0	0.75	6	2	7.5	0.25	260	47	62
15	1.0	0.75	7	1	7.5	0.50	282	76	87
15	1.0	0.75	4	1	15	0.125	49.5	16.4	4.05
15	1.0	0.75	4	2	15	0.125	51.5	13.7	3.56
15	1.0	0.75	5	1	15	0.75	54.8	22.2	6.12
15	1.0	0.75	9	1	15	0.5	51.5	40	10.3
15	1.0	0.75	9	2	15	0.88	50.4	20	5.25
16	1.0	0.25	2	1	22.5	0.125	10.4	17.8	0.92
16	1.0	0.25	2	2	22.5	0.125	12.8	12.2	0.79
16	1.0	0.25	3	1	22.5	0.75	24.0	18.7	2.24
16	1.0	0.25	3	2	22.5	0.75	23.4	18.2	2.14
16	1.0	0.25	6	1	22.5	0.25	15.7	17.0	1.34
16	1.0	0.25	6	2	22.5	0.25	13.6	20.4	1.38
16	1.0	0.25	7	1	22.5	0.50	22.2	26.6	2.94
16	1.0	0.25	7	2	22.5	0.88	19.6	14.3	1.38
16	1.0	0.25	4	1	15	0.125	44.8	14.7	3.28
16	1.0	0.25	4	2	15	0.125	44.0	17.5	3.85
16	1.0	0.25	5	1	15	0.75	47.3	23.6	5.68
16	1.0	0.25	5	2	15	0.75	53.0	25.6	6.85
16	1.0	0.25	9	1	15	0.50	55.5	35.4	9.8
16	1.0	0.25	9	2	15	0.88	52.2	22.2	9.8
17	1.0	0.25	3	1	15	0.75	49.5	28.6	7.05
17	1.0	0.25	3	2	15	0.75	49	27.6	6.85
17	1.0	0.25	6	1	15	0.25	47.0	26.2	6.15
17	1.0	0.25	6	2	15	0.25	47.5	23.4	5.57
17	1.0	0.25	7	1	15	0.50	50	36.8	9.2
17	1.0	0.25	7	2	15	0.88	46	18.7	4.28
17	1.0	0.25	4	1	7.5	0.125	163	25.0	20.2
17	1.0	0.25	4	2	7.5	0.125	161	29	23.2
17	1.0	0.25	5	1	7.5	0.75	175	52	45.2
17	1.0	0.25	5	2	7.5	0.75	187	49	46
17	1.0	0.25	8	1	7.5	0.25	178	41	36.6
17	1.0	0.25	8	2	7.5	0.25	172	38.7	33.2
17	1.0	0.25	9	1	7.5	0.50	194	67.5	65.7
17	1.0	0.25	9	2	7.5	0.88	178	27.6	24.5
18	3.0	0.25	3	1	15	0.25	53.2	27.5	9.3
18	3.0	0.25	3	2	15	0.50	58	62	16.2
18	3..0	0.25	4	1	30	0.25	19.7	21	2.6
18	3.0	0.25	4	2	30	0.50	23.2	35	4.53
18	3.0	0.25	8	1	30	1.5	28.5	110	13.6
18	3.0	0.25	8	2	30	2.0	32.4	100	21.4
18	3.0	0.25	9	1	30	2.5	31.8	67.8	16.3
18	3.0	0.25	9	2	30	2.75	36.2	42.5	12.3

Table 1.4.2d. Shock-wave parameters from underwater explosions of cast spherical charges of 100-kg TNT in a shallow basin with sandy bottom. Devices PID-9.

Test No.	Water Level, m	Depth Charge, m	Device No.	Ray No.	Distance, m	Depth Sensor, m	ΔP_m, kg/cm^2	τ, μsec	I, kg-s/m^2
19	3.0	0.5	3	1	15	0.25	87.5	27.5	22.6
19	3.0	0.5	3	2	15	0.50	96	62	38.0
19	3..0	0.5	6	1	15	1.50	124	194	129.0
19	3.0	0.5	6	2	15	2.0	119	224	167.0
19	3.0	0.5	7	1	15	22.5	134	146.2	117
19	3.0	0.5	7	2	15	2.75	142.5	100	97
19	3.0	0.5	4	1	30	0.25	29.6	22.9	4.5
19	3.0	0.5	4	2	30	0.50	38.2	40.3	7.55
19	3.0	0.5	5	1	30	1.0	39.6	86.2	17.6
19	3.0	0.5	5	2	30	1.5	49.2	138	32.4
19	3..0	0.5	8	1	30	11.5	52.0	133	31.8
19	3.0	0.5	8	2	30	2.0	49.2	113	38.9
19	3.0	0.5	9	1	30	2.5	51.5	67.5	17.3
19	3.0	0.5	9	2	30	2.75	58.5	44.5	13.0
20	3.0	1.0	3	1	15	0.25	120	27.8	28.8
20	3.0	1.0	3	2	15	0.50	128	62	50.0
20	3..0	1.0	6	1	15	1.5	146	235	186
20	3.0	1.0	6	2	15	2.0	138	202	188
20	3.0	1.0	7	1	15	2.5	148	138	115
20	3.0	1.0	7	2	15	2.75	150	120	108
20	3.0	1.0	4	1	30	0.25	37.6	28.8	7.10
20	3.0	1.0	4	2	30	0.50	51.2	47.8	16.5
20	3.0	1.0	5	1	30	1.0	51.9	83.5	33
20	3.0	1.0	5	2	30	1.5	63.0	127.6	51
20	3..0	1.0	8	1	30	1.5	57.8	123	58.5
20	3.0	1.0	8	2	30	2.0	61	110	64.5
20	3.0	1.0	9	1	30	2.5	67.7	67.8	23.5
20	3.0	1.0	9	2	30	2.75	64.2	53.6	17.4
21	3.0	1.5	3	1	15	0.25	146	35.7	47
21	3.0	1.5	3	2	15	0.50	142.0	75.7	108
21	3..0	1.5	6	1	15	1.5	147.5	238	196
21	3.0	1.5	6	2	15	2.0	134.0	185	136
21	3.0	1.5	7	1	15	2.5	146	110	75.5
21	3.0	1.5	7	2	15	2.75	144	96.2	63.5
21	3.0	1.5	4	1	30	0.25	54.2	42.3	14.2
21	3.0	1.5	4	2	30	0.50	67.0	66.5	27.6
21	3.0	1.5	5	1	30	1.0	58.5	117	47.5
21	3.0	1.5	5	2	30	1.5	66	138	52.5
21	3..0	1.5	8	1	30	1.5	61.2	140	55
21	3.0	1.5	8	2	30	2.0		113	36.2
21	3.0	1.5	9	1	30	2.5	56.0	67.3	17.2
21	3.0	1.5	9	2	30	2.75	54.3	35	10

Table 1.4.2e. Shock-wave parameters from underwater explosions of cast spherical charges of 100-kg TNT in a shallow basin with sandy bottom. Devices PID-9.

Test No.	Water Level, m	Depth Charge, m	Device No.	Ray No.	Distance, m	Depth Sensor, m	ΔP_m, kg/cm^2	τ, μsec	I, kg-s/m^2
22	3.0	2.75	4	1	15	0.25	118	78.5	73
22	3.0	2.75	4	2	15	0.50	125	143	112
22	3..0	2.75	5	1	15	1.0	124	249	162
22	3.0	2.75	5	2	15	1.5	124.8	286	186
22	3.0	2.75	8	1	15	1.5	116	252	146
22	3.0	2.75	8	2	15	2.0	104	210	109
22	3.0	2.75	9	1	15	2.5	83	104	28
22	3.0	2.75	9	2	15	2.75	79.5	64	25
22	3.0	2.75	3	1	30	0.25	39.4	35.7	14
22	3.0	2.75	3	2	30	0.50	41.5	64.3	21.8
22	3..0	2.75	6	1	30	1.5	38.8	173	32.5
22	3.0	2.75	6	2	30	2.0	29.4	227	20.8
23	3.0	0.0	4	1	15	0.25	41.0	27.6	11.4
23	3.0	0.0	4	2	15	0.50	47.5	48.5	13.8
23	3..0	0.0	5	1	15	1.0	660.0	86	25.8
23	3.0	0.0	5	2	15	1.5	60.5	118	34.1
23	3.0	0.0	8	1	15	1.5	60.0	122	47.5
23	3.0	0.0	8	2	15	2.0	69.8	154	62.8
23	3.0	0.0	9	1	15	2.5	72.2	130.5	56.8
23	3.0	0.0	9	2	15	2.75	79.5	81.7	52.0
23	3.0	0.0	3	1	30	0.25	15.7	15.7	1.54
23	3.0	0.0	3	2	30	0.50	18.0	27.2	2.8
23	3..0	0.0	6	1	30	1.5	19.3	93.7	11.2
23	3.0	0.0	6	2	30	2.0	20.0	124	13.4
23	3.0	0.0	7	1	30	2.5	29.0	65.4	14.9
23	3.0	0.0	7	2	30	2.75	28.0	39.3	7.9
24	3.0	2.0	4	1	7.5	0.25	308	115	206.0
24	3.0	2.0	4	2	7.5	0.50	314	178	389.0
24	3..0	2.0	8	1	7.5	1.50	314	408	715
24	3.0	2.0	8	2	7.5	2.0	320	408	6577
24	3.0	2.0	9	1	7.5	2.5	313	123	284
24	3.0	2.0	9	2	7.5	2.75	312	119	276
24	3.0	2.0	3	1	22.5	0.25	73.5	35.8	24
24	3.0	2.0	3	2	22.5	0.50	78	71.6	45
24	3.0	2.0	6	1	22.5	1.50	93	138	93.5
24	3.0	2.0	6	2	22.5	2.0	94	153	73.2
24	3.0	2.0	7	1	22.5	2.5	87	117	34
24	3.0	2.0	7	2	22.5	2.75	59	106	9.1

Table 1.4.2g.   Shock-wave parameters from underwater explosions of cast spherical charges of 100-kg TNT in a shallow basin with sandy bottom. Devices PID-9.

Test No.	Water Level, m	Depth Charge, m	Device No.	Ray No.	Distance, m	Depth Sensor, m	ΔP_m, kg/cm^2	τ, µsec	I, kg-s/m^2
25	3.0	0.25	4	1	7.5	0.25	157	57	61
25	3.0	0.25	4	2	7.5	0.50	202	89	120
25	3..0	0.25	8	1	7.5	1.50	218	228	244
25	3.0	0.25	8	2	7.5	2.0	255	262	334
25	3.0	0.25	9	1	7.5	2.5	265	220	300
25	3.0	0.25	9	2	7.5	2.75	273	147	240
25	3.0	0.25	3	1	22.5	0.25	32..6	27.6	5.7
25	3.0	0.25	3	2.	22.5	0.50	43.7	50.0	11.9
25	3.0	0.25	6	1	22.5	1.50	51	114	36.0
25	3.0	0.25	6	2	22.5	2.0	47.6	138	40.0
25	3.0	0.25	7	1	22.5	2.5	43.6	95	35.0
25	3.0	0.25	7	2	22.5	2.75	33.5	65.4	11.2
26	3.0	0..5	3	1	7.5	0.25	286	64.5	82
26	3.0	0.5	3	2	7.5	0.5	312	107	208
26	3..0	0.5	2	1	7.5	1.0	260	236	408
26	3.0	0.5	2	2	7.5	1.5	265	348	665
26	3.0	0.5	6	1	7.5	1.5	303	265	530
26	3.0	0.5	6	2	7.5	2.0	300	215	376
26	3.0	0.5	7	1	7.5	2.5	292	154	217
26	3.0	0.5	7	2	7.5	2.75	322	124	139
26	3.0	0.5	4	1	22.5	0.25	55.2	38.6	11.3
26	3.0	0.5	4	2	22.5	0.5	70	59.5	23.8
26	3.0	0.5	5	1	22.5	1.0	73.2	110	43.8
26	3.0	0.5	5	2	22.5	1.5	76	174	70
26	3.0	0.5	8	1	22.5	1.5	77.5	165	73
26	3.0	05	8	2	22.5	2.0	81.5	157	78
26	3.0	0.5	9	1	22.5	2.5	91.2	98.5	68.5
26	3.0	0.5	9	2	22.5	2.75	110	77.5	51.5
27	3.0	1.0	3	1	7.5	0.25	310	64.3	117
27	3.0	1.0	3	2	7.5	0.5	340	108	246
27	3..0	1.0	2	1	7.5	1.0	310	197	490
27	3.0	1.0	2	2	7.5	1.5	310	300	480
27	3.0	1.0	6	1	7.5	1.5	316	273	390
27	3.0	1.0	6	2	7.5	2.0	322	165	335
27	3.0	1.0	4	1	22.5	0.25	55.7	38.6	11.4
27	3.0	1.0	4	2	22.5	0.5	71.8	56	29.4
27	3.0	1.0	5	1	22.5	1.0	74.6	116	48.0
27	3.0	1.0	5	2	22.5	1.5	82.3	165	69.2
27	3..0	1.0	8	1	22.5	1.5	78.6	161	66.0
27	3.0	1.0	8	2	22.5	2.0	82.5	167	67.0
27	3.0	1.0	9	1	22.5	2.5	100.6	100	57.0
27	3.0	1.0	9	2	22.5	2.75	125	77	49

Table 1.4.2h.   Shock-wave parameters from underwater explosions of cast spherical charges of 100-kg TNT in a shallow basin with sandy bottom. Devices PID-9.

Test No.	Water Level, m	Depth Charge, m	Device No.	Ray No.	Distance, m	Depth Sensor, m	ΔP_m, kg/cm^2	τ, μsec	I, kg-s/m^2
28	3.0	1.5	3	1	7.5	0.25	322	71	169
28	3.0	1.5	3	2	7.5	0.5	322	130	272
28	3..0	1.5	2	1	7.5	1.0	322	283	670
28	3.0	1.5	2	2	7.5	1.5	294	435	730
28	3.0	1.5	6	1	7.5	1.5	304	292	554
28	3.0	1.5	6	2	7.5	2.0	318	204	340
28	3.0	1.5	7	1	7.5	2.5	299	186	412
28	3.0	1.5	7	2	7.5	2.75	340	166	570
28	3.0	1.5	4	1	22.5	0.25	70.2	37	21.6
28	3.0	1.5	4	2	22.5	0.5	85.5	67	34.2
28	3..0	1.5	5	1	22.5	1.0	88.6	138	57.0
28	3.0	1.5	5	2	22.5	1.5	90.0	153	88.0
28	3.0	1.5	8	1	22.5	1.5	88.5	157	100
28	3.0	1.5	8	2	22.5	2.0	100	165	81.5
28	3.0	1.5	9	1	22.5	2.5	97	89	52.0
28	3.0	1.5	9	2	22.5	2.75	109	65	36.2
29	3.0	2.75	3	1	7.5	0.25	214	62	80.6
29	3.0	2.75	3	2	7.5	0.5	222	149	199
29	3..0	2.75	2	1	7.5	1.0	222	262	270
29	3.0	2.75	2	2	7.5	1.5	183	297	286
29	3.0	2.75	6	1	7.5	1.5	184	260	236
29	3.0	2.75	6	2	7.5	2.0	182	214	200
29	3.0	2.75	7	1	7.5	2.5	177	106	77.5
29	3.0	2.75	7	2	7.5	2.75	178	100	70
29	3.0	2.75	4	1	22.5	0.25	35	35.7	12.3
29	3.0	2.75	4	2	22.5	0.5	37.6	68	23.4
29	3..0	2.75	5	1	22.5	1.0	35.6	153	37.4
29	3.0	2.75	5	2	22.5	1.5	33.6	220	39.6
29	3.0	2.75	8	1	22.5	1.5	33.2	223	49
29	3.0	2.75	8	2	22.5	2.0	30.2	157	29.6
29	3.0	2.75	9	1	22.5	2.5	33	232	23.4
29	3.0	2.75	9	2	22.5	2.75	32	128	13.8

Table of 1.4.3. Shock-wave parameters estimated using digitized oscillograms from underwater explosions of cast spherical charges of 100-kg TNT in a shallow basin with sandy bottom.

R, m	h, m	ΔP_m, kg/cm^2	τ, μs	I, kg-s/m^2	E_+, kg-m/m^2	E_{+mid}, kg-m/m^2	E_{1mid}, kg-m	E_{1mid}/E_0, %	E_{mid}, kg-m
Test 1, depth of basin 1 m, depth of charge 0.75 m									
15		30	47	5.3	6.6	7.09	667	0.0016	584
15		24	43	6.3	7.58				
Test 2, depth of basin 1 m, depth of charge 0.75 m									
7.6	0.5	142	62	45	313	341	16178	0.039	
7.6	0.5	159	62	47.5	369				
45.5	0.5	6.26	13.7	0.41	0.103	0.103	29.25	0.00007	
45.5	0.5	6.16	15.5	0.42	0.102				
Test 3, depth of basin 1 m, depth of charge 0.75 m									
15	0.75	41.1	25	6.6	13.8	14.2	1334	0.00325	
15	0.75	46.5	29	6.8	14.6				
45.5	0.75	4.2	15.6	0.36	0.065	0.065	18.5	0.000044	
45.5	0.75	4.1	21.2	0.38	0.065				
Test 4, depth of basin 1 m, depth of charge 0.5 m									
7.5	0.5	173	56	50	419	354	16652	0.040	
7.5	0.75	155	49	38	288.8				
15	0.75	36.6	21	4.9	9.2	11	1030	0.0025	
15	0.75	40.5	28	6.64	12.7				
30	0.5	12.1	21	1.27	0.69	0.73	137	0.00033	
30	0.5	11.2	27	1.51	0.76				
Test 5, depth of basin 1 m, depth of charge 0.5 m									
7.5	0.25	188	68	56	447	445	20235	0.0484	
7.5	0.5	163	66	55	443				
15	0.5	46	34	7.9	17.2	18.1	1707	0.0041	
15	0.5	46	37	8.9	19				
30	0.75	10	17.3	0.87	0.39	0.31	58.4	0.00014	
30	0.75	7.8	16.6	0.65	0.23				
Test 6, depth of basin 1 m, depth of charge 0.5 m									
15	0.125	33.4	14.5	2.42	3.23	11.73	1105	0.00264	1176
15	0.25	41.8	25	5.24	10.1				
15	0.50	48.8	36	8.75	19.3				
15	0.75	49.4	29	7.14	14.3				
30	0.5	11.7	17.9	1.05	0.56	0.60	114	0.00027	
30	0.75	12.3	19	1.16	0.64				
Test 7, depth of basin 0.95 m, depth of charge 0.25 m									
15	.125	21	10	1.07	1.06	7.86	702.3	0.00159	801
15	0.25	26.4	25.4	3.37	3.86				
15	0.5	41.7	33.1	6.9	12.9				
15	0.75	44.3	29.9	6.7	13.6				

Test 8, depth of basin 0.95 m, depth of charge 0.25 m									
15	0.125	38.5	13.6	2.57	4.43	9.16	863	0.0021	887
15	0.25	37	21.9	4.05	6.68				
15	0.5	49.4	29	7.0	15.7				
15	0.75	44	23.2	5.1	9.82				
30	0.125	6.9	8.3	0.28	0.1	0.31	57.7	0.00017	59.8
30	0.25	9.6	11.9	0.52	0.22				
30	0.5	12	18.7	1.12	0.6				
30	0.75	10.4	12.3	0.64	0.3				

Test 9, depth of basin 0.5 m, depth of charge 0.25 m									
7.5	0.125	57.1	10.1	2.86	7.3	11.7	274	0.00065	
7.5	0.25	61	18.6	5.578	15.3				
7.5	0.25	56.8	20.6	5.68	14				
7.5	0.375	53.1	15.7	4.17	9.9				
15	0.25	11.7	10.4	0.611	0.36	0.42	19.5	0.000045	
15	0.25	13.5	11.6	0.78	0.47				

Test 10, depth of basin 0.25 m, depth of charge 0.0 m									
7.5	0.125	14.4	6.4	0.66	0.48	0.48	5.62	0.000013	

Test 11, depth of basin 0.25 m, depth of charge 0.0 m									
7.5	0.125	16.7	8	0.58	0.44	0.44	5.18	0.000012	

Test 12, depth of basin 1.0 m, depth of charge 0.5 m									
15	0.125	39	15	2.92	5.27	7.64	719.3	0.00173	780
15	0.125	41.2	14.1	2.98	5.38				
15	0.5	39	35	6.7	11.3				
15	0.75	42.6	20.3	4.4	8.6				
22.5	0.25	26.3	14.9	1.96	2.37	1.79	170	0.00041	211
22.5	0.75	17.8	16.1	1.46	1.21				

Test 13, depth of basin 1.0 m, depth of charge 0.5 m									
7.5	0.125	142.5	28.2	20.8	143	414	19502	0.0465	16877
7.5	0.125	170	26.3	22.4	189				
7.5	0.25	176	79.5	77.5	716				
7.5	0.25	188	83	78	710				
7.5	0.5	190	65	61.5	543				
7.5	0.75	146	33.6	25	181.7				
15	0.25	40.5	24.8	5.0	9.9	14.8	1394	0.0033	1306
15	0.5	39.6	34	6.7	12.1				
15	0.75	50.5	38.4	9.7	22.3				

Test 14 depth of basin 1.0 m, depth of charge 0.75 m									
15	0.25	69	27	7.8	22	20.3	1908	0.0046	1650
15	0.75	61.2	23.4	7.3	18.5				
22.5	0.125	23.4	10	1.17	1.24	1.96	272	0.00066	322.5
22.5	0.125	22.4	8.7	0.97	0.98				
22.5	0.5	24.8	26.6	3.3	3.92				
22.5	0.75	23.2	16.2	1.82	2.1				
22.5	0.875	22.5	13.2	1.42	1.58				

Test 15, depth of basin 1.0 m, depth of charge 0.75 m									
7.5	0.25	260	47	67	834	648	30501	0.073	25784
7.5	0.25	184	45	43.3	379				
7.5	0.5	282	76	87	965				
7.5	0.75	210	40	42	412				
15	0.125	49.5	16.4	4.05	9.19	14.1	1327	0.0032	1493
15	0.125	51.5	13.7	3.56	8.06				
15	0.5	51.5	40	10.3	25.3				
15	0.75	54.8	22.2	6.12	15.6				
15	0.88	50.4	20	5.25	12.27				
Test 16, depth of basin 1.0 m, depth of charge 0.25 m.									
15	0.125	44.8	14.7	3.28	6.30	13.3	1251	0.0032	1473
15	0.125	44	17.5	3.85	7.4				
15	0.5	55.5	35.4	9.8	23.7				
15	0.75	47.3	23.6	5.68	12.1				
15	0.75	53	25.6	6.85	16.4				
15	0.88	52.2	22.2	5.8	13.6				
22.5	0.125	10.4	17.8	0.92	0.42	1.42	198	0.00048	221.7
22.5	0.125	12.8	12.2	0.79	0.45				
22.5	0.25	15.7	17	1.34	0.93				
22.5	0.25	13.6	20.4	1.38	0.83				
22.5	0.5	22.2	26.6	2.94	2.88				
22.5	0.75	24	18.7	2.24	2.4				
22.5	0.75	23.4	18.2	2.14	2.27				
22.5	0.88	19.8	14.3	1.38	1.19				
Test 17, depth of basin 1.0 m, depth of charge 0.25 m									
7.5	0.125	163	25	20.2	146.5	302	14212	0.034	15226
7.5	0.125	161	29	23.2	166.3				
7.5	0.25	172	38.7	33.2	286				
7.5	0.25	178	41	39.6	325				
7.5	0.5	194	67.5	65.3	564				
7.5	0.75	175	52	45.2	352				
7.5	0.75	187	49	46	380				
7.5	0.88	178	27.6	24.5	194				
15	0.25	47.5	23.4	5.57	12.8	14.3	1345	0.0032	1212
15	0.25	47	26.2	6.15	13.4				
15	0.5	50	36.8	9.2	20.4				
15	0.75	49.5	28.6	7.05	15.5				
15	0.75	49	27.6	6.85	14.9				
15	0.88	46	18.7	4.28	8.69				
Test 18, depth of basin 3.0 m, depth of charge 0.25 m									
15	0.25	53.2	27.5	9.3	24.2	32.9	9269	0.022	
15	0.5	50.8	62	16.2	41.5				
30	0.25	19.7	21	2.6	2.53	19.6	11090	0.027	10572
30	0.50	23.2	35	4.53	5.02				
30	1.5	28.5	110	13.6	17.3				

30	2.0	32.4	100	21.4	36.1				
30	2.5	31.8	67.8	16.3	29.6				
30	2.75	36.2	42.5	12.3	27.2				
Test 19, depth of basin 3.0 m, depth of charge 0.5 m									
15	0.25	87.5	27.5	22.6	59.7	563.2	159167	0.38	159123
15	0.5	96	62	38	186				
15	1.5	124	194	129	705				
15	2.0	119	224	167	949				
15	2.5	134	146.2	117	723				
15	2.75	142.5	100	97	756.4				
30	0.25	29.6	22.9	4.5	6.9	44.4	25067	0.06	2482
30	0.50	38.2	40.3	7.55	12.9				
30	1.0	39.6	86.2	17.6	30.9				
30	1.5	49.2	138	32.4	66.6				
30	1.5	52	133	31.8	68.3				
30	2.0	49.2	113	38.9	100				
30	2.5	51.5	67.5	17.3	37.2				
30	2.75	58.5	44.5	13.0	32				
Test 20, depth of basin 3.0 m, depth of charge 1.0 m									
15	0.25	120	34	27.7	183	875.5	247416	0.59	260004
15	0.5	128	62	47.8	328				
15	1.5	146	235	216	1678				
15	2.0	138	202	167	1139				
15	2.5	148	138	123	1020				
15	2.75	150	120	97	797				
30	0.25	37.6	28.8	6	11.1	93.2	52678	0.13	61706
30	0.5	51.2	47.8	16.5	38				
30	1.0	51.9	83.5	18	44				
30	1.5	63	127.6	48.7	164				
30	1.5	57.8	123	43	130				
30	2	61	110	49	172				
Test 21, depth of basin 3.0 m, depth of charge 1.5 m									
15	0.25	146	35.7	37	290	673	190286	0.42	213174
15	0.5	142	75.7	84.6	700				
15	1.5	147.5	238	196	1343				
15	2.0	134	185	136	843				
15	2.5	146	110	75.5	478				
15	2.75	144	96.2	63.5	386				
30	0.25	54.2	42.3	14.2	39.8	100	56614	0.14	53334
30	0.5	67	66.5	27.6	95.7				
30	1.0	58.5	117	47.5	148				
30	1.5	66	138	52.5	170				
30	1.5	61.8	140	55	179.2				
30	2.0	60	113	36.2	103				
30	2.5	56	67.3	17.2	38.9				
30	2.75	54.3	35	10	26.3				

Test 22, depth of basin 3.0 m, depth of charge 2.75 m									
15	0.25	118	78.5	73	484	562.4	155925	0.38	149126
15	0.5	125	143	112	701				
15	1.0	124	249	162	864				
15	1.5	124.8	286	186	990				
15	1.5	116	252	146	709				
15	2.0	104	210	109	486				
15	2.5	83	104	47.6	179				
15	2.75	79.5	64	25	86.2				
30	0.25	39.4	35.7	10.1	21.1	35	19785	0.048	19000
30	0.50	41.5	64.3	19.3	42.8				
30	1.5	38.8	173	32.5	52.9				
30	2.0	29.4	227	20.8	23.3				
Test 23, depth of basin 3.0 m, depth of charge 0.0 m									
15	0.25	41	27.6	6.9	15	113	31877	0.08	32377
15	0.5	47.5	48.5	10.6	24.4				
15	1.0	60	86	22.9	66				
15	1.5	60.5	118	25.2	67.8				
15	1.5	60	122	35	103.2				
15	2.0	69.8	154	48.0	158.8				
15	2.5	72.2	406	76.8	248				
15	2.75	79.5	81.7	48.3	220.4				
30	0.25	15.7	20	1.54	1.26	10.8	6095	0.015	5698
30	0.5	18	27.2	2.8	2.45				
30	1.5	19.3	93.7	11.2	11.1				
30	2.0	20	124	13.4	11.4				
30	2.5	29	65.4	15.7	27.3				
30	2.75	28	39.3	7.5	11				
Test 24, depth of basin 3.0 m, depth of charge 2.0 m									
7.5	0.25	308	115	206	3343	6630	936765	2.24	910266
7.5	0.5	314	178	389	7169				
7.5	1.5	314	408	715	10319				
7.5	2.0	320	408	657	9606				
7.5	2.5	313	123	284	4718				
7.5	2.75	312	119	276	4624				
22.5	0.25	73.5	35.8	19.6	80.5	200	84690	0.2	98151
22.5	0.5	78	71.6	39.2	162				
22.5	1.5	93	138	93.5	471				
22.5	2.0	94	153	73.2	328				
22.5	2.5	87	117	34	115				
22.5	2.75	59	106	19.1	42				
Test 25, depth of basin 3.0 m, depth of charge 0.25 m									
7.5	0.25	157	101	62	523.4	2663	377756	0.9	383010
7.5	0.5	202	89	120	1316				
7.5	1.5	218	228	244	2517				
7.5	2.0	255	262	334	4146				

7.5	2.5	265	220	300	3977				
7.5	2.75	273	147	240	3500				
22.5	0.25	32.6	27.6	5.7	8.99	51.4	21810	0.05	23182
22.5	0.5	43.7	50	11.9	23.1				
22.5	1.5	51	114	36	87.5				
22.5	2.0	47.6	138	40	87				
22.5	2.5	43.6	95	33.4	85				
22.5	2.75	33.5	65.4	11.2	17				

Test 26, depth of basin 3.0 m, depth of charge 0.5 m

7.5	0.25	286	64.5	87	1150	4669	659771	1.58	610559
7.5	0.5	312	107	208	3208				
7.5	1.0	260	236	408	5467				
7.5	1.5	265	348	665	9653				
7.5	1.5	303	265	530	8277				
7.5	2.0	300	215	376	5254				
7.5	2.5	292	154	217	2634				
7.5	2.75	322	124	139	1712				
22.5	0.25	55.2	38.6	11.3	29.5	228	96616	0.23	95227
22.5	0.5	70	59.5	23.8	81.7				
22.5	1.0	73.2	110	43.8	154.6				
22.5	1.5	76	174	70	255				
22.5	1.5	77.5	165	73	285				
22.5	2.0	81.5	157	78	338				
22.5	2.5	91.2	98.5	68.5	382				
22.5	2.75	110	77.5	51.5	297				

Test 27, depth of basin 3.0 m, depth of charge 1.0 m

7.5	0.25	310	64.3	119	1961	6518	921045	2.2	906887
7.5	0.5	340	108	224	3894				
7.5	1.0	310	197	406	7018				
7.5	1.5	320	292	569	8723				
7.5	1.5	316	273	611	10278				
7.5	2.0	322	165	389	7236				
22.5	0.25	55.7	38.6	12	32	225	95732	0.23	96529
22.5	0.5	71.8	56	23.3	83				
22.5	1.0	74.6	116	48	190				
22.5	1.5	82.5	163	61.5	226.4				
22.5	1.5	78.6	161	57.6	210				
22.5	2.0	82.5	138	72.7	324				
22.5	2.5	109	100	69.4	417				
22.5	2.75	123.7	82	51	324.4				

Test 28, depth of basin 3.0 m, depth of charge 1.5 m

7.5	0.25	322	71	169	3111	6944	981138	2.35	936254
7.5	0.5	322	130	272	4370				
7.5	1.0	322	283	570	9477				
7.5	1.5	294	435	730	10219				
7.5	1.5	304	292	554	8571				

7.5	2.0	318	204	340	4801				
7.5	2.5	299	186	412	6964				
7.5	2.75	340	166	420	8036				
22.5	0.25	70.2	37	19.5	79.6	267	113142	0.271	106279
22.5	0.5	85.5	67	34.2	138				
22.5	1.0	88.6	138	57	219				
22.5	1.5	90	153	88	398				
22.5	1.5	88.5	157	100	503				
22.5	2.0	100	165	81.5	376				
22.5	2.5	97	89	52	239				
22.5	2.75	109	65	36.2	181				
Test 29, depth of basin 3.0 m, depth of charge 2.75 m									
7.5	0.25	214	62	80.6	878	1521	214921	0.52	208824
7.5	0.5	222	149	199	2108				
7.5	1.0	222	262	270	2424				
7.5	1.5	183	297	286	2353				
7.5	1.5	184	260	236	1819				
7.5	2.0	182	214	200	1591				
7.5	2.5	177	106	77.5	524				
7.5	2.75	178	100	70	471				
22.5	0.25	45	35.7	10	21.5	56.8	24087	0.058	22944
22.5	0.5	37.6	68	22.5	53.7				
22.5	1.0	35.6	153	37.4	80.9				
22.5	1.5	33.6	220	39.6	79.1				
22.5	1.5	33.2	223	49	109				
22.5	2.0	30.2	157	29.6	63.7				
22.5	2.5	33	232	23	28.5				
22.5	2.75	32	128	13.8	18.2				

Table 1.4.4. Shock-wave energy in a reservoir with water level $H_b = 1$ m, explosion depth H = 0.75 m, M = 100-kg TNT.

No. test/H_b/H	R, m	h, m	E_+, kg-m/m^2	E_{+mid}, kg-m/m^2	E_f, kg-m/m^2	E_{1mid}, kg-m	E_{mid}, kg-m	E_{mid}/E_0, %
15/1/0.75	7.5	0.25	379	647.5	14405	30497	25784	0.062
15/1/0.75	7.5	0.25	834					
15/1/0.75	7.5	0.5	965					
15/1/0.75	7.5	0.75	412					
2/1/0.75	7.6	0.5	313	341	14020	16275	---	
2/1/0.75	7.6	0.5	369					
15/1/0.75	15	0.125	9.19	13.96	3479	1315	1294	0.0031
15/1/0.75	15	0.125	8.06					
14/1/0.75	15	0.25	22					
1/1/0.75	15	0.5	6.6					
1/1/0.75	15	0.5	7.58					
15/1/0.75	15	0.5	25.3					
3/1/0.75	15	0.75	13.8					
3/1/0.75	15	0.75	14.6					
14/1/0.75	15	0.75	18.5					
15/1/0.75	15	0.75	15.6					
15/1/0.75	15	0.88	12.3					
14/1/0.75	22.5	0.125	1.29	1.974	1515	279	310.8	0.00074
14/1/0.75	22.5	0.125	0.98					
14/1/0.75	22.5	0.5	3.92					
14/1/0.75	22.5	0.75	2.1					
14/1/0.75	22.5	0.875	1.58					
2/1/0.75	45.5	0.5	0.103	0.084	358	23.93	18	4.3E-5
2/1/0.75	45.5	0.5	0.102					
3/1/0.75	45.5	0.75	0.065					
3/1/0.75	45.5	0.75	0.065					

Table 1.4.5. Shock-wave energy in a reservoir with water level $H_b = 1$ m, explosion depth $H = 0.5$ m, $M = 100$-kg TNT.

No. test/H_b/H	R, m	h, m	E_+, kg-m/m^2	E_{+mid}, kg-m/m^2	E_f, kg-m/m^2	E_{1mid}, kg-m	E_{mid}, kg-m	E_{mid}/E_0, %
13/1/0.5	7.5	0.125	143	408.1	14405	19222	16167	0.039
13/1/0.5	7.5	0.125	189					
13/1/0.5	7.5	0.25	716					
13/1/0.5	7.5	0.25	710					
5/1/0.5	7.5	0.25	447					
4/1/0.5	7.5	0.5	419					
5/1/0.5	7.5	0.5	443					
13/1/0.5	7.5	0.5	543					
4/1/0.5	7.5	0.75	289					
13/1/0.5	7.5	0.75	182					
6/1/0.5	15	0.125	3.23	12.0	3479	1130	1077	0.0026
12/1/0.5	15	0.125	5.27					
12/1/0.5	15	0.125	5.38					
13/1/0.5	15	0.25	9.9					
6/1/0.5	15	0.25	10.1					
5/1/0.5	15	0.5	17.2					
5/1/0.5	15	0.5	19.0					
6/1/0.5	15	0.5	19.3					
12/1/0.5	15	0.5	11.3					
13/1/0.5	15	0.5	12.1					
13/1/0.5	15	0.75	22.3					
12/1/0.5	15	0.75	8.6					
4/1/0.5	15	0.75	12.7					
4/1/0.5	15	0.75	9.2					
6/1/0.5	15	0.75	14.3					
12/1/0.5	22.5	0.25	2.37	1.79	1515	253	--	
12/1/0.5	22.5	0.25	1.21					
4/1/0.5	30	0.5	0.69	0.55	840	103.6	77.1	0.0002
4/1/0.5	30	0.5	0.76					
6/1/0.5	30	0.5	0.56					
5/1/0.5	30	0.75	0.39					
5/1/0.5	30	0.75	0.23					
6/1/0.5	30	0.75	0.64					

Table 1.4.6. Shock-wave energy in a reservoir with water level H_b = 1 m, explosion depth H = 0.25 m, M = 100-kg TNT.

No.test/H_b/H	R, m	h, m	E_+, kg-m/m^2	E_{+mid}, kg-m/m^2	E_f, kg-m/m^2	E_{1mid}, kg-m	E_{mid}, kg-m	E_{mid}/ E_0, %
17/1/0.25	7.5	0.125	146.5	301.7	14405	14211	15226	0.036
17/1/0.25	7.5	0.125	166.3					
17/1/0.25	7.5	0.25	286					
17/1/0.25	7.5	0.25	325					
17/1/0.25	7.5	0.5	564					
17/1/0.25	7.5	0.75	352					
17/1/0.25	7.5	0.75	380					
17/1/0.25	7.5	0.88	194					
7/1/0.25	15	0.125	1.06	11.89	3479	1120	1083	0.0026
8/1/0.25	15	0.125	4.43					
16/1/0.25	15	0.125	6.3					
7/1/0.25	15	0.25	3.86					
8/1/0.25	15	0.25	6.68					
17/1/0.25	15	0.25	12.8					
17/1/0.25	15	0.25	13.4					
7/1/0.25	15	0.5	12.9					
8/1/0.25	15	0.5	15.7					
16/1/0.25	15	0.5	23.7					
17/1/0.25	15	0.5	20.4					
7/1/0.25	15	0.75	13.6					
8/1/0.25	15	0.75	9.82					
16/1/0.25	15	0.75	12.1					
16/1/0.25	15	0.75	16.4					
17/1/0.25	15	0.75	15.5					
17/1/0.25	15	0.75	14.9					
16/1/0.25	15	0.88	13.6					
17/1/0.25	15	0.88	8.69					
16/1/0.25	22.5	0.125	0.42	1.42	1515	200.8	227	5.4E-4
16/1/0.25	22.5	0.125	0.45					
16/1/0.25	22.5	0.25	0.93					
16/1/0.25	22.5	0.25	0.83					
16/1/0.25	22.5	0.5	2.88					
16/1/0.25	22.5	0.75	2.4					
16/1/0.25	22.5	0.75	2.27					
16/1/0.25	22.5	0.88	1.19					

Table 1.4.7. Shock-wave energy in a reservoir with water level $H_b = 3$ m, explosion depth $H = 0.0$ m, $M = 100$-kg TNT.

No. test/H_b/H	R, m	h, m	E_+, Kg-m/m²	E_{+mid}, kg-m/m²	E_f, kg-m/m²	E_{1mid}, kg-m	E_{mid}, kg-m	E_{mid}/ $E_{0,\%}$
23/3/0.0	15	0.25	15	113	14405	31877	32377	0.078
23/3/0.0	15	0.5	24.4					
23/3/0.0	15	1.0	66					
23/3/0.0	15	1.5	67.8					
23/3/0.0	15	1.5	103.2					
23/3/0.0	15	2.0	158.8					
23/3/0.0	15	2.5	248					
23/3/0.0	15	2.75	220.4					
23/3/0.0	30	0.25	1.26	10.75	840	6095	5697	0.014
23/3/0.0	30	0.5	2.45					
23/3/0.0	30	1.5	11.1					
23/3/0.0	30	2.0	11.4					
23/3/0.0	30	2.5	27.3					
23/3/0.0	30	2.75	11.0					

Table 1.4.8. Shock-wave energy in a reservoir with water level $H_b = 3$ m, explosion depth $H = 0.25$ m, $M = 100$-kg TNT.

No. test/H_b/H	R, m	h, m	E_+, kg-m/m²	E_{+mid}, kg-m/m²	E_f, kg-m/m²	E_{1mid}, kg-m	E_{mid}, kg-m	E_{mid}/ $E_{0,\%}$
25/3/0.25	7.5	0.25	523.4	2663	14405	376282	383010	0.916
25/3/0.25	7.5	0.5	1316					
25/3/0.25	7.5	1.5	2517					
25/3/0.25	7.5	2.0	4146					
25/3/0.25	7.5	2.5	3977					
25/3/0.25	7.5	2.75	3500					
18/3/0.25	15	0.25	24.2	32.9	3479	9298		-
18/3/0.25	15	0.50	41.5					
25/3/0.25	22.5	0.25	8.99	51.4	1515	21810	23182	0.056
25/3/0.25	22.5	0.5	23.1					
25/3/0.25	22.5	1.5	87.5					
25/3/0.25	22.5	2.0	87					
25/3/0.25	22.5	2.5	85					
25/3/0.25	22.5	2.75	17					
18/3/0.25	30	0.25	2.53	19.6	840	11090	10572	0.025
18/3/0.25	30	0.5	5.02					
18/3/0.25	30	1.5	17.3					
18/3/0.25	30	2.0	36.1					
18/3/0.25	30	2.5	29.6					
18/3/0.25	30	2.75	27.2					

Table 1.4.9. Shock-wave energy in a reservoir with water level H_b = 3 m, explosion depth H = 0. 5 m, M = 100-kg TNT.

No. test/H_b/H	R, m	h, m	E_+, kg-m/m^2	E_{+mid}, kg-m/m^2	E_f, kg-m/m^2	E_{1mid}, kg-m	E_{mid}, kg-m	E_{mid}/ E_0, %
26/3/0.5	7.5	0.25	1150	4669	14405	659771	610569	1.46
26/3/0.5	7.5	0.5	3208					
26/3/0.5	7.5	1.0	5467					
26/3/0.5	7.5	1.5	9653					
26/3/0.5	7.5	1.5 .	8277					
26/3/0.5	7.5	2.0	5254					
26/3/0.5	7.5	2.5	2634					
26/3/0.5	7.5	2.75	1712					
19/3/0.5	15	0.25	59.7	563	3479	159167	159153	0.381
19/3/0.5	15	0.5	186					
19/3/0.5	15	1.5	705					
19/3/0.5	15	2.0	949					
19/3/0.5	15	2.5	723					
19/3/0.5	15	2.75	756.4					
26/3/0.5	22.5	0.25	29.5	228	1515	96610	95227	0.228
26/3/0.5	22.5	0.5	81.7					
26/3/0.5	22.5	1.0	154.6					
26/3/0.5	22.5	1.5	255					
26/3/0.5	22.5	1.5	285					
26/3/0.5	22.5	2.0	338					
26/3/0.5	22.5	2.5	382					
26/3/0.5	22.5	2.75	297					
19/3/0.5	30	0.25	6.9	44.4	840	25095	24810	0.059
19/3/0.5	30	0.5	12.9					
19/3/0.5	30	1.0	30.9					
19/3/0.5	30	1.5	66.6					
19/3/0.5	30	1.5	68.3					
19/3/0.5	30	2.0	100					
19/3/0.5	30	2.5	37.2					
19/3/0.5	30	2.75	32					

Table 1.4.10. Shock-wave energy in a reservoir with water level $H_b = 3$ m, explosion depth $H = 1$ m, $M = 100$-kg TNT.

No.test/H_b/H	R, m	h, m	E_+, kg-m/m^2	E_{+mid}, kg-m/m^2	E_f, kg-m/m^2	E_{1mid}, kg-m	E_{mid}, kg-m	E_{mid}/E_0, %
27/3/1.0	7.5	0.25	1961	6518	14405	921045	906887	2.17
27/3/1.0	7.5	0.5	3894					
27/3/1.0	7.5	1.0	7018					
27/3/1.0	7.5	1.5	8723					
27/3/1.0	7.5	1.5	10278					
27/3/1.0	7.5	2.0	7236					
27/3/1.0	7.5	2.5	2634					
27/3/1.0	7.5	2.75	1712					
20/3/1.0	15	0.25	183	875	3479	247416	260004	0.622
20/3/1.0	15	0.5	328					
20/3/1.0	15	1.5	1678					
20/3/1.0	15	2.0	1139					
20/3/1.0	15	2.5	1020					
20/3/1.0	15	2.75	797					
27/3/1.0	22.5	0.25	32	225	1515	95732	96529	0.23
27/3/1.0	22.5	0.5	83					
27/3/1.0	22.5	1.0	190					
27/3/1.0	22.5	1.5	226.4					
27/3/1.0	22.5	1.5	210					
27/3/1.0	22.5	2.0	324					
27/3/1.0	22.5	2.5	417					
27/3/1.0	22.5	2.75	324.4					
20/3/1.0	30	0.25	11.1	93.2	840	52678	61706	0.148
20/3/1.0	30	0.5	38					
20/3/1.0	30	1.0	44					
20/3/1.0	30	1.5	164					
20/3/1.0	30	1.5	130					
20/3/1.0	30	2.0	172					

Table 1.4.11. Shock-wave energy in a reservoir with water level $H_b = 3$ m, explosion depth $H = 1.5$ m, $M = 100$-kg TNT.

No. test/H_b/H	R, m	h, m	E_+, kg-m/m^2	E_{+mid}, kg-m/m^2	E_f, kg-m/m^2	E_{1mid}, kg-m	E_{mid}, kg-m	E_{mid}/E_0, %
28/3/1.5	7.5	0.25	3111	6944	14405	981138	936254	2.24
28/3/1.5	7.5	0.5	4370					
28/3/1.5	7.5	1.0	9477					
28/3/1.5	7.5	1.5	10219					
28/3/1.5	7.5	1.5	8571					
28/3/1.5	7.5	2.0	4801					
28/3/1.5	7.5	2.5	6964					
28/3/1.5	7.5	2.75	8036					
21/3/1.5	15	0.25	290	673	3479	190286	213174	0.51
21/3/1.5	15	0.5	700					
21/3/1.5	15	1.5	1343					
21/3/1.5	15	2.0	843					
21/3/1.5	15	2.5	478					
21/3/1.5	15	2.75	386					
28/3/1.5	22.5	0.25	79.6	267	1515	113142	106279	0.254
28/3/1.5	22.5	0.5	138					
28/3/1.5	22.5	1.0	219					
28/3/1.5	22.5	1.5	398					
28/3/1.5	22.5	1.5	503					
28/3/1.5	22.5	2.0	376					
28/3/1.5	22.5	2.5	239					
28/3/1.5	22.5	2.75	181					
21/3/1.5	30	0.25	39.8	100	840	56614	53334	0.128
21/3/1.5	30	0.5	95.7					
21/3/1.5	30	1.0	148					
21/3/1.5	30	1.5	170					
21/3/1.5	30	1.5	179.2					
21/3/1.5	30	2.0	103					
21/3/1.5	30	2.5	38.9					
21/3/1.5	30	2.75	26.3					

Table 1.4.12. Shock-wave energy in a reservoir with water level $H_b = 3$ m, explosion depth $H = 2$ m, $M = 100$-kg TNT.

No. test/H_b/H	R, m	h, m	E_+, kg-m/m^2	E_{+mid}, kg-m/m^2	E_f, kg-m/m^2	E_{1mid}, kg-m	E_{mid}, kg-m	E_{mid}/E_0, %
24/3/2.0	7.5	0.25	3343	6630	14405	936765	910266	2.18
24/3/2.0	7.5	0.5	7169					
24/3/2.0	7.5	1.5	10319					
24/3/2.0	7.5	2.0	9606					
24/3/2.0	7.5	2.5	4718					
24/3/2.0	7.5	2.75	4624					

24/3/2.0	22.5	0.25	80.5	200	1515	84690	97608	0.23
24/3/2.0	22.5	0.5	162					
24/3/2.0	22.5	1.5	471					
24/3/2.0	22.5	2.0	328					
24/3/2.0	22.5	2.5	115					
24/3/2.0	22.5	2.75	42					

Table 1.4.13. Shock-wave energy in a reservoir with water level $H_b = 3$ m, explosion depth $H = 2.75$ m, $M = 100$-kg TNT.

No. test/H_b/H	R, m	h, m	E_+, kg-m/m^2	E_{+mid}, kg-m/m^2	E_f, kg-m/m^2	E_{1mid}, kg-m	E_{mid}, kg-m	E_{mid}/ E_0, %
29/3/2.75	7.5	0.25	878	1521	14405	214921	208824	0.50
29/3/2.75	7.5	0.5	2108					
29/3/2.75	7.5	1.0	2424					
29/3/2.75	7.5	1.5	2353					
29/3/2.75	7.5	1.5	1819					
29/3/2.75	7.5	2.0	1591					
29/3/2.75	7.5	2.5	524					
29/3/2.75	7.5	2.75	471					
22/3/2.75	15	0.25	484	562.4	3479	155925	149146	0.357
22/3/2.75	15	0.5	701					
22/3/2.75	15	1.0	864					
22/3/2.75	15	1.5	990					
22/3/2.75	15	1.5	709					
22/3/2.75	15	2.0	486					
22/3/2.75	15	2.5	179					
22/3/2.75	15	2.75	86.2					
29/3/2.75	22.5	0.25	21.5	56.8	1515	24087	22944	0.055
29/3/2.75	22.5	0.5	53.7					
29/3/2.75	22.5	1.0	80.9					
29/3/2.75	22.5	1.5	79.1					
29/3/2.75	22.5	1.5	109					
29/3/2.75	22.5	2.0	63.7					
29/3/2.75	22.5	2.5	28.5					
29/3/2.75	22.5	2.75	18.2					
22/3/2.75	30	0.25	21.1	35	840	19785	19000	0.046
22/3/2.75	30	0.5	42.8					
22/3/2.75	30	1.0	52.9					
22/3/2.75	30	1.5	23.3					
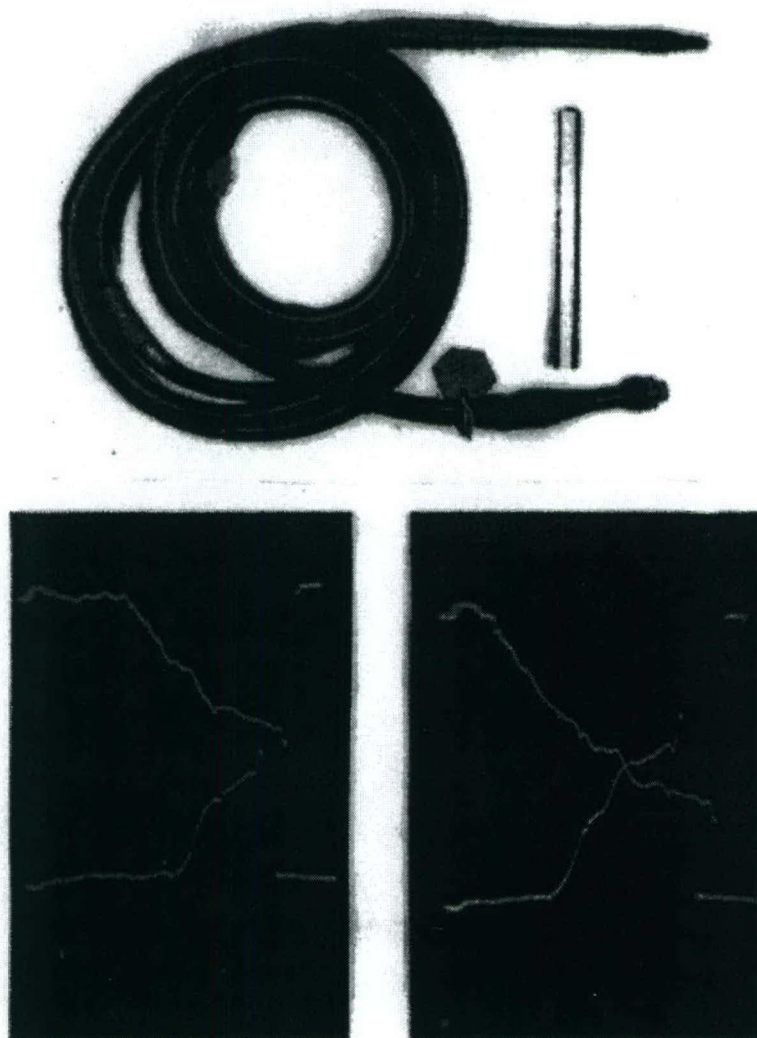
Figure 1.4.1. Photographs of a piezoelectric gauge (PID-9) and example of oscillograph records.
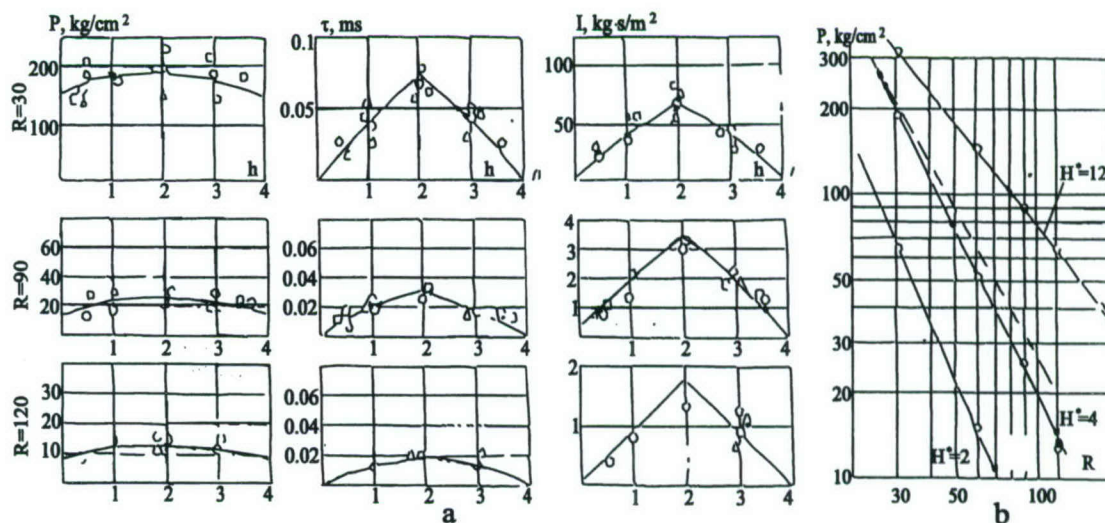
Figure 1.4.2. (a) Shock-wave parameters as functions of sensor depth in the reservoir with sand on the bottom, water level $H_b = 4R_0$. (b) Shock-wave peak overpressure as a function of range, explosions in the middle of the reservoir, water levels $H^* = 2R_0, 4R_0, 12R_0$. Depth and ranges are given in units of charge radius $R_0 = 0.25$ cm.
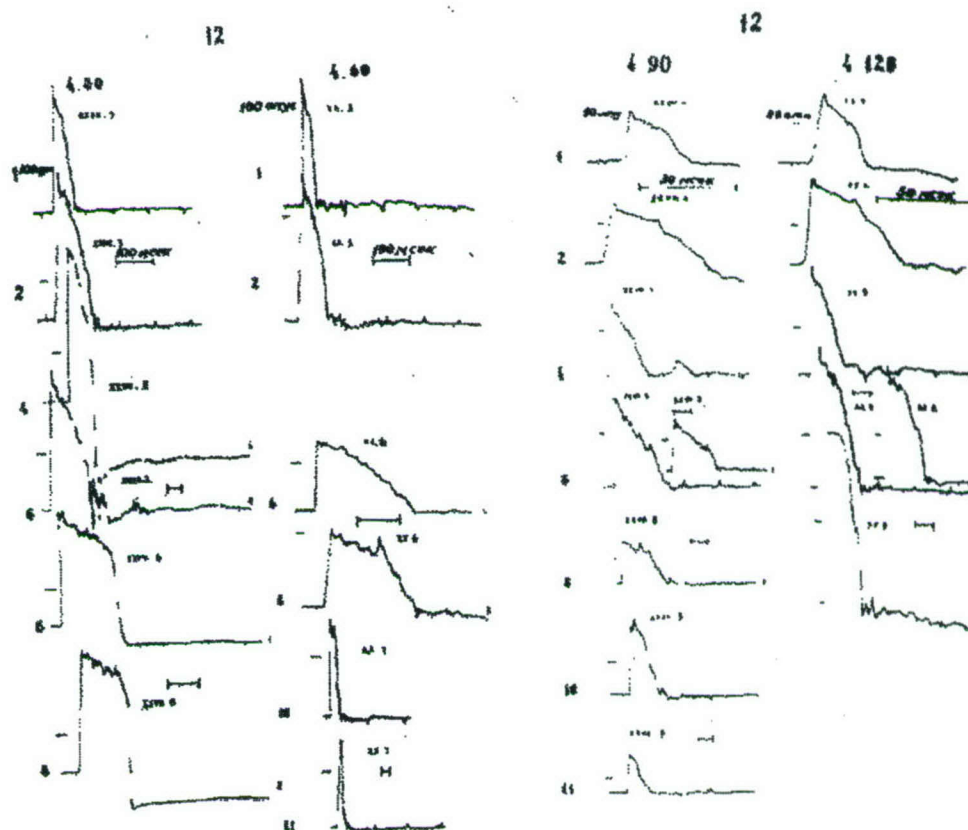
Figure 1.4.3. Oscillogram records of shock waves recorded with gauges PID-9. Water level $= 12 R_0$. Digits marking figures show explosion depth and distance between explosion and gauge in units of charge radius $R_0 = 0.25$ cm (e.g., 4.30 means explosion depth $4R_0$ and distance $30R_0$).
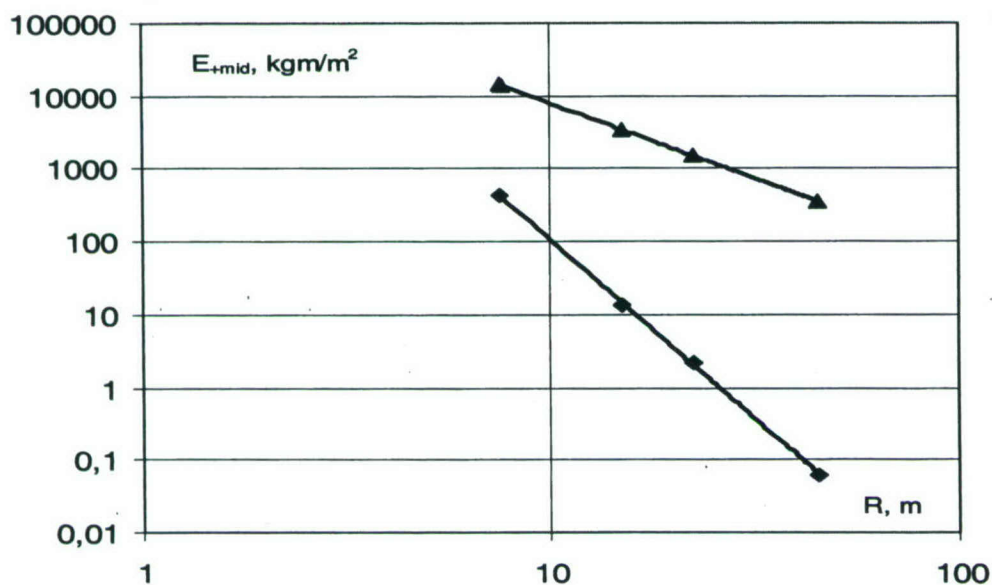
Figure 1.4.4. Shock-wave specific energy E_{+mid} (diamonds) averaged over measurements at different sensor depths, versus distance between explosion and sensor, R. Explosion depth 0.75 m, water level 1 m. Triangles denote specific energy (energy density flux) E_f, calculated using Cole's formula for boundless water.
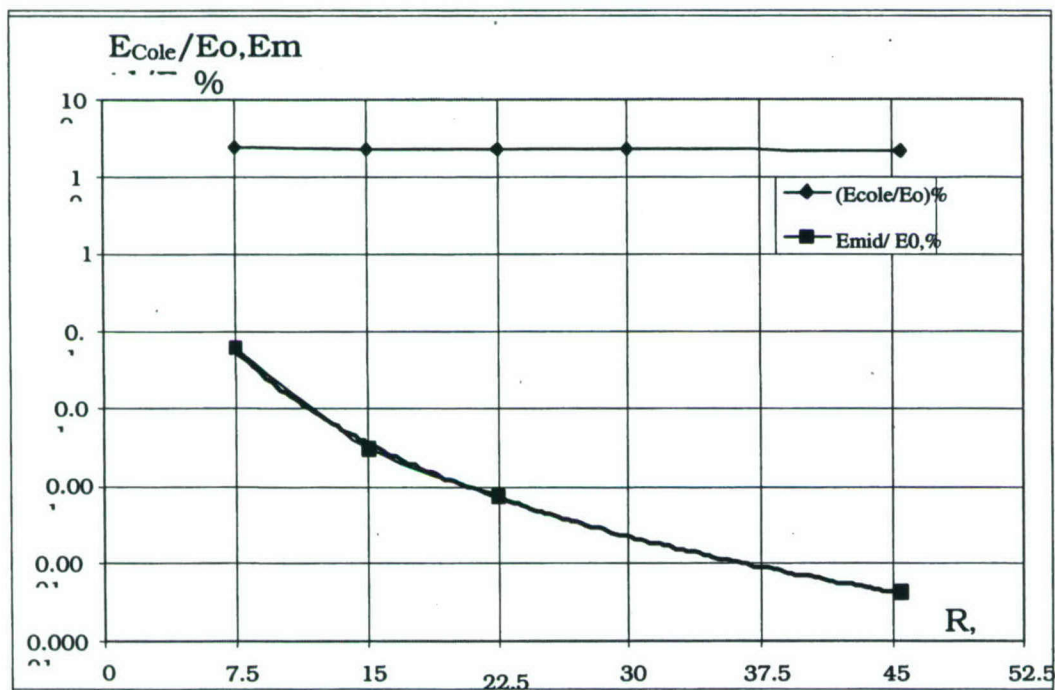
Figure 1.4.5. Dependence of E_{mid}/E_0 (squares) on distance R. Explosion depth 0.75 m, water level 1 m. Diamonds show E_{Cole}/E_0 for boundless water.
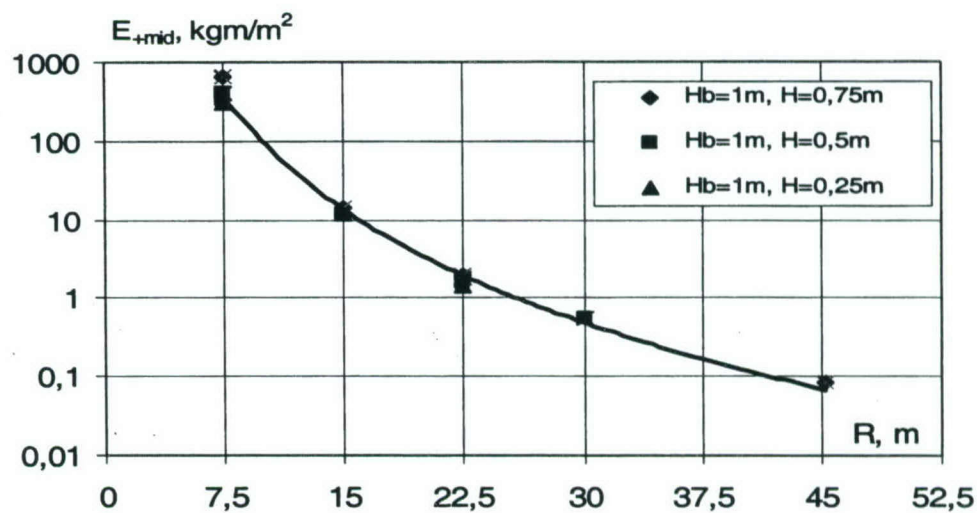
Figure 1.4.6. Dependence of shock-wave specific energy $E_{+\,mid}$ on distance R. Explosion depths 0.25, 0.5, and 0.75 m. Water 1 m.
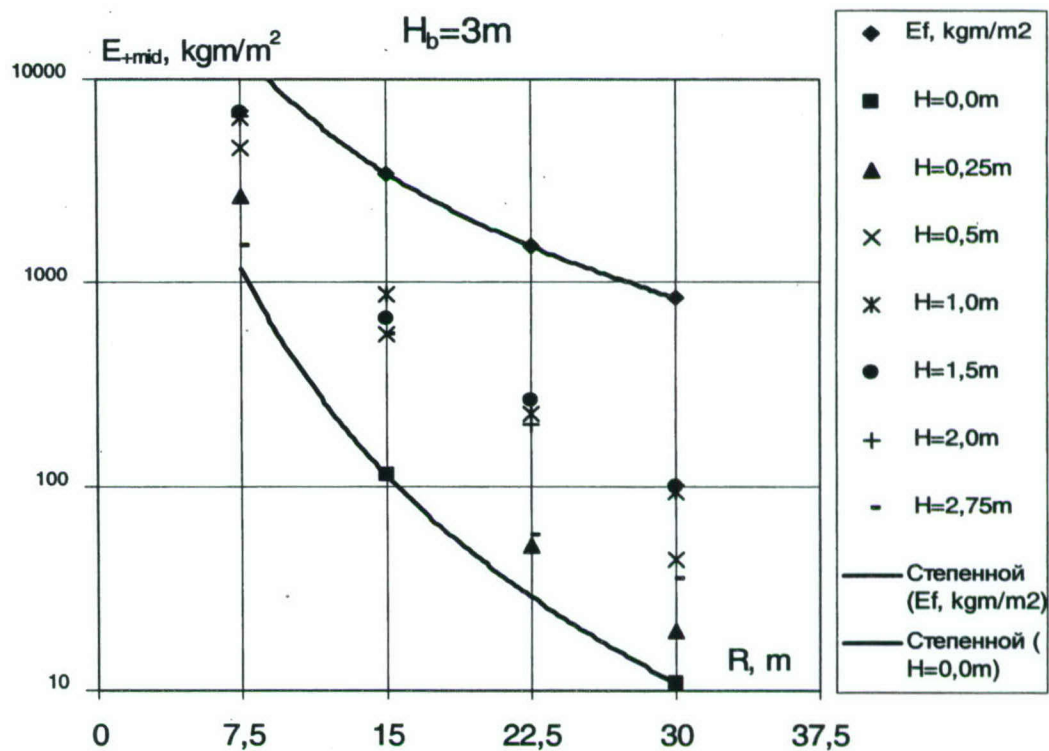
Figure 1.4.7. Dependence of shock-wave specific energy $E_{+\,mid}$ on distance R. Explosion depths 0.0, 0.25, 0.5, 1.0, 1.5, 2.0, and 2.75 m. Water level 3 m.

A-60
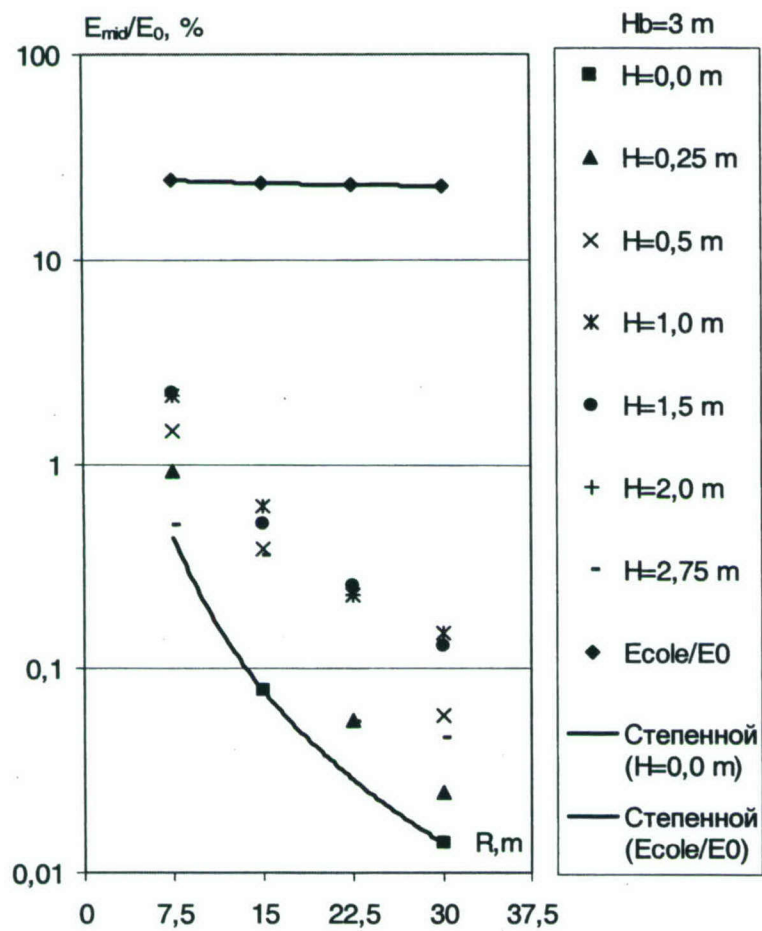
Figure 1.4.8.   Dependence of E_{mid}/E_0 % on distance R. Explosion depths H = 0.0, 0.25, 0.5, 1.0, 1,.5, 2,.0, and 2.75 m. Water level 3 m. E_{Cole}/E_0 is calculated for boundless water.

1.5 Shock-wave parameters in air from underwater explosions in shallow reservoirs

The parameters of air shock waves from underwater explosions of 100-kg TNT cast spherical charges were measured using two piezoelectric gauges. The gauges were calibrated using a hydraulic press to determine the static sensitivity coefficient, S_s, and explosions to determine the dynamic sensitivity coefficient, S_d. In the first case, the sensor was immersed in a container with water, where the pressure was increased by 10-atm increments, usually up to 80 atm. The pressure was then abruptly (within 1 msec) decreased to zero. The voltage from the gauge was registered with an oscillograph of input electric capacity, $C = 157$ pF. The gauge signal is determined by $U = SP/C$, where U is in [mV], S is the sensitivity of the gauge in [mV*pF/atm] (either static, S_s, or dynamic, S_d), and P is the pressure in [atm]. The parameters of the gauges used are shown in Table 1.5.1 below.

Table 1.5.1. Parameters of air gauges.

№	S_d, mV pF/atm	S_s, mV pF/atm	C, pF
9	47.5	50.6	157
12	50.5	51.6	157
14	47.0	51.2	157
27	47.7	51.6	157

The scheme of sensor installation is shown in Figure 1.5.1. In all explosion experiments the time of registration was 34 ms and the wavelength about 10-16 ms. The gauges were installed within 4 to 5 m of each other. The interval between time marks on the oscillograms is 1 ms. Examples of oscillograms of air shock waves recorded on the bank of the reservoir are shown in Figure 1.5.2. Digitized records are available in MS Excel files (Ch15_7_26_025, Ch15_11_28_0, Ch15_12_204_05, etc. Sheet names show test number, distance to sensor, and charge depth as in the following example: Ch15_7_26_025 - Chapter 1.5, test No. 7, explosion-sensor distance 26 m, charge depth 0.25 m).

The explosions were photographed at different frequencies using high-speed cameras. These photographs were further used for a near-filed characterization of the parameters of surface phenomena and waves refracted into air.

Table 1.5.2 shows from left to right: test number; water level; charge depth; distance R between charge and sensor; measured peak overpressure ΔP_m; measured specific impulse I; measured duration τ; specific energy E calculated in acoustic approximation; calculated total energies E_1 (in MJ) and E_2 (in kg TNT); and E_2/E_0 for shock waves, where E_0 is the energy of explosion. Both E_1 and E_2 are calculated form $2\pi E R^2$, with appropriate change in units. To compute the quantities in the two last columns, the following considerations were used. The explosion energy of 1 kg TNT was taken as 4.18 MJ $= 4.18*10^6$ J, hence the (specific?) heat of explosion is 4.18 MJ/kg. Also, 1 kgm = 10 J = (10 J)/(4.18 MJ/kg) = $2.39*10^{-6}$ kg TNT. Thus, the values in the column under E_2 were obtained by dividing the values in the column under E_1 by 4.18 MJ. Similarly, for 100 kg TNT, $E_0 = 418$ MJ, hence the percentage values in the last column.

Table 1.5.2. Parameters of air shock waves from the 100-kg TNT underwater explosions.

No test	Water level, m	Charge depth, m	Distance, m	ΔP_m, kg/cm^2	I, kgs/m^2	τ, ms	E, kgm/m^2	E_1, MJ	E_2, kg TNT	E_2/E_0 %
1	1	0.75	17.4	0.124	6.67	15	124.6	2.37	0.56	0.56
				0.138	6.3	15	115.2	2.19	0.523	0.523
2	1	0.75	12.6	0.13	5.92	15	102	1.02	0.244	0.244
			17.4	0.16	7.2	15	155	2.95	0.705	0.705
3	1	0.75	13.2	0.12	7.2	14.9	123	1.35	0.32	0.32
14	1	0.75	15	0.16	6.9	14.7	145	2.05	0.489	0.49
			19	0.13	6.1	14.5	107.8	2.44	0.583	0.58
15	1	0.75	16.4	0.175	7.8	14.7	183.1	3.09	0.739	0.74
			20.7	0.165	5.7	13.6	104.6	2.82	0.674	0.67
4	1	0.5	14	0.36	8	10.0	289	3.55	0.85	0.85
			17.5	0.28	9.5	11.5	338	6.5	1.55	1.55
5	1	0.5	17.4	0.32	10.1	11.2	412	7.83	1.87	1.87
			21	0.23	8.6	12.5	251	6.94	1.66	1.66
12	1	0.5	20.4	0.28	8.1	12.9	275	7.18	1.72	1.72
			24	0.26	8.1	12.1	239	8.65	2.07	2.07
13	1	0.5	25	0.21	6.8	12.8	170	6.67	1.59	1.59
			29	0.165	5.05	12.0	99.4	5.25	1.26	1.26
9	0.5	0.25	22	0.45	13.5	11.8	719	21.8	5.22	5.22
			26	0.39	12.9	12.9	598	25.4	6.07	6.07
7	0.95	0.25	21	0.39	12.64	12	608	16.8	3.87	3.87
			26	0.31	11.8	16	379	16.1	3.84	3.84
8	0.95	0.25	20.5	0.42	13.9	11.9	745	19.7	4.70	4.70
			25.6	0.32	10.2	11.6	417	17.2	4.11	4.11
16	1	0.25	30	0.26	10.2	14.3	332	18.8	4.49	4.49
			35	0.22	9.2	14.9	258	19.9	4.74	4.74
17	1	0.25	26	0.32	11.8	13.6	464	19.7	4.7	4.7
			30	0.27	10.9	14.8	366	20.7	4.95	4.95
18	3	0.25	28	0.24	6.9	13.4	169	8.34	1.99	1.99
			29	0.265	10.9	14.8	366	19.3	4.62	4.62
25	3	0.25	31	0.2	10.1	14.8	291	17.6	4.19	4.19
			33	0.23	12.6	16.0	320	21.9	5.23	5.23
10	0.25	0	26	0.35	16	14.2	727	30.9	7.37	7.37
			29.9	0.36	10.6	12.9	514	28.9	6.9	6.9
11	0.25	0	28	0.5	27.5	17.9	1882	92.6	22	22
			31	0.46	18	14.0	1032	62.3	14.9	14.9
23	3	0	32	0.3	11	13.5	405	26.1	6.23	6.23
			36	0.26	10.8	12.4	403	32.8	7.82	7.82

(Note: In B. Khristoforov's opinion, the high values for the energy E in explosion No. 11 are not in error, as the remaining shock wave parameters for this explosion are also higher. Other data for from this test will be re-examined, such as photographs of the explosion cloud).

In addition to the 100-kg TNT explosions, laboratory tests were carried out detonating spherical charges of pressed PETN (5.85 MJ/kg), each with a radius $R_0 = 3$ mm, in the center of a cylindrical steel basin. The diameter of the basin was 300 mm and its length 92 mm. It was filled with 80-mm thick sand layer covered by 12 mm of water (i.e., 4 charge radii R_0). The explosion depths in these experiments were $H = 0, 1, 2$, and $3R_0$ (i.e., 0 mm, 3 mm, 6 mm, and 9 mm). The explosions were photographed with a high-speed camera with frequency of 125,000 frames/sec using the half-shadow method. The charge density and weight were 1.5 g/cm^3 and 0.17 g, respectively. This weight is equivalent to an explosion of 0.218 g TNT. The spherical charges in these experiments were prepared using a special procedure to assure similarity with larger explosions. First PETN was dissolved in acetone. Then water was added to induce precipitation in the form of "snowflakes", which were extracted and dried up, forming a powder-like substance. The grain size of the powder was very small, of the order of microns, thus assuring good detonation characteristics for the small charges and complete explosive transformation (?). The pressed PETN was further dipped in steam-soften paraffin, in order to cover the charges with a thin water-resistant film. The charges were then suspended at various depths in the water tank, using electric impulses to push them towards the center of the basin.

Figs. 1.5.3 and 1.5.4 show half-shadow photographs of the PETN laboratory explosions with charge depths 1, 2 and $3R_0$. Figure 1.5.5 shows the speed of air shock waves measured from the half-shadow photographs versus the distance from the charge. Figure 1.5.6 illustrates the dependence of peak overpressure ΔP_m in air on the scaled distance from the charge, R/R_0, for different explosion depths. These are compared with calculated values using the empirical formula of M.A. Sadovsky for an explosion in air [1, 2]:

$$\Delta P_{m \ Calc} = 14.3/(R/R_0) + (907/(R/R_0)^2) + (43600/(R/R_0)^3) \tag{1}$$

where the peak pressure is calculated in [kg/cm^2]. (Note: the original Sadovsky's formula features $R/q^{1/3}$ [m/kg$^{1/3}$] instead of R/R_0; formula (1) above is modified by B. Khristoforov).

Table 1.5.3a, b shows scaled weights and radii M_{equ}, R_{equ} (as R_{equ}/R_0, M_{equ}/M_0) of the equivalent charges which if detonated in air, would yield the same peak overpressure ΔP_m at the same distances R, as a charge of weight M_0 or radius R_0 detonated underwater. The overpressure ΔP_m Calc from an air explosion was calculated using formula (1) as above. All these were computed for different charge depths, as indicated in the table.

Table 1.5.3a. Peak overpressure ΔP_m of shock waves in air, R_{eku}/R_0, and M_{equ}/M_0 versus dimensionless distance R/R_0 from underwater explosions of 0.17-g PETN charges, detonated at depths H = 0, 1, 2 and $3R_0$ in a basin of depth $4R_0$.

R/R₀	Blasts in air $\Delta P_{m\ Calc}$, kg/cm²	H=0 R₀ ΔP_m, kg/cm²	R_{equ}/R_0	M_{equ}/M_0	H=1 R₀ ΔP_m kg/cm²	R_{equ}/R_0	M_{equ}/M_0
16	15.08				1.41	0.375	0.053
20	8.43				1.23	0.438	0.084
25	4.81	3.14	0.838	0.587	1.05	0.51	0.133
30	3.1	2.37	0.89	0.71	0.92	0.577	0.193
35	2.17	1.91	0.95	0.86	0.83	0.641	0.263
40	1.61	1.53	0.975	0.927	0.74	0.69	0.326
50	1.00	1.10	1.043	1.14	0.63	0.794	0.50
60	0.69	0.84	1.1	1.342	0.53	0.87	0.66

Table 1.5.3b (continuation of table 1.5.3a)

R/R₀	H=2 R₀ ΔP_m, kg/cm²	R_{equ}/R_0	M_{equ}/M_0	H=3 R₀ ΔP_m, kg/cm²	R_{equ}/R_0	M_{equ}/M_0
	0.675	0.263	0.0183			
6		0.308	0.0293	0.465	0.269	0.0194
4		0.363	0.048	0.401	0.311	0.030
1		0.413	0.0706	0.351	0.345	0.041
		0.472	0.105	0.312	0.377	0.053
1		0.503	0.127	0.274	0.396	0.062
2		0.567	0.182	0.225	0.438	0.084
8		0.641	0.263	0.189	0.47	0.104

Figure 1.5.7 shows the dependence of ΔP_m of air shock waves on R/R_0 for different charge depths from the 100-kg TNT underwater explosions and the PETN laboratory experiments. A comparison is shown with calculations from the empirical formula of M.A. Sadovsky for an explosion on ground [1, 2]:

$$\Delta P_{m\ Calc\ 2} = 17.9/(R/R_0) + (1390/(R/R_0)^2) + (87200/(R/R_0)^3) \qquad (2)$$

where pressure is in [kg/cm²]. (Note: Like formula (1), formula (2) has been modified by B. Khristoforov to include R/R_0 instead of $R/q^{1/3}$ in the original Sadovsky's formula).

Figs.1.5.8 to 1.5.13 show the dependence of energy of the shock wave in air on distance R from the 100-kg TN underwater explosions. Different charge depths are featured, as indicated in the figures.

Figs. 1.5.8 and 1.5.9 show these relationships for the specific energy E [kgm/m^2] and the ratio E_2/E_0. As an example, as the explosion depth decreases from 0.75 to 0.25 m, the specific energy E of the shock wave in air at distance R = 22.5 m increases almost 7 times. As the distance R increases, the energy E first increases due to additional transfer of energy from the water shock wave, and then decreases because of the predominant influence of the expansion of the air shock wave. As the explosion depth decreases, the total energy of the shock wave in air, $E_2 = 2\pi R^2 E$, increases, along with the specific energy E. For shallow charge depths (i.e., H=0.25 m), E_2/E_0 increases slowly with distance.

Figure 1.5.10 shows the dependence of specific energy E on distance for a charge depth of 0.25 m, as the water level in the reservoir varies (0.5 m, 1 m, and 3 m). The specific energy E increases with decreasing reservoir depth. Figure 1.5.11 shows the same for a surface explosion (charge depth H = 0 m) and two basin depths (0.25 m and 3 m). The specific energy of shock waves in air increases as the water level in the reservoir decreases.

Figure 1.5.12 shows E_2/E_0 versus distance for a half-immersed charge (depth H = 0 m) in a reservoir with water levels H_b = 0.25 m and 3 m. As the water level in the basin decreases, the total energy transferred from the explosion into air increases. Similar results are seen in Figure 1.5.13 for charge depth 0.25 m in a reservoir with varying water level (3 m, 1 m, and 0.5 m).

Bibliography

[1] Яковлев Ю.С. Гидродинамика взрыва. 1963 Ленинград. Судпромгиз.
(Yakovlev, Y. S., *Explosion Hydrodynamics*, 1963, Sudpromgiz Publ., Leningrad)

[2] Садовский, М.А., Геофизика и физика взрыва, М., Наука, 1999, 355 с.
(Sadovsky, M.A., *Geophysics and Physics of Explosion*, M., Nauka Publ., 1999, pp. 355.

Cut at AA
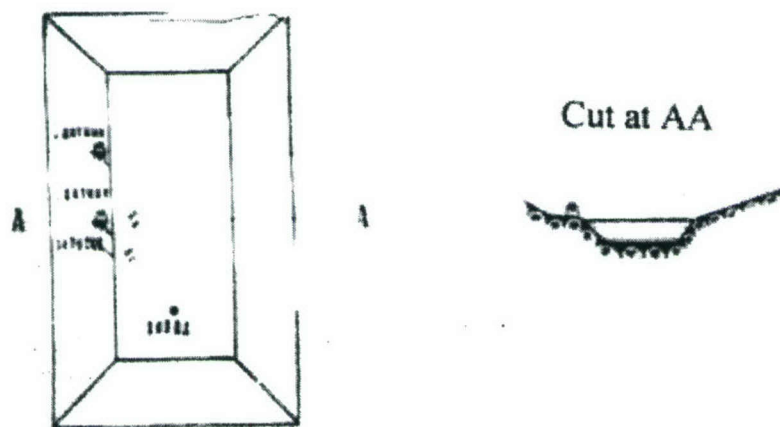
Scheme installation of sensors
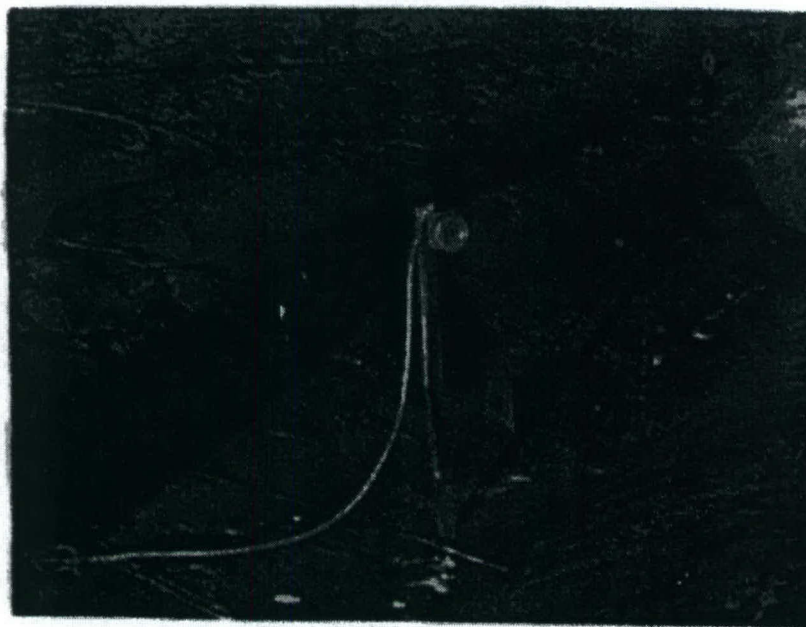
Figure 1.5.1. Scheme of sensor installation.
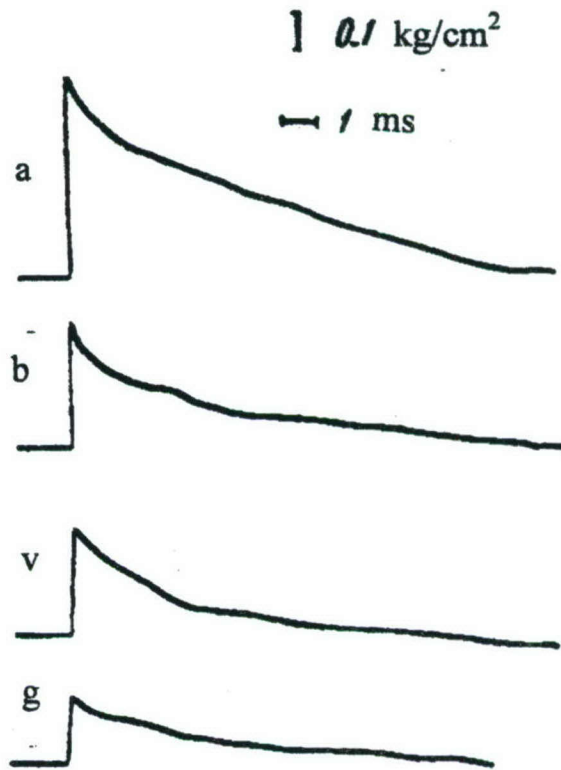
Figure 1.5.2. Oscillograph records of air shock waves from a 100-kg TNT explosion. Sensors placed on the bank of the reservoir, water level $H_b = 1$ m: (a) charge on ground, distance to sensor R=17.4 m; (b) underwater explosion with depth H = 0.25 m, distance to sensor R = 26 m; (v) H = 0.5 m, R = 20.4 m; (g) H = 0.75 m, R = 16.4 m.

Figure 1.5.3. Shadow photographs in air 160 μs after an underwater explosion of a spherical charge of 0.17 g PETN (equivalent to 0.218 g TNT). Explosion depths are (a) $1R_0$ and (b) $3R_0$. Basin depth (i.e., water level) is $4R_0$ ($R_0 = 3$ mm).
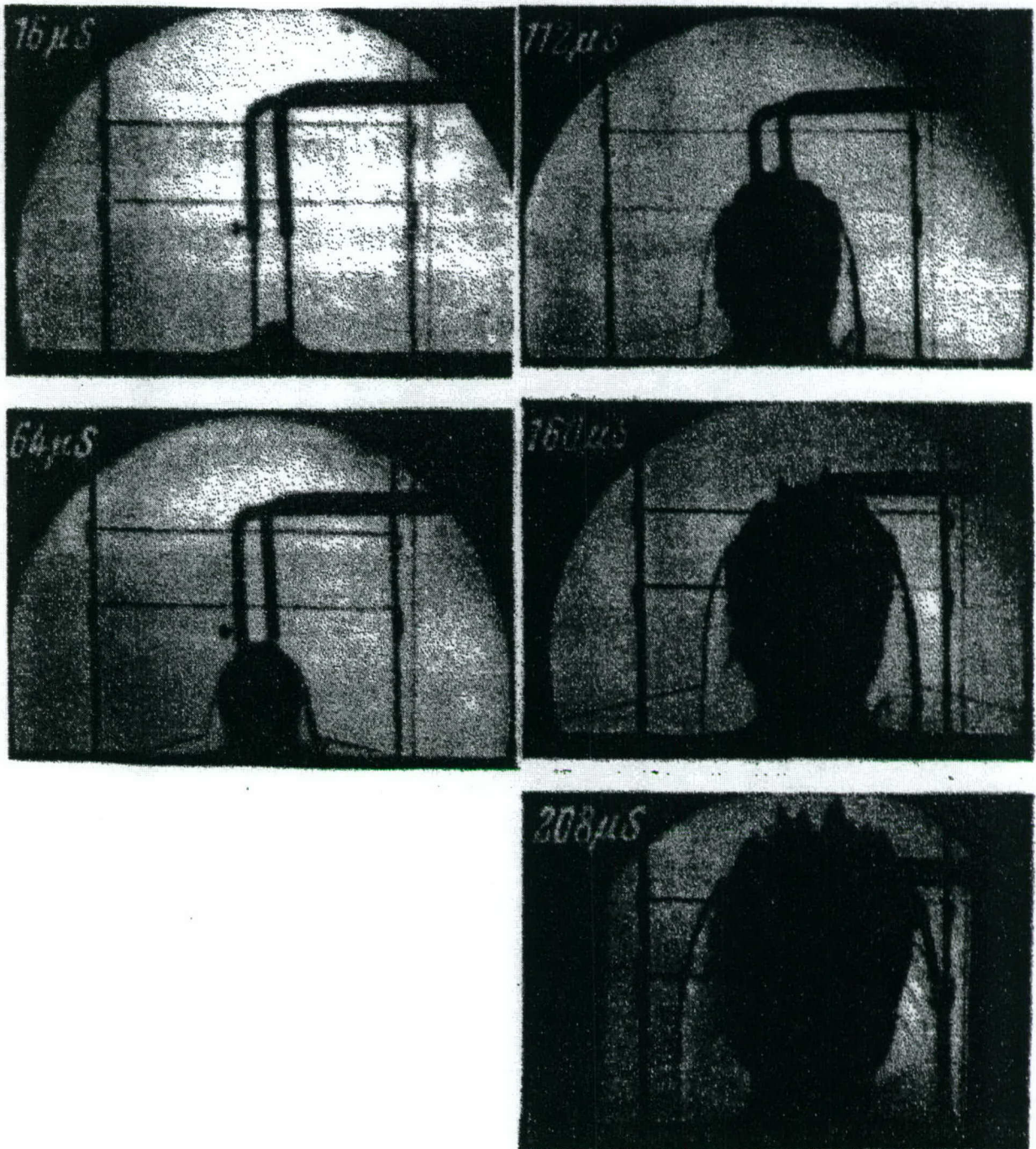
Figure 1.5.4.   Shadow photographs in air of an underwater explosion of a spherical charge of 0.17 g PETN at depth $2R_0$. Basin depth is $4R_0$ ($R_0 = 3$ mm). Times after explosion are shown in the upper left corners of the photographs.
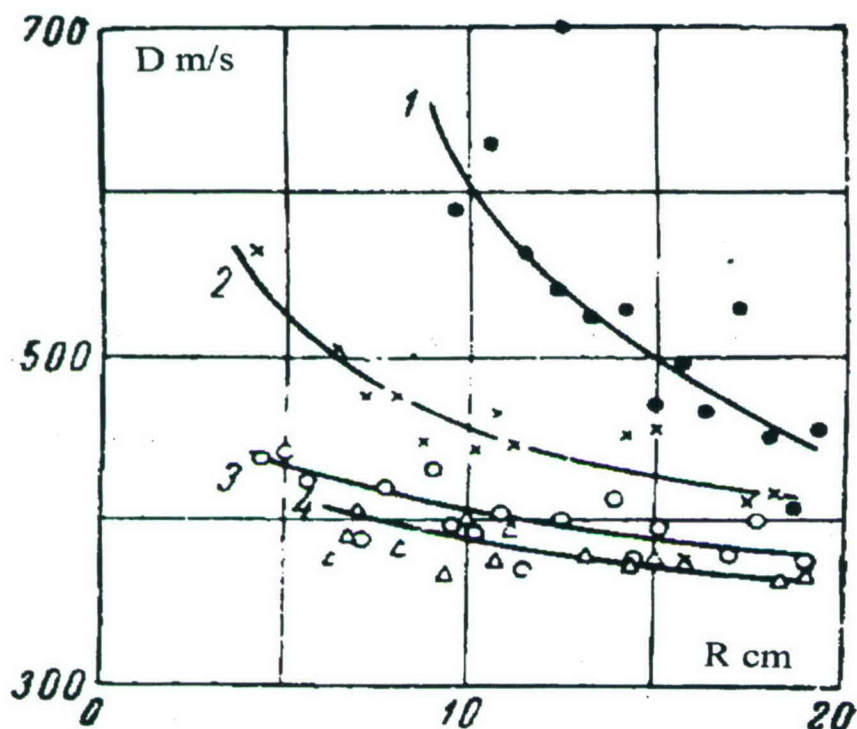
Figure 1.5.5.   Dependence of speed of air shock wave on distance from underwater explosions of spherical charges of 0.17 g PETN. Velocities were measured from high-speed photographs. Curves 1, 2, 3, and 4 denote explosion depths H = 0, 1, 2, and $3R_0$ (R_0 = 3 mm). Basin depth is $4R_0$.
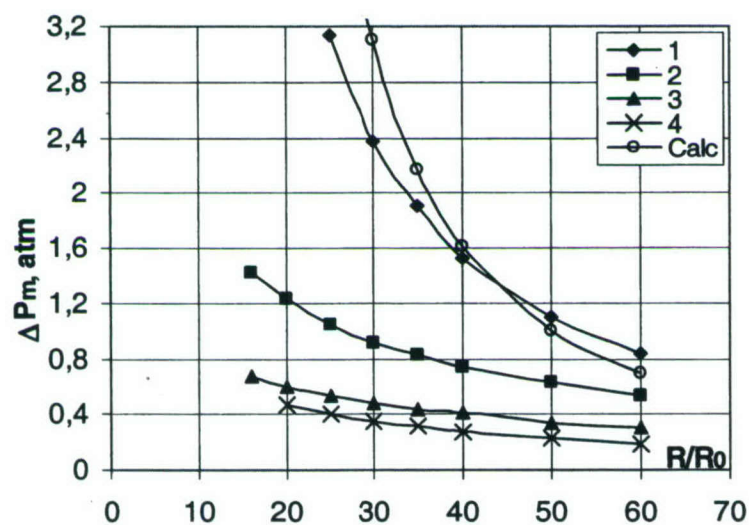
Figure 1.5.6.   Dependence of peak overpressure of air shock wave on scaled distance from underwater explosions of spherical charges of 0.17g PETN. Individual data, not shown here, were obtained through processing the velocity data from Figure 1.5.5. Fitted curves 1, 2, 3, and 4 correspond to explosion depths H = 0, 1, 2, and $3R_0$ (R_0 = 3 mm); Calc - denotes calculations for explosion in air, using modified formula (1) of M.A. Sadovsky [1, 2].
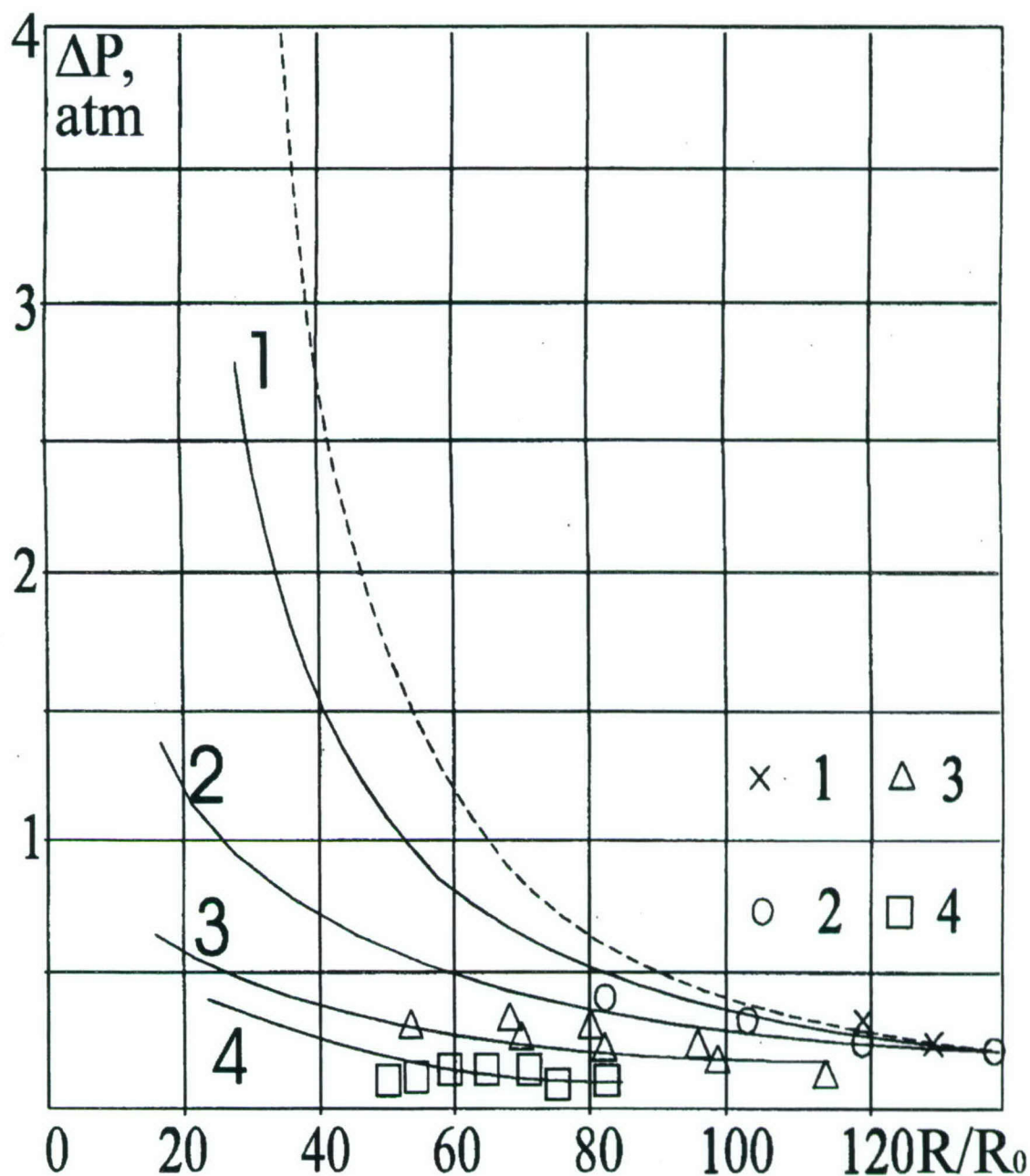
Figure 1.5.7. Dependence of peak overpressure of air shock wave on scaled distance R/R_0 for different explosion depths. Curves are based on the laboratory 0.17-g PETN data and are extended from the pressure curves shown in Figure 1.5.6 (individual PETN data are not shown). Symbols show data from the 100-kg TNT explosions. Data were obtained through processing of high-speed photographs for the PETN charges and were measured with gauges for the 100-kg TNT explosions. Curves 1, 2, 3, and 4 correspond to explosion depths $H = 0, 1, 2,$ and $3R_0$. Dashed line denotes calculated values from a ground explosion, using modified formula (2) of M. A. Sadovsky [1, 2].
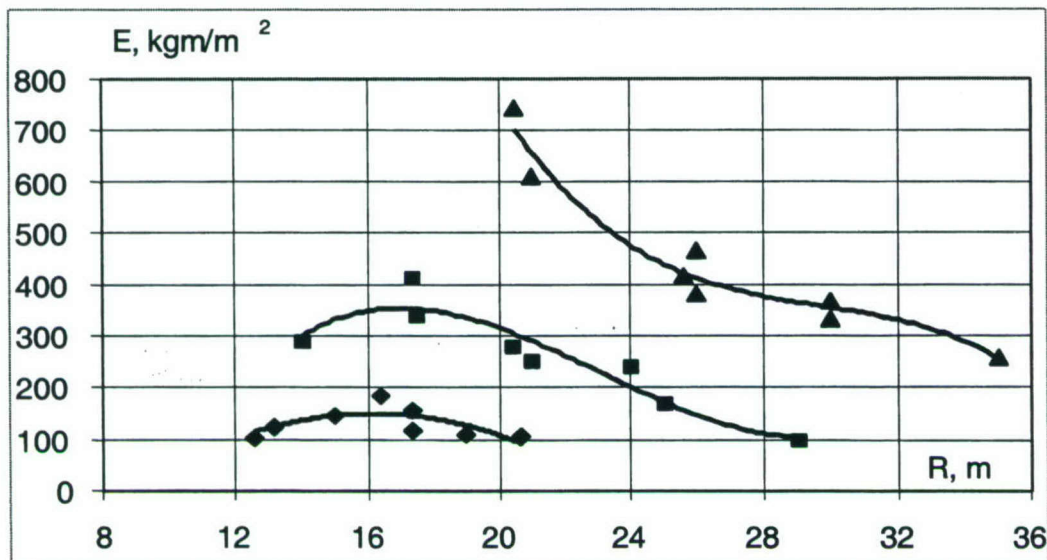
Figure 1.5.8. Dependence of specific energy of shock wave in air on distance from 100-kg TNT underwater explosions at depths H = 0.25 m (triangles), H = 0.5m (squares), and H = 0.75 m (rhombi) in a reservoir with water level 1 m.
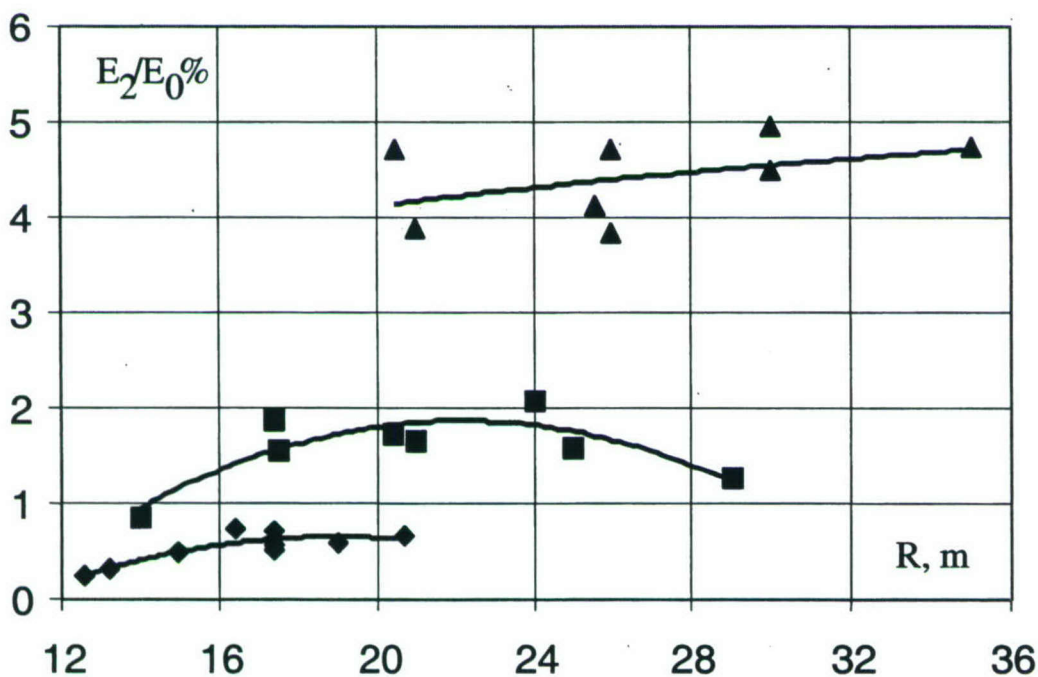
Figure 1.5.9. Dependence of the ratio of energy of air shock wave to energy of explosion, E_2/E_0, on distance from 100-kg TNT underwater explosions at depths H = 0.25 m (triangles), H = 0.5m (squares), and H = 0.75 m (rhombi). Water level in reservoir was 1 m.
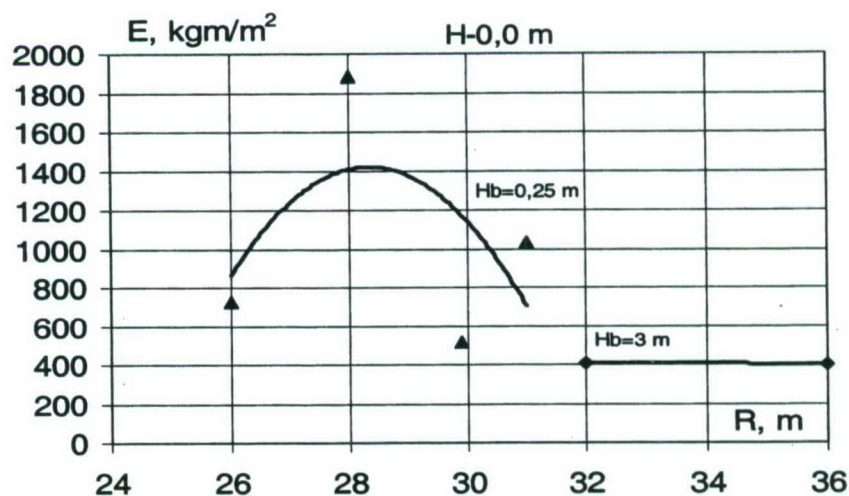
Figure 1.5.11.   Specific energy of shock wave in air versus distance from 100-kg TNT underwater explosions at depth H = 0.0 m (half-immersed); water level - 3 m (rhombi) and 0.25 m (triangles).
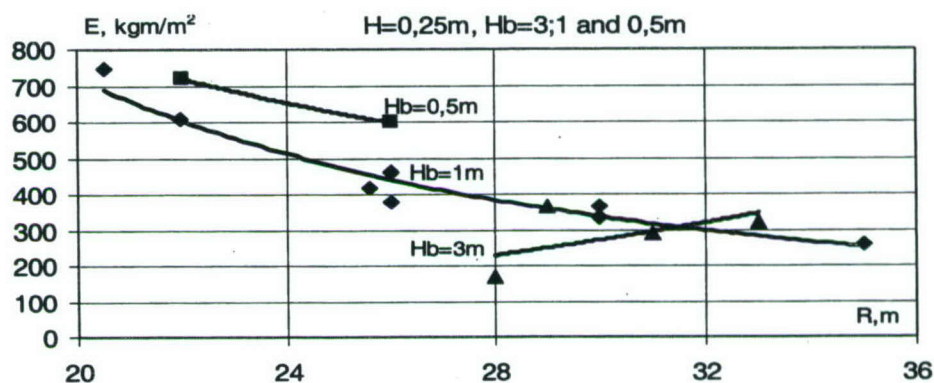
Figure 1.5.10. Dependence of specific energy of shock wave in air on distance from 100-kg TNT underwater explosions at depth H = 0.25 m. Water level in reservoir - 3 m (triangles), 1 m (rhombi) and 0.5 m (squares).
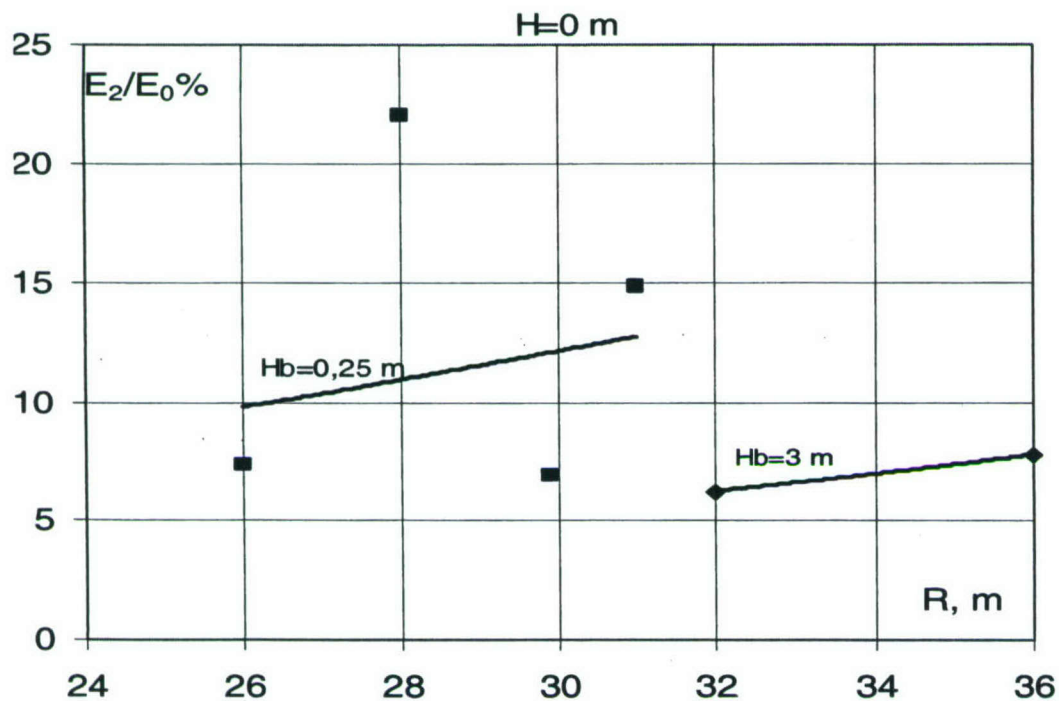
Figure 1.5.12. Dependence of the ratio of energy of shock wave to energy of explosion, E_2/E_0, on distance from underwater 100-kg TNT explosions at depth H = 0.0 m (half-immersed); water levels H_b = 0.25 m (squares) and H_b = 3.0 m (rhombi).
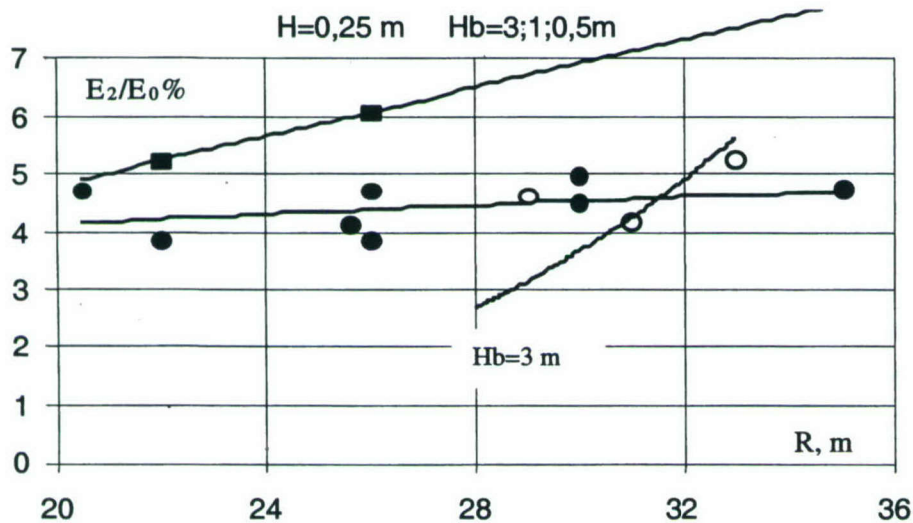
Figure 1.5.13. Dependence of the ratio of energy of shock wave to energy of explosion, E_2/E_0, on distance from 100-kg TNT underwater explosions at depth H = 0.25 m; water level - 3 m (open circles), 1 m (filled circles) and 0.5 m (squares).

1.6 Measurements in ground from underwater explosions of 100-kg TNT cast spherical charges in shallow reservoirs.

Ground measurements of the parameters of shock waves from the 100-kg TNT charges were made in the sand layer on the bottom of the reservoir (Table 1.6.1). Preliminary tests were carried out with 5-kg and 1-kg charges. The homogeneous sand layer on the bottom was about 3-m thick. A clay layer of thickness ~1 m and another layer of homogeneous sand laid beneath the upper sand layer. The velocities of longitudinal and shear sound waves (i.e., P- and S- waves) measured in the upper bottom layer were 270 and 100 m/s, respectively [Note by M. Eneva – as a reminder from previous chapters, the top air-saturated sand layer was characterized by a very low sound velocity, comparable to velocity in air]. These low speeds are due to the presence of air bubbles in the sand. The ground measurements were made from tests 1 to 11, for which the water level varied between 1 m and 0.25 m. The water was pumped out after each explosion, the crater was filled, and water was poured again before the next explosion. Measurements were made of wave and mass velocities, as well as of shock-wave overpressure. [Note by M. Eneva - see Chapter 1.4 for other details on these explosions].

Strain and piezoelectric gauges were used to measure the overpressure. Each piezoelectric gauge consisted of two circular plates of a 20-mm diameter and 2.5-mm thickness, with own frequency of 50 kHz. Static calibration was applied to the gauges. The registration from the piezoelectric gauges was recorded on cathode ray oscillograph devices PID-9, and from the strain gauges on mirror galvanometer oscillograph MPO-2.

Vibrographs VIB-3F were used to measure mass speed. Its registered emf is proportional to the speed of relative motion of a magnet connected to the massive case of the device and the coil on a pendulum. The free periods of the pendulum in the vertical and horizontal directions were 0.6 s and 0.4 s, respectively. The maximum deviation of the pendulum was 10 mm. The registration was carried out on a mirror galvanometer oscillograph OSHA –9, with the help of 11 vibrators, on a photographic film of width 330 mm, with speeds of recording 4 to 60 cm/s. In addition, a vibrograph VBP was used to record large motions.

The gauges to measure the overpressure and the vibrographs were buried in the ground at depths of 0.5 and 2 m. Both the radial and the vertical components of the parameters were measured.

Table 1.6.1. Test configurations, from which peak-overpressure measurements in were made with strain gauges in the ground.

Test No.	Water Level, m	Charge Depth, m
1, 2, 3	1.0	0.75
4, 5, 6	1.0	0.5
7, 8	0.95	0.25
9	0.5	0.25
11	0.25	0.0

Figure 1.6.1 shows oscillograms of ground velocity of at distances from 7.5 m to 45 m, recorded from test No. 3. The records were made with vibrographs VIB-3. Time-travel curves of different waves were constructed using characteristic points on the oscillograms. Figure 1.6.2 and Figure 1.6.3 show oscillograms of overpressure recorded from tests No. 3 and No. 5. Table 1.6.2 shows pressure measurements at characteristic points, using digitized oscillogram records from strain gauges. The characteristic points in the overpressure wave are shown schematically in Figure 1.6.3a. The speed of the first arrival is 1600 m/s.

Figure 1.6.4 shows crater profiles from various explosions (tests No. 3-5, No. 7-11). The wave pattern in Figure 1.6.3a can be divided into three groups. Group 1 arises in the hypocenter and has a maximum speed of displacement. The lower speeds of wave groups 2 and 3 are caused by refraction in water and air. These arrivals are well separated at large distances, but overlap in the near field. At explosion of a (the test 11) Most of the energy from test No. 11 (half-immersed charge) is transmitted to air and the effect of the air shock waves on the ground in this case is comparable to the intensity of ground waves.

The digitized records of overpressure oscillograms recorded with strain gauges are included in 50 Excel files - Ch16_1_7_2H; Ch16_1_7_2Z; Ch16_2_7_2H; Ch16_3_75_0.5Z; Ch16_4_7_2H; Ch16_5_7_2H, etc. The notations used are as follows: Ch16_1_7_2H - chapter 1.6, test No. 1, distance R = 7 m, sensor depth h = 2 m, H and Z are the horizontal and vertical components of the signals.

Table 1.6.3 shows maximum overpressure ΔP_m, specific impulse I, duration τ, as well as calculations of the specific energy E in kgm/m^2, total energy E_1 in MJ, total energy E_2 in kg TNT and E_{mid}/E_0 for shock waves in the ground. E_0 is the energy of explosion. $E = \int(\Delta P^2/\rho C)dt$ was calculated in acoustic approximation from the digitized data, using $\rho = 1.95$ g/cm^3 and C = 270 m/s. E_1 and $E_2 = 2\pi E(R^2+h^2) = 2\pi Er^2$; $E_{mid} = [(E_{2Z})^2 + (E_{2H})^2)]^{1/2}$.

Figure 1.6.5 to 1.6.8 show specific energy in ground E and E_{mid}/E_0 from tests No. 4 to 6 (H_b=1 m, H = 0.5 m) versus distances R and r. Figure 1.6.9 and 1.6.10 show E and E_{mid}/E_0 versus distance r, from tests No. 1 to 3 (H_b = 1 m, H = 0.75 m). Figure 1.6.11 shows E_z and E_H versus r, from in tests No. 7 and 8 (H_b = 1 m and H = 0.25 m). Figure 1.6.12 shows E_{mid}/E_0 % versus distance r from tests No. 7, 8, 9, and 11.

These figures show that as the range R increases from 4 m to 7.5 m, there is almost an order of decrease in E and E_{mid}/E_0. Also, the horizontal component of energy E_H is much larger than the vertical component E_Z. At a distance of 7.5 m, increasing sensor depth from 0.5 m to 2 m does not affect the energy, which remains within the limits of measurement errors. Strong shock-wave energy absorption is observed in the near field. It appears that the explosion configurations do not influence systematically the shock-wave parameters. The significant data scatter is caused by variations in the sound speed in the ground, due to changes from previous explosions and pumping of water in and out of the reservoir.

Table 1.6.2. Characteristic points from digitized overpressure oscillograms recorded with strain gages (see Figure 1.6.3a). Time t is in ms, ΔP is in kg/cm^2.

Test No.	R, m	h, m	H, Z	First signal t_1	t_1^1	t_1^{11}	ΔP_1	Second signal t_2	t_2^1	t_2^{11}	ΔP_2	Third signal t_3	t_3^1	t_3^{11}	ΔP_3
1	7.5	0.5	Z	5	6	11	0.87	15	15.5	18	1.3	20.5	21.5	35	1.75
	7.5	0.5	H	5.5	5.5	10	0.9	15	15.5	17.5	1.3	21	22.5	40	1.62
1	7	2.0	Z	15	21.5	-	1.4	-	39	51	0.7				
	7	2.0	H	15	21		1.3		38	47	0.78				
2	7.5	0.5	Z	8.5	10	15	0.4	21	22	24	0.7	26	28	40	1.28
	7	2.0	Z	15	22.5		2.2		32.5		1.7				
	7	2.0	H	23.5	24		1.8		39	48	1.0				
3	7.5	0.5	Z	10	11	14.	0.5	23.	25	26	0.6	27.5	31	42	1.85
	7.5	0.5	Z	6.5	8	5	0.5	5	26		2.2		32	44	2.0
	7.5	0.5	H	10	11	16	0.5	25	25		0.9		29.5	45	3.14
	7	2.0	Z	14	19.5	16	2.8	24			1.0				
	7	2.0	H	13	19		3.5				1.9				
4	7.5	0.5	Z	7.0	8.0	15	0.7	26	26.5		2.2		31	49	1.9
	7.5	0.5	H	11.5	12	18	0.8	25.	26.5		1.2		31	53	3.4
	7.0	2.0	Z	15	21.		1.8	5	32.5	42.5	0.9				
	7.0	2.0	H	15	21.5		2.5		34	50	1.3				
5	4	0.5	Z	4	6.5	8.5	11.3	8.5	9.5	10.7	1.5				
	4	0.5	H	4.8	11.5		9.4		27.5	41	3.6				
	7.5	0.5	Z	8	8.5	13.	0.4				0.6		33.5		1.2
	7.5	.05	H	7.5	8.5	5	0.2	25	29		1.1		35	45.5	1.5
	7	2.0	H	14	21	13	2.6		33.5	41	1.4				
	7	2.0	Z				1.8								
6	4	0.5	Z	5	6		9.8		9.5	13	5.7				
	4	0.5	H	5	12.5	25.	9.5	25.	27	37	3.8				
	7.5	0.5	Z	9	9.5	5	0.2	5	25.5		0.7				
	7.5	0.5	H	9	9.5	14	0.2	24.	25		1.3				
	7	2.0	Z	15	20.5	15	1.9	5							
	7	2.0	H	15	21.5	40	2.9	24	32.5	40	1.4				
7	4	0.5	Z	5	5.5	8	2.4	8	9	9.5	1.7				
	4	0.5	H	9	13.5		1.29		20.5	43	3.2				
	7.5	0.5	Z						25.5		0.8		30.5	34	1.0
	7.5	0.5	H	5				24.	25.5		1.3		27.5	44.5	2.3
	7.0	2.0	Z	17.5	23		1.2	5	31	40	1.0				
	7.0	2.0	H	20	24		1.4		33.5	43	1.3				
8	4	0.5	Z	5	5.5		3.6		8.5	10.5	1.0				
	4	0.5	H	4.8	12	21	22.1	21	22.5	27	4.7				
	7.5	0.5	Z	9	9.5	12	0.2	23	25		1.1		29	37	1.27
	7.5	0.5	H					23.5	25		1.1		28.5	45.5	1.9
	7	2.0	Z	15	19.5		2.1		30	38	1.0				
	7	2.0	H	18	20.5		2.6		30	40	1.3				
9	4	0.5	Z	11	11.5	13	2								
	4	0.5	H	11	13	26	16.7								
	7.5	0.5	H	20	26	42	1.9								
	7.5	0.5	Z	20	25.2		1.1		27	30	1.1				
	7	2	Z	19	21		0.9		29	37.5	1.2				
	7	2	H	20	23		0.8		25		1.05		30	37.5	1.0
11	4	0.5	Z	3	3.2	6.5	3.9	8	8.5	12	1.3	17	17.5	18.5	2.9
	4	0.5	H	3	4	6.5	12.5	8	9.5	10.5	1.3	17	18.5	24	2.8
	7.5	0.5	H	3	3.4	5	0.4	14	16.5	25	0.5	30	32	37	0.5
	7	2	Z	20	22		0.62		24		1		30	36	1
	7	2	H	20	23		0.3		24.5		0.9		32.5	38	0.7

Table of 1.6.3. Shock-wave parameters in ground.

R, m	h, m	ΔP_m, kg/cm^2	τ, ms	I, kgs/m^2	E, kgm/m^2	E_1, MJ	E_2, kg TNT	E_{mid}, kg TNT	E_{mid}/E_0 %
Test 1, depth of basin 1m, depth of charge 0.75m									
7.5	Z	1.75	30	99.2	15.5	0.055	0.013	0.029	0.029
7.5	5H	1.62	34.5	160.6	30.2	0.107	0.026		
7	2Z	1.4	36	220	34.6	0.115	0.028	0.032	0.032
7	2H	1.3	32	158	19.7	.0.066	0.016		
Test 2, depth of basin 1m, depth of charge 0.75m									
7.5	0.5Z	1.28	31.5	62.6	5.36	0.019	0.0046	0.0046	0.0046
7	2Z	2.2	28	278	71.8	0.239	0.057	0.0654	0.0654
7	2H	1.8	24.5	215	40.5	0.135	0.032		
Test 3, depth of basin 1m, depth of charge 0.75m									
7.5	0.5Z	1.85	32	150	30.6	0.109	0.0260	0.088	0.088
7.5	0.5H	3.14	35	290	102	0.362	0.0866		
7.5	0.5Z	2.2	37.5	162	33.6	0.119	0.0285	0.089	0.089
7	2Z	2.8	27	260	65.6	0.218	0.0522	0.122	0.122
7	2H	3.5	27.5	390	138	0.459	0.110		
Test 4, depth of basin 1m, depth of charge 0.5m									
7.5	0.5Z	2.2	42	251	53.2	0.189	0.0452	0.134	0.134
7.5	0.5H	3.4	41.5	396	149	0.529	0.1265		
7	2Z	1.8	27.5	197	34.5	0.115	0.0275	0.078	0.078
7	2H	2.5	35	368	91	0.303	0.0725		
Test 5, depth of basin 1m, depth of charge 0.5m									
4	0.5Z	11.3	6.7	215	319	0.325	0.078	0.218	0.218
4	0.5H	9.4	36.2	942	833	0.850	0.203		
7.5	0.5Z	1.2	39	92.5	7.28	0.026	0.0062	0.024	0.024
7.5	0.5H	1.5	38	157	27.6	0.098	0.0234		
7	2H	2.6	27	288	84.4	0.281	0.067	0.067	0.067
7	2Z	1.8							
Test 6. depth of basin 1m. depth of charge 0.5m									
4	0.5Z	9.8	8	378	417	0.426	0.102	0.39	0.39
4	0.5H	9.5	32	1361	1540	1.57	0.376		
7.5	0.5Z	1.26	33	110	14.8	0.0526	0.0126	0.052	0.052
7.5	0.5H	1.9	20	243	59.4	0.211	0.0504		
7	2Z	1.9	25	180	36.1	0.12	0.0287	0.069	0.069
7	2H	2.9	25	268	78.1	0.26	0.0622		
Test 7, depth of basin 1m, depth of charge 0.25m									
4	0.5Z	2.4	4.5	56.1	16.4	0.016	0.004	0.052	0.052
4	0.5H	3.2	34	544.1	213.6	0.218	0.052		
7.5	0.5Z	1.0	8.9	57.1	8.18	0.029	0.0069	0.057	0.057
7.5	0.5H	2.3	20.6	242.1	66.9	0.236	0.057		
7	2Z	1.2	22.5	128	18	0.06	0.0143	0.032	0.032
7	2H	1.4	23	193	36.1	0.12	0.0288		
Test 8, depth of basin 1m, depth of charge 0.25m									

4	0.5Z	3.6	5.5	64.6	20.9	0.021	0.0051	1.35	1.35
4	0.5H	22.1	22.2	1997	5503	5.62	1.344		
7.5	0.5Z	1.27	8.9	76.4	9.48	0.034	0.0081	0.065	0.065
7.5	0.5H	1.9	20.6	266.5	75.4	0.268	0.064		
7	2Z	2.11	23	195.3	45.8	0.153	0.0365	0.065	0.065
7	2H	2.6	22	261	67.4	0.225	0.054		
Test 9, depth of basin 0.5m, depth of charge 0.25m									
4	0.5Z	2	2	18.9	5.1	0.005	0.0013	0.61	0.61
4	0.5H	16.7	21.2	1065	2485	2.54	0.61		
7.5	0.5Z	1.1	10	50	7.36	0.026	0.0063	0.02	0.02
7.5	0.5H	1.9	22	125	22.1	0.078	0.019		
7	2Z	1.2	18.5	122.3	17.5	0.058	0.014	0.021	0.021
7	2H	1.05	18.5	122	19.3	0.064	0.015		
Test 11, depth of basin 0.25m, depth of charge 0.0m									
4	0.5Z	3.9	15.5	87.4	24.5	0.025	0.006	0.68	0.68
4	0.5H	12.5	21	299	271	0.2278	0.067		
7.5	0.5H	0.51	34	56.3	3.41	0.0121	0.003	0.003	0.003
7	2Z	1.0	16	103	14.3	0.048	0.0114	0.015	0.015
7	2H	0.9	18	97.7	12.3	0.041	0.0098		

a

R=45 m. N 18 Z

R=30 m. N 42 Z

R=15 m. N 35Z

R=7.5m. N30Z

R=7.5m. N17Z

R=7.5m, N48H

R=15m, N46H

R=30m, N49H

b
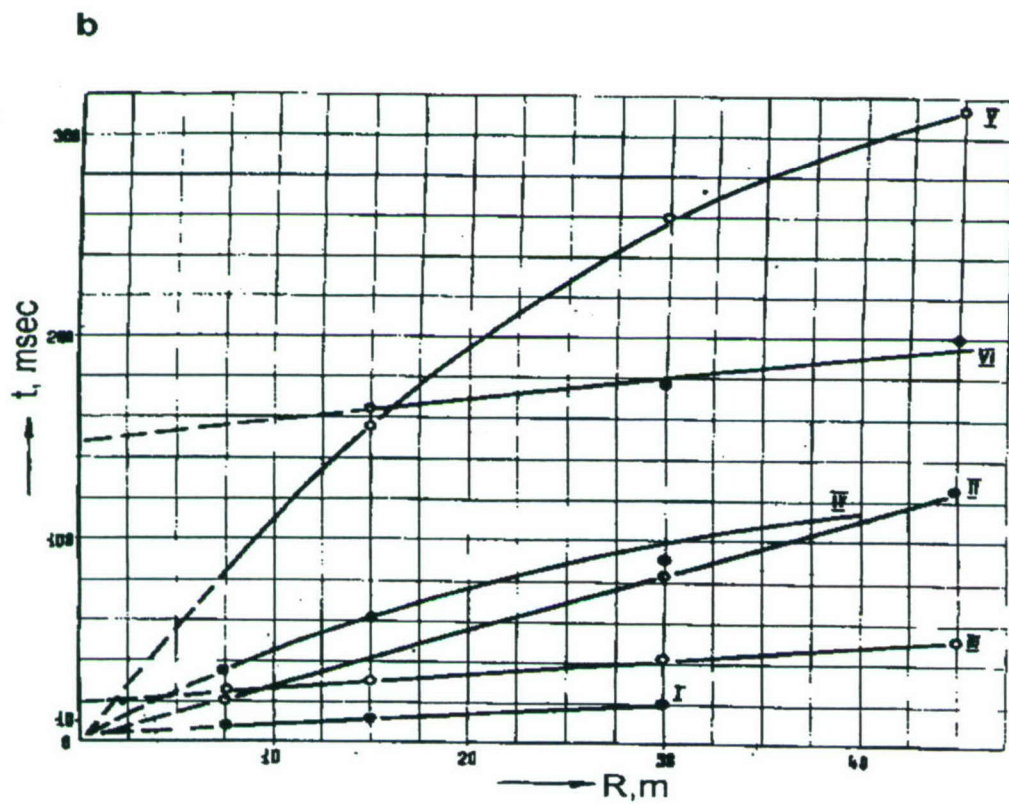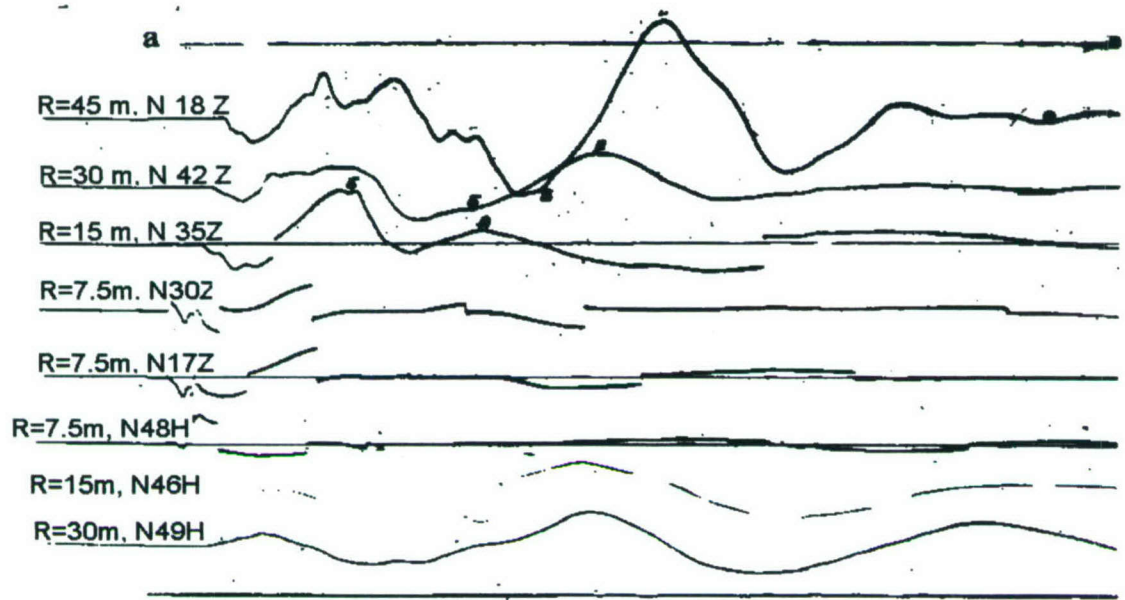
Figure 1.6.1.   (a) Ground speed in test No. 3. (b) Travel-time curves constructed on the basis of characteristic points from the oscillograms in (a).
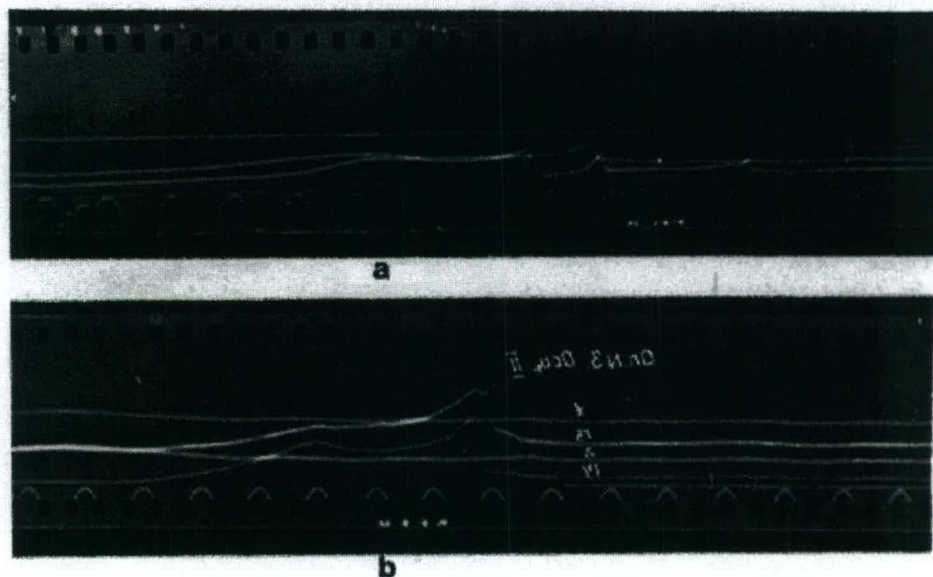
Figure 1.6.2.   Oscillograms of overpressure from test No. 3. (a) distance R = 7.5 m, sensor depth h = 0.5m; (b) R = 7 m, h = 2 m.
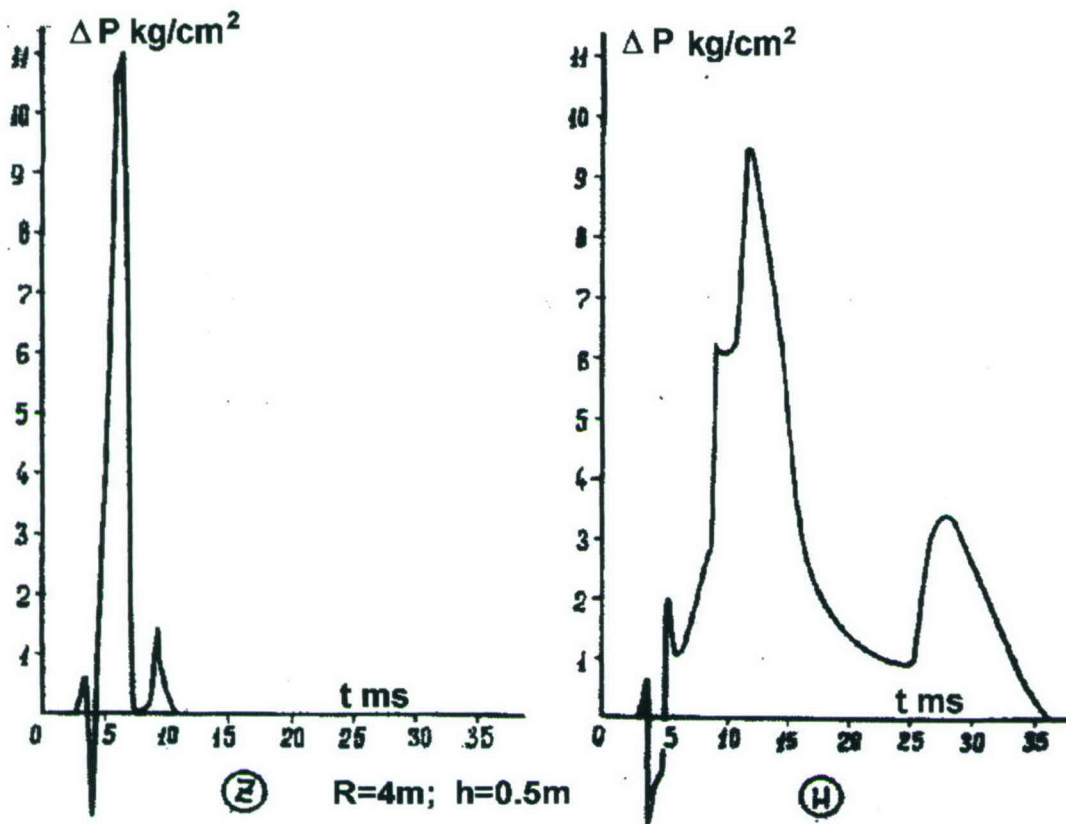
Figure 1.6.3.   Overpressure from test No. 5. Distance R = 4 m, sensor depth h = 0.5 m, Z and H are vertical and horizontal components, respectively.
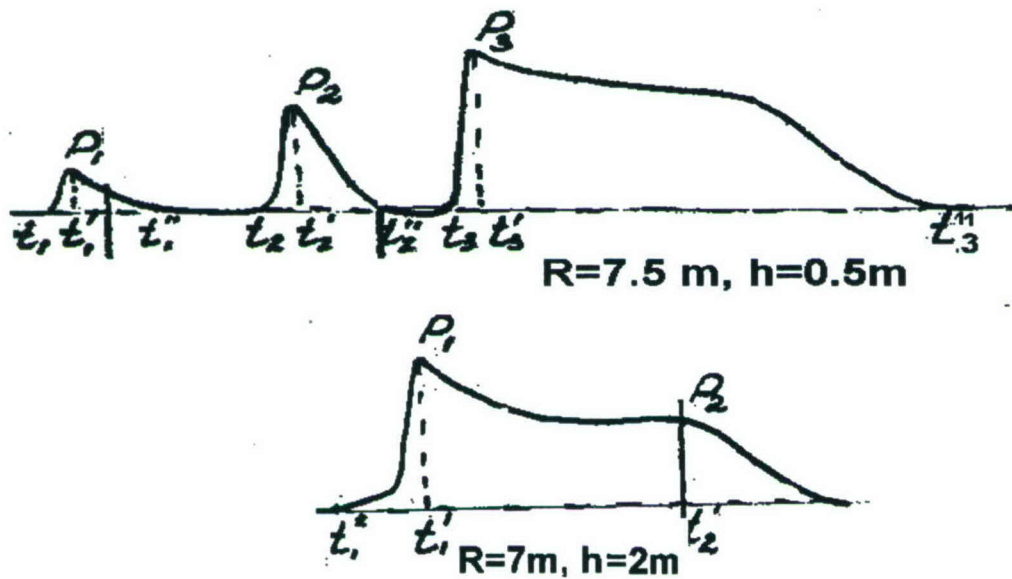
Figure 1.6.3.a. Characteristic points in the overpressure waves at distance R = 7.5 m, sensor depth h = 0.5 m and distance R = 7 m, sensor depth h = 2 m.
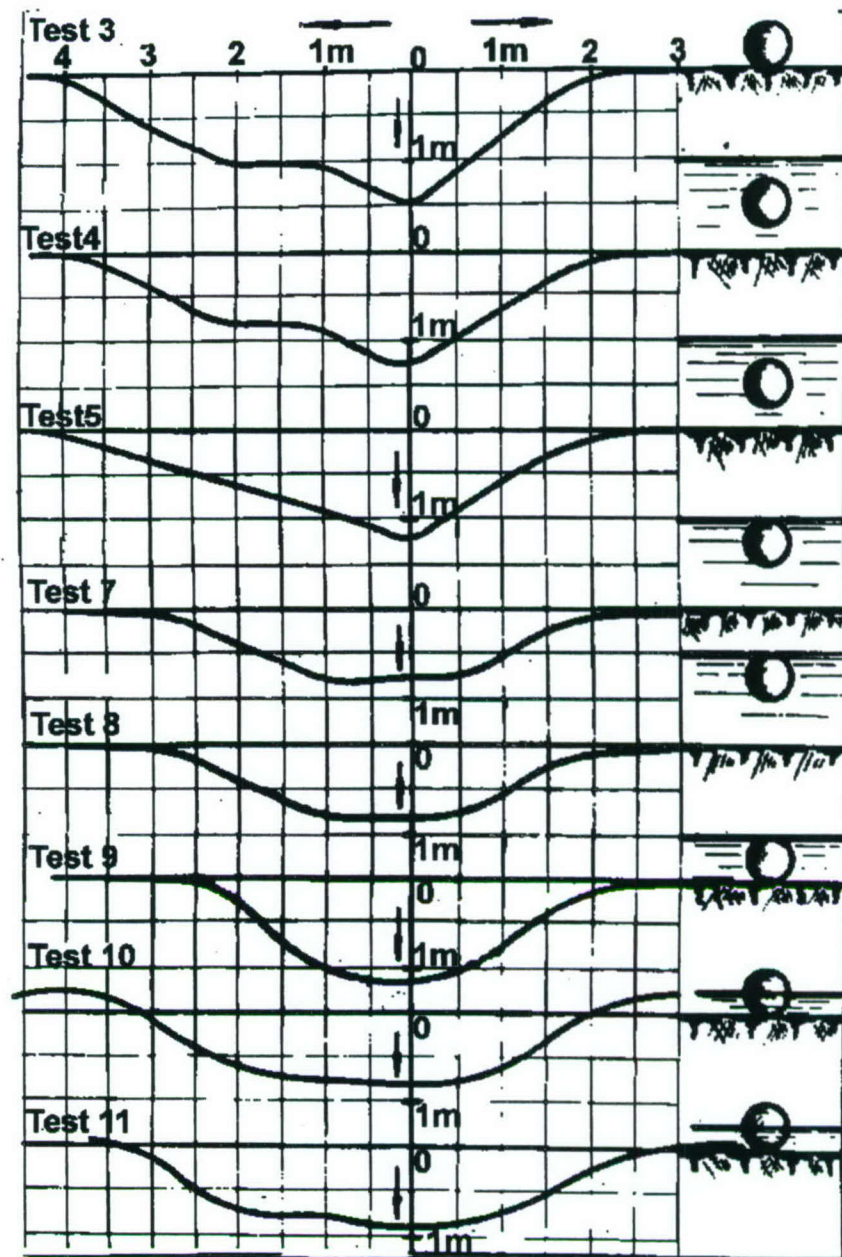
Figure 1.6.4. Crater profiles from 100-kg TNT explosions.
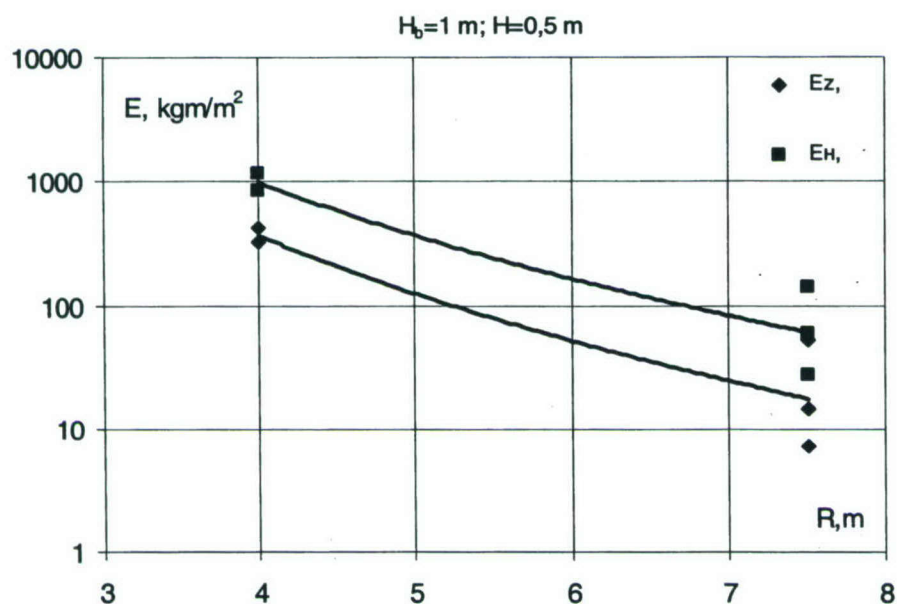
Figure 1.6.5. Specific energy of ground shock wave versus distance R from underwater explosions at depth H = 0.5 m, water level 1 m, sensor depth h=0.5 m. E_H and E_Z denote the horizontal and vertical components of the signals.
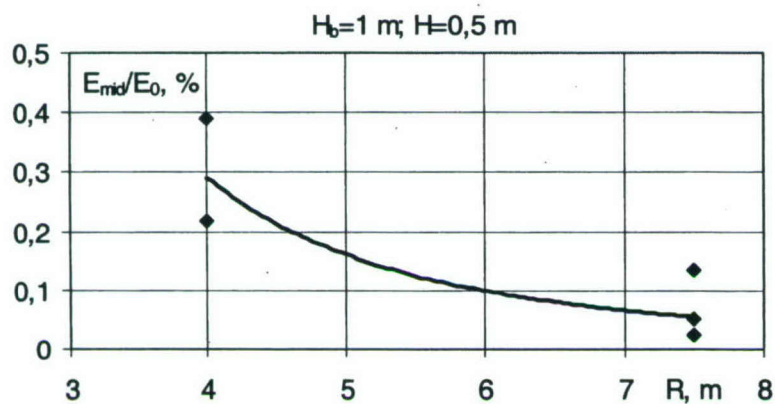
Figure 1.6.6. Ratio of energy of shock wave to energy of explosion versus distance R from underwater explosions with depth H = 0.5 m, water level 1 m, sensor depth 0.5 m.

A-85

Figure 1.6.7.   Specific energy of ground shock wave versus distance $r = (R^2 + h^2)^{1/2}$ from underwater explosions with depth H = 0.5 m, water level 1 m, gauge depths h = 0.5 and 2 m.

Figure 1.6.8.   Energy of ground shock wave to energy of explosion versus distance r from underwater explosions with depth H = 0.5 m, water level 1 m, gauge depths h = 0.5 and 2 m.

E kgm/m²   H_b=1 m; H=0,75 m

150

125

100

75

50

25

0

♦ Ez,
■ EH,

7,25 7,3 7,35 7,4 7,45 7,5 7,55

r, m

Figure 1.6.9.   Specific energy of ground shock wave versus distance $r = (R^2 + h^2)^{1/2}$ from underwater explosions with depth H = 0.75 m, water level 1 m.

E_{mid}/E_0 %   H_b= 1m; H=0,75 m

0,15

0,12

0,09

0,06

0,03

0

7,2 7,3 7,4 7,5 7,6

r, m

Figure 1.6.10.   Energy of ground shock wave to energy of explosion versus distance r from underwater explosions with depth H = 0.75 m, water level 1 m.

A-87
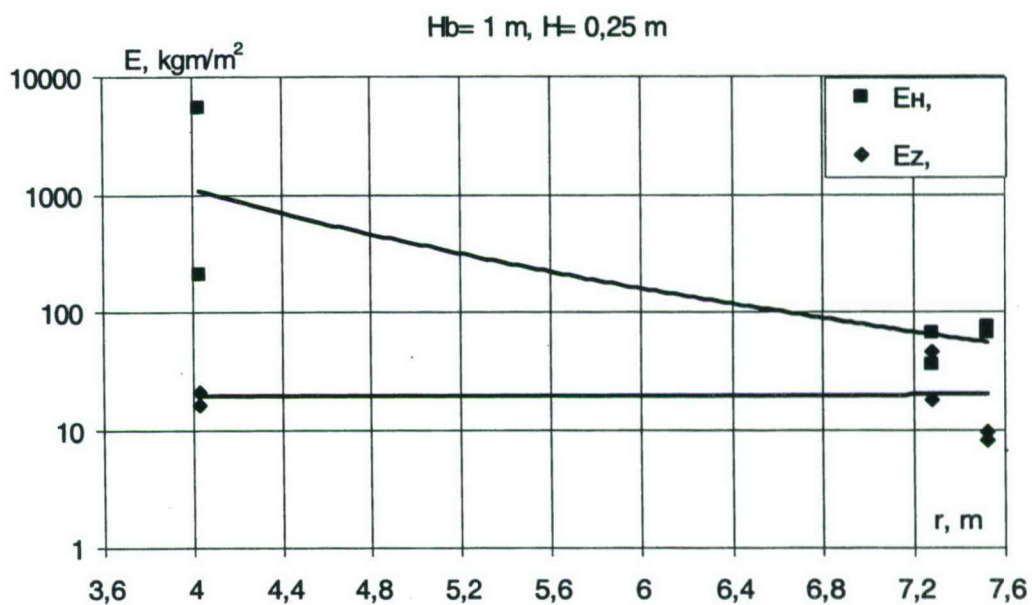
Figure 1.6.11. Specific energy of ground shock wave versus distance $r = (R^2 + h^2)^{1/2}$ from underwater explosions with depth $H = 0.25$ m, water level 1 m.
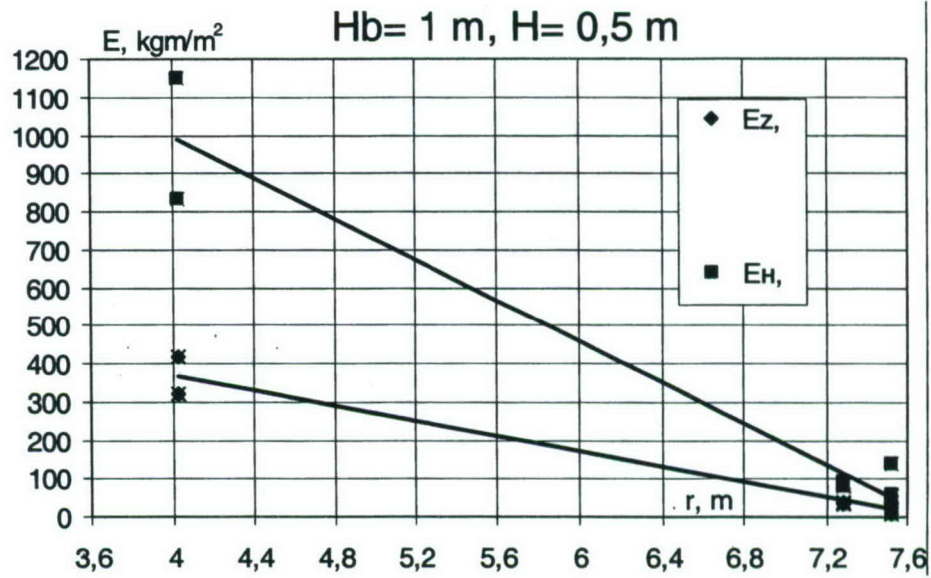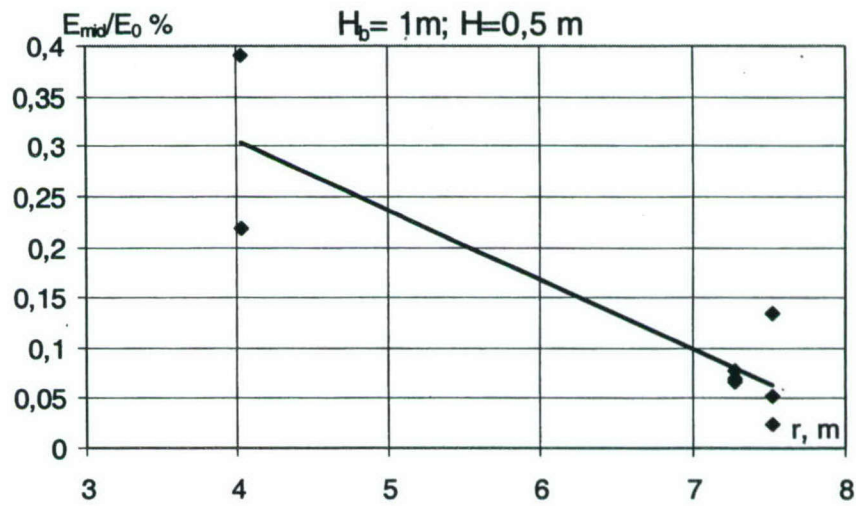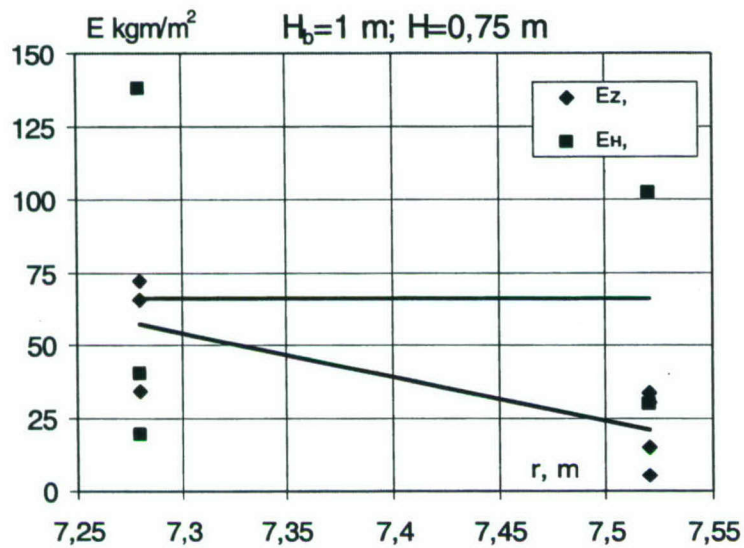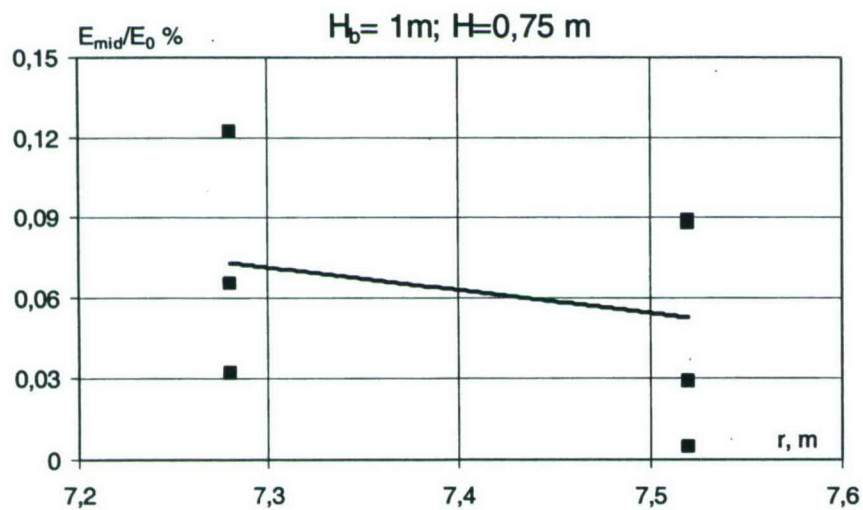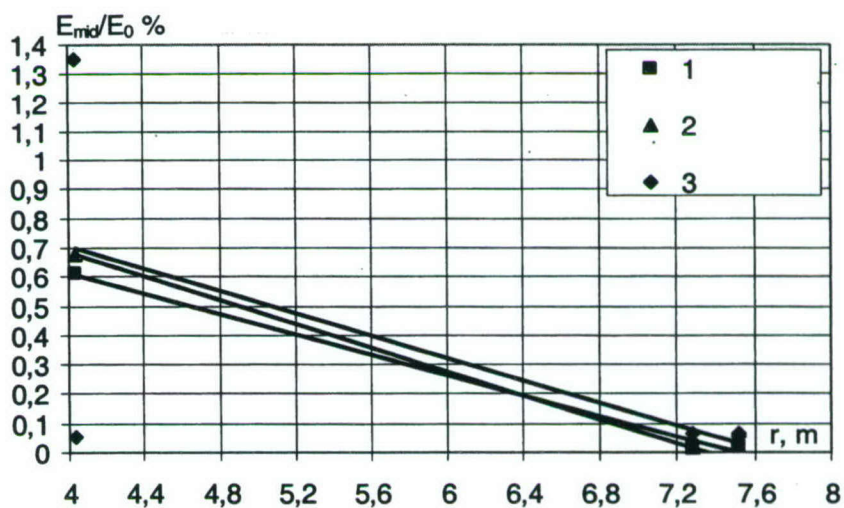

Figure 1.6.12. Energy of ground shock wave to energy of explosion versus distance r from underwater explosions. 1- $H = 0.25$ m, $H_b = 0.5$ m; 2- $H=0.0$ m, $H_b = 0.25$ m; 3 - $H = 0.25$ m, $H_b =1.0$ m.

1.7   Measurements form surface HE explosions.

1.7.1   Explosion of 1000 t TNT on the coast of Matochkin Shar.

Explosion of 1000 t TNT was conducted on August 25, 1987, 18.00.00 Moscow time, on the southern coast of the strait Matochkin Shar, approximately 100 m from the coast line (73.38 N; 54.78E). Measurements of parameters of a crater and pressure waves in air, water and ground are described below.

Shock waves in air were measured on the coast of the strait, using devices SD-725 and DD-10 (recorders of pressure), as well as using the method of hodographs. The pressure waves in water refracted from air and the bottom were measured from a specially equipped ship, at a distance of 590 m from the explosion (Figure 1.7.1). The pressure gauges were immersed at depths 2 to 9 m on the front and back of the ship (Figure 1.7. 2). The bottom was deeper than 10 m.

The explosion was carried out in the central bottom point of a charge, placed on a coastal strip of width 300-400 m, inclined from south to north (towards the strait) at 3^0 to 12^0, in an area of eternal freeze. The frozen soil reaches 300 m in depth. In the summer, the top layers of the soil (shingles) thaw up to depth of 3.6-4.8 m. Down to depth of about 20 m, there are alternating layers of sand and clay with shingle. The characteristic density of the soil at depths to sea level is 1.62-1.75 g/cm^3, the velocity of longitudinal waves (P) is about 3 km/sec. The sound velocity and the soil density increase with depth. Below the layer of sedimentary deposits, there is a rocky base with P-wave velocity of about 5.3 km/sec.

The charge was contained in 24,000 bags with TNT, with a total weight of 974 t. It had the shape of a cylinder of a diameter 17.8 m and height 4.6 m, with a top in the shape of a truncated cone of height 1.6 m and diameter of the top basis 3.8 m. In the middle of the charge, 880 boxes with cast TNT of total weight 22 t were placed. In the top part of the charge, 165 boxes with cast TNT of total weight 4 t were added.

A photograph of the explosion is shown on Figure 1.7.3. The explosion plume rose to about 3.5 km up in the air. The explosion crater had a radius of 26.7 m and depth of 16.5 m. Its bottom and sides consisted of frozen soil fragments. Table 1.7.1a shows results from the processing of the oscillograms of the air shock wave.

Table 1.7.1a. Results of the processing of the oscillograms of the air shock wave.

R, m	Δp_m, atm	t_+, ms	I_+, kgs/m²	E_+, kgm/m²	E_+10^{-6}, MJ	E_+/E_0, %	t, ms	E, kgm/m²	$E10^{-6}$ MJ	E/E_0, %
60.5	23.9	46.5	2566							
68	21.2	57.8	2552							
70	20.2	43.54	3050							
75	18.5	55.5	2178							
93	9.2	82	1941.5							
125	8.9	107	1660							
164	5.5	132	1216							
187	3.7	155	1340							
216	2.6	164	1050							
315	1.15	211	632							
317	1.12	221	981							
320	1.12	229	807							
405	0.71	307	638.4	52124	0.537	12.8	908	60248	0.621	14.9
472	0.56	296	510	33698	0.471	11.28	876	38558	0.539	12.9
484	0.55	302	579	37766	0.556	13.3	893	50454	0.742	17.78
554	0.45	330	486	25467	0.491	11.7	976	34748	0.671	16
593	0.37	388	613	34120	0.755	18.6	1780	49277	1.09	26.03
674	0.39	392	366	16137	0.46	11	1160	20371	0.58	13.9
680	0.38	381	420	17367	0.504	12.1	1127	21184	0.615	14.72
771	0.367	420	377	14290	0.54	12.9	1243	17768	0.672	16.1
956	0.21	507	313	7108	0.41	9.76	1560	8660	0.498	11.9
996	0.13	782	354	5680	0.355	8.49	1789	5749	0.359	8.6
1208	0.112	446	207	3074	0.28	6.74	1910	4072	0.37	8.93
1262	0.126	528	229	3994	0.4	9.7	1562.	5050	0.505	12.1
1593	0.102	598	220	3084	0.491	11.8	1794	3839	0.612	14.6
2030	0.063	612	143.5	1253	0.324	7.75	1870	1552	0.422	10.1
2446	0.049	774	136.8	927	0.348	8.3	2360	1141.5	0.429	10.3
2833	0.0385	773.8	130.2	780.3	0.288	6.9	2267	809	0.374	8.94
3010	0.042	811	98	456.8	0.26	6.22	2500	593	0.337	8.1
3443	0.038	844	86.4	354.3	0.264	6.31	2600	462.8	0.345	8.24
4184	0.026	850	75.3	244	0.268	6.41	2210	302	0.332	7.94

Figure 1.7.4 shows examples of oscillograms and experimental dependencies of peak overpressure, duration and impulse of the positive phase of the air shock wave on distance. The dot-dashed lines show values calculated according formulae given by M. A. Sadovsky for explosion of cast TNT on a rigid surface, valid in the range $R^0 = R/M^{1/3} > 0.8$ m/kg$^{1/3}$ [1, 2].

$$\Delta P = 0.95/(R^0) + 3.9/(R^0)^2 + 13.0/(R^0)^3$$
$$t_+ = 1.35 M^{1/6} R^{1/2} \tag{1}$$
$$I = 35 M^{2/3}/R$$

The significant deviation from formulae (1) in the near zone is due to the influence of the plastic properties of the ground and the rather low charge density.

Figure 1.7.5 shows schematically the wavefields in water and air, for a homogeneous bottom of rock.

Examples of oscillograms of water overpressure are shown in a Figure 1.7.6 and Figure 1.7.7 a, b. The first arrivals to the gauges are that of P- and S-waves refracted from the bottom into water. These arrivals last for about 200 msec after the explosion. After that, with a delay of about 800 msec, waves arrive that are refracted from air. Their duration is also about 200 msec. The dotted lines show the overpressure-time curve as calculated from the acoustic method for waves refracted from air in water and reflected from the shipboard.

Figure 1.7.8a shows an oscillogram of the vertical speed Vz of the ground, recorded by a coastal gauge at a distance 590 m from the epicenter of the explosion. Figure 1.7.8b shows a comparison of the measured (dotted line, depth 8 m, point 1 on ship front) and calculated (solid line) dependence of overpressure in water on time. The overpressure is calculated using a formula for plane waves $\Delta P = \rho C V_z$ where ρ and C are the density and speed of longitudinal waves in ground, taking into account the influence of the overpressure wave reflected from the free water surface. There is a satisfactory quantitative agreement between the calculated and observed values in the beginning of the oscillogram. A record duration of up to 250 msec is necessary to reveal the direct wave in water (T-phase) propagating from the coast at a speed of 1.43 km /sec (Figure 1.7.6a).

Measurements of the characteristics of the overpressure waves are given in Table 1.7.1, where ΔP_1, t_{+1} and ΔP_2, t_{+2} denote the maximum amplitudes of overpressure and times of positive phases in the first and second groups of waves of seismic origin, respectively (Figure 1.7.6a). Figure 1.7.9 shows the dependence of ΔP_1 and ΔP_2 on gauge depth. The peak overpressure decreases as the gauges approach the free surface, due to the superimposition of a reflected rarefaction wave.

Table 1.7.1 Characteristics of overpressure waves in water.

№ point	h, m	ΔP_1, kg/cm^2	t_{+1} , ms	ΔP_2, kg/cm^2	t_{+2}, ms
1	8	0.78	19	0.5	10
2	7	0.76	20	0.46	11.5
3	5	0.53	18	0.18	10
4	6	0.64	19.5	0.38	10.5
5	4	0.45	18	0.23	10
6	2	0.21	18	0.13	11
7	9	0.86	19	0.38	11
8	8	0.76	19	0.45	12
9	5	0.46	18	0.14	9
10	8	0.74	19	0.25	10
11	5	0.46	18	0.22	8.5
12	2	0.14	18	0.08	12

References

7. Yakovlev Yu.S. Hydrodynamics of explosion. Sudpromgiz. 1961.

8. M.A. Sadovsky. Geophysics and physics of explosion. M. Nauka 1999.
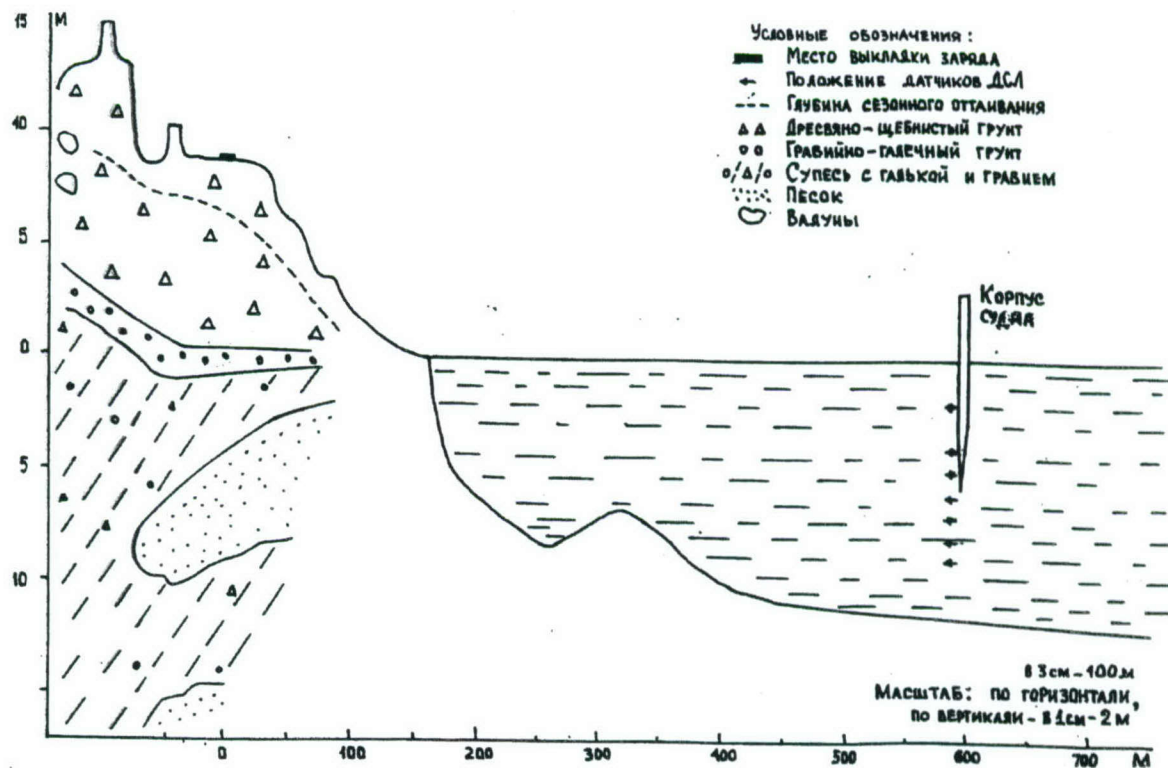
Figure 1.7.1. Schematic representation of the test site, the bottom and the basin in direction to the ship.
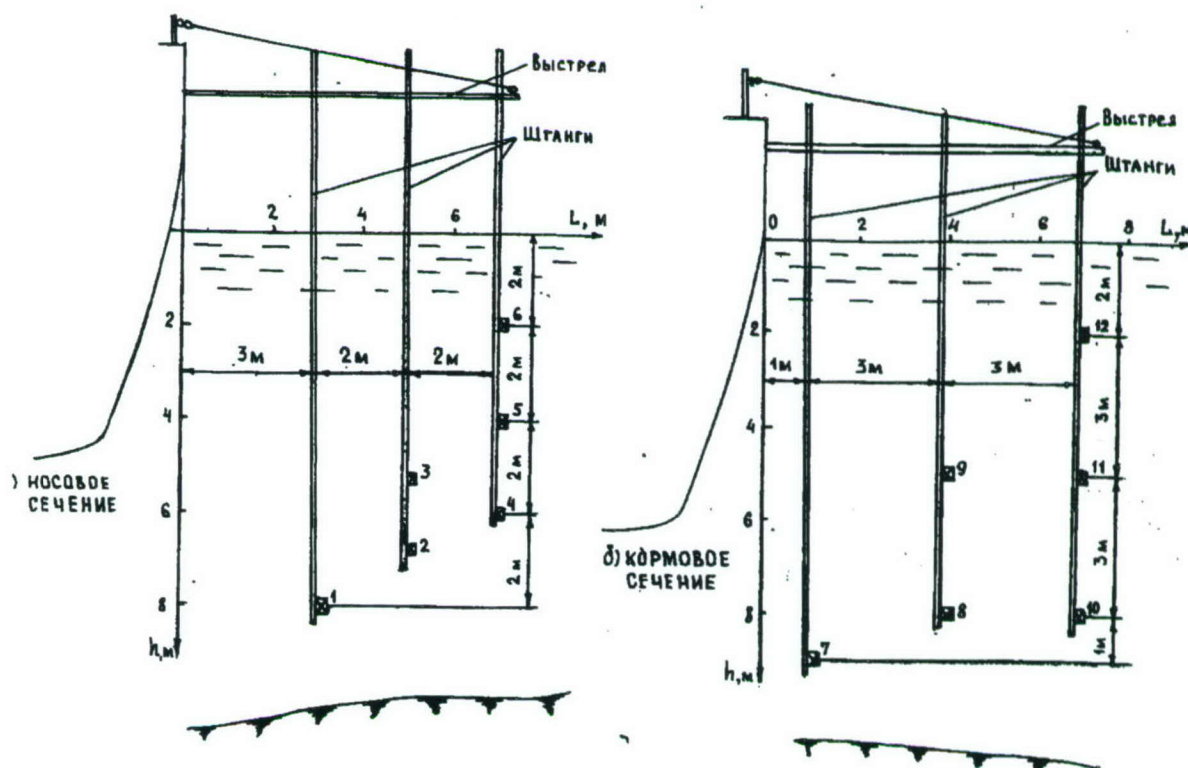
Figure 1.7.2.   Positions of pressure gauges recording the underwater waves. Left – front of the ship, right – back of the ship.
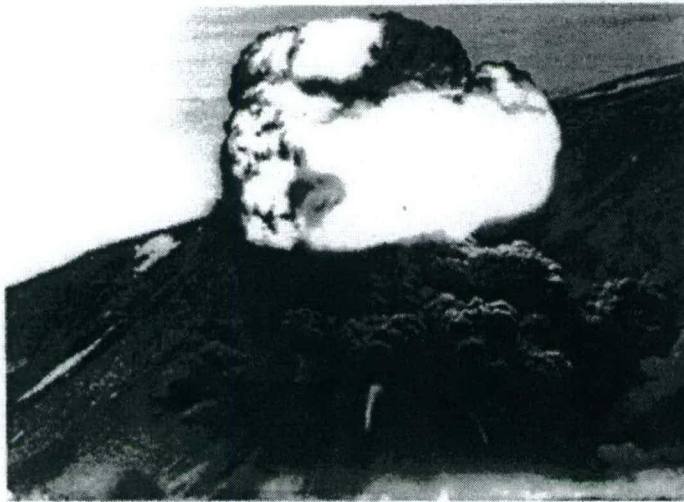
Figure 1.7.3. A photograph of the 1000-t explosion on August 25, 1987 at 18.00.00 Moscow time, detonated on the southern coast of the strait of Matochkin Shar, approximately 100 meters from the coastal line (73.38N; 54.78E).
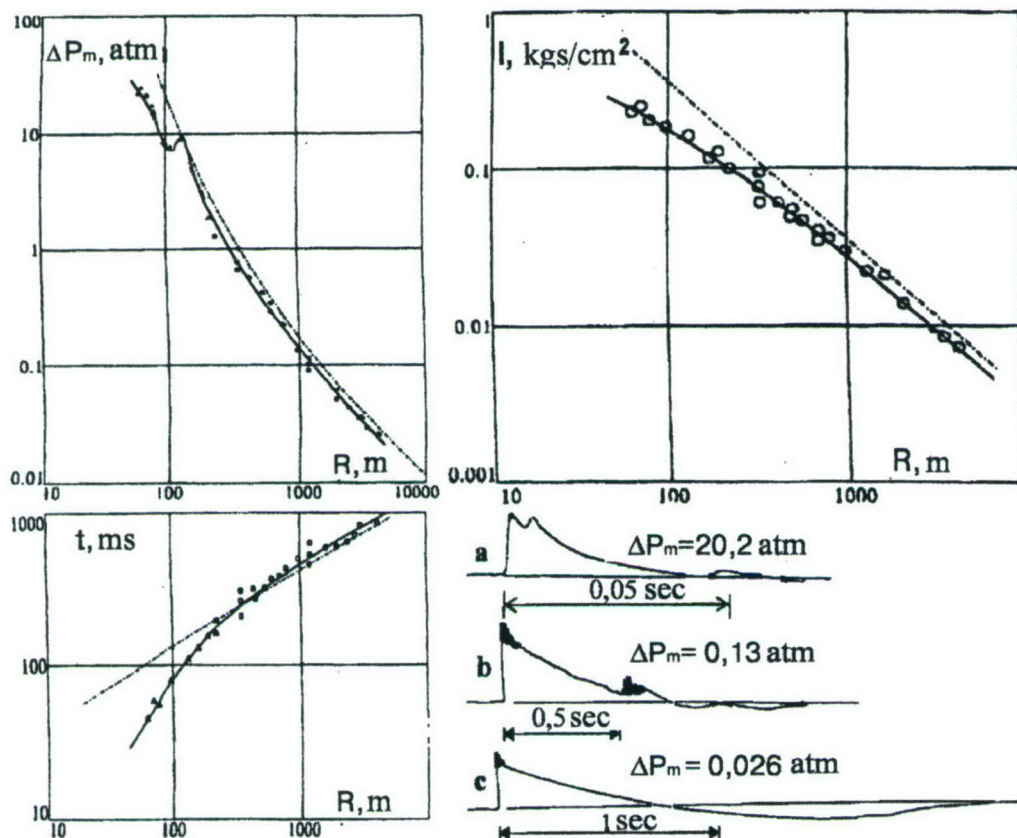
Figure1.7.4. Dependence of peak overpressure, duration and specific impulse of compression of the air shock wave on distance from the coast [explosion epicenter?]. Solid lines - approximation to the experimental data; dot-dash lines – calculated from the formulas of M.A. Sadovsky. Examples of records of the air shock wave at distances (a) 70 m, (b) 997 m and (c) 4184 m.
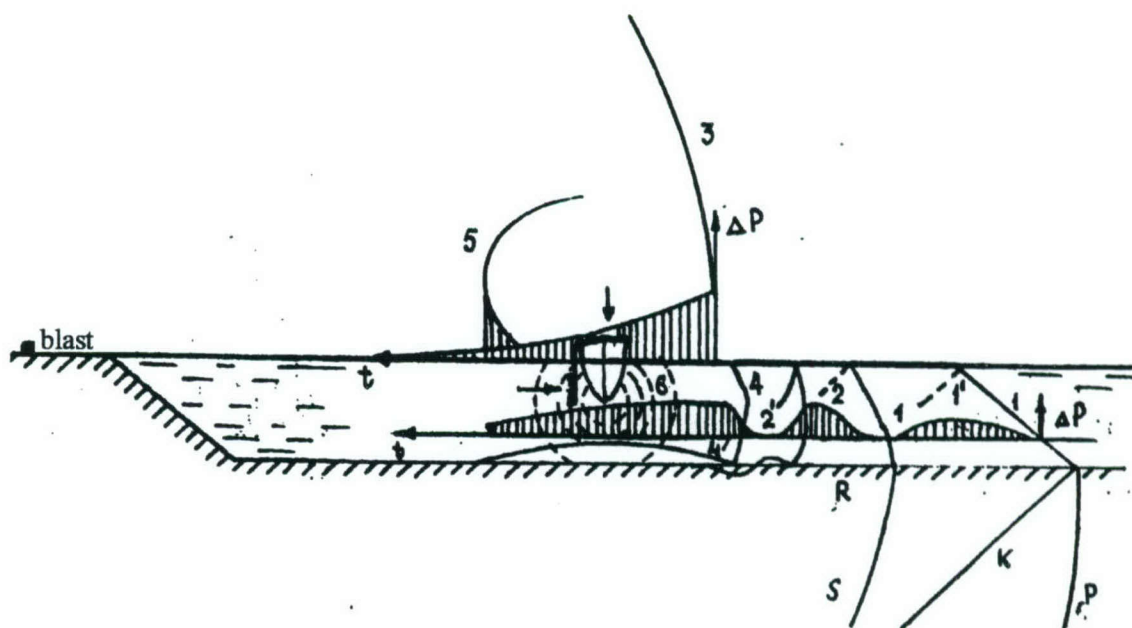
Figure 1.7.5. Schematic representation of the wavefield in a basin with a homogeneous bottom of rock. P, S, K, and R - longitudinal, transverse, conic and interface [head ?] waves in the bottom. 1 - waves of seismic origin; 2 - diffraction underwater wave; 3 - air shock wave; 4 – compressional wave from an air wave; 5 – air wave reflected from the board of the ship; 6 – diffraction wave; $1^1, 2^1$, and 3^1 - waves reflected from the surface and the bottom of the basin.
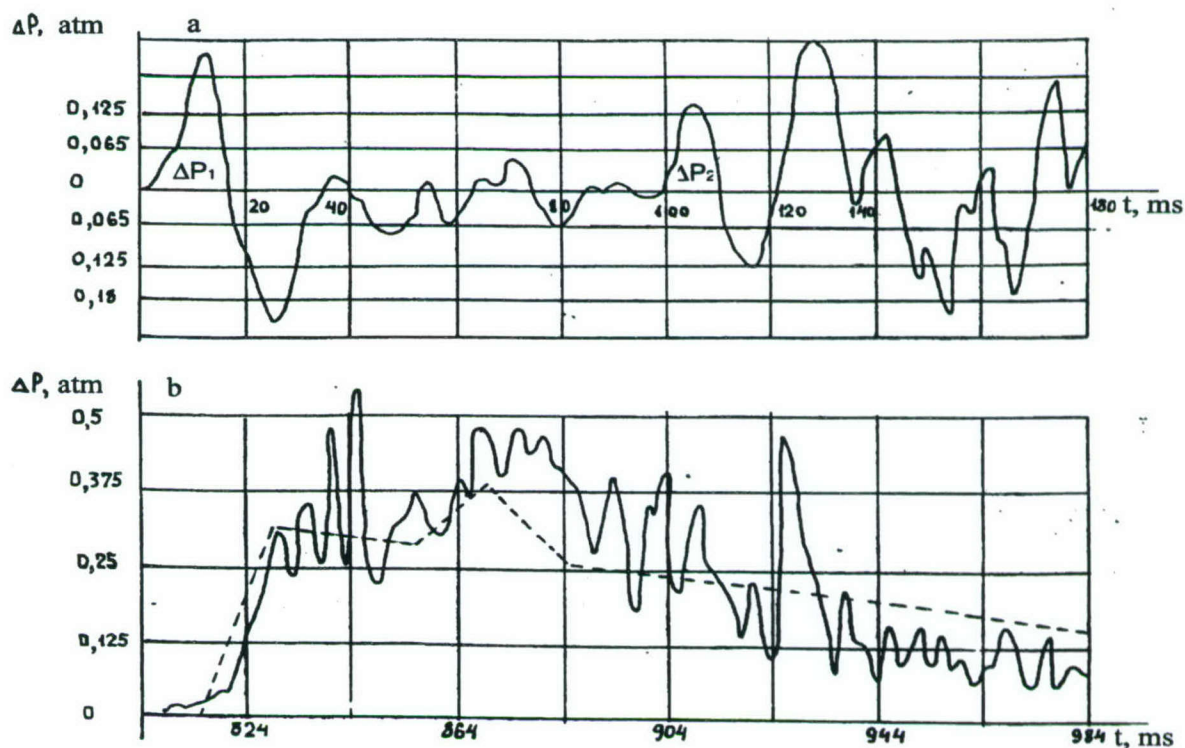
Figure 1.7.6. Records of water overpressure waves measured from the ship front (point 6 in Figure 1.7.2; gauge depth h = 2 m).
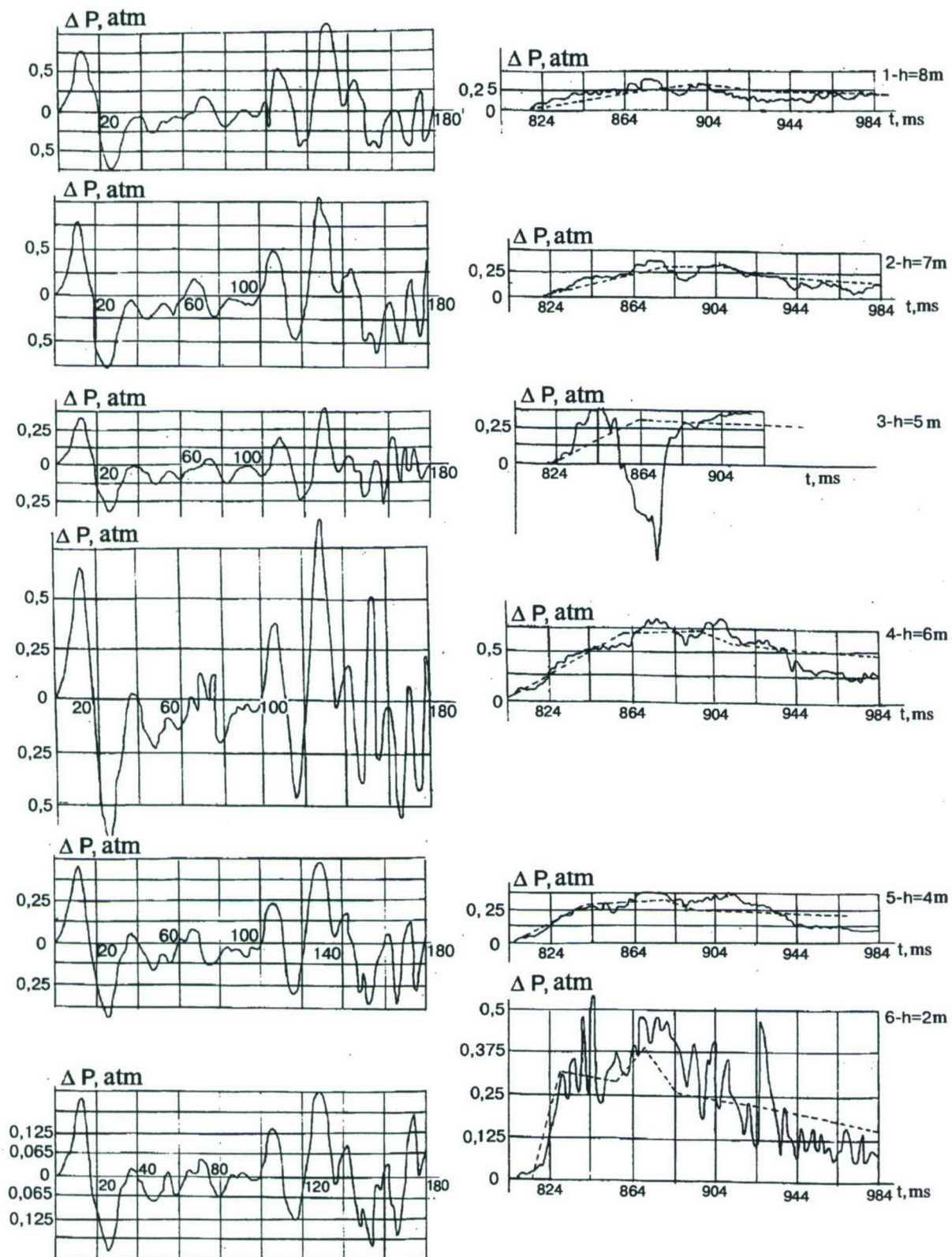
Figure 1.7.7a. Records of overpressure waves in water at points 1 to 6 (Figure 1.7.2).
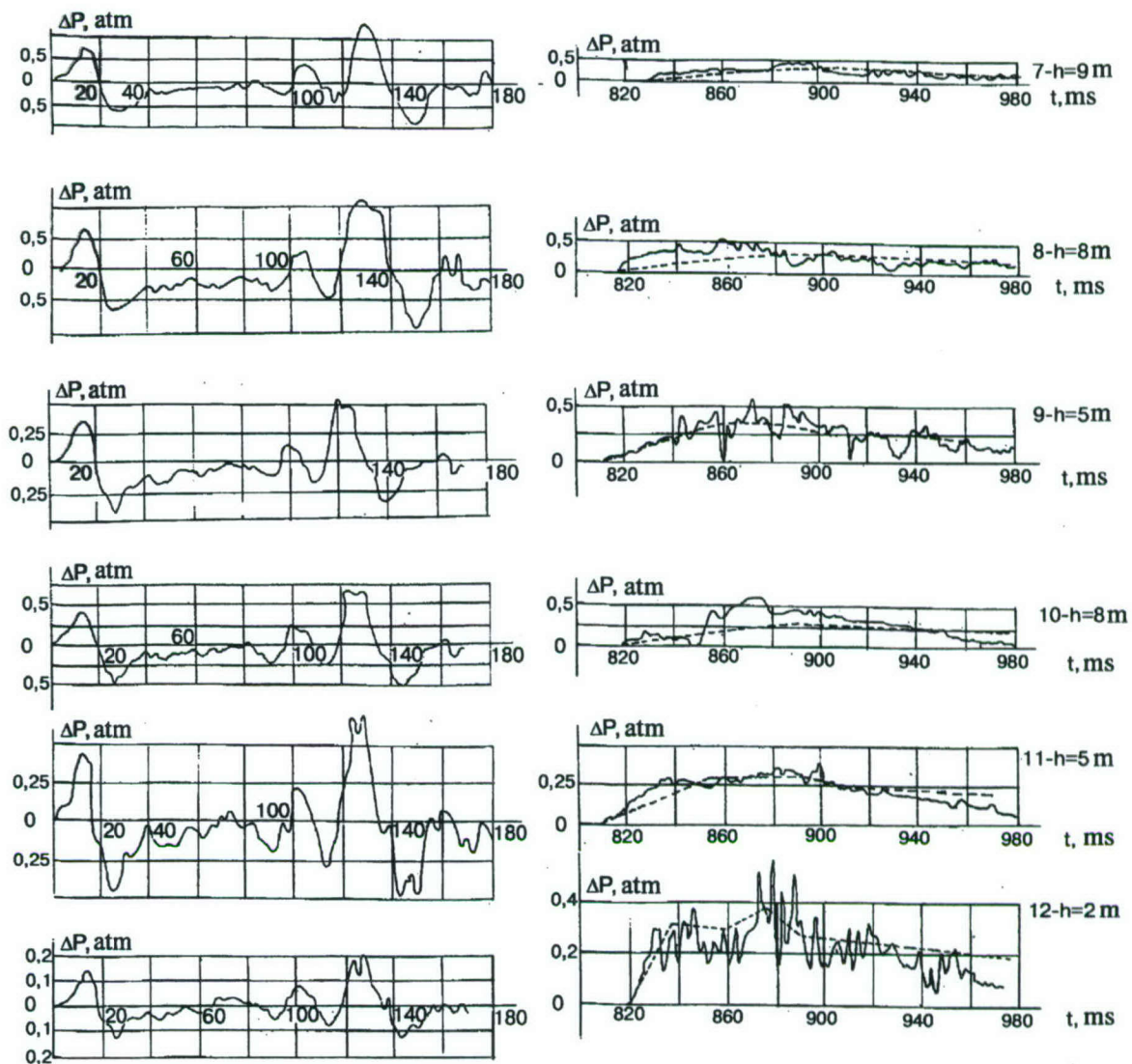
Figure 1.7.7b. Records of overpressure waves in water at points 7 to 12 (Figure 1.7.2).
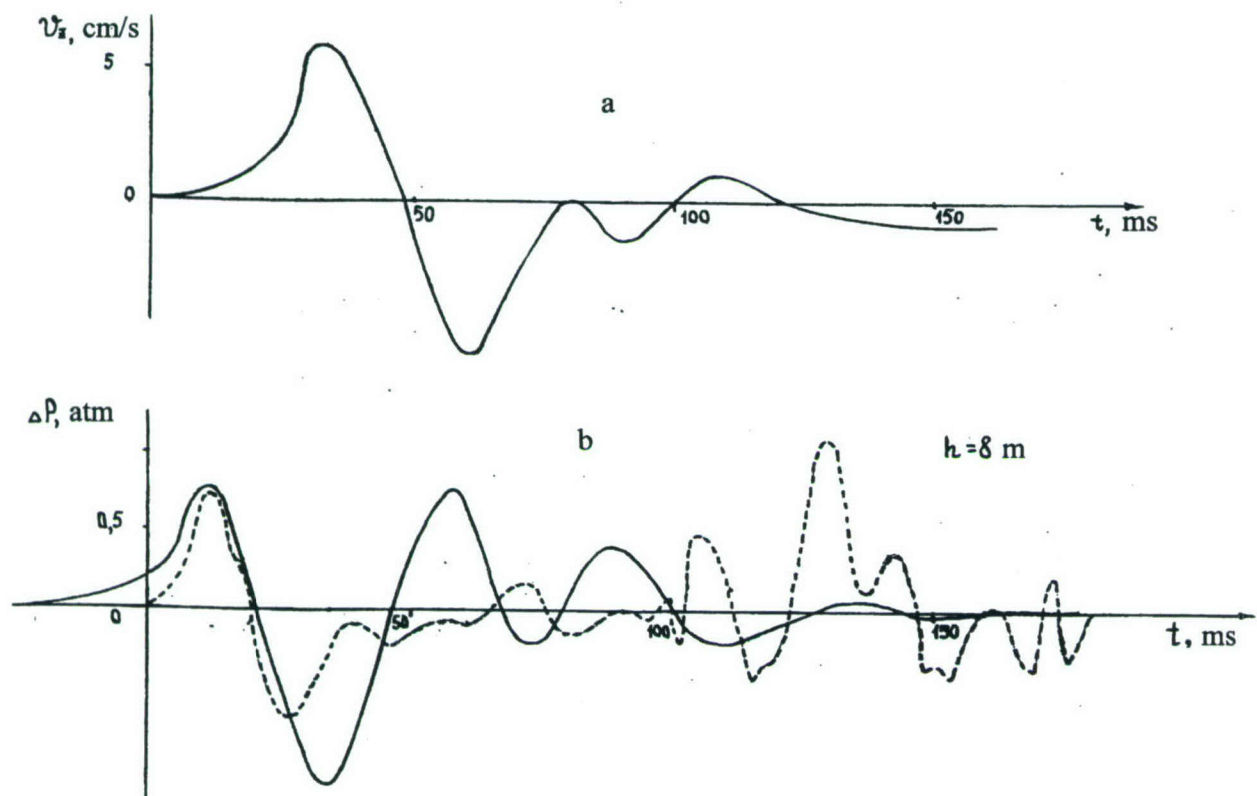
Figure 1.7.8. Comparison of records of vertical particle speed on the coast (a) and pressure of the underwater wave (b) at identical distance (590 m). Dotted line – observed pressure in water, solid line – calculated values.
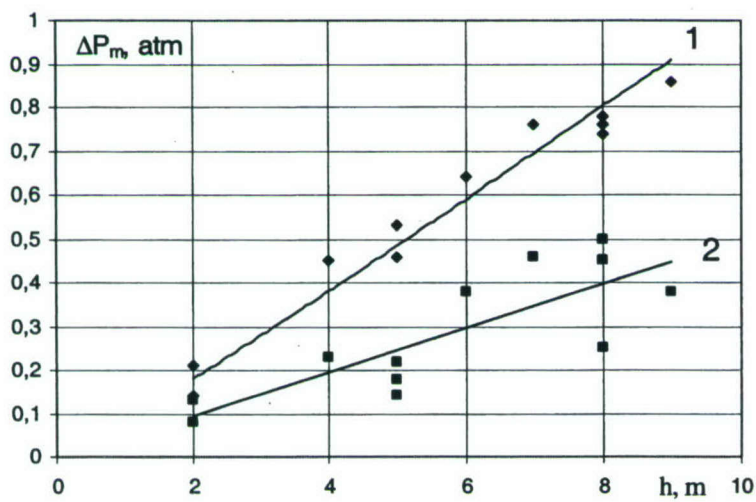
Figure 1.7.9. Dependence of the peak overpressure in the first and second groups of water waves (denoted by 1 and 2) on gauge depth h.

1.7.2. Measurements from HE explosions on the water surface.

Measurements of shock waves parameters in water, air and ground from explosions of half-immersed cast spherical charges of 100-kg TNT are shown in Tables 1.7.2, 1.7.3, 1.7.4, and 1.7.4a. The following notations are used in these tables: basin depth H_b, distance R, gauge depth h, $R_0 = 0.246$ m – is the charge radius, peak overpressure ΔP_m, duration t, specific impulse I, specific energy of shock waves E, E_{+mid}, kgm/m^2 - averaged from measurements of E at different depth for a given distance R, E_{1mid}, kgm = $2\pi R H_b E_{+mid}$, E_0 - energy of explosion., $E_1 = E_2 = 2\pi E R^2$.

Figure 1.7.10 shows dependence in air and water of the ratio of shock wave energy to the energy of explosion, E/E_0 %, on distance R from a half-immersed 100-kg TNT charge, basin depth $H_b = 3$ m (test No. 23). Figure 1.7.11 shows the dependencies of E/E_0 % in air, ground and water on distance R from half-immersed 100-kg TNT blasts, basin depth $H_b = 0.25$ m (tests N0. 10 and No. 11). The largest portion of energy from such explosions is transferred to air, a smaller portion goes in the ground, and the smallest portion is water.

Table 1.7.2. Parameters of water shock waves measured by piezoelectric gauges from half-immersed explosions of 100-kg TNT.

№ test	R/R_0	h/R_0	ΔP_m, kg/cm^2	t, µs	I, kgs/m^2	E, kgm/m^2	E_{1mid}, kgm	E_{1mid}/E_0, %
Test № 23; basin depth $H_b = 3.0$ m; charge depth H = 0.0 m								
23	120	1.0	15.7	20	1.54	1.26	6095	0.015
	120	2.0	18.0	27.2	2.80	2.45		
	120	6.0	19.3	97.3	11.2	11.3		
	120	8.0	20	124	13.4	11.4		
	120	10	29	65.4	14.9	27.3		
	120	11	28	39.3	7.9	11		
	60	1	41.0	27.6	11.4	15		
	60	2	47.5	48.5	13.8	24.4	31877	0.08
	60	4	60	86	25.8	66		
	60	6	60.5	118	34.0	67.8		
	60	6	60	122	47.5	103.2		
	60	8	69.8	154	62.8	158.8		
	60	10	72.2	131	56.8	248		
	60	11	79.5	81.7	52	220.4		
Test № 10; basin depth H_b=0.25 m; H=0.0 m								
10	30	0.5	14.4	6.4	0.66	0.48	5.62	0.000013
Test № 11; basin depth H_b=0.25 m; H=0.0 m								
11	30	0.5	16.7	8	0.58	0.44	5.18	0.000012

The characteristic wave pattern of above-water explosions is shown in Figure 1.7.12 for a deep basin. There are three waves in water - refracted, epicentral (caused by the impact of yields of explosion) and a wave originating from the air wave at distances $R > 18$ $m/kg^{1/3}$, where it begins to lag behind the refracted wave. Figure 1.7.13 shows characteristic details of the wavefield in the near zone of a half-immersed charge for deep basins.

Figure 1.7.14 to Figure 1.7.16 show optical and piezoelectric measurements of peak overpressure in water and air from explosions of small charges above the surface of water and ground.

Table of 1.7.3. Parameters of air shock waves measured by piezoelectric gauges from half-immersed explosions of 100-kg TNT charges.

№ test	Depth basin, m	Distance, m	ΔP_m, kg/cm^2	I, kg s/m^2	τ, ms	E, kgm/m^2	E_1, MJ	E_2/E_0 %
10	0.25	26	0.35	16	14.2	727	30.9	7.37
10	0.25	29.9	0.36	12	12.9	514	28.9	6.9
11	0.25	28	0.5	27.5	17.9	1882	92.6	22
11	0.25	31	0.46	18	14.0	1032	62.3	14.9
23	3	32	0.30	11	13.5	405	26.1	6.23
23	3	36	0.26	10.8	12.4	403	32.8	7.82

Table 1.7.4. Results of digitization of strain and piezoelectric (*) gauges. Overpressure oscillograms in ground from half-immersed explosions of 100-kg TNT charges. Characteristic points from Figure 1.6.4a for the near-filed zone, t is in ms, ΔP is in kg/cm^2.

Test, №	R, M	H, m	H, Z	t_1 / ΔP_1	t_1^1	t_1^{11}		t_2 / ΔP_2	t_2^1	t_2^{11}		t_3 / ΔP_3	t_3^1	t_3^{11}	
10	4	0.5	Z*	6	6.5	11	1.7	17	17.	20	11.2				
	4	1	Z*	5	10	12.5	0.7	12.	5	17.	2.7				
	7	0.5	Z*	8	10	15	1.9	5	13.	5	0.4				
	7	0.5	H*	9.5	10	16	0.4	25	5	35	0.8				
	7	2	Z*	10	24	35	2.4	25	26	28					
								25.							
								5							
11	4	0.5	Z*	5.8	6	14	1.7	16.	17.	23	3.4				
	4	0.5	Z	3	3.2	6.5	3.9	5	5	12	1.3	17	17.	18.5	2.9
	4	0.5	H	3	4	6.5	12.5	8	8.5	10.	1.3	17	5	24	2.8
	7	0.5	Z*	9	11	20	1.6	8	9.5	5	0.7		18.		
	7	0.5	H*	10	11	12	0.5	24	25	27	0.9		5		
	7.5	0.5	H	3	3.4	5	0.4	23	24.	29.	0.5	30		37	0.5
	7	2.0	Z*	17.5	22.		1.2	14	5	5	2.2		32	36	1.0
	7	2.0	Z	20	5		0.62		16.	25	1.0			38	0.7
	7	2.0	H	20	22		0.3		5	35	0.9		30		
					23				23.				32.		
									5				5		
									24						
									24.						
									5						

Table of 1.7.4a. Shock-wave parameters in ground from half-immersed explosions of 100-kg TNT charges.

R, m	h, m	ΔP_m, kg/cm²	τ, ms	I, kgs/m²	E, kgm/m²	E_1, MJ	E_2, kg TNT	E_{mid}, kg TNT	E_{mid}/E_0 %
Test 10, depth of basin 0.25 m, depth of charge 0.0 m									
4	0.5Z*	11.2	14	164	162.6	0.166	0.04	0.04	0.04
4	1.0Z*	2.7	12.5	93.7	24.7	0.026	0.0063	0.063	0.063
7	0.5Z*	1.9	27	82.3	14.7	0.046	0.011	0.011	0.011
7	0.5H*	0.8	18.5	21.7	1.2	0.0037	0.0009		
7	2Z*	2.4	25	221	58.7	0.195	0.047	0.047	0.047
Test 11, depth of basin 0.25 m, depth of charge 0.0 m									
4	0.5Z*	3.4	17.2	138	42	0.043	0.01	0.068	0.068
4	0.5Z	3.9	15.5	87.4	24.5	0.025	0.006		
4	0.5H	12.5	21	299	271	0.228	0.067		
7	0.5Z*	1.6	18	74	11.7	0.036	0.0086	0.0089	0.0089
7	0.5H*	0.9	19.5	34	3	0.0093	0.0022		
7.5	0.5H	0.51	34	56.3	3.41	0.0121	0.003	0.003	0.003
7	2Z*	2.2	17.5	109	22.4	0.0744	0.0178	0.0175	0.0175
7	2Z	1.0	16	103	14.3	0.048	0.0114		
7	2H	0.9	18	97.7	12.3	0.041	0.0098		
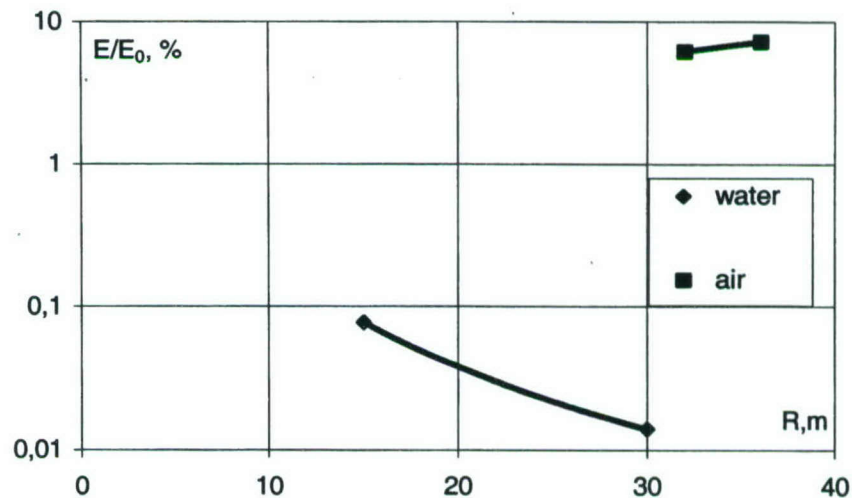
Figure 1.7.10. Dependence of E/E_0 % in air and water on distance R from a half-immersed explosion of 100-kg TNT, test No. 23. Basin depth H_b=3 m.
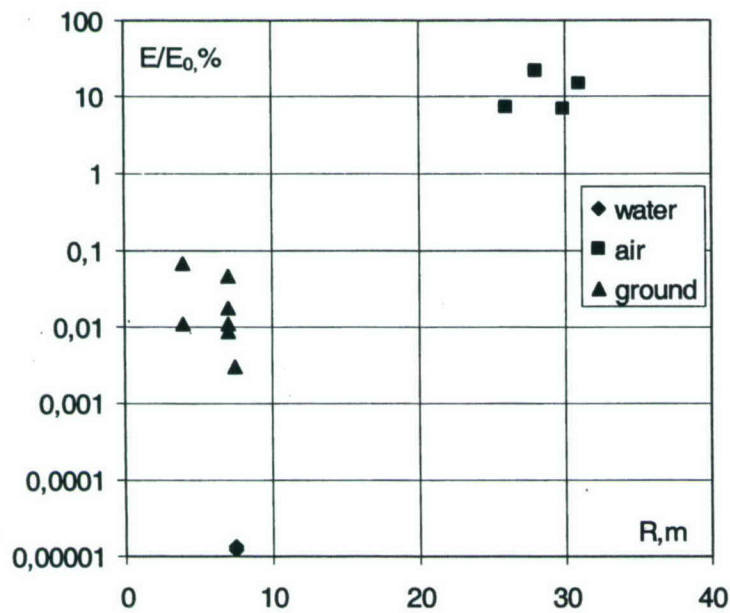
Figure 1.7.11. Dependence of E/E_0 % in air, ground and water on distance R from half-immersed explosions of 100-kg TNT charges, tests No. 10 and No.11. Basin depth H_b =0.25 m.
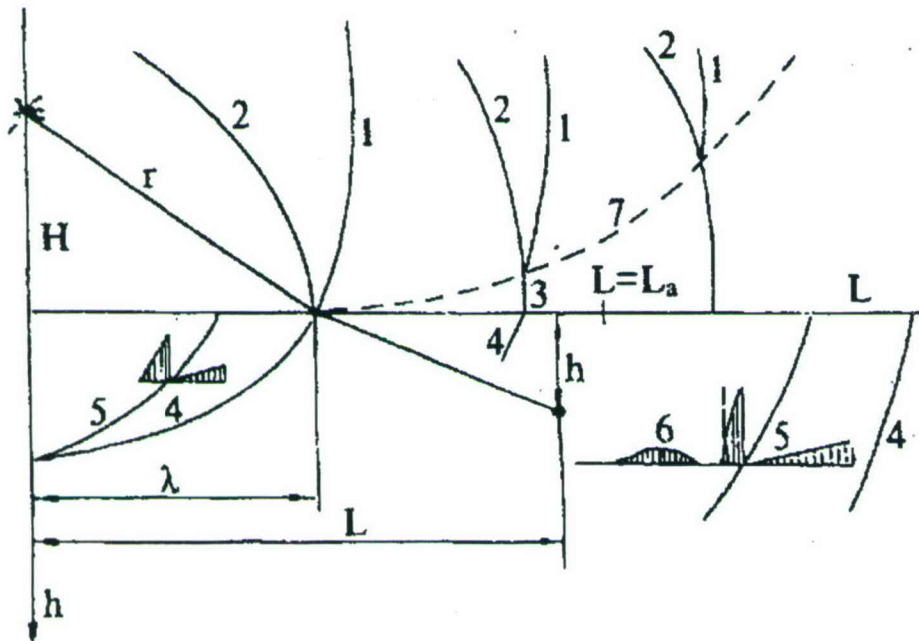
Figure 1.7.12. Waves from above-water explosions. 1, 2, and 3 - direct, reflected and Mach waves in air. 4, 5, and 6 - refracted, epicentral and compressional waves in water.
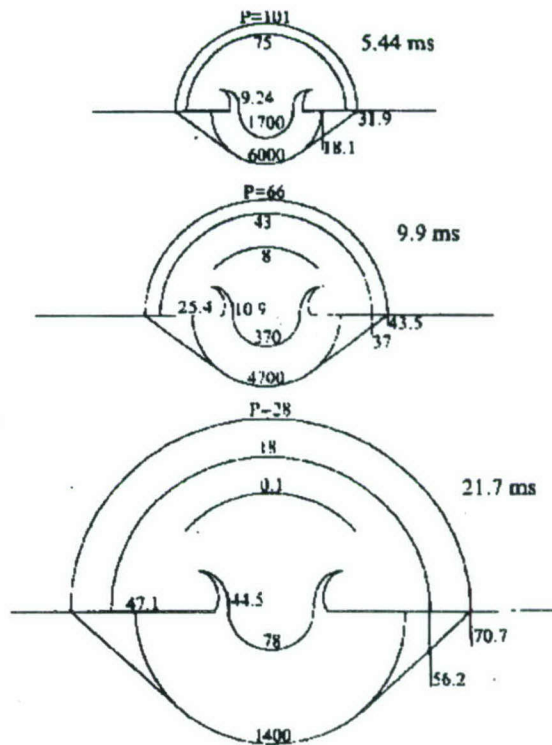
Figure 1.7.13. Characteristic details of the wavefield in the near zone of a half-immersed 1-kt TNT explosion. Pressure in atmospheres is indicated along the vertical axis, range in meters is shown along the horizontal axis.
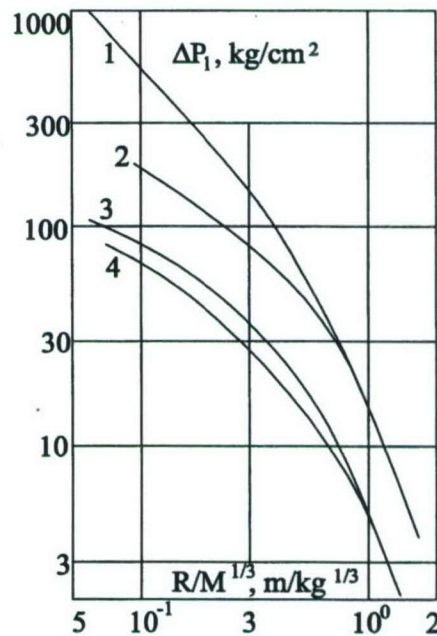
Figure 1.7.14. Dependence of the peak overpressure ΔP_1 kg/cm^2 of the air shock wave in the near zone on scaled distance $R/M^{1/3}$ from explosions of spherical PETN charges with densities 1600 and 400 kg/m^3 and lead azid charges with density 1600 and 850 kg/m^3 (curves 1 to 4, respectively).
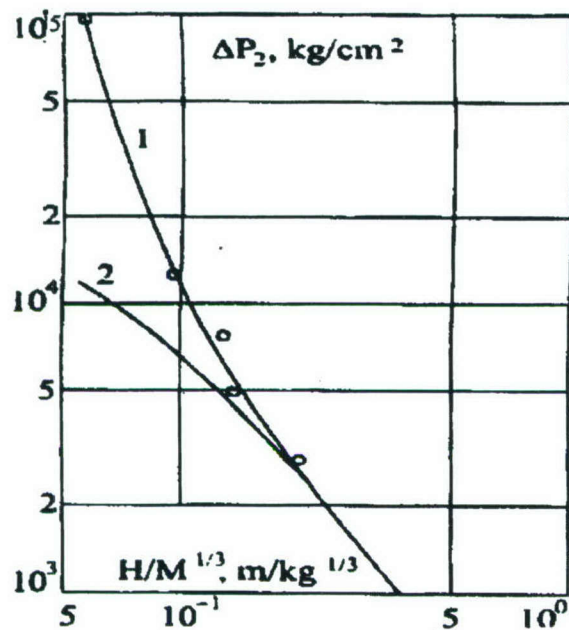
Figure 1.7.15. Peak overpressure ΔP_2 of the refracted in water shock wave versus scaled height $H/M^{1/3}$ above water from explosions of spherical charges of PETN. 1 - experiment, 2 - calculated reflected overpressure from a rigid wall.
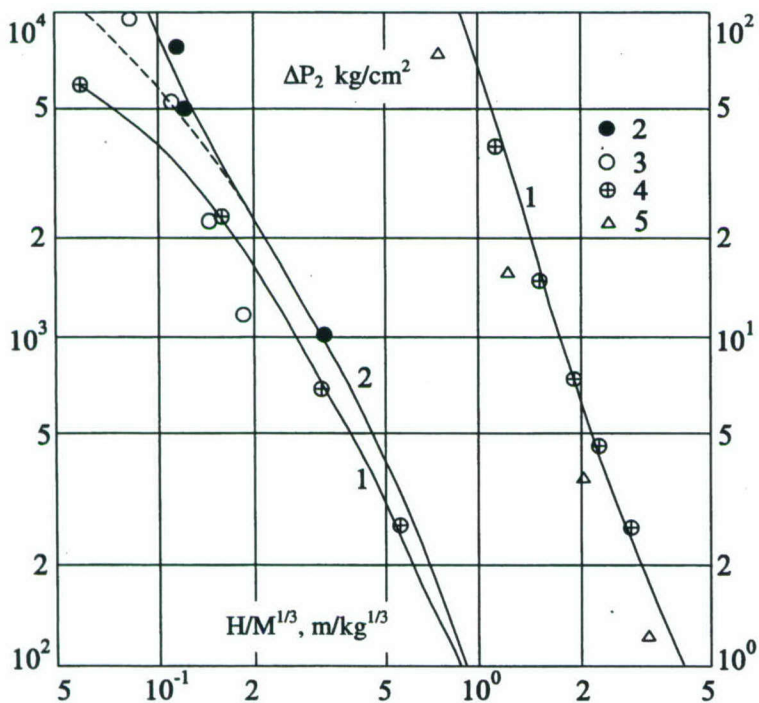
Figure 1.7.16. Peak overpressure ΔP_2 of the shock wave reflected from a rigid wall, versus scaled height $H/M^{1/3}$ of explosions of different HE. M - TNT equivalent. calculation for cast TNT, 2 - PETN with 1600 kg/m^3 density, 3 - TNT/RDX –50%/50%, 4 - cast TNT, 5 - nuclear explosions.

Digital data of measurements in water, air and ground from explosions of half-immersed cast spherical charges of 100-kg TNT and of the 1000-t TNT explosion on the coast of Matochkin Shar are shown in tables 1.7.1 to 1.7.4 (Word file-Tab17_1_2_3.doc); 28 Excel files: 4 files with measurements in air - Ch17A_10_26; Ch17A_10_29; Ch17A_11_28; Ch17A_11_31 (e.g., notations: Ch17A_10_26 - Chapter 1.7, air, test 10, distance 26 m); 5 files with measurements in ground – Ch17G_11_4_06H, Ch17G_11_4_06Z, Ch17G_11_7.5_05H, Ch17G_11_7_2H, Ch17G_11_7_2Z (e.g., notations: Ch17G_11_4_06H - Chapter 1.7, ground, test 11, distance 4 m, depth 0.6 m, horizontal component of pressure); 8 files with measurements in water from test 23 at distance $60R_0$ - Ch17W_4_60_1; Ch17W_4_60_2; Ch17W_5_60_4; Ch17W_5_60_6;Ch17W_8_60_6a; Ch17W_8_60_8; Ch17W_9_60_10; Ch17W_9_60_11; 6 files with measurements in water from test 23 at distance $120R_0$ - Ch17W_3_120_1; - Ch17W_3_120_2; - Ch17W_6_120_6; - Ch17W_6_120_8; - Ch17W_7_120_10; - Ch17W_7_120_11; 3 files with measurement of shock waves in air from the 1000-t TNT explosion- Fig174a, Fig 174 b, Fig 174 c.

1.8. Effect of depth of underwater explosions on the parameters of shock wave and energy transferred in water, air and ground.

In order to characterize the effect of depth of underwater explosions in shallow basins on the shock wave parameters and the energy transferred to air, ground and water, the oscillograms of shock waves from 100-kg TNT explosions of different depths H were digitized. The water level in the reservoir was varied: H_b = 2, 4 and 12 R $_0$ (i.e., 0.5 m, 1 m, and 3 m). There was air-saturated sand on the bottom. [Note by M. Eneva – the explosion configurations, results of measurements, and the reservoir dimensions and characteristics of the bottom were also described in Chapters 1.4 to 1.6]. Table 1.8.1 points to the MS Excel files containing digitized data of pressure and impulse in water (Chapter 1.4), air (Chapter 1.5) and ground (Chapter 1.6) for the 29 underwater explosions. [Note by M. Eneva – the filenames contain numbers pointing to the individual explosions. The names given in the table are actually the names of the sheets within the MS Excel files].

Figure 1.8.1 to 1.8.6 show several examples from the IDG archives.

Figure 1.8.1 shows the dependence of the maximum overpressure of the shock waves in air on the relative distance R/R_0 for different charge depths and water level $4R_0$. The curves 1, 2, 3, and 4 correspond to depths of charge H = 0, 1, 2, $3R_0$. They are constructed using data from the processing of high-speed shadow photos of laboratory explosions of spherical PETN charges of small weight (near zone) and 100-kg TNT charges (far zone). The dotted line denotes calculated values using the formula of M. A. Sadovsky for explosion in the air, where the charge is on the ground.

Figure 1.8.2 to 1.8.6 present measured and estimated parameters of the shock waves in water from the 100-kg TNT explosions. The measurements were made with piezoelectric gauges at distances 30, 60, 90 and $120R_0$ (i.e., 7.5 m, 15 m, 22.5 m, and 30 m) – see Chapter 1.4. The distances and gauge depths are expressed in units of charge radius R_0 = 0.25 m. The signal registration was done using devices PID-9 and PEU-3. PID-9 was the perfect device for the purpose and only its data were shown in earlier chapters. The data recorded by PEU-3 are shown for the first time here.

Figure 1.8.2 displays experimental points from three charge depths (H = 1, 2, $3R_0$) in a basin with water level $4R_0$. The curves are calculated using theoretical representations [Note by M. Eneva – I assume that formulas from Kozachenko and Khristoforov, 1970, are used]. The measurements indicate that in reservoirs of depth $H_b \leq 4 R_0$, the parameters of shock waves in the studied range of distances, do not appear to depend on depth of explosion. The dependence on depth decreases as distance from explosion increases, where the parameters of shock waves are determined by nonlinear interaction of the direct wave with waves of unloading [Note by M. Eneva – I assume rarefaction is meant here], repeatedly reflected from the bottom and the free surface.

Figure 1.8.3 to 1.8.5 show predicted values (lines) and experimental data (circles – recorded by PID-9 and crosses – recorded by PEU-3). These figures show the dependence on sensor depth of the maximum overpressure, pulse duration and specific impulse of the shock wave in water, for

explosion depths H = 1, 4, 6 R_0 (i.e., 0.25 m, 0.5 m, and 1.5 m) and water level 12R_0 (i.e., 3 m) The relationships used to calculate the predicted values take into account the nonlinear processes of reflection of shock waves in water from the free surface and the low-velocity bottom.

Figure 1.8.6 shows the dependence of maximum overpressure of shock wave in water on water level, for explosion and sensor depths H = h = 1R_0. The dotted lines show predictions for boundless liquid.

Figure 1.8.7 to 1.8.10 show the ratio of shock-wave energy to energy of explosion, E/E_0, versus distance R in air, water and ground, for explosions depths H = 0.75, 0.5 and 0.25 m, and water level H_b = 1 m. Figure 1.8.11 displays the same for explosion depth H = 0.25 m and basin depth H_b = 0.5 m. Figure 1.8.12 shows the energy ratio for a half-immersed charge, H = 0.0 m, and water level H_b = 0.25 m. Finally, Figure 1.8.13 and 1.8.14 show this ratio for a full reservoir, H_b =3.0 m; and explosion depths H = 0 and 0.25 m; measurements in ground were not made from tests in full basin.

The air-saturated sand on the bottom has an effect as the free surface [Note by M. Eneva – because the sound velocity in this layer is 270 m/s]. In a basin 12R_0 deep, both regular and nonregular reflection was observed from the free surface and the bottom, depending on the explosion/gauge relative positions. For water level 4R_0 and lower, only nonregular reflection was observed in the studied distance range from both surfaces. In such conditions, the shock-wave parameters peak in the center of the reservoir regardless of explosion depth, since rarefaction waves are reflected from both surfaces.

At large distances from the explosions a critical regime is established due to multiple reflections. In such a regime overpressure depends little on charge and gauge positions and is determined mostly by the effect of the reservoir surfaces.

These measurements show that the largest portion of energy at large distances from explosions in shallow basins is transferred to the air shock waves. The energy of shock waves in ground and water is smaller than the energy of shock waves in air by an order of magnitude or more. As the charge approaches the bottom, the portion of energy transferred to the ground increases and can surpass the energy of shock wave in water. As the water level and explosion depth increases, the energy of shock wave in water increase, while the energy of shock wave in air decreases, but still exceeds the energy of shock wave in water.

Table 1.8.1.

№ tests	Depth Basins H_b, m	Charge Depth H, m	Water			Air		Ground		
			Names of sheets	R,m	h,m	Names of sheets	R,m	Names of Sheets	R,m	h,m
1	1.0	0.75	Ch14_14_4_3_2	15	0.5	Ch15_1_174_075	17.4	Ch16_1_7_2H	7	2
			Ch14_14_4_3_2_	15	0.5			Ch16_1_7_2Z	7	2
								Ch16_1_7.5_05H	7.5	0.5
								Ch16_1_7.5_05Z	7.5	0.5
2	1.0	0.75	Ch14_25_4-3_2_	7.6	0.5	Ch15_2_174_075	17.4	Ch16_2_7_2H	7	2
			Ch14_25_4-3_2	7.6	0.5	Ch15_2_126_075	12.6	Ch16_2_7_2Z	7	2
			Ch14_22_4_3_2_	45.5	0.5			Ch16_2_7.5_05Z	7.5	0.5
			Ch14_22_4_3_2	45.5	0.5					

№ tests	Depth Basins H_b, m	Charge Depth H, m	Water Names of sheets	R,m	h,m	Air Names of sheets	R,m	Ground Names of Sheets	R,m	h,m
3	1.0	0.75	Ch14_34_4_3_3	15	0.75	Ch15_3_132_075	13,2	Ch16_3_7_2H	7	2
			Ch14_34_4_3_3_	15	0.75			Ch_16_3_7_2Z	7	2
			Ch14_32_4_3_3	45.5	0.75			Ch16_3_7.5_05H	7.5	0.5
			Ch14_32_4_3_3_	45.5	0.75			Ch16_3_7.5_05Z	7.5	0.5
4	1.0	0.50	Ch14_45_4-2_2	7.5	0.5	Ch15_4_14_05	14	Ch16_4_7_2H	7	2
			Ch14_45_4-2_3	7,5	0.75	Ch15_4_175_05	17,5	Ch16_4_7_2Z	7	2
			Ch14_44_4_2_3	15	0.75			Ch16_4_7.5_05H	7.5	0.5
			Ch14_44_4_2_3_	15	0.75			Ch16_4_7.5_05Z11	7.5	0.5
			Ch14_43_4_2_2	30	0.5			Ch16_3_7.5_05Z6		
			Ch14_43_4_2_2_	30	0.5					
5	1.0	0.50	Ch14_55_4_2_1	7.5	.25	Ch15_5_174_05	17.4	Ch16_5_4_0.5H	4	0.5
			Ch14_55_4-2_2	7.5	.5	Ch15_5_21_05	21	Ch16_5_4_0.5Z	4	0.5
			Ch14_54_4_2_2_	15	0.5			Ch16_5_7_2H	7	2
			Ch14_54_4_2_2	15	0.5			Ch16_5_7.5_05H	7.5	0.5
			Ch14_53_4_2_3	30	0.75			Ch16_5_7.5_05Z	7.5	0.5
			Ch14_53_4_2_3_	30	0.75					
6	1.0	0.50	Ch14_64_4_2_05	15	0.125			Ch16_6_4_05H	4	0.5
			Ch14_64_4_2_1	15	0.25			Ch16_6_4_05Z	4	0.5
			Ch14_65_4_2_2	15	0.50			Ch16_6_7_2H	7	2
			Ch14_65_4_2_3	15	0.75			Ch16_6_7_2Z	7	2
			Ch14_63_4_2_2	30	0.5			Ch16_6_7.5_05H	7.5	0.5
			Ch14_63_4_2_3	30	0.75			Ch16_6_7.5_05Z	7.5	0.5
7	0.95	0.25	Ch14_74_4_1_05	15	.125	Ch15_7_21_025	21	Ch16_7_4_05H	4	0.5
			Ch14_74_4_1_1	15	0.25	Ch15_7_26_025	26	Ch16_7_4_05Z	4	0.5
			Ch14_75_4_1_2	15	0.5				7	2
			Ch14_75_4_1_3	15	0.75			Ch16_7_7_2H	7	2
								Ch16_7_7_2Z	7.5	0.5
								Ch16_7_7.5_05H	7.5	0.5
								Ch16_7_7.5_05Z		
8	0.95	0.25	Ch14_84_4_1_05	15	0.125	Ch15_8_205_025	20.5	Ch16_8_4_05H	4	0.5
			Ch14_84_4_1_1	15	0.25	Ch15_8_256_025	25.6	Ch16_8_4_05Z	4	0.5
			Ch14_85_4_1_2	15	0.5			Ch16_8_7_2H	7	2
			Ch14_85_4_1_3	15	0.75			Ch16_8_7_2Z	7	2
			Ch14_82_4_1_05	30	0.125			Ch16_8_7.5_05H	7.5	0.5
			Ch14_82_4_1_1	30	0.25			Ch16_8_7.5_05Z	7.5	0.5
			Ch14_83_4_1_2	30	0.5					
			Ch14_83_4_1_3	30	0.75					
9	0.50	0.25	Ch14_94_2_1_05	7.5	0.125	Ch15_9_22_025	22	Ch16_9_4_05H	4	0.5
			Ch14_95_2_1_1_	7.5	0.25	Ch15_9_26_025	26	Ch16_9_4_05Z	4	0.5
			Ch14_95_2_1_1	7.5	0.25			Ch16_9_7_2H	4	2
			Ch14_94_2_1_1.5	7.5	0.325			Ch16_9_7_2Z	7	2
			Ch14_93_2_1_1	15	0.25			Ch16_9_7.5_05H	7	0.5
			Ch14_93_2_1_1__	15	0.25			Ch16_9_7.5_05Z	7	0.5
									7.5	
									7.5	
10	0.25	0.0	Ch14_105_1_0_05	7.5	0.125	Ch15_10_26_00	26			
						Ch15_10_299_00	29.9			
11	0.25	0.0	Ch14_115_1_0_05	7.5	0.125	Ch17A_11_28_	28	Ch17G_11_4_06H	4	4
						Ch15_11_31_0.0	31	Ch17G_11_4_06Z	4	4
								Ch17G_11_7_2H	7	7
								Ch17G_11_7_2Z	7	7
								Ch17G_11_7.5_05H	0.5	7.5
12	1.0	0.50	Ch14_124_4_2_05	15	0.125	Ch15_12_204_05	20.4			
			Ch14_124_4_2_05_	15	0.125	Ch15_12_24_05	24			
			Ch14_129_4_2_2	15	0.5					
			Ch14_125_4_2_3	15	0.75					
			Ch14_126_4_2_1	22.5	0.25					
			Ch14_123_4_2_3	22.5	0.75					

№ tests	Depth Basins H_b, m	Charge Depth H, m	Water			Air			Ground		
			Names of sheets	R,m	h,m	Names of sheets	R,m	h,m	Names of Sheets	R,m	h,m
13	1.0	0.50	Ch14_134_4_2_05	7.5	0.125	Ch15_13_25_05	25				
			Ch14_134_4_2_05	7.5	0.125	Ch15_13_29_05	29				
			Ch14_138_4_2_1	7.5	0.25						
			Ch14_138_4_2_1_	7.5	0.25						
			Ch14_139_4_2_2	7.5	0.5						
			Ch14_135_4_2_3.	7.5	0.75						
			Ch14_136_4_2_1	15	0.25						
			Ch14_137_4_2_2	15	0.5						
			Ch14_133_4_2_3	15	0.75						
14	1.0	0.75	Ch14_143_4_3_3	15	0.75	Ch15_14_15_0.75	15				
			Ch14_146_4_3_1	15	0.25	Ch15_14_19_075	19				
			Ch14_144_4_3_05	22.5	0.125						
			Ch14_144_4_3_05_	22.5	0.125						
			Ch14_145_4_3_3	22.5	0.75						
			Ch14_149_4_3_2	22.5	0.5						
			Ch14_149_4_3_3.5	22.5	0.875						
15	1.0	0.75	Ch14_153_4_3_3.	7.5	0.75	Ch15_15_164_0.7 5	16.4 20.7				
			Ch14_156_4_3_1	7.5	0.25						
			Ch14_156_4_3_1_	7.5	0.25	Ch15_15_207_075					
			Ch14_157_4_3_2.	7.5	0.5						
			Ch14_154_4_3_0.5	15	0.125						
			Ch14_154_4_3_05_	15	0.125						
			Ch14_155_4_3_3	15	0.75						
			Ch14_159_4_3_2	15	0.5						
			Ch14_159_4_3_3.5	15	0.88						
16	1.0	0.25	Ch14_164_4_1_05	15	0.125	Ch15_16_30_025	30				
			Ch14_164_4_1_05	15	0.125	Ch15_16_35_025	35				
			Ch14_169_4_1_2	15	0.5						
			Ch14_165_4_1_3	15	0.75						
			Ch14_165_4_1_3_	15	0.75						
			Ch14_169_4_1_3.5	15	0.88						
			Ch14_162_4_1_05	22.5	0.125						
			Ch14_162_4_1_05_	22.5	0.125						
			Ch14_166_4_1_1	22.5	0.25						
			Ch14_166_4_1_1_	22.5	0.25						
			Ch14_167_4_1_2	22.5	0.5						
			Ch14_163_4_1_3	22.5	0.75						
			Ch14_163_4_1_3_	22.5	0.75						
			Ch14_167_4_1_3.5	22.5	0.88						
17	1.0	0.25	Ch14_174_4_1_05	7.5	0.125	Ch15_17_26_025	26				
			Ch14_174_4_1_05_	7.5	0.125	Ch15_17_30_025	30				
			Ch14_178_4_1_1	7.5	0.25						
			Ch14_178_4_1_1_	7.5	0.25						
			Ch14_179_4_1_2	7.5	0.5						
			Ch14_175_4_1_3	7.5	0.75						
			Ch14_175_4_1_3_	7.5	0.75						
			Ch14_179_4_1_3.5	7.5	0.88						
			Ch14_176_4_1_1	15	0.25						
			Ch14_176_1_1_	15	0.25						
			Ch14_177_4_1_2	15	0.5						
			Ch14_173_4_1_3	15	0.75						
			Ch14_173_4_1_3_	15	0.75						
			Ch14_177_4_1_3.5	15	0.88						

№ tests	Depth Basins H_b, m	Charge Depth H, m	Water Names of sheets	R,m	h,m	Air Names of sheets	R,m	Ground Names of Sheets	R,m	h,m
18	3.0	0.25	Ch14_183_12_1_1	15	0.25	Ch15_18_299_025	29.9			
			Ch14_183_12_1_2	15	0.50	Ch15_18_26_025	26			
			Ch14_184_12_1_1	30	0.25					
			Ch14_184_12_1_2	30	0.50					
			Ch14_188_12_1_6	30	1.5					
			Ch14_188_12_1_8	30	2.0					
			Ch14_189_12_1_10	30	2.5					
			Ch14_189_12_1_11	30	2.75					
19	3.0	0.50	Ch14_193_12_2_1	15	0.25					
			Ch14_193_12_2_2	15	0.50					
			Ch14_196_12_2_6	15	1.5					
			Ch14_196_12_2_8	15	2.0					
			Ch14_197_12_2_10	15	2.5					
			Ch14_197_12_2_11	15	2.75					
			Ch14_194_12_2_1	30	0.25					
			Ch14_194_12_2_2	30	0.50					
			Ch14_195_12_2_4	30	1.0					
			Ch14_195_12_2_6	30	1.5					
			Ch14_198_12_2_6	30	1.5					
			Ch14_198_12_2_8	30	2.0					
			Ch14_199_12_2_10	30	2.5					
			Ch14_199_12_2_11	30	2.75					
20	3.0	1.0	Ch14_203_12_4_1	15	0.25					
			Ch14_203_12_4_2	15	0.5					
			Ch14_206_12_4_6	15	1.5					
			Ch14_206_12_4_8	15	2.0					
			Ch14_207_12_4_10	15	2.5					
			Ch14_207_12_4_11	15	2.75					
			Ch14_204_12_4_1	30	0.25					
			Ch14_204_12_4_2	30	0.5					
			Ch14_205_12_4_4	30	1.0					
			Ch14_205_12_4_6	30	1.5					
			Ch14_208_12_4_6	30	1.5					
			Ch14_208_12_4_1	30	2.0					
21	3.0	1.50	Ch14_213_!2_6_1	15	0.25					
			Ch14_213_!2_6_2	15	0.50					
			Ch14_216_!2_6_6	15	1.5					
			Ch14_216_!2_6_8	15	2.0					
			Ch14_217_!2_6_10	15	2.5					
			Ch14_217_!2_6_11	15	2.75					
			Ch14_214_!2_6_1	30	0.25					
			Ch14_214_!2_6_2	30	0.50					
			Ch14_215_!2_6_4	30	1.0					
			Ch14_215_!2_6_6	30	1.5					
			Ch14_218_!2_6_6	30	1.5					
			Ch14_218_!2_6_8	30	2.0					
			Ch14_219_!2_6_10	30	2.5					
			Ch14_219_!2_6_11	30	2.75					

№ tests	Depth Basins H_b, m	Charge Depth H, m	Water			Air		Ground		
			Names of sheets	R,m	h,m	Names of sheets	R,m	Names of Sheets	R,m	h,m
22	3.0	2.75	Ch14_224_12_11_1	15	0.25					
			Ch14_224_12_11_2	15	0.50					
			Ch14_225_12_11_4	15	1.0					
			Ch14_225_12_11_6	15	1.5					
			Ch14_228_12_11_6	!5	1.5					
			Ch14_228_12_11_8	15	2.0					
			Ch14_229_12_11_1	15	2.5					
			0	15	2.75					
			Ch14_229_12_11_1	30	0.25					
			1	30	0.50					
			Ch14_223_12_11_1	30	1.50					
			Ch14_223_12_11_2	30	2.0					
			Ch14_226_12_11_6							
			Ch14_226_12_11_8							
23	3.0	0.0	Ch14_234_12_0_1	15	0.25	Ch15_23_32_0.0	32			
			Ch14_234_12_0_2	15	0.5	Ch15_23_36_00	36			
			Ch14_235_12_0_4	15	1.0					
			Ch14_235_12_0_6	15	1.5					
			Ch14_238_12_0_6	15	1.5					
			Ch14_238_12_0_8	15	2.0					
				15	2.5					
			Ch14_239_12_0_10	30	2.75					
			Ch14_239_12_0_11	30	0.25					
			Ch14_233_12_0_1	30	0.50					
			Ch14_233_12_0_2	30	1.5					
			Ch14_236_12_0_6	30	2.0					
			Ch14_236_12_0_8	30	2.5					
				30	2.75					
			Ch14_237_12_0_10							
			Ch14_237_12_0_11							
24	3.0	2.0	Ch14_244_12_8_1	7.5	0.25					
			Ch14_244_12_8_2	7.5	0.50					
			Ch14_248_12_8_6	7.5	1.5					
			Ch14_248_12_8_8	7.5	2.0					
			Ch14_249_12_8_10	7.5	2.5					
			Ch14_249_12_8_11	7.5	2.75					
			Ch14_243_12_8_1	22.5	0.25					
			Ch14_243_12_8_2	22.5	0.50					
			Ch14_246_12_8_6	22.5	1.5					
			Ch14_246_12_8_8	22.5	2.0					
			Ch14_247_12_8_10	22.5	2.5					
			Ch14_247_12_8_11	22.5	2.75					
25	3.0	0.25	Ch14_254_12_1_1	7.5	0.25	Ch15_25_31_025	31			
			Ch14_254_12_8_2	7.5	0.50	Ch15_25_33_025	33			
			Ch14_258_12_8_6	7.5	1.5					
			Ch14_258_12_8_8	7.5	2.0					
			Ch14_259_12_8_10	7.5	2.5					
			Ch14_259_12_8_11	7.5	2.75					
			Ch14_253_12_8_1	22.5	0.25					
			Ch14_253_12_8_2	22.5	0.50					
			Ch14_256_12_8_6	22.5	1.5					
			Ch14_256_12_8_8	22.5	2.0					
			Ch14_257_12_8_10	22.5	2.5					
			Ch14_257_12_8_11	22.5	2.75					

№ tests	Depth Basins H_b, m	Charge Depth H, m	Water			Air		Ground		
			Names of sheets	R,m	h,m	Names of sheets	R,m	Names of Sheets	R,m	h,m
26	3.0	0.50	Ch14_263_12_2_1	7.5	0.25					
			Ch14_263_12_8_2	7.5	0.50					
			Ch14_262_12_8_4	7.5	1.0					
			Ch14_262_12_8_6	7.5	1.5					
			Ch14_266_12_8_6	7.5	1.5					
			Ch14_266_12_8_8	7.5	2.0					
			Ch14_267_12_8_10	7.5	2.5					
			Ch14_267_12_8_11	7.5	2.75					
			Ch14_264_12_8_1	22.5	0.25					
			Ch14_264_12_8_2	22.5	0.50					
			Ch14_265_12_8_4	22.5	1.0					
			Ch14_265_12_8_6	22.5	1.5					
			Ch14_268_12_8_6	22.5	1.5					
			Ch14_268_12_8_8	22.5	2.0					
			Ch14_269_12_8_10	22.5	2.5					
			Ch14_269_12_8_11	22.5	2.75					
27	3.0	1.0	Ch14_273_12_4_1	7.5	0.25					
			Ch14_273_12_4_2	7.5	0.50					
			Ch14_272_12_4_4	7.5	1.0					
			Ch14_272_12_4_6	7.5	1.5					
			Ch14_276_12_4_6	7.5	1.5					
			Ch14_276_12_4_8	7.5	2.0					
			Ch14_274_12_4_1	7.5	0.25					
			Ch14_274_12_4_2	22.5	0.50					
			Ch14_275_12_4_4	22.5	1.0					
			Ch14_275_12_4_6	22.5	1.5					
			Ch14_278_12_4_6	22.5	1.5					
			Ch14_278_12_4_8	22.5	2.0					
			Ch14_279_12_4_10	22.5	2.5					
			Ch14_279_12_4_11	22.5	2.75					
28	3.0	1.50	Ch14_283_12_6_1	7.5	0.25					
			Ch14_283_12_8_2	7.5	0.50					
			Ch14_282_12_8_4	7.5	1.0					
			Ch14_282_12_8_6	7.5	1.5					
			Ch14_286_12_8_6	7.5	1.5					
			Ch14_286_12_8_8	7.5	2.0					
			Ch14_287_12_8_10	7.5	2.5					
			Ch14_287_12_8_11	7.5	2.75					
			Ch14_284_12_8_1	22.5	0.25					
			Ch14_284_12_8_2	22.5	0.50					
			Ch14_285_12_8_4	22.5	1.0					
			Ch14_285_12_8_6	22.5	1.5					
			Ch14_288_12_8_6	22.5	1.5					
			Ch14_288_12_8_8	22.5	2.0					
			Ch14_289_12_8_10	22.5	2.5					
			Ch14_289_12_8_11	22.5	2.75					

№ tests	Depth Basins H_b, m	Charge Depth H, m	Water			Air		Ground		
			Names of sheets	R,m	h,m	Names of sheets	R,m	Names of Sheets	R,m	h,m
9	3.0	2.75	Ch14_293_12_1_1_	7.5	0.25					
			Ch14_293_12_8_2	7.5	0.50					
			Ch14_292_12_8_4	7.5	1.0					
			Ch14_292_12_8_6	7.5	1.5					
			Ch14_296_12_8_6	7.5	1.5					
			Ch14_296_12_8_8	7.5	2.0					
			Ch14_297_12_8_10	7.5	2.5					
			Ch14_297_12_8_11	7.5	2.75					
			Ch14_294_12_8_1	22.5	0.25					
			Ch14_294_12_8_2	22.5	0.50					
			Ch14_295_12_8_4	22.5	1.0					
			Ch14_295_12_8_6	22.5	1.5					
			Ch14_298_12_8_6	22.5	1.5					
			Ch14_298_12_8_8	22.5	2.0					
			Ch14_299_12_8_10	22.5	2.5					
			Ch14_299_12_8_11	22.5	2.75					
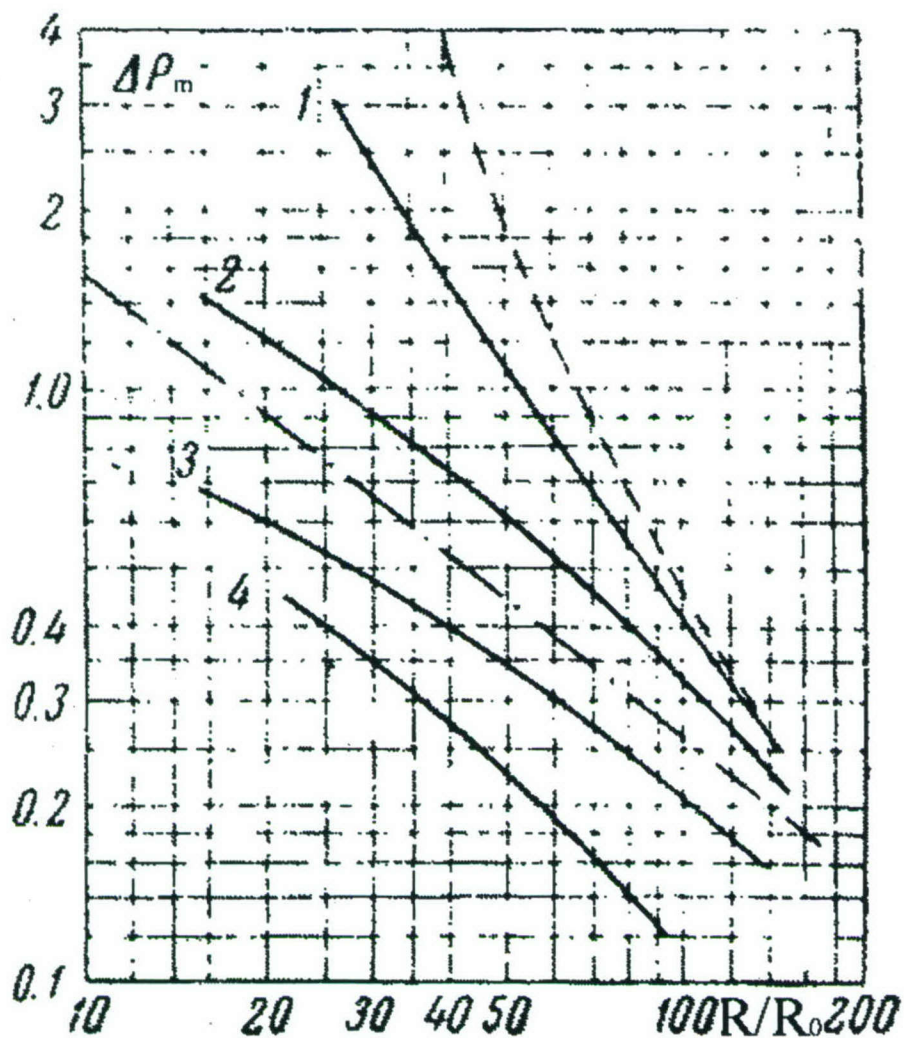
Figure 1.8.1. Dependence of maximum overpressure of shock waves in air, on distance R given in units of charge radius R_0. Water level was $4 R_0$. Curves 1, 2, 3, and 4 correspond to charge depths $H = 0$, 1, 2, and $3R_0$. They are based on the data obtained through the processing of high-speed shadow photos of laboratory explosions of small-weight spherical PETN (in the near zone) and 100-kg TNT charges (in the far zone). Dotted line is calculated using Sadovsky's formula for explosion air, charge on the ground.
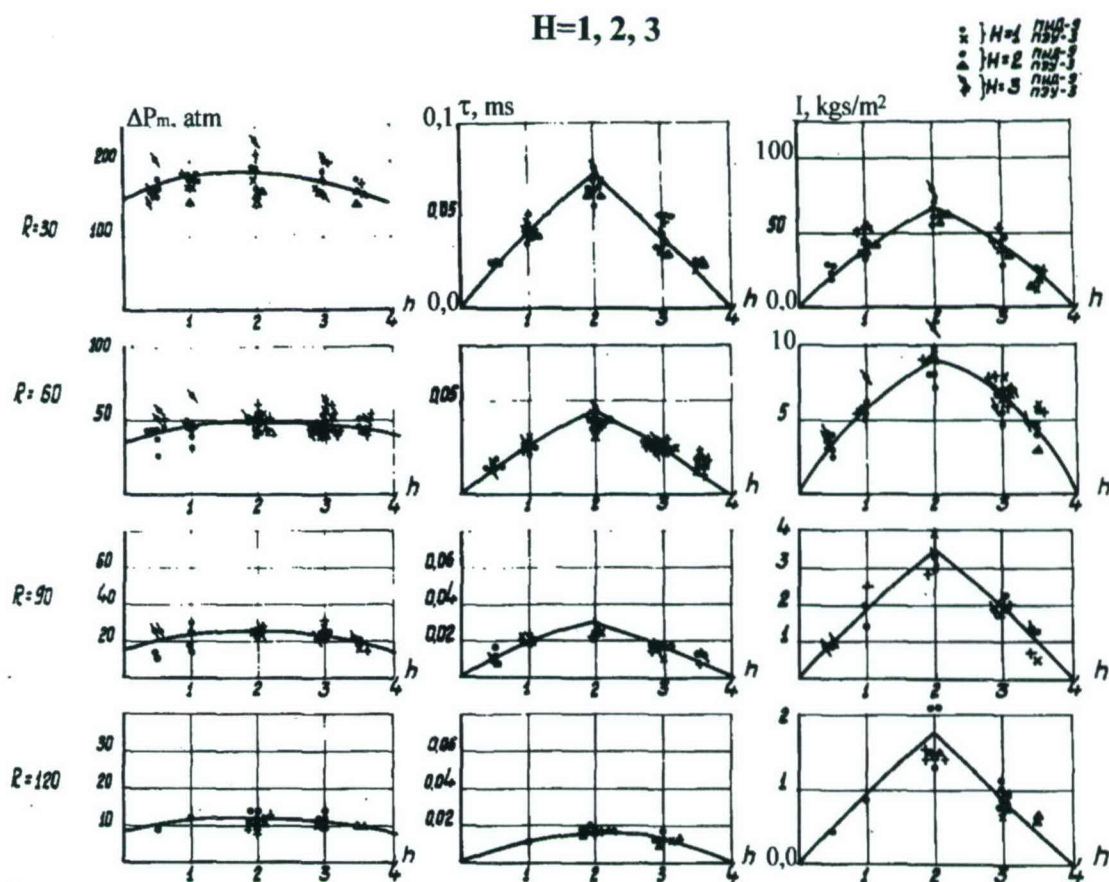
Figure 1.8.2. Dependence of shock-wave parameters in water on gauge depth h, at different distances R from the 100-kg TNT charges, and for three charge depths H = 1, 2, and 3R$_0$. Water level was 4R$_0$. Curves represent the calculated values based on the developed theoretical representations [Note by M. Eneva – I assume that Kozachenko & Khristoforov formulae were used]. R. H and h are in units of charge radius.
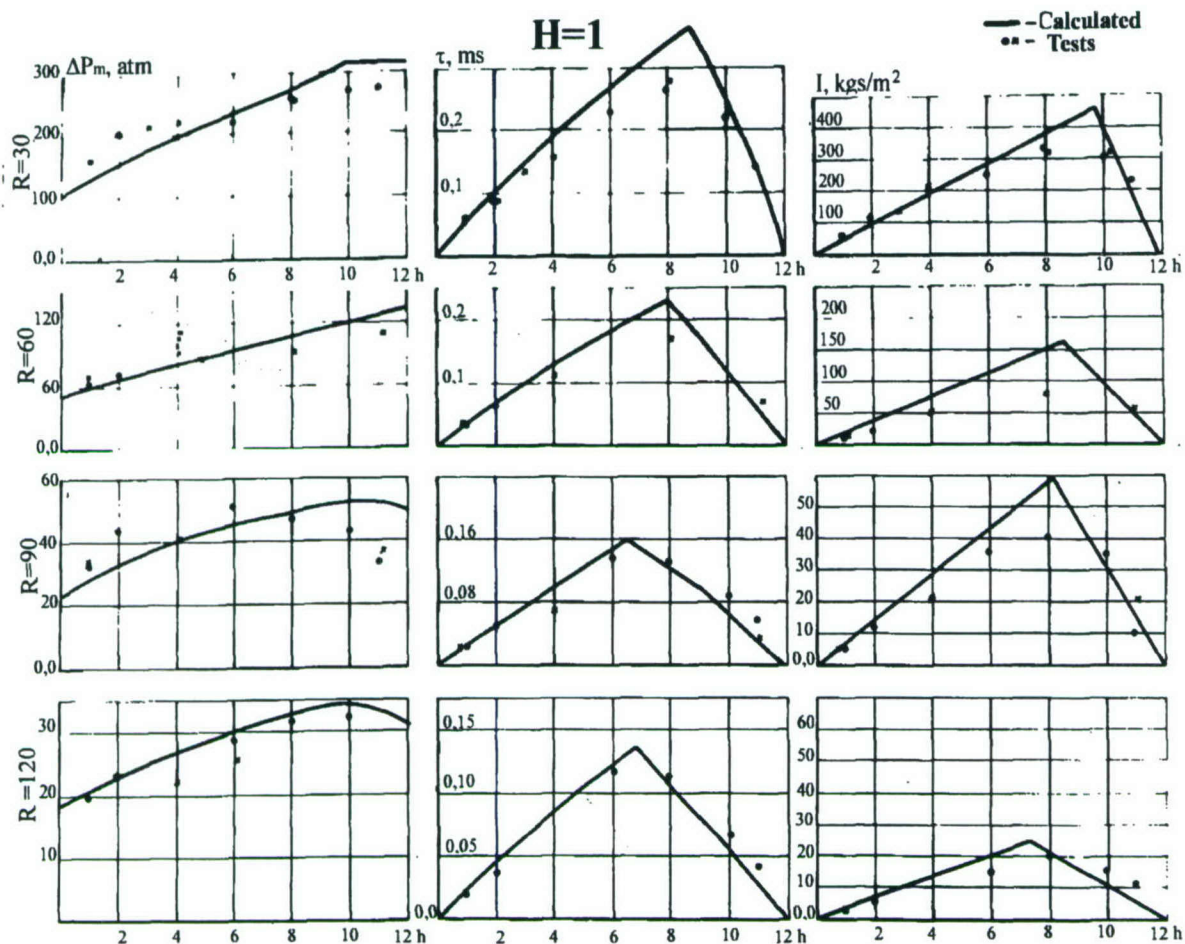
Figure 1.8.3. Calculations (lines) and experimental data (circles – measured with PID-9; crosses –measured with PEU-3) representing the dependence of maximum overpressure, duration and specific impulse of the water shock wave from the 100-kg TNT explosions, on sensor depth h. The charge depth was H = 1R₀ in the water level was 12R₀.
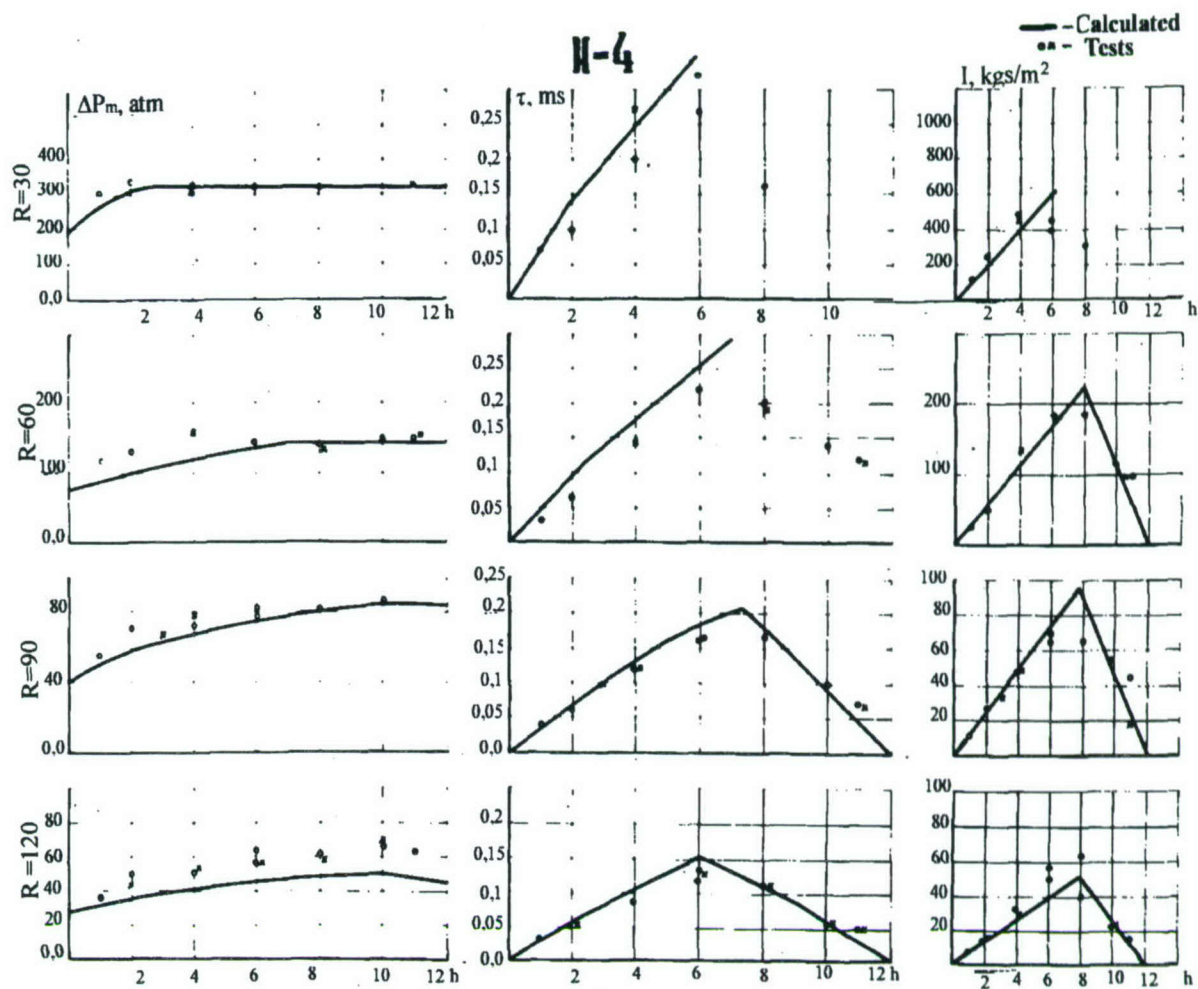
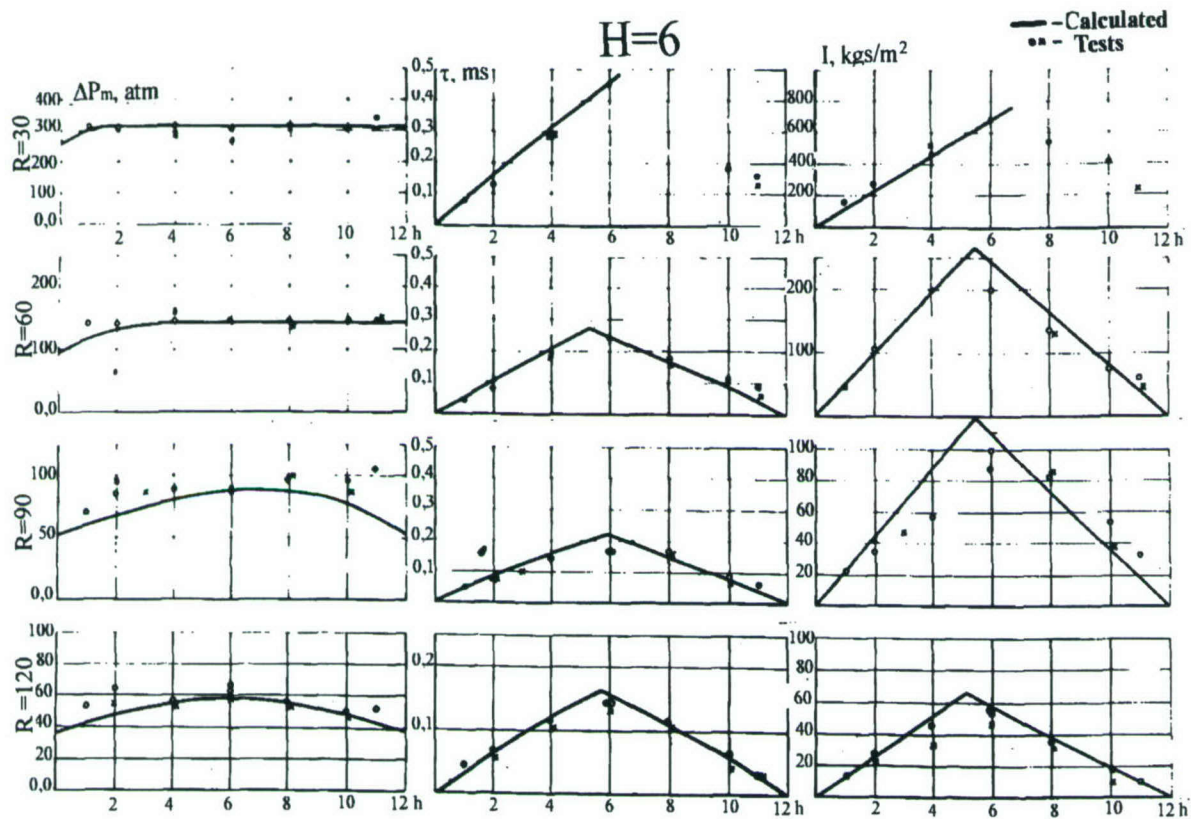Figure 1.8.4. Same as previous figure, but charge depth is H = 4R$_0$. Water level was 12R$_0$.

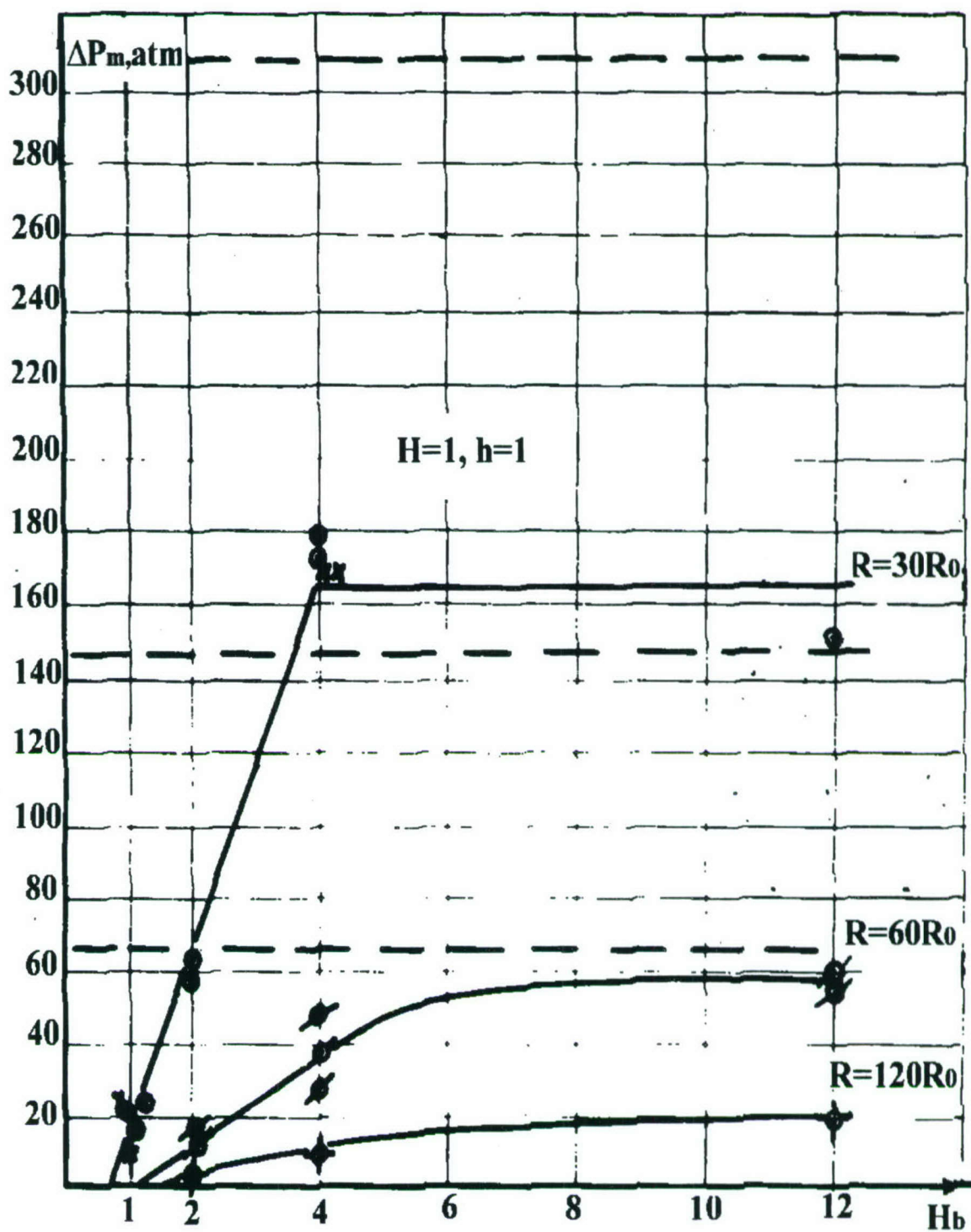**Figure 1.8.5.** Same as two previous figures, but charge depth was H = 6 R₀. Water level was 12R₀.

Figure 1.8.6. Dependence of maximum overpressure of shock wave in water on water level H_b, for three distances. Charge and sensor depths were $1R_0$. Dotted lines show calculations in boundless liquid. H_b, H and h are units of charge radius.
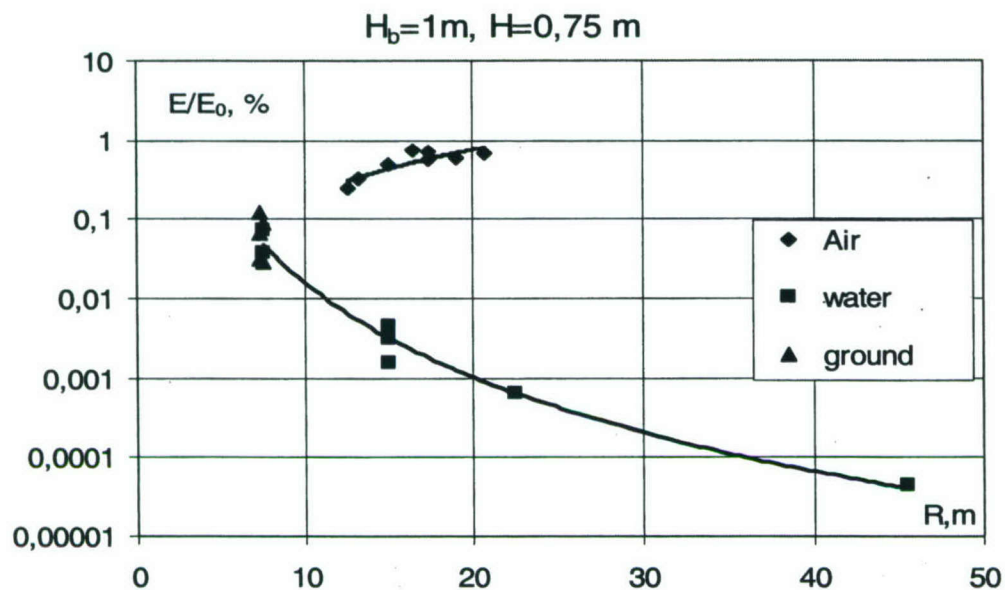
Figure 1.8.7. Dependence of the ratio E/E_0 % of shock-wave energy to energy of 100-kg TNT explosion, on distance R in air, water and ground. Charge depth 0.75 m (i.e., $3R_0$), water level 1 m (i.e., $4R_0$).
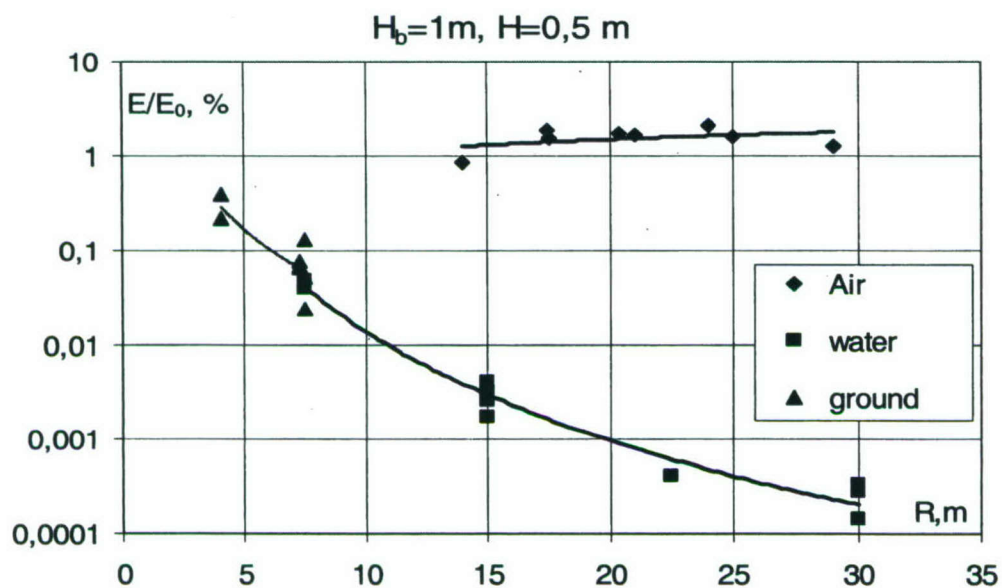

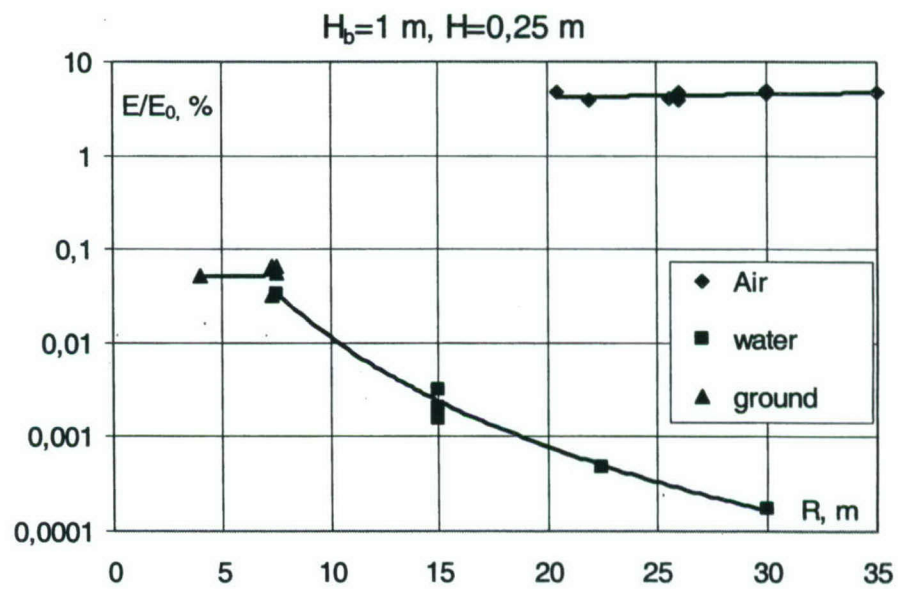. Figure 1.8.8. Same as previous figure, but charge depth is 0.5 m ($2R_0$).

Figure 1.8.10. Same as two previous figures, but explosion depth is 0.25 ($1R_0$).
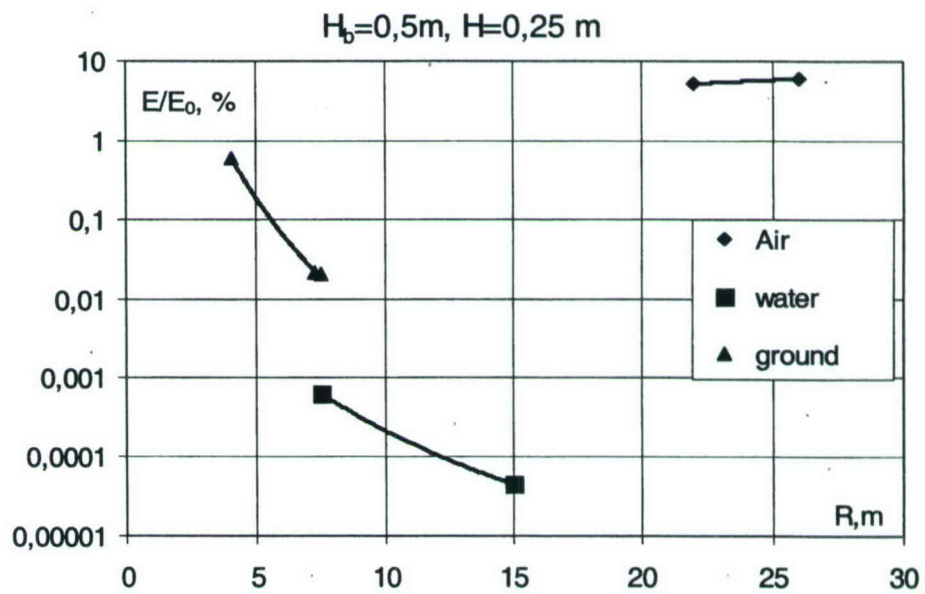

Figure 1.8.11. Same as three previous figures, but charge depth is 0.25 m and water level is 0.5 m.
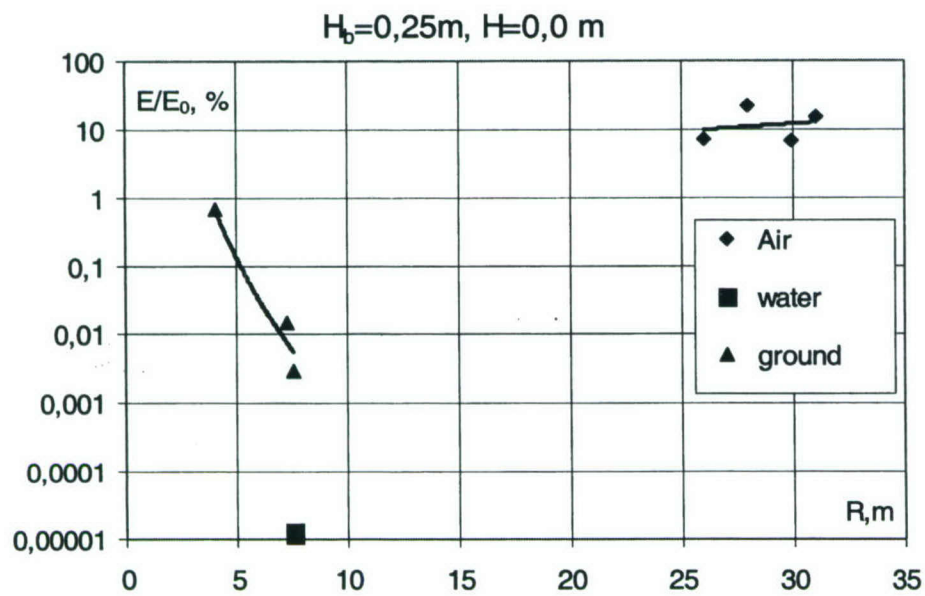
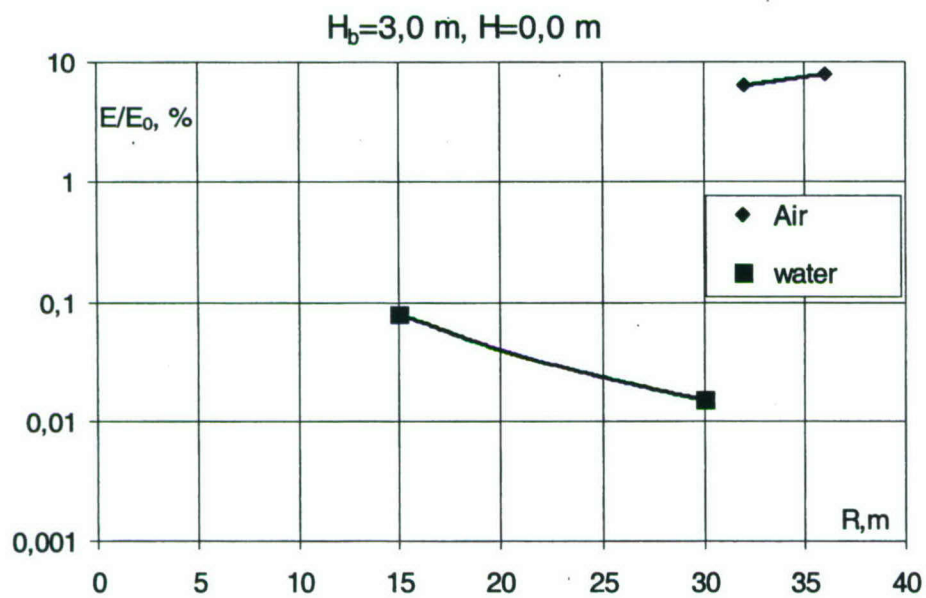Figure 1.8.12. same as four previous figures, but charge is half-immersed (H = 0 m) and water levels is 0.25 m.

Figure 1.8.13. Same as previous figure, but charge is half-immersed (H = 0 m) in a full reservoir (water level 3 m).
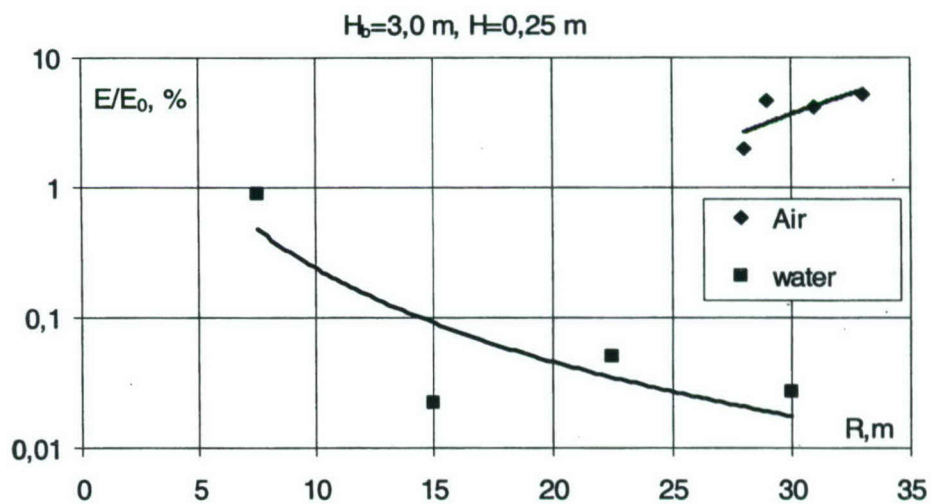
Figure 1.8.14. Same as previous figure, but charge is immersed at depth 0.25 m in a full reservoir (water level 3 m).

2.1.   Characteristics of underground nuclear explosions

Table 2.1 lists underground nuclear explosions, from which underwater measurements have been made. These tests were conducted at two different sites of Novaya Zemlya. Explosions 1, 2 and 3 were conducted in mines on the southern coast of Matochkin Shar strait. Explosion 4 took place in a borehole located Northwest from the Bay of Chernaya. The yields and co-ordinates in the table were obtained from the IDG seismological data. Data from various seismological stations are occasionally quite different.

Explosion 1 (27.10.1966) was conducted inside two adjacent mines, A-1 and A-2, with a time delay of several milliseconds. The complete yield of the explosion was about 800 kt. About 15 minutes after the explosion, radioactive inert gases were vented into the atmosphere, reaching a total quantity of 3.7×10^{17} Bq.

Explosion 2 was the largest underground explosion ever conducted in the USSR. Four devices were simultaneously blown up at a scaled depth of about 95 m/kt$^{1/3}$ in mine A-4, as well as in an additional vertical mine of depth 500 m.

Explosion 3 in mine A-11 was also multi-charge one, including five charges.

A single charge was detonated during explosion 4, conducted at the southern edge of the test site in mine Yu - 5N, practically without any gas leakage into the atmosphere. Seismic waves refracted into water were recorded at various depths and in various frequency bands at station SP-22 in the Arctic Ocean.

Table 2.1. Underground explosions

№	Date	Yield, кт	Coordinates
1	10.27.66	800	73.40N 54.57E
2	09.12. 73	4000	73.32N 54.97E
3	08.29. 74	1500	73.41N 54.93E
4	11.02. 74	2000	70.81N 53.91E

2.2 Measurements of maximum overpressure in water from the coastal underground nuclear explosions 1966-1974

During explosions 1 to 3 at the coast of Matochkin Shar in 1966, 1973, and 1974, peak overpressure of shock waves was measured using membrane gauges MID-3 at six points along the strait and in the Barents Sea. The measurements sites are shown in Figure 2.1.1a. They were at scaled distances $R^0 = R/M^{1/3} = 1000$ to 3000 m/kt$^{1/3}$. Table 2.2 shows the measured values of the maximum overpressure ΔP_m.

Deformation of elastic membrane in MID-3 proportional to overpressure was measured by a lead probe deformation. Air pressure in the sensors was equal to the hydrostatic one.
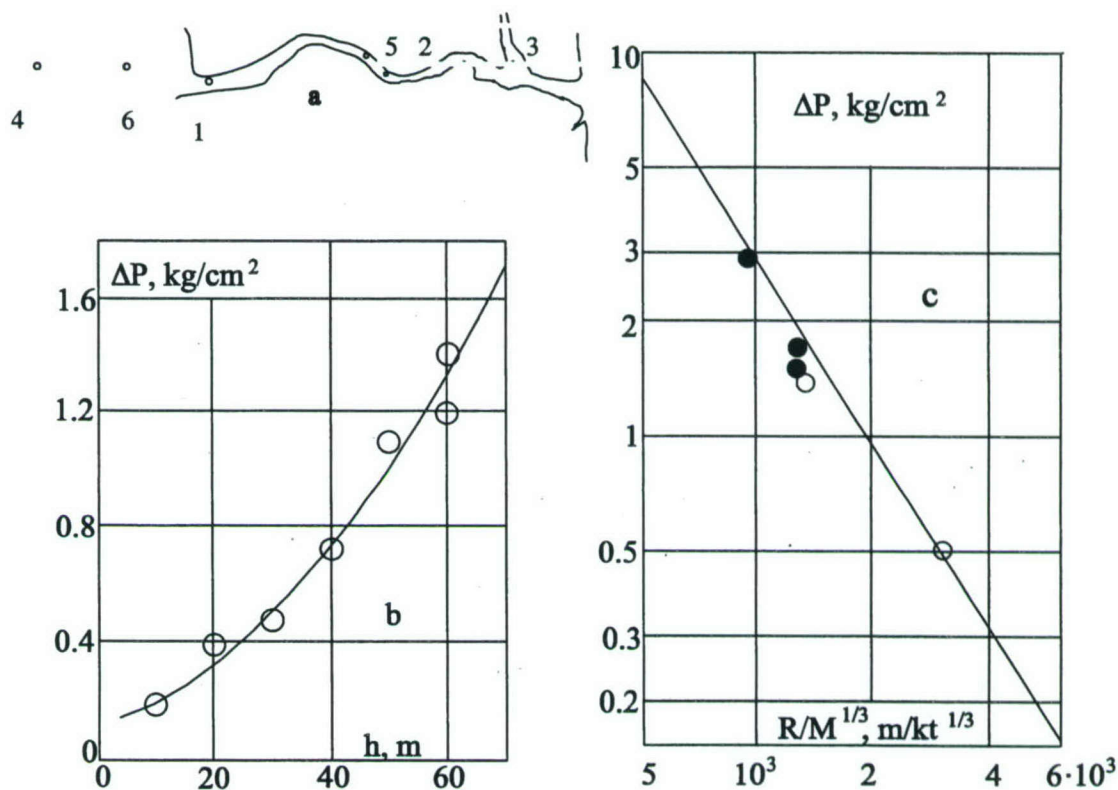

Figure2.2.1a, b, c. Scheme of the locations of the points of observation in the Barents Sea and Matochkin Shar strait during the underground explosions - (a). Shock wave peak overpressure (ΔP_m kg/cm$^{1/2}$) as a function of sensor depth h for explosion №3 at a scaled distance $R^0 = 1350$ m/kt$^{1/3}$ - (b). ΔP_m as a function of $R/M^{1/3}$ m/kt$^{1/3}$ - (c).

Table 2.2.

	Date	[1] measuring points	Depth basin,m	Depth device,m	Distance, $R/Y^{1/3}$, $m/kt^{1/3}$	ΔP_m, kg/cm^2
1	1966	1	21.5	19.5	1280	1.5-1.7
2	1973	2	70	40	985	3.0
3	1973	3	60	40	2460	2.2
4	1973	4	60	40	3150	1.18
5	1974	5	70	10	1350	0.18
6	1974	5	70	20	1350	0.36
7	1974	5	70	30	1350	0.46
8	1974	5	70	40	1350	0.72
9	1974	5	70	50	1350	1.1
10	1974	5	70	60	1350	1.2-1.4
11	1974	6	29	2	3000	-
12	1974	6	29	12	3000	0.33
13	1974	6	29	22	3000	0.51
14	1974	6	29	29	3000	0.76
15	1974	6	29	29	3000	0.66
16	1974	6	29	29	3000	0.50

Figure 2.2.1b shows a characteristic dependence of the shock wave peak overpressure ΔP on sensor depth h as recorded from explosion 3 at point 5, at a scaled distance of R^0=1350 $m/kt^{1/3}$. The peak overpressure ΔP increases from 0.18 to 1.3 atm when the sensor depth h increases from 10 to 60 m (the basin was 70 m deep).

The dependence obtained is characteristic for a wavefield in water, determined by a superposition of the seismic compressional wave refracted from the ground into water and the rarefaction wave reflected from the free surface. The mechanical measurements have allowed us to estimate the evolution in time of sound impulse and energy in water.

The vertical component of the particle velocity of the seismic waves in the near-filed zone, where attenuation depends only little on frequency, is determined by the following expression:

$$V_z = 12000/(R^0)^{1.6} \text{ m/sec.}$$

From this expression one can obtain overpressure in the refracted wave in the form

$$\Delta P = V_z \rho C = 180000/(R^0)^{1.6} \text{ kg/cm}^2,$$

where R^0 is measured in $m/kt^{1/3}$, ρ is the water density and C is the sound speed in water. The solid line in Figure 2.2.1c shows a predicted curve $\Delta P(R^0)$ for the refracted wave. In the range R^0 =1000÷3000 $m/kt^{1/3}$, the curve is consistent with experimental data near the bottom of the basin where the measurements were conducted.

2.3 Results of measurements on station SP-22 at large distances from underground nuclear explosion 11.02.74.

During explosion 4 (11.02. 74) of 2 Mt yield, measurements were conducted at station SP-22 with co-ordinates 82°13.8'N, 185°27.7'E, installed on an ice-floe of a size 2 x 5 km and 26 to 28 m thick, drifting in the Arctic Ocean with bottom depth 2700 to 3000 m. The station was 1500 km away from the continent and 3000 km from the epicentre. Seismic signals refracted into water were measured with hydrophones and seismometers. Preliminary noise measurements had been conducted in the period from 15 October to 1 November, 1974.

The vertical component of the ice motion was measured with an LDF seismometer with natural period of 1 sec and with a borehole seismometer SD-1F at depth of 6 m. Overpressure in the water was measured with four hydrophones with piezoelectric sensors - "Ocenolog-3 and 4", PDS-21 and "Sphere", placed at depths 470 m, 70 m, 190 m, and 270 m, respectively. The latter had a spherical piezosensor 7.5 cm in diameter, with a 0.6-cm thick shell. Its sensitivity was up to 130 μV/dyne/cm^2 and it had a high inner capacity, which allowed to improve its sensitivity at low frequencies and provided a flat amplitude-frequency characteristic. Parallel piezoelements were used in the "Oceanolog-3 and 4" in order to increase the pass band. The hydrophones were connected to transistor preamplifiers with a high entry resistance and amplification factor 20, which were installed in a submersible container. On the exit of the preamplifiers were installed resister dividers with coefficients of signal reduction 3, 30, 300 for "Ocenolog-4", and 1000, 100 and 10 for the remaining hydrophones. The signals from each divider were passed on to a galvanometer of type GB-III-B5, using two-loop oscillographs. The hydrophone signals were passed to three channels with different sensitivity. Time was marked with second marks on the oscillograms. Speed of registration was 22 mm / sec during operation.

The hydrophone characteristics and channel parameters are shown in Table 2.3.1. The asterisk indicates modes in which registration was not carried out. Table 2.3.2 shows the sensitivity of the various links and channels of registration. Table 2.3.3 shows the amplitude - frequency characteristics of the channels of registration.

While registration of the explosion was carried out, an active ice-floe drift took place, with a speed increasing from 1.2 to 6.5 miles per day, with a noise reduction of about two orders. Table 2.3.4 lists the values of noise overpressure recorded on SP-22, measured by four hydrophones before the explosion. The noise overpressure increased with depth from 47 to 350 dyne/cm^2 at frequency of 1.5 Hz. During a passive drift, the noise pressure measured by hydrophone Sfera at depth of 470 m did not exceed 1.7 dyne/cm^2.

Table 2.3.1. Hydrophone characteristics and channel parameters. The asterisk indicates modes in which registration was not carried out; K - amplification factor of amplifier; β - attenuation factor of divider; galvanometers of type ГБ-Ш-Б5 (GB-SH-B5)

Hydrophone name	Depth, m	Gauge type	Number of gauges	K	β	№ Galvanometer
PDS-21	190	PDS-21	1	20	β=1000 β=100 β=10	6937 6820 6832
Okeano-log-3	470	PKS-4	3	20	β=1000 β=100 β=10	6879 6758 6659*
Okeano-log-4	70	PKS-4	4	20	β=3 β=30 β=300	6744 6798 6906
Sfera	270	Sfera	1	20	β=1000 β=100 β=10	6924 6687 6862*

Table 2.3.2. Sensitivity of the various links and channels of the hydrophones

*Hydrophone type and depth	S_p -Piezoelement sensitivity, mcV/dyne/cm^2	S_{ag} Amplifier-galvanometer sensitivity, mm/mcV	S - Hydrophone sensitivity, mm/dyne/cm^2
Okeanolog-4, 70 m	195	0.01	1.05
PDS-21, 190 m	10,7	0.07	0.75
Sfera, 270 m	130	0.013	1.7*
Okeanolog-3, 105 m	105	0.085	8.4
Sfera, 470 m	130	0.08	10.0**

*- Operating mode
**-Trial registration

Table 2.3.3. Amplitude-frequency characteristic of hydrophones. K-sensitivity, mm/dyne/cm^2

f, Hz	"PDC-21", K, mm/dyne/cm^2	"Sfera", Trial registration, K, mm/dyne/cm^2	"Sfera", working mode, K, mm/dyne/cm^2	"Okeanolog-4", K, mm/dyne/cm^2
0.1	0.61			
0.2	0.75	8.2	1.40	4.21
0.25	0.75	8.5	1.48	4.64
0.3	0.74			
0.35	0.73	9.7	1.65	5.0
0.4	0.72			
0.5	0.65	10.0	1.7	5.0
0.6	0.62			

0.7	0.58			
0.75	0.56	9.5	1.61	
0.8	0.54			
0.9	0.5o			
1.0	0.47	8.0	1.37	4.45
1.5	0.35	6.2	1.06	3.35
2.0	0.28	4.8	0.81	2.86
2.5	0.24	4.0	0.68	2.34
3.0	0.21			
4.0	0.15			
5.0	0.1	2.25	0.38	1.26
6.0	0.08	0		
8	0.03			
10	0.02			

Table 2.3.4. Values of noise overpressure on SP-22, measured with four hydrophones before explosion.

	Depth H, m	Frequency, f, Hz	2A, mm	S, sensitivity mm/dyne/cm^2	ΔP, dyne/cm^2	
Okeanolog-4,	70	1.5	50	1.05	47	Active
PDS-21,	190	1.5	100	0.75	133	drift
Sfera,	270	1.5	600	1.70	350	ice-floe
Okeanolog-3	470	1.5	2400	8.4	300	
Sfera	470	1.25	10	7.0	1.4	Passive
		1.6	10-	6.0	1.7	drift
						ice-floe

These hydrophones made it possible to measure overpressures from 40000 dyne/cm^2 to 0.3-0.4 dyne/cm^2 with frequency band from 0.1 to 4 Hz and internal noise level of 30 μV. Since signal-to-internal noise ratio should be higher than 2-3, only signals larger than 1 dyne/cm^2 could be measured. The frequency band for the refracted seismic signal was optimal. Frequencies above 2 Hz were of low amplitude due to higher attenuation in the Earth and were not measured at large distances.

An active drift with mean velocity increase from 1.2 to 6.5 miles per day had begun before the explosion. This increased noise level beneath the ice-floe. During the passive drift phase, the noise level in the 1.2 to 1.6 Hz band was of 1.4 to 1.7 dyne/cm^2 at depth 470 m. During the active drift phase, noise level at 1.5 Hz was 35 to 200 times larger and reached 50 to 350 dyne/cm^2.

Figure 2.3.1a,b shows records obtained by seismographs and hydrophones from a nuclear explosion. Figure 2.3.1a shows records on two channels (1 and 2) of the borehole seismometer SD-1F at depth of 6 m. These records show the vertical motion of the ice-floe, with amplification factors Vg = 3000 and 22000, and there is no deformation by noise. Channels 3 and 4 show records of the overpressure from the explosion made by hydrophone PDS-21 at depth 270 m. at noise level at signal reduction β = 1000 and 100, respectively. On channel 5 the galvanometer

did not work and registration was not carried out. On channels 6, 7, and 8 the signals of hydrophone Oceanolog-4 at depth 70 m registered at $\beta = 3; 30;$ and 300. On channels 6 and 7 signals were at noise level, and signal did not get recorded on channel 8 records due to large signal reduction of $\beta = 300$.

Channels 1 and 2 in Figure 2.3.1b show records from the LDF seismometer in the ice. The vertical motion of the ice-floe was recorded with amplification factors $Vg = 7000$ and 35000, without deformation by noise. Channels 3, 4, and 5 registered overpressure of explosion by hydrophone PDC-21 at depth 190 m, with signal reduction of $\beta = 1000, 100$ and 10, respectively. Due to large signal reduction, $\beta = 1000$, there was no signal on channel 3. Signals on channels 4 and 5 were registered at noise level. Channel 6 was closed. Channels 7 and 8 (hydrophone Oceanolog-3 at depth 470 m) registered at $\beta = 100$ and 1000; signals were at a noise level.

Table 2.3.5 shows the values of overpressure ΔP caused by seismic waves on SP-22; the average of these measurements is 225 dyne / cm^2, which is lower than the noise level. Values $2A = 2a*\beta$, where 2a is double the amplitude of the signal recorded on the oscillogram, and $\Delta P = 2A/S$.

Tables 2.3.6 and 2.3.7 show the digital records of overpressure for hydrophone PDC-21 and Oceanolog-3, record duration is 8 sec. Tables 2.3.8 and 2.3.9 show digital records of the longitudinal wave P made with seismograph LDF ($Vg = 35000$) and SD-1F ($Vg = 2500$), where Vg is the amplification factors of the seismic signals (oscillogram $Vg = 3000$). Record duration is 4.15 and 3.27 sec, respectively.

Table 2.3.5. Overpressure due to seismic waves from the explosion, recorded with hydrophones on SP-22.

	Depth, m	2A. mm	S, mm/dyne/cm^2	ΔP, dyne/cm^2
Okeanolog-4,	70	225	1.05	214
PDS-21,	190	170	0.75	228
Sfera,	270	380	1.70	224
Okeanolog-3	470	1950	8.4	232

The average overpressure above is 225 dyne/ cm^2, below the noise level, vertical displacement of the ice recorded by the seismographs at about 3 μm. Spectral analysis has shown different frequency content of the signal and the noise, making it possible to detect the signal by filtering. Figure 2.3.2 shows the result of filtering of the record of the overpressure wave in the channel with hydrophone Oceanolog-3.

Analysis of P wave signals measured by seismometers established at the surface and at a depth of 6 m was conducted for the initial 2 to 4 sec. Zero phase spectral analysis has revealed direct P and reflected PP waves.

Scaled distance to the station was $R^0 = R/M^{1/3} = 318$ km/$kt^{1/3}$. At this distance, the predicted overpressure in the refracted into water seismic wave, $\Delta P = 330$ dyne/cm^2, is close to the measured overpressure.

Table 2.3.6. Digitised record of overpressure, Hydrophone PDC-21, part of the record - duration 8 s.

-3.0	-57.5	-20	15.6	-95	-47.8
-59	-39	8.0	-4.0	-69	5.8
-99	-48.5	41	-100	-29	8.1
-96	-38	50.2	-106.2	-67	-18.2
-32	-34	20	-74	-101.7	-6.2
-47	-18	12	-26.8	-26.5	12.8
-34	41	45.8	-29	2.0	67.9
-2.0	48	-3.0	-14.8	23	5.0
49.8	-1.0	5.0	-42.6	31.9	13.5
44.5	-61	42.5	-53	41	24
21	-52	22.5	15	25	-34.1
-6.0	-25	27	60	22.5	-42
14.5	-85	23	76	35.3	-21.1
21	-66	-33	43.2	27	34
-20	-28	-49	36.5	-6.5	24
-38	-2.0	-23	27.2	27.5	-44
-47	-57.2	-35	21.5	40	-18
-38	-44	-56	-26	43	40
-18	-49	-45	-59.5	17.5	-8.0
-52	-48	-12.5	-89.8	-6.5	22
49	12	-42.5	-51	-24.8	-15.5
-32	56	-18	-14	-48	-33
6.8	49.5	3.0	-12	-82	-7.5
10	57	-17	11.2	-107.6	1.2
26.5	20	1.5	43.2	-73	0.0
18	-51	29	42	-38	18.2
-16	-44	13.2	48.2	-8.0	
-24	2.0	25	80.3	-12	
-45	2.0	18.2	20	-40	
-70.2	-5.2	6.0	-33	-75	

Table 2.3.7 Digitised record of overpressure, hydrophone Oceanolog-3, duration 8 s, $\Delta t = 0.0457$ s.

-17	-26.5	-47	-2.1	-76.8	-16.1
-76	-43	-37	-39.1	-48	-17.5
-72	-23	-23	-109.2	49.8-	2.5
-45	-60	31	-121	-42	32.1
-32.2	-62	39	-66.9	-7.0	46
-60.2	-10	25	-3.1	15.1	31.8
-60	27	53.5	33.1	35	38.5
20	76	33.5	-12	76	20
-24	105.3	-24	-38	94	-24
-14.2	64	-2.0	9.1	77.6	-14.2

-18	16	61.9	81.1	80	-18
41.8	2.5	99.8	108.8	86	41.8
55.8	-5.0	85.8	95.9	60	55.8
14	-45.5	30	73	45.3	14
-4.0	-64.9	-33.2	27.5	66	-34.8
-42	-29	-37.2	-34,5	104	0.0
-50.5	4.8	-74	-61	115	47.8
-29	15.3	-83	-81.7	82	59
-13.8	5.0	-25	-51.2	36.1	33
-13.5	-27.5	21	-22.2	10	12.8
-19.5	-42	10	-17.9	-27.2	24
-10	14	0.0	-3.0	-78	43.5
46	79	25.5	-22.2	-107.2	43
92	121	20	43.5	-81	28
62.5	100	-1.2	69	-33	2.6
42	24	34	82.9	-31.1	-26
55.9	-6.0	120	58.5	-100	
17.5	-14	134.5	8.1	-113	
-41.5	-50.5	61.5	-41.9	-52.8	
-36	-46	5.0	-85.5	-9.2	

Tables 2.3.8. Digitised record of longitudinal wave P, seismograph LDF (Vg = 35000), duration 4.15 s.

0.9	-10	18	12	18	33
1.0	-18	10	22	5.0	40
1.3	-24	0.0	30	-20	45
1.7	-28	-10	40	-35	46
2.5	-29	-18	46	-60	43
4.0	-27	-25	53	-75	34
6.0	-21	-32	56	-87	26
9.0	-14	-35	58	-89	19
10	-6.0	-35.2	60	-88	13
13	7.0	-32	59	-65	7.0
14	15	-28	56	-49	3.0
13	21	-21	52	-32	-1.8
10	26	-14	47	-10	-2.3
4.0	26.7	-5.0	41	9.0	-2.0
-2.0	24	4.0	30	18	

Table 2.3.9. Digitised record of the longitudinal wave P, seismograph SD-1F (Vg = 2500), duration 3.27 s.

0.0	-2.7	3.8	-7.0	14	-16
0.1	-4.3	3.0	-5.5	14.5	-17
0.4	-5,5	2.0	-3.8	14	-16.8
0.8	-6.0	0.7	-2.0	13.8	-15.5
1.3	-6.2	-1.5	-0.5	13	-13
2.0	-6.0	-3.0	1.5	11	-10
2.5	-5.0	-5.5	3.5	8.0	-7.5
3.0	-4.0	-7.0	5.5	5.0	-4.0
3.0	-2.2	-8.0	7.5	1.0	-1.0
2.5	0.0	-8.8	9.5	-2.0	
1.5	1.5	-9.0	11	-6.0	
0.5	3.0	-8.8	12.5	-9.0	
-0.8	4.0	-8.0	13.5	-13.5	
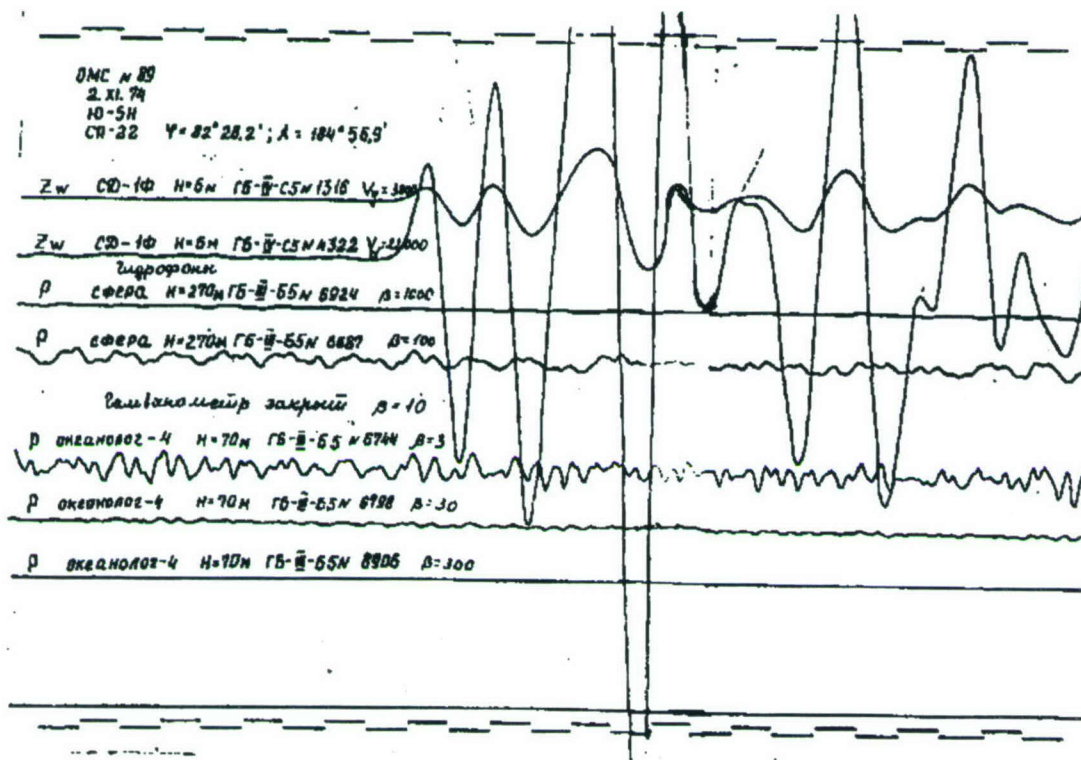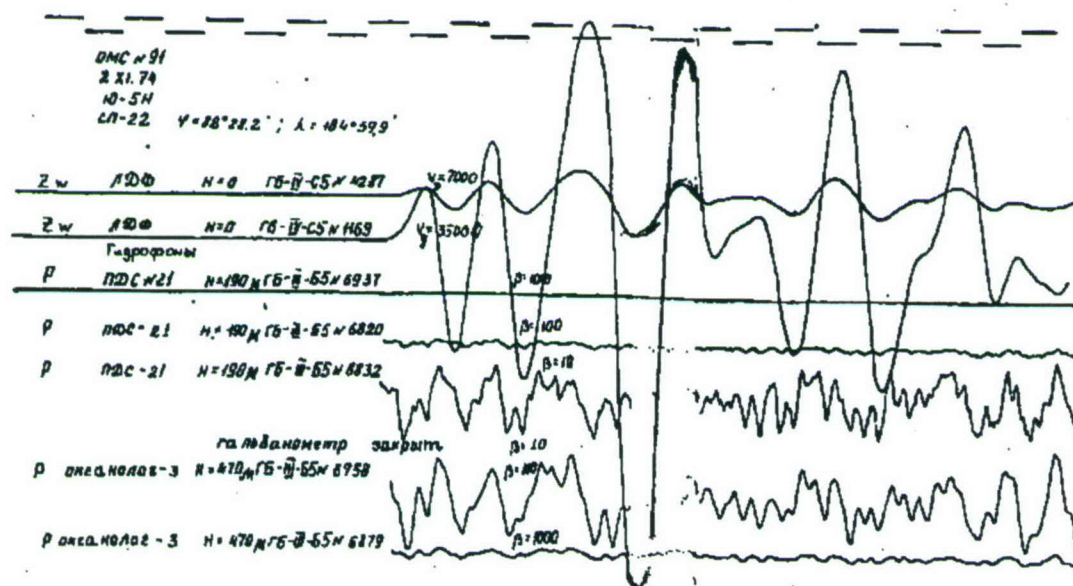
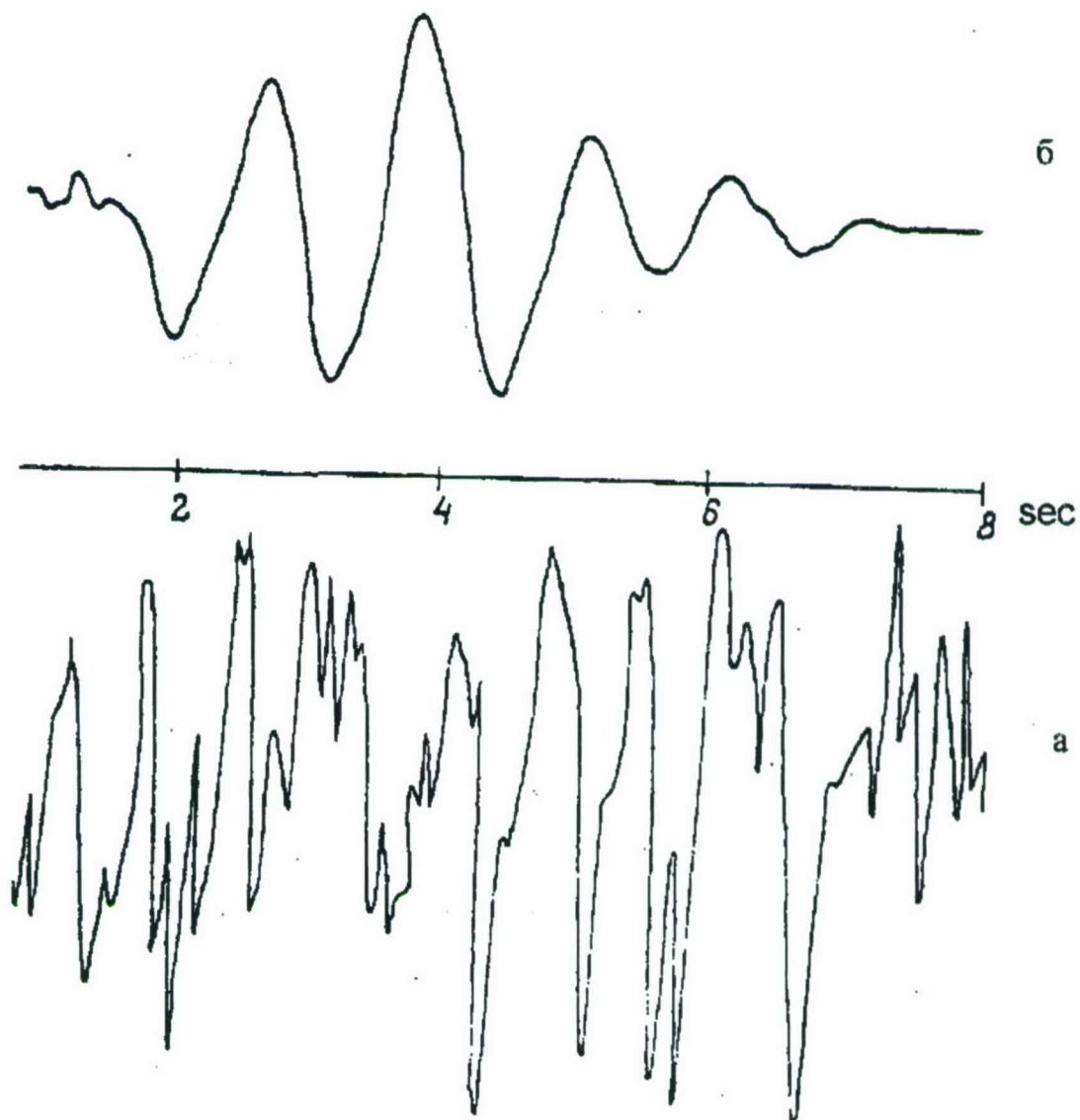Figure 2.3.1a, b. Signals from underground nuclear explosion recorded at SP-22.

Figure2.3.2. Signal recorded by hydrophone PDC-21. (a) Record of a useful signal during an active drift of the ice-floe. (b) Result of filtering.

APPENDIX B
DATA AVAILABLE ELECTRONICALLY

Data received from IDG are made available electronically for download from Maxwell's anonymous ftp-site and on a tape. Three main folders are included: "Final Report", "Edited Russian Text & Data", and "Original Russian Text & Data".

The folder "Final Report" contains MS Word files with the text of the final report (Final_HydroRusia.doc) and Appendices A and B (Final_Appendix_A_B.doc). Appendix A contains an edited version of the Russian text. The final report and Appendices A and B are made available both as hard copies and in electronic form.

The folder "Edited Russian Text & Data" contains in separate sub-folders the edited Russian chapters that comprise Appendix A. The sub-folders are named with the chapter names ("CH1.1_edited", "CH1.2_edited", etc.). Each sub-folder has a MS Word files with the edited text of the respective chapter. Some of the sub-folders contain MS Excel files with data and charts – either edited data (e.g., in folder "CH1.5_edited"), or various computations, including REFMS modeling, used in our analysis (e.g., in folder "CH1.4_edited"). All these files are made available only electronically (anonymous ftp-site and tape).

The folder "Original Russian Text & Data" is also made available only electronically (anonymous ftp-site and tape). It contains text and data as originally received from IDG, without any changes. The folder consists of (1) MS Word files with the latest versions of the original Russian chapters, arranged in separate sub-folders ("Chapter 1.1", "Chapter 1.2", etc.); (2) a folder "Russian Publications" with *.gif files of some Russian articles; and (3) MS Excel files with the original digitized data, included in the folders of the appropriate chapters, as described in the text. As an example, all original digitized data related to shock waves in water are included in MS Excel files in the folder "Chapter 1.4", measurements in air are in folder "Chapter 1.5", and measurements in ground – in folder "Chapter 1.6". These data are not manipulated in any way. When the data are manipulated, the files are included in the previous main folder, "Edited Russian Text & Data". As an example, various computations relevant to shock waves in water are in MS Excel files included in folder "Final Report/CH1.4_edited".

DISTRIBUTION LIST
DTRA 01-19

DEPARTMENT OF DEFENSE

DIRECTOR
DEFENSE INTELLIGENCE AGENCY
BUILDING 6000
WASHINGTON, DC 20340-5100
     ATTN: DTIB

DIRECTOR
DEFENSE RESEARCH AND ENGINEERING
3030 DEFENSE PENTAGON
WASHINGTON, D.C. 20301-3030
     ATTN: DDR&E, ROOM 3E808

DEFENSE TECHNICAL INFORMATION
CENTER
8725 JOHN J. KINGMAN ROAD, SUITE 0944
FT. BELVOIR, VA 22060-6218
2 CYS   ATTN: DTIC/OCA

DEFENSE THREAT REDUCTION AGENCY
8725 JOHN J. KINGMAN ROAD MS 6201
FT. BELVOIR, VA 22060-6201
     ATTN: TDND, CPT. BARBER

OFFICE OF THE SECRETARY OF DEFENSE
CHEMICAL DEMILITARIZATION AND THREAT
REDUCTION OFFICE
1515 WILSON BOULEVARD, SUITE 720
ARLINGTON, VA 22209-2402
     ATTN: P. WAKEFIELD
     ATTN: DR. S. MANGINO

DEPARTMENT OF THE ARMY

US ARMY SMDC
SMDC-TC-YD
P.O. BOX 1500
HUNTSVILLE, AL 35807 3801
     ATTN: B. ANDRE

DEPARTMENT OF THE AIR FORCE

AIR FORCE RESEARCH LABORATORY
29 RANDOLPH ROAD
HANSCOM AFB, MA 01731
     ATTN: RESEARCH LIBRARY
     ATTN: VSBL, R. RAISTRICK

USAF AT USGS
2201 SUNRISE VALLEY DRIVE MS 951
RESTON, VA 20192
     ATTN: R. BLANDFORD
     ATTN: R. JIH

AIR FORCE TECHNICAL APPLICATIONS CTR
1030 S. HIGHWAY AIA
PATRICK AFB, FL 32925 3002
     ATTN: CA/STINFO
     ATTN: TTR, D. CLAUTER

     ATTN: CTI, DR. B. KEMERAIT
     ATTN: TT, DR. D. RUSSELL
     ATTN: TTR, F. SCHULTZ
     ATTN: TTR, G. ROTHE
     ATTN: TTR, V. HSU
     ATTN: DR. B. NGUYEN
     ATTN: DR. E. SMART
     ATTN: DR. G. WAGNER
     ATTN: DR. M. WOODS

DEPARTMENT OF THE NAVY

NAVAL RESEARCH LABORATORY
4555 OVERLOOK AVE, SW, CODE 7643
WASHINGTON, DC 20375 0001
     ATTN: DR. D. DROB

DEPARTMENT OF ENERGY

NATIONAL NUCLEAR SECURITY
ADMINISTRATION
1000 INDEPENDENCE AVE SW
WASHINGTON, DC 20585 0420
     ATTN: L. CASEY
     ATTN: G. KIERNAN

UNIVERSITY OF CALIFORNIA
LAWRENCE LIVERMORE NATIONAL LAB
P.O. BOX 808
LIVERMORE, CA 94551 9900
     ATTN: MS L205, DR. D. HARRIS
     ATTN: MS 205, TECHNICAL STAFF

LOS ALAMOS NATIONAL LABORATORY
P.O. BOX 1663
LOS ALAMOS, NM 87545
     ATTN: MS C335, DR. S. R. TAYLOR

PACIFIC NORTHWEST NATIONAL
LABORATORY
P.O. BOX 999
1 BATTELEE BOULEVARD
RICHLAND, WA 99352
     ATTN: MS P8-20, T. HEIMBIGNER
     ATTN: MS K8-29, DR. N. WOGMAN

SANDIA NATIONAL LABORATAORIES
MAIL SERVICES
P.O. BOX 5800
ALBUQUERQUE, NM 87185 1363
     ATTN: WILLIAM GUYTON

OTHER GOVERNMENT

DEPARTMENT OF STATE
2201 C STREET NW
WASHINGTON, DC 20520
     ATTN: R. MORROW, ROOM 5741

US GEOLOGICAL SURVEY
905 NATION CENTER
12201 SUNRISE VALLEY DR
RESTON, VA 20192
    ATTN: W. LEITH

US GEOLOGICAL SURVEY
345 MIDDLEFIELD RD MS 977
MENLO PARK, CA 94025
    ATTN: S. DETWEILER
    ATTN: DR. W. MOONEY

DOD CONTRACTORS

BATTELLE
MANAGER, ENERGETIC SYSTEMS &
SECURITY TECHNOLOGIES
505 KING AVE
COLUMBUS, OH 43201-2693
    ATTN: NEAL OWENS (7-2-081)

BBN CORPORATION
1300 N 17TH STREET, SUITE 1200
ARLINGTON, VA 22209
    ATTN: DR. D. NORRIS
    ATTN: R. GIBSON
    ATTN: J. PULLI

CENTER FOR MONITORING RESEARCH
1953 GALLOWS ROAD, SUITE 260
VIENNA, VA 22182 3997
    ATTN: DR. K. L. MCLAUGLHLIN
    ATTN: DR. R. WOODWARD
    ATTN: DR. R. NORTH
    ATTN: DR. X. YANG
    ATTN: LIBRARIAN

ENSCO, INC.
P.O. BOX 1346
SPRINGFIELD, VA 22151 0346
    ATTN: D. BAUMGARDT
    ATTN: Z. DER

WESTON GEOPHYSICAL CORPORATION
27 BEDFORD ST, SUITE 102
LEXINGTON, MA 02420
    ATTN: DR. D. REITER
    ATTN: J. LEWKOWICZ
    ATTN: DR. A. ROSCA
    ATTN: DR. I. TIBULEAC
    ATTN: M. JOHNSON

WESTON GEOPHYSICAL CORPORATION
917 ELLIS AVE SUITE 222
LUFKIN, TX 75904
    ATTN: DR. J. BONNER

WESTON GEOPHYSICAL CORPORATION
411 NW 26TH ST
GAINESVILLE, FL 32607
    ATTN: DR. S. RUSSELL

ITT INDUSTRIES
ITT SYSTEMS CORPORATION
1680 TEXAS STREET SE
KIRTLAND AFB, NM 87117 5669
2 CYS   ATTN: DTRIAC
    ATTN: DARE

TITAN
1900 CAMPUS COMMONS DR SUITE 400
RESTON, VA 20191
    ATTN: DR. C. P. KNOWLES

MISSION RESEARCH CORPORATION
8560 CINDERBED ROAD, SUITE 700
NEWINGTON, VA 22122
    ATTN: DR. M. FISK

MULTIMAX, INC
1441 MC CORMICK DRIVE
LANDOVER, MD 20785
    ATTN: DR. I. N. GUPTA
    ATTN: W. RIVERS

MULTIMAX, INC
1090 N HIGHWAY A1A SUITE D
INDIANLATIC, FL 32903
    ATTN: DR. H. GHALIB

SCIENCE APPLICATIONS INTERNATIONAL
CORP
10260 CAMPUS POINT DRIVE
SAN DIEGO, CA 92121 1578
    ATTN: DR.M. ENEVA
    ATTN: DR. G. E. BAKER
    ATTN: DR. J. STEVENS
    ATTN: DR. D. ADAMS

SCIENCE APPLICATIONS INT'L CORP
1227 S. PATRICK DR SUITE 110
SATELITTE BEACH, FL 32937
    ATTN: DR. M. FELIX
    ATTN: DR. H. GIVEN

URS CORPORATION
566 EL DORADO STREET
PASADENA, CA 91109 3245
    ATTN: DR. C. SAIKIA
    ATTN: DR. G. ICHINOSE

**DIRECTORY OF OTHER (LIBRARIES AND
UNIVERSITIES)**

BOSTON COLLEGE
INSTITUTE FOR SPACE RESEARCH
140 COMMONWEALTH AVENUE
CHESTNUT HILL, MA 02167
    ATTN: DR. D. HARKRIDER

BROWN UNIVERSITY
DEPARTMENT OF GEOLOGICAL SCIENCES
75 WATERMAN STREET
PROVIDENCE, RI 02912 1846
    ATTN: PROF. D. FORSYTH

CALIFORNIA INSTITUTE OF TECHNOLOGY
DIVISION OF GEOLOGY & PLANETARY
SCIENCES
PASADENA, CA 91125
    ATTN: PROF. D. HELMBERGER
    ATTN: PROF. THOMAS AHRENS

UNIVERSITY OF CALIFORNIA BERKELEY
281 MCCONE HALL
BERKELY, CA 94720 2599
    ATTN: PROF. B. ROMANOWICZ
    ATTN: DR. D. DREGER

UNIVERSITY OF CALIFORNIA
DAVIS, CA 95616
    ATTN: R.H. SHUMWAY, DIV
        STATISTICS

UNIVERSITY OF CALIFORNIA SAN DIEGO
LA JOLLA, CA 92093 0225
    ATTN: DR.L. DEGROOT - HEDLIN
    ATTN: DR. M. HEDLIN
    ATTN: PROF. F. VERNON
    ATTN: PROF. J. BERGER
    ATTN: PROF. J. ORCUTT
    ATTN: DR. G. D'SPAIN

UNIVERSITY OF CALIFORNIA SANTA CRUZ
INSTITUTE OF TECTONICS
SANTA CRUZ, CA 95064
    ATTN: DR. R. S. WU
    ATTN: PROF. T. LAY

UNIVERSITY OF COLORADO BOULDER
DEPT OF PHYSICS, CAMPUS BOX 390
BOULDER, CO 80309
    ATTN: DR.R. ENGDAHL
    ATTN: M. RITZWOLLER
    ATTN: PROF. C. ARCHAMBEAU

COLUMBIA UNIVERSITY
LAMONT DOHERTY EARTH OBSERVATORY
PALISADES, NY 10964
    ATTN: DR. J. XIE
    ATTN: DR. W. Y. KIM
    ATTN: PROF. P.G. RICHARDS
    ATTN: DR. M. TOLSTOY

UNIVERSITY OF CONNECTICUT
DEPARTMENT OF GEOLOGY & GEOPHYSICS
STORRS, CT 06269 2045
    ATTN: PROF. V.F. CORMIER, U-45,
        ROOM 207

CORNELL UNIVERSITY
DEPARTMENT OF GEOLOGICAL SCIENCES
3126 SNEE HALL
ITHACA, NY 14853
    ATTN: PROF. M.A. BARAZANGI

HARVARD UNIVERSITY
HOFFMAN LABORATORY
20 OXFORD STREET
CAMBRIDGE, MA 02138
    ATTN: PROF. A. DZIEWONSKI
    ATTN: PROF. G. EKSTROM

INDIANA UNIVERSITY
DEPARTMENT OF GEOLOGICAL SCIENCES
1005 10TH STREET
BLOOMINGTON, IN 47405
    ATTN: PROF. G. PAVLIS

IRIS
1200 NEW YORK AVENUE, NW SUITE 700
WASHINGTON, DC 20005
    ATTN: DR. D. SIMPSON
    ATTN: DR. VAN DER VINK

IRIS
1408 NE 45TH ST #201
SEATTLE, WA 98105
    ATTN: DR. T. AHERN

MASSACHUSETTS INSTITUTE OF
TECHNOLOGY
EARTH RESOURCES LABORATORY
42 CARLETON STREET
CAMBRIDGE, MA 02142
    ATTN: DR. W. RODI
    ATTN: PROF. M.N. TOKSOZ

MICHIGAN STATE UNIVERSITY LIBRARY
450 ADMINISTRATION BUILDING
EAST LANSING, MI 48824
    ATTN: K. FUJITA

NEW MEXICO STATE UNIVERSITY
DEPARTMENT OF PHYSICS
LAS CRUCES, NM 88003
    ATTN: PROF. J. NI
    ATTN: PROF. T. HEARN

NORTHWESTERN UNIVERSITY
DEPARTMENT OF GEOLOGICAL SCIENCES
1847 SHERIDAN RD
EVANSTON, IL 60208
    ATTN: PROF. E. OKAL

PENNSYLVANIA STATE UNIVERSITY
GEOSCIENCES DEPARTMENT
403 DEIKE BUILDING
UNIVERSITY PARK, PA 16802
    ATTN: PROF. C. AMMON
    ATTN: PROF. S. ALEXANDER
    ATTN: DR. A. NYBLADE

DISTRIBUTION LIST
DTRA 01-19

SAN DIEGO STATE UNIVERSITY
DEPARTMENT OF GEOLOGICAL SCIENCES
SAN DIEGO, CA 92182
  ATTN: PROF. S. M. DAY

SOUTHERN METHODIST UNIVERSITY
DEPARTMENT OF GEOLOGICAL SCIENCES
P.O. BOX 750395
DALLAS, TX 75275
  ATTN: B. STUMP
  ATTN: E. HERRIN
  ATTN: P. GOLDEN

UNIVERSITY OF HAWAII- MANOA
P.O. BOX 1599
KAILUA-KONA, HI 96745 1599
  ATTN: DR. M. A. GARCES

UNIVERSITY OF MISSISSIPPI
1 COLISEUM DRIVE
UNIVERSITY, MS 38677
  ATTN: PROF. H. BASS

UNIVERSITY OF SOUTHERN CALIFORNIA
520 SEAVER SCIENCE CENTER
UNIVERSITY PARK
LOS ANGELES, CA 90089 0483
  ATTN: PROF. C. G. SAMMIS
  ATTN: PROF. T. JORDAN

WASHINGTON UNIVERSITY
DEPARTMENT OF EARTH PLANT SCIENCE
ONE BROOKINGS DRIVE
SAINT LOUIS, MO 63130 4899
  ATTN: DR. G. SMITH

UNIVERSITY OF WISCONSIN MADISON
1215 W DAYTON ST
MADSION, WI 53706 1600
  ATTN: DR. C. THURBER

ST LOUIS UNIVERSITY
P.O. BOX 8148
PIERRE LACLEDE STATION
ST LOUIS, MO 63156 8148
  ATTN: PROF. B. J. MITCHELL
  ATTN: PROF. R. HERRMAN

UNIVERSITY OF MEMPHIS
3890 CENTRAL AVE
MEMPHIS, TN 38152
  ATTN: DR. J. PUJOL
  ATTN: DR. C. LANGSTON

UNIVERSITY OF TEXAS AUSTIN
P.O. BOX 7726
AUSTIN, TX 78712
  ATTN: DR. J. PULLIAM
  ATTN: DR. M. SEN

UNIVERSITY OF TEXAS EL PASO
DEPT OF GEOLOGICAL SCIENCES
EL PASO, TX 79901
  ATTN: PROF. G. KELLER
  ATTN: DR. D. DOSER
  ATTN: DR. A. VELASCO